Geochemical and petrological investigation into the magmatic system at Soufrière Hills Volcano, Montserrat

A thesis submitted to the

School of Environmental Sciences

of the

University of East Anglia

in partial requirement for the degree of

Doctor of Philosophy

Melissa Plail

29 November 2013

Abstract

Andesite lavas from the current eruption of the Soufrière Hills Volcano, Montserrat exhibit evidence for magma mingling, related to the intrusion of mafic magma at depth. The processes of mass transfer and flux of material involved in the interaction between mafic and silicic magmas are crucial for understanding eruption dynamics. Detailed textural, petrological and geochemical analyses coupled with field observations are used to define a classification scheme for mafic enclave types in erupted andesite from phase V (2009–2010). Type A are closest to a mafic end-member, whereas type B are significantly hybridised. Type A quench crystallisation is driven by rapid thermal equilibration during injection into the andesite. Type B enclaves form from a slower cooling vesiculating hybridised melt layer. Type C, are a composite of types A and types B, representing an interface between the types. Geochemical modelling shows that since the start of the current eruption that the dominant control on the range of enclave bulk compositions has changed from fractional crystallisation to mixing of the mafic end-member and host andesite. A change in selected elements concentrations in the mafic end-member is observed from phases I to III, halting in phase V. Volatile flux from the mafic to andesite magmas plays a vital role in eruption dynamics, but evidence for vapour transport in the erupted lavas is rarely preserved. Geochemical and petrological evidence is presented for the segregation and transport of metal-bearing vapour in shear fractures generated in the shallow conduit or dome during magma ascent. Elevated metal concentrations (Cu, Au, Ag, Pb, Zn) indicate magmatic vapours transport. Volatiles were resorbed into the partial melt generated during frictional heating (>1000 °C) at the slip surface as a peraluminous partial melt recrystallised. The shear zones provide evidence for degassing and an insight into controls on eruption style.

Contents

Appendix

List of Figures

Chapter 1

Chapter 2

Chapter 3

Chapter 4

Chapter 5

Chapter 6

List of Tables

Acknowledgements

Chapter 1: Introduction

Andesites are the most common volcanic rock type erupted at convergent margins, and as such are regarded as fundamental to the formation and evolution of continental crust (Rudnick, 1995). The generation of andesitic compositions is widely believed to take place via multiple episodes of mixing between felsic and mafic magmas (*e.g.* Eichelberger *et al., 2000;* Reubi & Blundy, 2009) or assimilation of mafic plutonic roots by ascending silicic melts (Dungan & Davidson, 2004). Petrographic evidence for such processes can be observed, for example, in the form of complex zoning patterns in adjacent crystals that may have differing age histories and melt inclusion compositions or via the presence of cumulate nodules and mafic enclaves. These observations indicate that andesite magma bodies are essentially hybrids that form incrementally over time, rather than by simple fractionation (*e.g.* Davidson *et al.,* 2005; Reubi & Blundy, 2009; Miller *et al.,* 2010). However, the process of generating almost uniform hybrid andesitic bulk compositions that are erupted at the surface is still not fully understood. The study of an ongoing andesitic eruption involving magma mixing is a unique opportunity to examine the process and effect of mafic magma transfer to andesite. Acid-intermediate eruptions, fuelled by additions of heat and volatiles from depth, can produce hazardous eruptions at the surface (*e.g.* Mt. St Helens 1980; Pinatubo 1991; Merapi 2010), providing additional motivation for this work.

1.1 Remobilisation of andesitic mush

Magma bodies of andesitic composition can reside for long periods in the shallow crust. Extensive crystallisation and degassing of ascending crystal-rich intermediate magma will lead to the formation of rheologically-stiff crystal mushes, where convection is inhibited owing to their high bulk viscosities (Huber *et al.,* 2010). Andesitic magma bodies can therefore stall and remain stored in the shallow crust for long periods of time (Annen *et*

al., 2006). An injection of hotter volatile-rich mafic magma is often inferred to be the catalyst required to reheat and remobilise or 'defrost' these crystal-rich magma bodies, thus triggering an eruption (*e.g.* Burgisser & Bergantz, 2011). Many andesitic lava dome-forming eruptions such as Unzen, Japan (1991-1995), Pinatubo, Philippines (1991) and Augustine volcano, Alaska (2006) have had mafic magma recharge ascribed as the eruption trigger (Pallister *et al.,* 1992; Nakamura, 1995; De Angelis *et al.,* 2013). The transfer of heat and gas from the intruding mafic magma is the key component of models that invoke remobilisation of a cooler crystal mush. The transfer of fluids rich in H_2O, CO_2 and sulphur from the intruding mafic magma into the andesite can increase the mass and volume of the vapour phase in the host magma. These gases may migrate through the chamber as a fluid phase efficiently advecting heat to the andesitic magma (*e.g.* Bachman & Bergantz, 2006). The presence of mafic enclaves (*e.g.* Fig.1.1; Bacon, 1986; Clynne, 1999; Browne *et al.,* 2006b), phenocryst disequilibria (*e.g.* Singer *et al.,* 1995; Tepley *et al.,* 1999; Nakagawa *et al.,* 2002) and 'excess sulphur' emissions (Wallace, 2001; Christopher et al., 2010; Wallace & Edmonds, 2011) observed in many andesitic lavas are invoked as key evidence of mass, volatile and heat transfer from an intruding mafic magma.
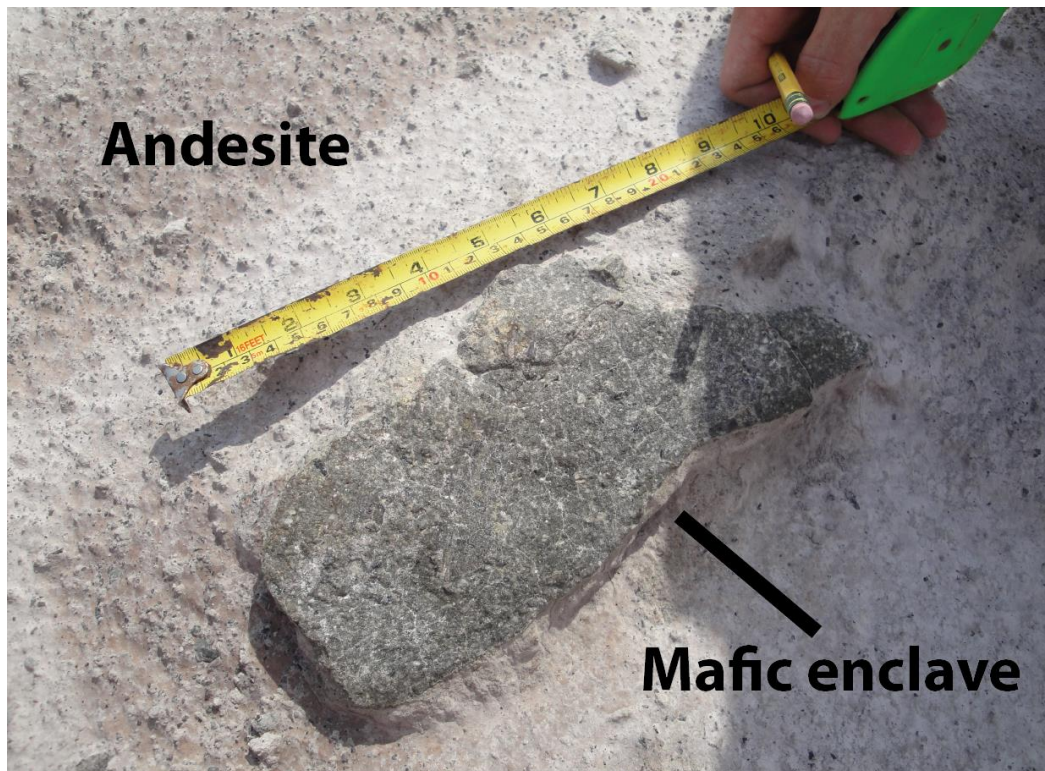
Figure 1.1: Example of a mafic enclave from Soufrière Hills Volcano, Montserrat in andesitic lava.

Models constraining the complex process of magma mixing vary hugely in the extent of physical and chemical interaction between mafic and silicic end-members; these can range from the formation of a vesiculating mafic layer at the base of the chamber (*e.g.* Eichelberger, 1980; Thomas & Tait, 1997) to the generation of a thermal plume able to transport mafic material to the upper reaches of chamber via viscous coupling (Snyder & Tait, 1996). These different processes have different implications for the style of formation of mafic enclaves; therefore the petrology of mafic enclaves can be used to constrain the nature of the interaction between mafic and andesitic magmas, and determine to what degree the two magmas have physically mixed. However, it is not always the case that eruption will occur after an apparent intrusion of mafic magma from depth (Werner *et al.,* 2011), and therefore it is crucial to have a better understanding of this dynamic process.

1.2 Significance of gas transport

One clear physical indication of magma interaction occurring at depth in the volcanic system is the emission of sulphur gases 'in excess' of that resulting from degassing of the host magma (*e.g.* Wallace, 2001; Christopher et al., 2010; Wallace & Edmonds, 2011). This results from decoupled release of gas from unerupted magma that is degassing at depth. Degassing of magma in the shallow magmatic system has a key role in determining how the ascending magma will erupt. As magma ascends, volatile exsolution occurs as a result of decreasing pressure. Viscous retardation of bubble growth may then lead to overpressures in the shallow magmatic system and subsequent explosive activity if sufficient permeability cannot develop quickly enough to circumvent this (*e.g.* Melnik & Sparks, 1999; Eichelberger, 1995, Gonnermann & Manga, 2007). Abrupt transitions in eruptive behaviour in andesitic lava domes from effusive to explosive activity are highly dependent on the mechanisms that allow volatile escape from the magma at shallow pressures *i.e.* the conduit (*e.g.* Jaupart & Allegre 1991*;* Woods & Koyaguchi, 1994; Melnik & Sparks, 1999; Sparks, 2003; Okumura *et al.,* 2013). Short term cyclic changes in eruption style are probably governed by complex coupled feedbacks between magma chamber pressure, and the degassing and crystallisation of ascending magma in the conduit, which can lead to abrupt changes in magma rheology, and subsequent development of behaviour of stick-slip behaviour of the ascending magma plug at the conduit walls (*e.g.* Melnik & Sparks, 1999; Denlinger & Hoblitt, 1999; Sparks *et al.,* 2000). For example, cyclic activity of dome growth and explosive eruptions at Lascar Volcano, Chile from

1984 to 1996 was linked to the changes in the permeability of the dome; where vigorous degassing via fumaroles was observed during beginning of the cycles of lava extrusion, and rapidly decreased before explosions (Matthews *et al.,* 1997). Therefore mechanisms that may promote efficient volatile escape as andesitic magma ascends in the conduit, such as the development of a permeable magma foam (*e.g.* Taylor *et al.,* 1983; Eichelberger, 1986) or fracture networks (*e.g.* Gonnermann & Manga, 2003; Tuffen *et al.,* 2003), which may promote efficient volatile escape, are not only important for our understanding of conduit dynamics, but are also critical for the understanding of hazardous switches in eruption style.

1.3 Significance of mafic enclaves

The presence of mafic enclaves in host lavas has been used to assess the degree of interaction between magmas (*e.g.* Bacon 1986; Koyaguchi 1986; Clynne 1999; Holness *et al.,* 2005; Martin *et al.,* 2005; Browne *et al.,* 2006). In this thesis the term 'enclave' is used to describe undercooled magmatic inclusions, which have formed as result of incomplete mixing (mingling) between coexisting magmas, where 'globules or fragments' of the intruding magma are entrained into a 'host magma'. Andesites are highly differentiated and as mafic enclaves may be geochemically the closest relation to the primary mantle-derived magma they may provide a snapshot into lower crustal processes. For example, variations in Rare Earth Element ratios (*e.g.* La/Yb and Dy/Yb) in arc magmas have been used determine the degree of 'cryptic amphibole fractionation' at mid-crustal levels (Davidson *et al.,* 2007). A large degree of amphibole fractionation at depth could act as 'sponge' for water from mantle-derived melts as amphibole contains H_2O, or could be a source for large volumes of hydrous melt as the amphibole stability curve is crossed thus increasing the potential for explosivity in derived magmas (Davidson *et al.,* 2007).

Mafic enclaves not only provide insights into lower crustal processes, but also have been primarily studied to assess the nature of the interaction between the coexisting magmas in the shallow magmatic system (*e.g.* Bacon 1986; Koyaguchi 1986; Clynne 1999; Holness *et al.,* 2005; Martin *et al.,* 2005; Browne *et al.,* 2006). The range of compositions and textures in a suite of mafic enclaves may preserve information on the dynamics and style of the mixing/mingling process, where the contrast in physical properties such as viscosity, density and temperature can be determined between magmas. A few prior studies

of mafic enclaves have investigated these processes by assigning enclave types on the basis of texture, petrology and geochemistry. In a study by Browne *et al.,* (2006) which examines the petrology and textures of mafic enclaves from Unzen, Japan, two types of enclaves were identified. The first enclave type 'equigranular' (medium-grained microphenocrysts in a matrix glass) was interpreted to have formed as a result of slower cooling in the mafic intrusion interior. In contrast, the second enclave type 'porphyritic' (large phenocrysts in a matrix of glass and smaller acicular crystals), defined by the presence of phenocrysts derived from the host dacite with uniform sized overgrowth rims, was interpreted to be the result of a single mixing event at the interface between the intruding and host magma. Geochemical analysis, on the suite of major and trace element concentrations from the 'equigranular' and 'porphyritic' enclave types using Polytopic Vector Analysis, identified two separate mafic end-member compositions linked to the enclave types (Vogel *et al.,* 2008). This is interpreted as evidence for repeated intrusion from two distinct mafic magmas over the lifetime of the volcano (Vogel *et al.,* 2008).

Other studies have examined the complex changes that can occur during mixing between magmas. A classic example of this complexity is observed from the study of volcanic material erupted over the course of 3 days during the Lassen Peak, California 1915 eruption described by Clynne (1999). Four different rock types (andesitic enclaves, black dacite, light dacite and dark andesite) are identified all showing evidence for magma mixing. These are interpreted to have been generated and in a specific order (Clynne, 1999): (1) Basaltic andesite intruded into the host dacite, where a partially hybridised andesitic foam layer formed. Undercooled andesitic enclaves derived from the foam layer were entrained (mingled) into the host light dacite. (2) Disaggregation of the andesitic enclaves into the host dacite produced the hybridised black dacite. (3) The temperature and viscosity contrast between the hybridised black dacite and intruding andesitic reduced. This enabled more efficient mixing to occur, resulting in the generation of a dark andesite layer. This sequence is interpreted as evidence for the inverse tapping of the magma reservoir, where the enclaves resided near the base of the chamber (Clynne, 1999).

Other studies have highlighted the importance of the temperature contrast and pre-eruptive H_2O content of coexisting magmas in determining eruptive dynamics. In a study by Holness *et al.,* (2005), dihedral angles between framework plagioclase crystals of mafic enclaves were measured and compared from differing lava flows in the Kameni islands,

Santorini, Greece. They demonstrate that differences in the textures of the enclaves can be linked to the H_2O content and temperature in differing temporal intrusions of the mafic magma, and conclude that overturn of the intruding mafic layer at the base of chamber is more likely with a hotter, wetter mafic magma.

1.4 Long-lived systems and possible temporal changes in mafic-felsic interaction

Questions remain about the nature and longevity of these shallow andesitic magma systems rejuvenated by mafic magma recharge. We understand little about whether the supply of mafic magma remains constant, from the same source, and what effect any variations might have on the interaction between mafic and andesitic magmas. The current eruption of Soufrière Hills Volcano, Montserrat is entering its 18th year at the time of writing, and is one of the longest-lived andesitic eruptions. Evidence from seismic tomography and thermal modelling suggests that smaller vertically-stratified zones of melt may exist in the shallow magmatic system rather than the concept of a single magma storage region, (*e.g.* Paulatto *et al.,* 2012). These zones may be stratified vertically in, for example, magma composition, temperature, viscosity and density. In a long-lived system questions arise about the effect of continuous or periodic mafic injection into the andesite. Can changes in the mafic magma supply be reflected in the geochemistry, and what effect might that have on mixing relationship between magmas? Where there is continued input of hotter mafic material over time, does the mixing relationship between the two magmas change? Changes in mafic enclave abundances have been documented in dome-forming eruptions such as Mt. Helen dome, Lassen Volcanic Center, California (Feeley *et al.,* 2008), where a reduction in the proportion of mafic enclaves heralded the end of the eruption. Changes in the degree of interaction between mafic and silicic magmas could have an effect on volatile, heat and mass transfer, all of which control eruptive behaviour. Dome growth at long-lived eruptions, such as Santiaguito, Guatemala, active since 1922, can often be characterised by periods of relatively high (of 3–5 years in length) and low (of 3–11 years in length) average magma discharge rates (Rose, 1972, 1987), which may be linked to perturbations in magma reservoirs (Melnik & Sparks, 2005). Thus, long-lived active systems, where the process of magma interaction can be monitored using petrological and geochemical analysis along with direct measurements such as gas

emissions, ground deformation, volcanic seismicity, are critical for understanding the style, timing and magnitude of recharge and eruption processes.

1.5 Soufrière Hills petrology and geochemistry

Soufrière Hills Volcano (SHV) is an ideal case study for the examination of mafic-silicic magma interaction over time and subsequent outgassing of the volatile phase; it is an active long-lived andesitic system with strong evidence for mafic recharge. Details of the 1995–2010 eruption at Soufrière Hills are summarised in section 1.7. The erupted SHV andesite lavas, which have been described in detail in previous studies (Devine *et al.,* 1998; Barclay *et al.,* 1998; Murphy *et al.,* 2000; Couch *et al.,* 2001; Humphreys *et al.,* 2009), have restricted bulk compositions (58–61 wt % SiO_2), and are highly porphyritic with up to 65 % phenocrysts (Fig. 1.2). The phenocryst assemblage is predominantly plagioclase + hornblende + orthopyroxene + Fe-Ti oxides. The groundmass assemblage is plagioclase + orthopyroxene + clinopyroxene + Fe-Ti oxides, and with variable amounts of rhyolitic glass.

Complex zoning patterns and disparate age histories of plagioclase phenocrysts indicate that the SHV andesite is a hybrid that has probably undergone multiple cooling and reheating events, and which resided in the shallow crust for 10^3–10^4 years prior to the current eruption (Zellmer *et al.,* 2003a,b). Excess sulphur emissions, mafic enclaves (Fig. 1.1, 1.2, 1.3), and phenocryst disequilibria textures (Edmonds *et al.,* 2001; Murphy *et al.,* 2000; Humphreys *et al.,* 2009) are all interpreted as evidence of an intrusion of a hotter volatile-saturated mafic magma at depth, which may have triggered the current eruption. Remobilisation and reheating of the crystal-rich andesite has been proposed to have been initialised via different models such as 'self-mixing', 'gas sparging' or 'a defrosting front' (Couch *et al.,* 2001; Bachmann & Bergantz, 2006; Burgisser & Bergantz, 2011), which are outlined in more detail in chapter 3. Fe-Ti oxide diffusion profiles constrain the timing of the interaction between the mafic and andesitic magmas to be on the order of days to weeks (Devine *et al.,* 2003). Eruption occurred at a critical point during mafic recharge when sufficient magmatic overpressure developed leading to the eruption of lava at the surface (*e.g.* Sparks *et al.,* 1977).
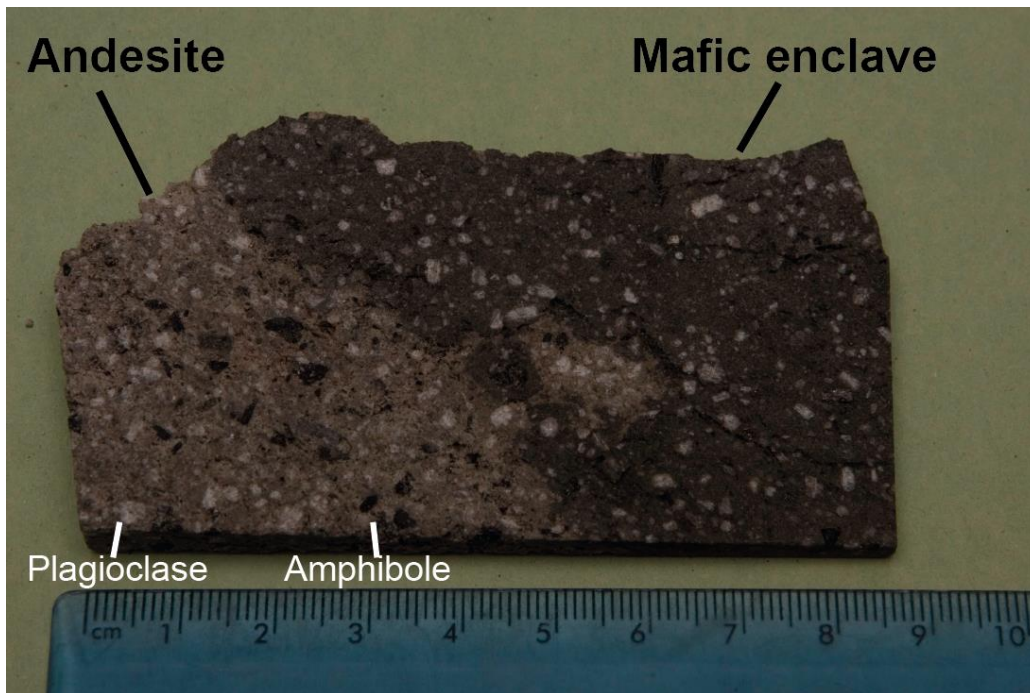
Figure 1.2: Image of Soufrière Hills andesite and mafic enclave. Andesite is porphyritic with large plagioclase and amphibole phenocrysts. Small inclusion of andesite in the mafic enclave highlights the complexity of interaction between the andesite and mafic magmas.

Lava dome extrusion is fed by a conduit to a depth of ~1 km *(e.g.* Costa *et al.,* 2007). Ground deformation modelling, geophysical surveys and petrographic analysis of the andesite suggests that a shallow chamber exists at a depth of 5.5 km to at least 7.5 km (Murphy *et al.,* 2000; Voight *et al.,* 2006; Elsworth *et al.,* 2008; Voight *et al.,* 2010; Mattioli *et al.,* 2010; Paulatto *et al.,* 2012), but is more likely to exist as diffuse zones of melt (Paulatto *et al.,* 2012). Melt inclusion data suggest that the shallow andesite magma chamber is zoned with respect to exsolved volatiles (4.3–11 vol % at 200–300MPa) (Edmonds *et al.,* 2014). To date there is no strong evidence to suggest that the andesite chamber might also be zoned in respect to temperature, density or composition, although localised differences near the mafic-andesite interface are likely to exist (Couch *et al.,* 2001). A deeper chamber, centred at around 12 km depth, which is connected to the shallower chamber, may be the source of mafic material intruding from depth (Elsworth *et al.,* 2008). Water contents of orthopyroxene phenocrysts further constrain a magma storage region with a depth of around 10 km (Edmonds *et al.,* 2014).
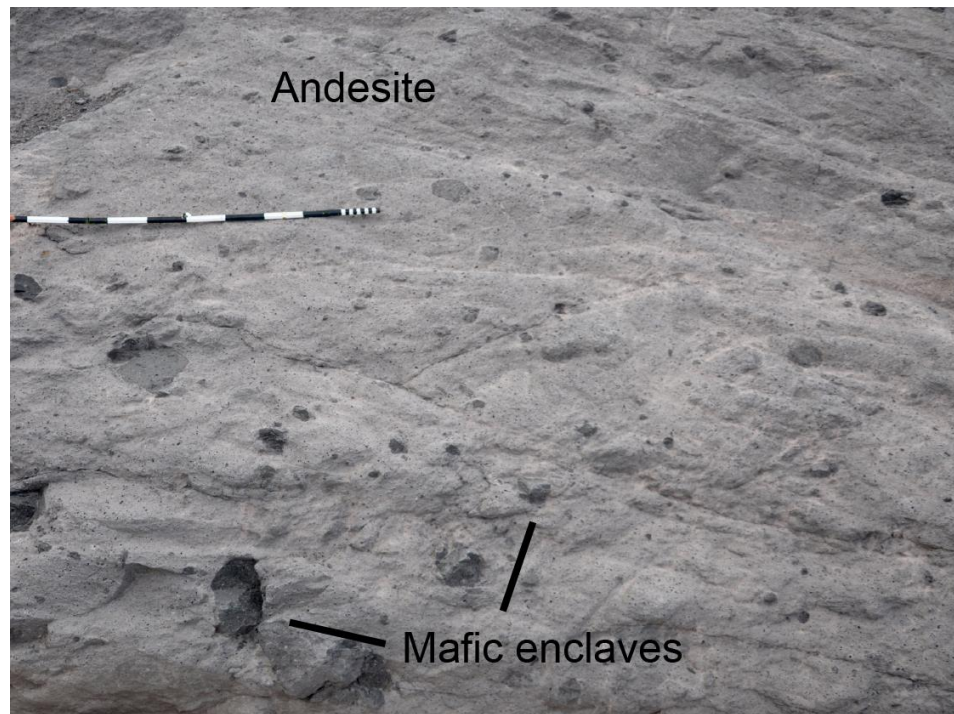
Figure 1.3: Image of mafic enclaves within a large andesitic lava block in Trant's (see locality map; fig. 1.6) deposited during the 11 February 2010 dome collapse at SHV, Montserrat. Length of colour blocks on scale is 10 cm with 2 cm intervals at right hand end.

Sulphur is contained in the pre-eruptive fluid phase, which is believed to be replenished by mafic magma intrusion and degassing (Edmonds *et al.,* 2001; Edmonds *et al.,* 2010; Wallace & Edmonds, 2011). Therefore 'excess sulphur' emissions (where the total amount of sulphur greatly exceeds that which would be emitted from the observed flux of andesitic magma) indicate the presence of mafic magma at depth. These emissions are high even during pauses in lava extrusion. Recent work indicates that not only does transfer of volatiles occur at the mafic-andesitic magma interface at depth, but also that vapour contained in mafic enclaves may contribute to the volatile budget, if they disaggregate within the andesite (Edmonds *et al.,* 2014). However, evidence for how the volatile phase derived from the andesite and mafic magmas is segregated from the shallow magmatic system is unclear. Since the start of the eruption sulphur gases (SO_2 and H_2S) have been outgassed continuously (Edmonds *et al.,* 2014). This coupled with the long-term inflation and deflation cycles of Montserrat during extrusive pauses (*e.g.* Elsworth *et al.,* 2008) implies a continuing process of mafic recharge over the course of the eruption.
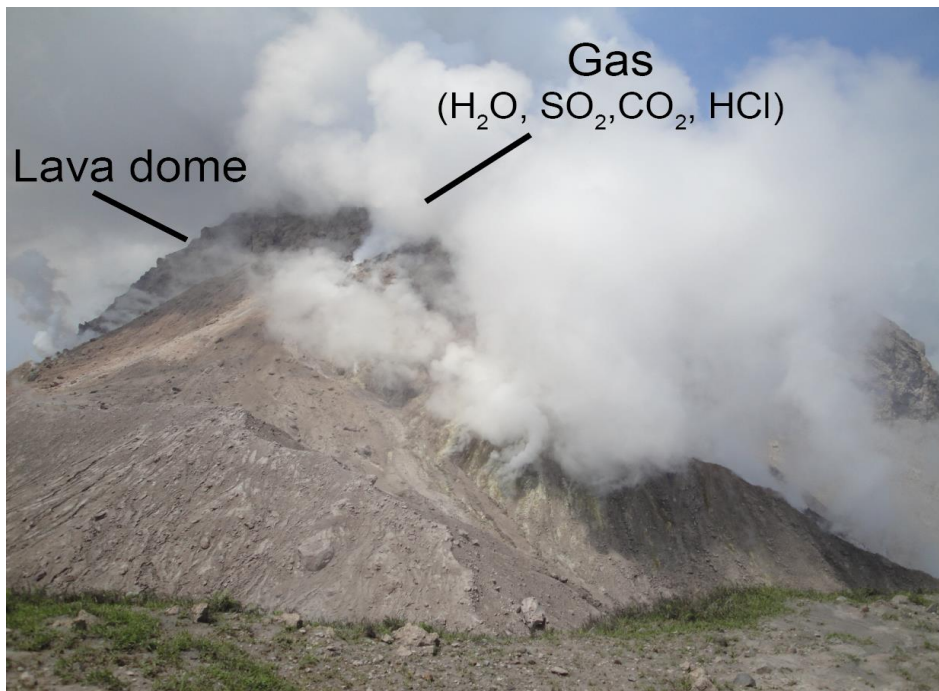
Figure 1.4: Image of south side of SHV lava dome taken on the 17 March 2010. Gases are emitted via fumaroles at points within the dome.

The observed proportion of mafic enclave abundances has apparently increased from 1 % in phase I to 12 % in phase IV (Murphy *et al.,* 2000; Mann, 2010, Barclay *et al.,* 2010; Komorowski *et al.,* 2010). The results of previous studies leave it unclear whether the mafic magma, which ranges from basaltic to basaltic andesite in composition (49–57 wt % SiO_2), has already undergone a degree of hybridisation at depth before interaction with the andesite in the shallow chamber or if it represents a mafic end-member (Zellmer *et al.,* 2003a). Changes in the concentrations of some major elements in the mafic enclaves erupted in phase III (detailed in chapter 4) hint at a possible change in the mafic end-member composition (Barclay *et al.,* 2010). Previous work in this area for Soufrière Hills has focussed on the early stages of mafic recharge and subsequent remobilisation of the andesitic magma, but 18 years on from the start of the eruption, we can now resolve changes in the length and style of extrusive periods, an increasing proportion of mafic enclaves and changing mafic enclave compositions. These observations have prompted a study of the temporal trends of a long-lived system dominated by magma mixing.

1.6 Soufrière Hills Volcano, Montserrat eruptive history (1995-2010)

Soufrière Hills Volcano (SHV) is located on the island of Montserrat in the Lesser Antilles arc (Fig. 1.5). The ~750 km long Lesser Antilles island arc was formed by the westward-dipping subduction of the North American plate beneath the Caribbean plate, with arc volcanism initiated at ~40 Ma (Briden *et al.,* 1979; Bouysse & Westercamp, 1990). Montserrat has three main volcanic centres: Silver Hills (2600-1200 ka), Centre Hills (950-550 ka) and the South- Soufrière Hills-Soufrière Hills complex (174 ka – present) (Fig.1.6) (Harford *et al.,* 2002). Preceding the start of the eruption in 1995, a series of volcano-seismic crises, where an increase in seismicity and fumarolic activity were observed, have been interpreted as failed attempts of the magma to reach the surface (Shepherd *et al.,* 1971; Aspinall *et al.,* 1998).
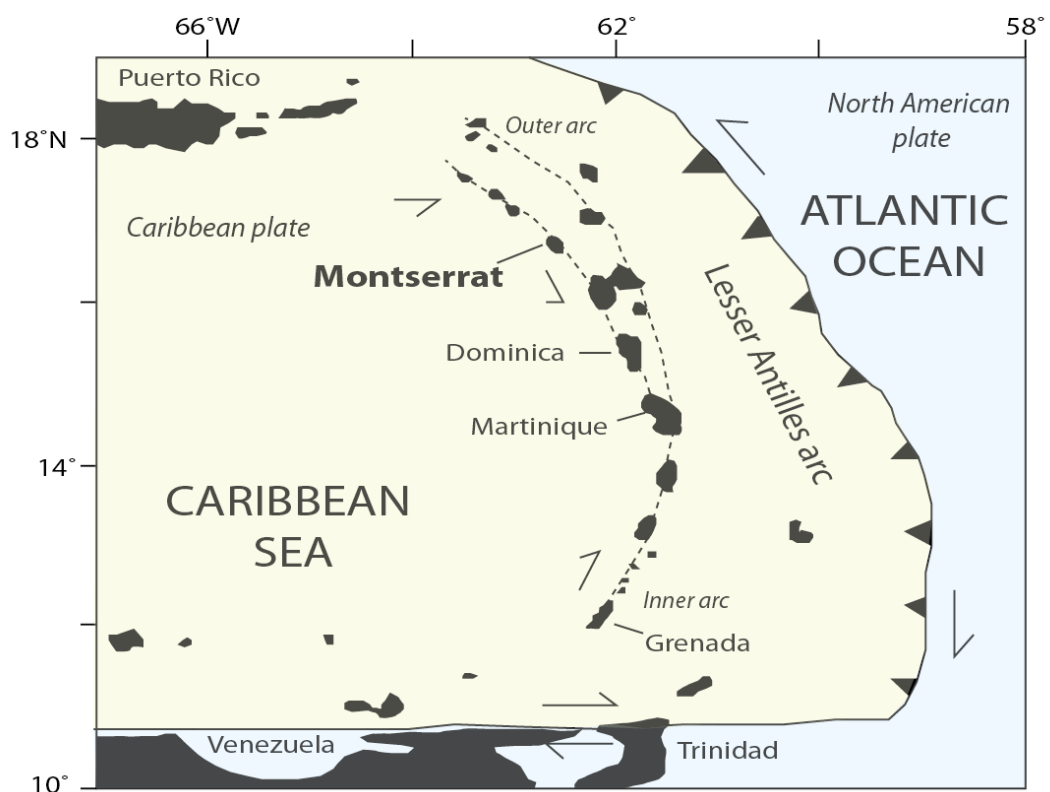
Figure 1.5: Tectonic setting of Montserrat. The North American plate is subducting under the Caribbean plate at a convergence rate of ~2 cm/yr. The Lesser Antilles arc is divided into two island chains north of Martinque. The younger (<20 Ma) active western island chain on which Montserrat is located, formed after the migration of the volcanic front to the west due to modification of the northern part of the slab orientation. The eastern older island chain is inactive.
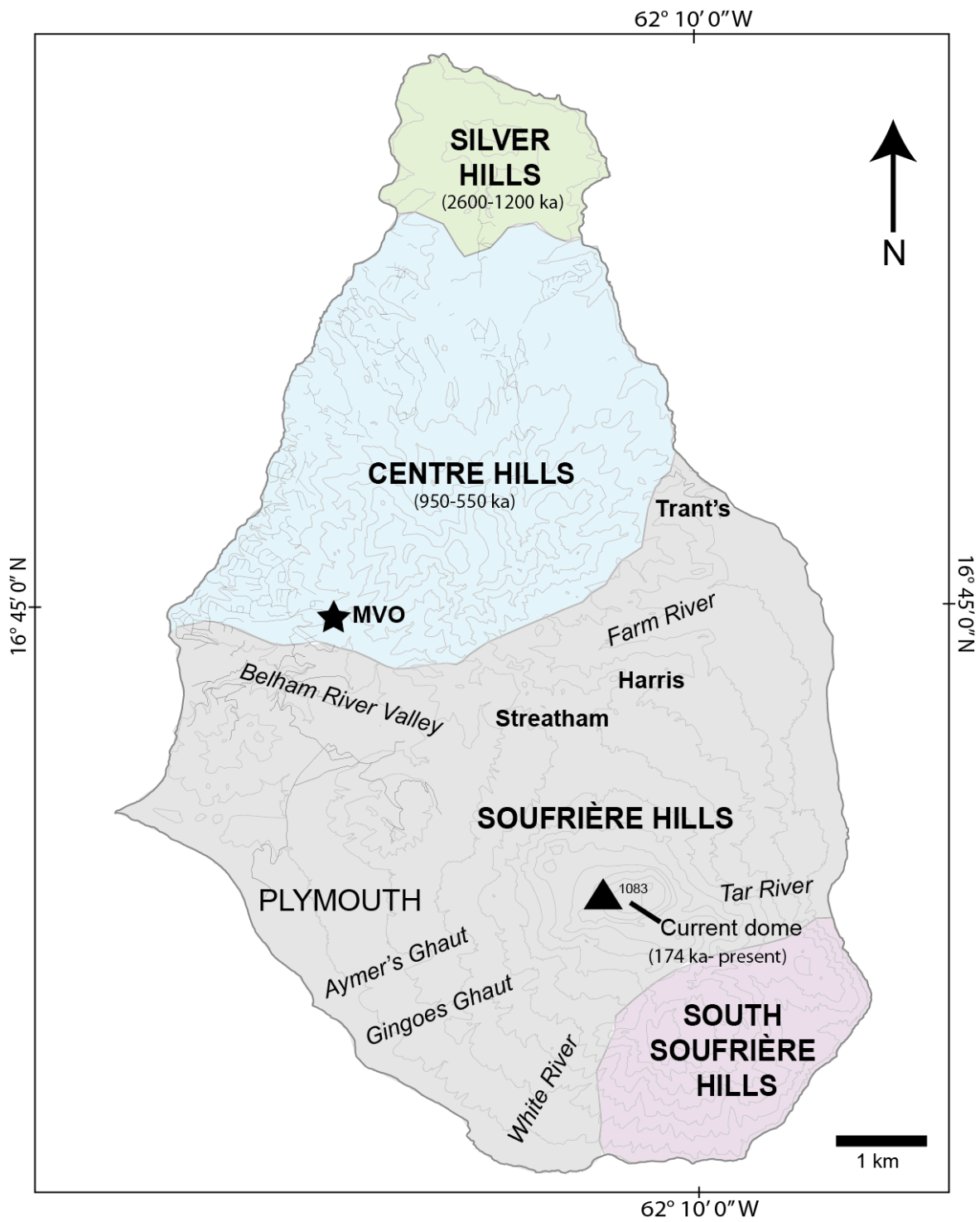
Figure 1.6: Montserrat locality map with the four main volcanic centres (Silver Hills, Centre Hills, Soufrière Hills and South Soufrière Hills) highlighted based on Ar-Ar geochronology (Harford *et al.,* 2002). Contours are in 100 m intervals and spot heights are in metres.

On the 18 July 1995 phreatic activity marked the start of the current eruption, which had been preceded by a series of earthquake swarms over the prior 3 years, perhaps indicative of movement of magma from depth. Lava extrusion was first observed in September 1995, and since then the current eruption of Soufrière Hills has had five phases of andesitic dome-forming activity (1995–2010), interrupted by pauses in lava extrusion. Over the course of the eruption, extrusive phase length has reduced from years (phases I-III) to months (phases IV-V); extrusive phase dates are given in table 1.1 and are referred to throughout the thesis. The cumulative volume of andesite lava erupted from 1995–2010 is around 1 km^3 (Fig.1.7; Wadge *et al.,* 2014); the majority of which was erupted in phases I to III, where the erupted volume was between 282–331 Mm^3 for each phase. The sharp reduction in erupted volume in phases IV and V to 39 Mm^3 and 74 Mm^3 respectively, coincided with the reduction in extrusive phase length (Wadge *et al.,* 2014).

Table 1.1: *SHV extrusive phase length and timings*

Phase I	Phase II	Phase III	Phase IV	Phase V
Nov. 95 - Mar. 98	Nov. 99 – Jul. 03	Aug. 05 – Apr. 07	Jul. 08 – Jan. 09	Oct. 09 – Feb. 10

Mafic material represented by mafic enclaves comprises on average 6 % (65 Mm^3) (Murphy *et al.,* 2000; Mann, 2010, Komorowski *et al.,* 2010; Barclay *et al.,* 2010; this work) of the total erupted material over the course of the eruption (Fig. 1.7). This total does not take into account the proportion of 'cryptic' mafic material (*e.g.* disaggregated enclaves) in the andesite, which was calculated as 6 % in a sample of phase III andesite (Humphreys *et al.,* 2012).
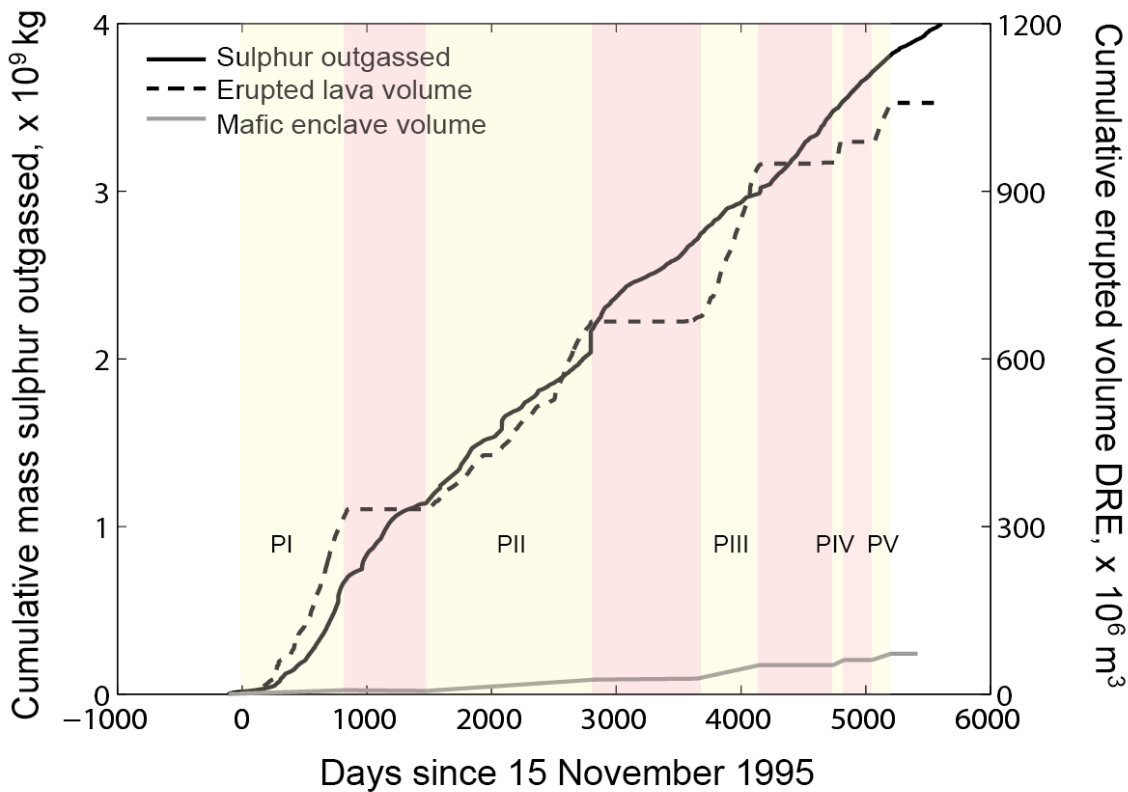
Figure 1.7: Plot adapted from Edmonds *et al.,* (2014) and Wadge *et al.,* (2014) showing total erupted lava volume and sulphur outgassed. Eruptive phases are highlighted in yellow, where PI = phase I, PII = phase II, PIII = phase III, PIV = phase IV, and PV = phase V; pauses are highlighted in red. The cumulative mafic enclave volume is plotted based on the maximum percentages recorded for each phase. Phase I: 1% (Murphy *et al.,* 2000); phase II: 5 % (Mann, 2010); phase III: 12 % (Barclay *et al.,* 2010); phase IV: 12 % (Komorowski *et al.,* 2010); phase V: 8 % (this study).

Dome material at the summit has built up over the extrusive phases, and despite removal of lava through dome collapse activity, the overall volume and structure of the dome reflects material extruded across the eruptive phases (*e.g.* Fig. 1.8). The majority of material removed from the dome occurs during extrusive phases, where the summit height of the dome usually reaches a maximum of ~1090–1100 a.s.l. (Herd *et al.,* 2005; Stinton *et al.,* 2014), with the height limit controlled perhaps by magmastatic pressure (Sparks, 1997). Dome growth will often switch direction during extrusive activity with shear lobes and lava spines forming (*e.g.* Watts *et al.,* 2002; Herd *et al.,* 2005; Stinton *et al.,* 2014 Wadge *et al.,* 2014), thus increasing the complexity and potential instability of the dome structure.
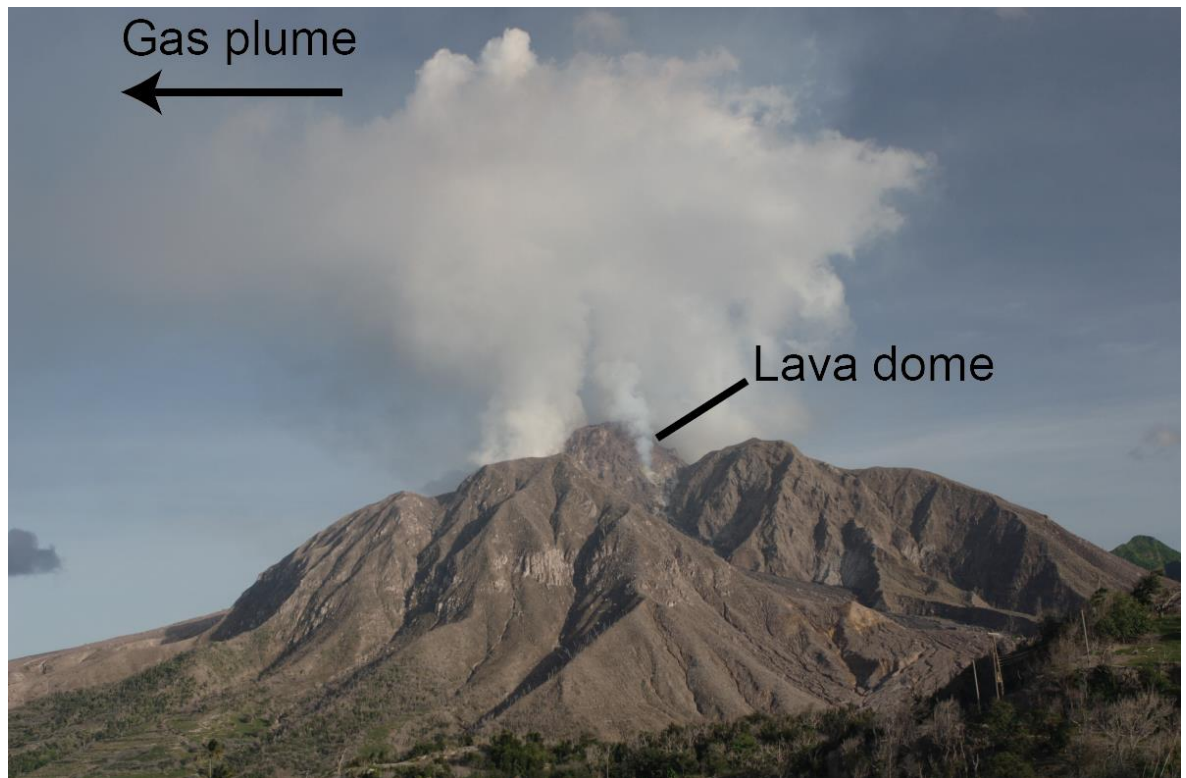
Figure 1.8: Clear image of the lava dome at SHV. Dome material present reflects several phases of extrusion. Continuous emission of gases via fumaroles around the dome creates a plume.

1.6.1 Eruptive activity

Activity over the course of the eruption has been a mixture of dome growth, vulcanian explosions, dome collapses, rockfalls and pyroclastic density currents (Fig. 1.9). This activity has impacted the southern half of the island (Fig. 1.6; 1.10), which was declared an exclusion zone in 1997, including the former capital town of Plymouth,. Although most resulting pyroclastic density currents generated from activity are confined to this exclusion zone (apart from in the Belham Valley; Fig. 1.6), the ash fallout associated with large dome collapses and vulcanian explosions impacts the entire island. Throughout all of the extrusive phases, sudden switches in eruptive style from explosions to extrusion to dome collapse have been common-place, these are summarised by Wadge *et al.,* (2014). However, each phase has been characterised by a dominant style of activity (Wadge *et al.,* 2014).

Figure 1.9: One of the numerous small pyroclastic density currents that have inundated Plymouth. Image taken on 3 September 2010 from the Montserrat Volcano Observatory.

Figure 1.10: Example of one of the many badly damaged buildings in the exclusion area. Image taken in Streatham after 11 February 2010 dome collapse.

16

1.6.1.1 Phases I to III

Phase I marked the start of lava extrusion, where increasing extrusion rates led to rapid dome growth culminating in some energetic dome collapses. On the 25 June 1997, a partial dome collapse with resulting pyroclastic density currents killed 19 people, which have been the only known fatalities from the current eruption (Loughlin *et al.,* 2002). Between August and October 1997, two series of sub-daily vulcanian explosions (Fig. 1.11) occurred generating a total of 88 explosions (Druitt *et al.,* 2002). The only significant lateral blast of the eruption to date occurred on Boxing day 1997, after the lava dome core was exposed following a debris avalanche associated with the collapse of Galway's wall (Sparks *et al.,* 2002). The sudden switches in activity and the unpredictability of phase I continued throughout the other eruptive phases. Phase II, with the longest period of extrusion (Table 1.1), was marked by 3 large dome collapses, the last of which preceded the end of extrusion. Although phase III had a large dome collapse during dome growth (20 May 2006), it was marked by fewer explosions and dome collapses relative to phases I and II (Wadge *et al.,* 2014).

Figure 1.11: Example of a vulcanian explosion at SHV taken on 10 January 2010 during phase V. Image courtesy of Adam Stinton.
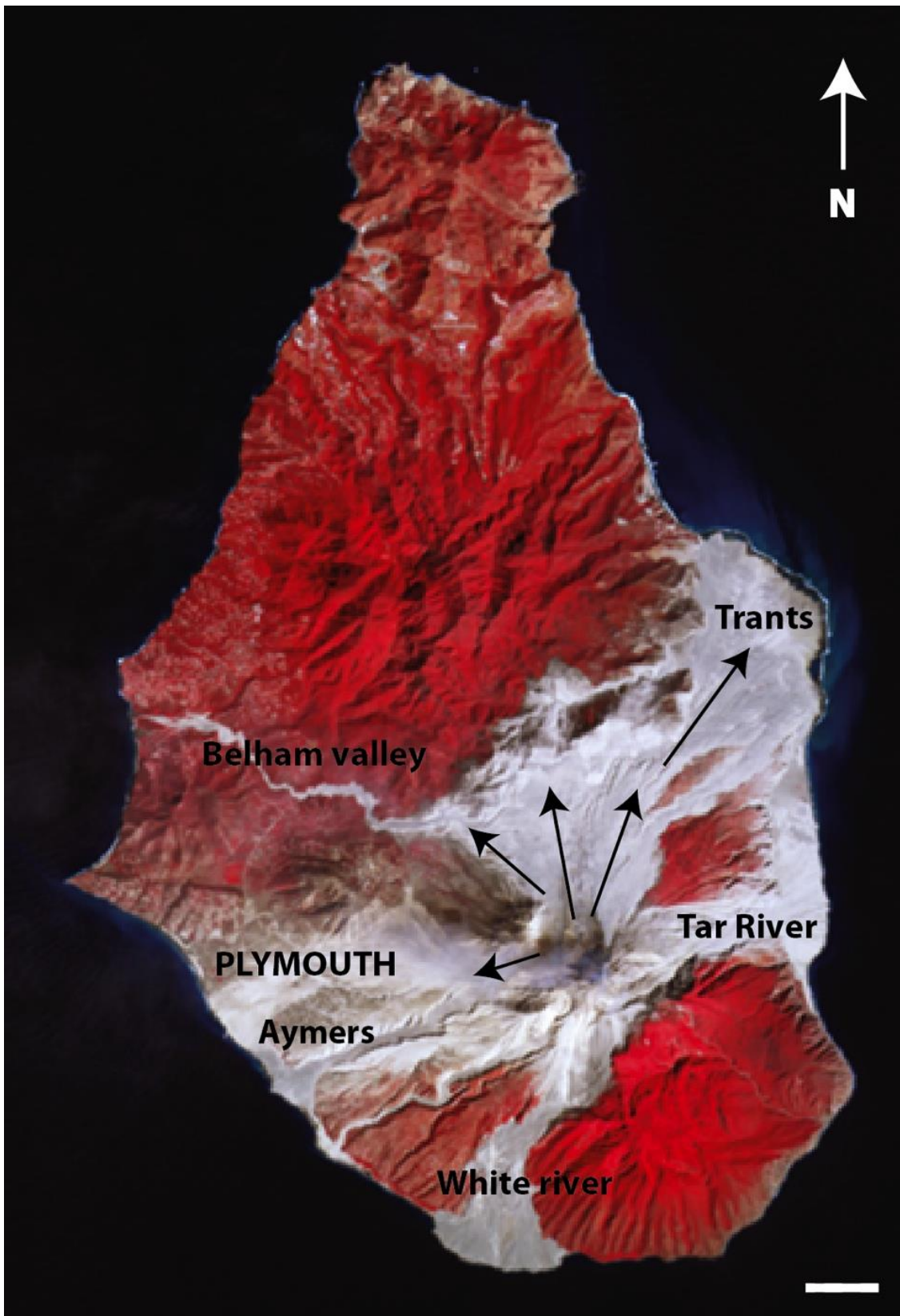
Figure 1.12: ASTER image of Montserrat taken after 11 February 2010 dome collapse on 23 February 2010 (© JAXA). The grey areas on the map highlight the extent of the total deposits from SHV phase V activity. Arrows indicate the direction and extent of the dome collapse deposits (phase V deposit map is shown in the methods chapter). Scale is 1 km.

1.6.1.2 Phase IV

Phase IV marked a change in eruptive pattern compared to phases I to III. The eruptive phase duration reduced to months from years in the earlier phases (Table 1.1). The phase was also characterised by high average extrusion rates (~7 ms^{-1}; Wadge *et al.,* 2014) and relatively frequent explosions. Extrusive activity was divided into 2 periods from July 2008 to September 2008 and December 2008 to January 2009, between these periods no extrusive activity was observed at the surface (Wadge *et al.,* 2014). The second period of activity was particularly intense with vulcanian explosions, increased seismicity and higher extrusion rates (Komorowski *et al.,* 2010). A series of four vulcanian explosions on 3 January 2009 marked the end of Phase IV (Komorowski *et al.*, 2010; Cole *et al.,* 2014); details of vulcanian explosions on the 3 January 2009 are discussed in more detail in chapter 5.

1.6.1.3 Phase V

Phase V activity was similar to the second part of phase IV, and was particularly intense over the short period of extrusive activity (9 October 2009 – 11 February 2010; Table 1.1) with 5 vulcanian explosions,10,000 rockfalls, and terminated after the 11 February 2010 dome collapse. Phase V was also characterised by sub-daily (3–14h) cycles of seismic and surface activity of rockfalls and ash venting generating plumes of <5 km with resulting PDCs (pyroclastic density currents) (Odbert *et al.,* 2014). However, overall seismic activity (long-period rockfall, hybrids and long-period earthquakes) in phase V reduced in frequency in comparison to previous phases (Odbert *et al.,* 2014).

Preceding lava extrusion 3 days of ash venting and a swarm of 24 VT (volcano-tectonic) earthquakes marked the start of activity on 5 October 2009 (Cole *et al.,* 2014). Phase V lava extrusion was divided into three multi-week cycles (Odbert *et al.,* 2014). Lava extrusion initially focussed on the SW and W sector of the dome summit in October and early November 2009 resulting in PDCs in White River, and Gingoes Ghaut for the first time in the eruption (Wadge *et al.,* 2014). The second period of extrusion switched to the NE-NW sector of the dome summit in mid-November to December 2009 (Wadge *et al.,* 2014). Three large vulcanian explosions occurred on the 8, 10 and 11 January 2010 (Cole

et al., 2014). The 8 January 2010 is the largest of the current eruption thus far (~2.7 x 10^6 m^3 DRE (dense rock equivalent)), generating a PDC in the Belham Valley with a runout of 6 km, which is the closest drainage system to currently populated areas (Wadge *et al.,* 2014). The final period of extrusion again focussed back to the W sector during the January 2010 vulcanian explosions and was coupled with a slight increase in seismicity (Odbert *et al.,* 2014). Two further vulcanian explosions occurred on the 5 and 8 February 2010 resulting in PDCs in Aymers Ghaut reaching the sea (Cole *et al.,* 2014). The average extrusive rate during phase V was high at ~7 ms^{-1} (Stinton *et al.,* 2014), although with variations from 35 ms^{-1} to 0.1 ms^{-1} (Odbert *et al.,* 2014). Over the course of phase V, ~74 x 10^6 m^3 of lava was extruded, of which 38 x 10^6 m^3 was added to the pre-existing dome, resulting in a total dome volume of 245 x 10^6 m^3 before the dome collapse on 11 February 2010 (Stinton *et al.,* 2014).

The 11 February 2010 dome collapse lasted for 107 minutes producing dome-collapse generated PDCs and high-energy surges, and culminated with two vulcanian explosions with a plume reaching 15 km in height associated to the second larger explosion (Cole *et al.,* 2014; Stinton *et al.,* 2014). Immediately prior to the dome collapse there was a slight increase in the frequency of long-period rockfall events, but unlike previous dome collapses at SHV no increase in the frequency of hybrid or long-period earthquakes were recorded indicating little pressurisation before collapse (Stinton *et al.,* 2014; Miller *et al.,* 1998; Calder *et al.,* 2002). The gravitational collapse of large unstable lobes of extruded lava on the northern flank of the dome is interpreted to be the likely cause of the dome collapse (Stinton *et al.,* 2014). Prior large dome collapses tended to be largely directed towards Tar River, but the 11 February 2010 dome collapse was directed towards the north east (towards Trants; Fig. 1.12) resulting in the complete destruction of the abandoned villages of Harris and Streatham (Fig. 1.10; Stinton *et al.,* 2014). During the event ~50 x 10^6 m^3 of dome and talus material was deposited primarily on the NE slopes (2–10 m in depth), and resulted in the progradation of the shoreline near Trant's by up to 650 m (Stinton *et al.,* 2014). Figure 1.12 is an ASTER image taken shortly after the 11 February dome collapse, and highlights where the total pyroclastic material was deposited during phase V. Total pyroclastic flow activity during Phase V had the most widespread distribution around the volcano of all the phases (Stinton *et al.,* 2014).

Figure 1.13: Example of a lahar in the Belham Valley on 17 April 2010.

1.6.2 Activity during extrusive pauses

Although the most intensive activity occurs during extrusive phases, activity is also observed in the pauses between extrusion. Episodes of ash venting are frequently observed, but large explosions, such as on the 3 March 2004 event that produced a 7 km eruption column also occur. Instabilities in the dome can lead to rockfalls sufficient to generate pyroclastic density currents. The extensive pyroclastic deposits and high rainfall levels at Montserrat has lead to widespread generation of lahars in the valleys around the volcano; where this is a particular hazard in the Belham Valley (Fig. 1.13; Darnell *et al.,* 2012).

21

1.6.3 SHV monitoring

The Montserrat Volcano Observatory (MVO) monitors Soufrière Hills, where ground deformation, gas emissions and seismicity are all continuously monitored to inform hazard assessment. Increased seismicity (low frequency earthquakes) has been observed prior to extrusion, and can yield information about magma movement in the conduit during extrusion (*e.g.* Neuberg, 2000; Neuberg *et al.,* 2006). HCl/SO_2 ratios have been observed to increase during extrusion, which is attributed to the dominance of low pressure degassing of andesite during magma ascent (*e.g.* Edmonds *et al.,* 2002; Oppenheimer *et al.,* 2002). Inflation and deflation trends on the island tracked by GPS and tilt meters are used to interpret whether magma continues to intrude from depth during extrusive pauses (*e.g.* Odbert *et al.,* 2014).

There is no in-house petrological monitoring of eruptive material. The identification of juvenile magma by analysing glass in ash generated from phreatic explosions, where there is no evidence of lava extrusion, may be used as the first evidence of magma rise. However, this can be extremely complicated where there is a mixture of older dome material present at the crater (Rowe *et al.,* 2008). Higher relative Li content in plagioclase crystals has been suggested as a tracer for juvenile plagioclase in ash in the early stages of an eruption (Rowe *et al.,* 2008); however, most observatories do not have the in-house analytical facilities to enable rapid cost-effective petrological assessment. Real-time petrological monitoring is therefore difficult in long-lived eruptions such at SHV, and unlike other monitoring techniques can require sample collection often in hazardous locations. Nonetheless studies such as these that investigate the petrological and geochemical temporal evolution of magmatic systems can be crucial for the interpretation of multi-parameter monitoring datasets. By contributing to our knowledge of how the mafic and andesite magma interact, and how volatiles move through the shallow system, this can feed further into hazard assessment at not only SHV, but also other andesitic magmatic systems.

1.7 Thesis motivation

This thesis seeks to address key questions about the processes of mass transfer and flux of material involved in the interaction between mafic and silicic magmas. The current eruption of Soufrière Hills Volcano indicates that there are possible changes in mafic-andesitic magma interaction over the 18 years of activity, which could perhaps influence magma system dynamics. Therefore the motivation behind the first strand of this thesis (chapters 3 and 4) was to assess the degree of interaction between magmas, and how any changes of the supply of the mafic component over the course of the eruption may affect that interaction. The supply of volatiles from the interaction between the mafic and andesitic magmas, either from the intruding magma at depth or from mafic enclaves (*e.g.* Edmonds *et al.,* 2014) is a key component in understanding the volatile budget at SHV. The second strand of the thesis (chapter 5) therefore focuses on evidence for the transport of the volatile phase through the andesite. The two strands are examined by the following questions:

1. What diversity in petrological characteristics is present in the enclave population, and can this be used to constrain magma mingling processes?
2. What are the main controls on the geochemical composition of the enclaves (fractionation versus mixing) and has this changed through the course of the eruption?
3. Have these mixing and mingling mechanisms changed in their character through the course of the eruption?
4. Given that the system appears to be extremely volatile-rich, how important is the mafic magma for supplying volatiles to the system?
5. Given that the bulk of the mafic magma does not erupt; is there textural evidence in the andesite that gives insights into the mechanisms of outgassing of volatiles sourced from mafic magma occurs?

To answer the above questions extensive sampling of the erupted deposits from the 5th (the latest extrusive phase at the time of writing) was undertaken, and geochemical, petrological and textural analysis of samples from extrusive phases III and IV and V were carried out.

1.8 Thesis structure

This thesis is divided into the following chapters, which are summarised here:

- Chapter 2 outlines the details of the field, geochemical, petrographic and textural methods employed in this thesis.

- Chapter 3 contains detailed textural, petrological and geochemical analysis of mafic enclaves sampled from phase V, which have been subdivided in three main enclave types. This enables a model to be presented interpreting the interactions between the andesite and mafic magmas at SHV.

- Chapter 4 examines the petrogenesis and controls on the mafic magmas compositions over the course of the eruption, using new geochemical trace element analyses from phases III and V. Fractional crystallisation and mixing models are applied to establish the dominant control on the mafic enclave geochemical trends. Specifically, the fractional crystallisation model applied to the range of reported mafic enclave compositions in phase I is tested on the new phase III and V geochemical data. The degree to which the mafic enclaves compositions are the result of mixing between the andesite and end-member mafic magmas is also examined. This geochemical modelling is used to establish how the interaction between the mafic and andesitic magmas may have changed over the course of the eruption.

- Chapter 5 presents petrological and geochemical analysis of andesitic shear fractures from phases IV and V, which show direct evidence for vapour transport through these fractures. A resulting model illustrating the life cycle of shear fractures in andesite is presented. This work also provides insights into the mechanisms for degassing in the shallow andesitic magma system, and how using metals as tracer for degassing in shear fractures that this process may be elucidated.

Chapters 3 and 5 have been accepted for publication in a Geological Society memoir and Earth and Planetary Sciences Letters respectively; details of the papers are outlined at the start of each chapter.

1.9 Key terms used in thesis

SHV: Soufrière Hills Volcano, Montserrat (see fig 1.6 for location).

SSH: South Soufrière Hills, Montserrat (see fig 1.6 for location).

Mafic enclave: In this thesis the term 'enclave' is used to describe undercooled magmatic inclusions, which have formed as result of incomplete mixing (mingling) between coexisting magmas, where 'gobules or fragments' of the intruding magma are incorporated in a 'host magma'.

Host magma: It is used to refer to the magma present in the magma chamber prior to a second magma intrusion and is the magma that 'hosts' the incorporated mafic enclaves. In this thesis it generally refers to the andesite magma at SHV.

Inherited phenocrysts: This refers to phenocrysts present in mafic enclaves that originated and grew in the host andesitic magma, but were incorporated into the mafic magma via mixing between magmas.

Chilled margin: A reduction in crystal size towards the margin of the enclave or an abrupt change to glass at the enclave margin.

Diktytaxitic: Term used to describe the groundmass texture often seen in mafic enclaves. This refers to interlocking network of elongate/tabular/acicular crystals with angular interstitial void spaces present between crystals.

Hybridised: The resulting mixed composition between mafic and silicic magmas.

Dates: All dates in the thesis use the following convention: day, month, year *e.g* 15 Nov 2009

Chapter 2: Methods

2.1 Field methods

2.1.1 Field sampling strategy

Samples of andesite and mafic enclaves were collected from a wide range of locations around SHV from deposits emplaced during phase V activity (Fig. 2.1; Table 2.1). Sample choice was based on choosing representative samples from each location where possible. With this type of sample collection it is important to note not just geographic location, but also the likely provenance and eruptive period of the entrained blocks. This is not always possible. Samples collected from the 11 February 2010 dome collapse deposits in the Trant's area are likely to have originated from a combination of phase III, IV and V domes. Although minor phase III deposits were incorporated into the collapse (Stinton *et al.,* 2014), the distinctive phase III lava described by Barclay *et al.,* (2010) is inferred only to be a minor component of the flow deposits based on field observations. The significantly larger extruded volume in phase V ($\sim 74 \times 10^6\,\mathrm{m}^3$; Stinton *et al.,* 2014) compared to phase IV ($\sim 39 \times 10^6\,\mathrm{m}^3$; Wadge *et al.,* 2014), implies that many of the samples collected from the 11 February dome collapse were derived from phase V. Samples that were collected from pyroclastic flow deposits in Aymers and White River (Figure 2.1) are derived from phase V dome growth alone, and were emplaced on the 5 February 2010 and the 16 October 2009 respectively (Stinton *et al.,* 2014). Pumice was sampled from explosions that occurred throughout phase V activity (Oct 2009 – Feb 2010). Phase IV samples are from 3 January 2009 Vulcanian explosion in lower Gages Fan (Table 2.1). Phase III samples are from the January 2007 pyroclastic density current into the Belham valley (Barclay *et al.*, 2010).
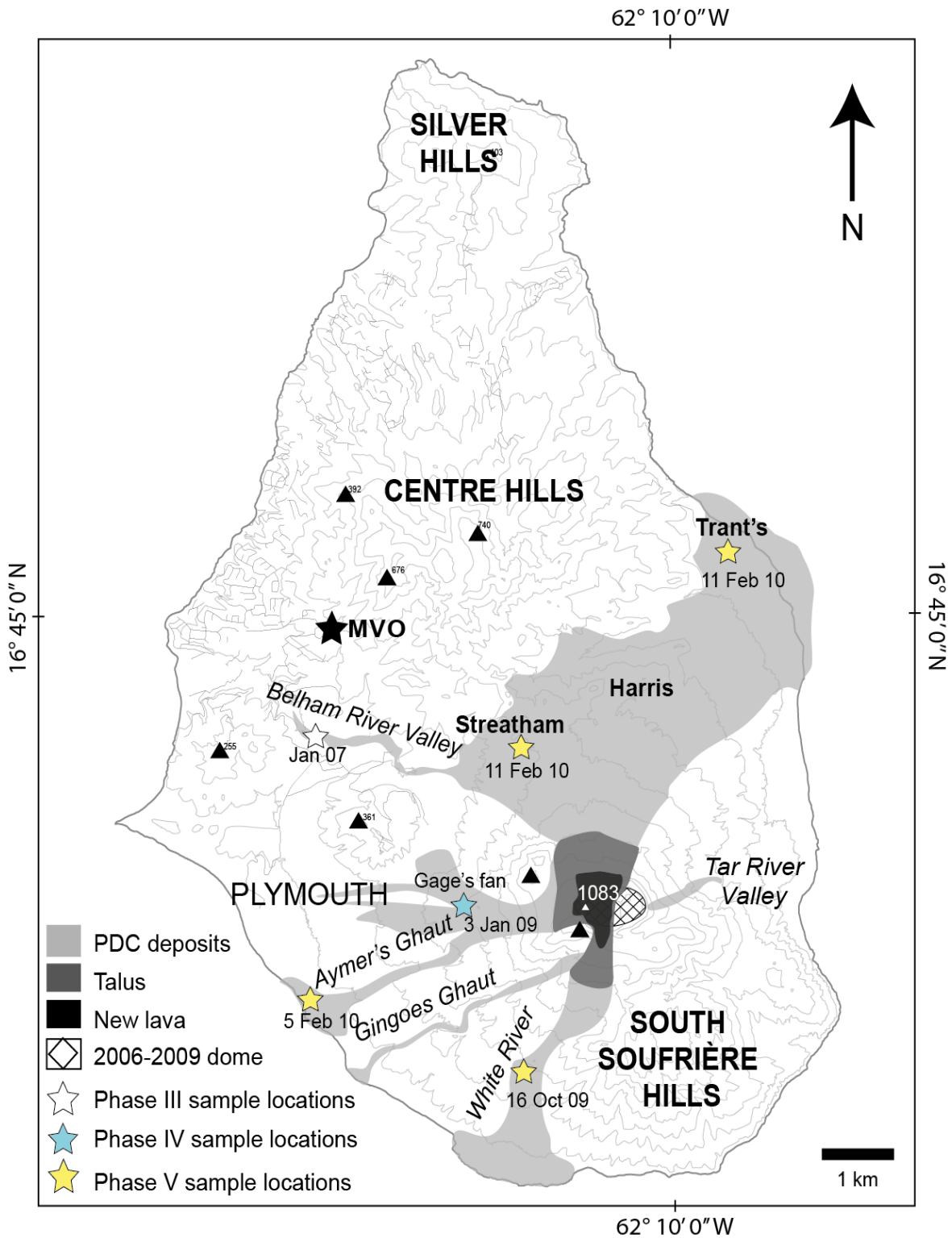
Figure 2.1: Map of deposits from phase V pyroclastic density activity with phase III, IV and V sample locations; the deposit distribution adapted from Stinton *et al.,* (2014). Grid references for phase V sample locations can be found in table 2.1. Deposit dates for sampled material are shown (see table 2.1). Pyroclastic density currents (PDC)

Table 2.1: *Phase III, IV and V sample locations*

Sample no.	Location	Grid location		Source	Date of emplacement
MO01-MO19	Belham Valley	NA		Pyroclastic density current (PDC)	Jan-2007
MVO1535	Lower Gages	NA		Vulcanian explosion	03-Jan-2009
MVO1537-MVO1539	White River	NA		PDC	Oct-2009
MT18-19, MVO1588, 1590,1591,1593	Aymers	583522	1846419	PDC	Jan-2010
MVO1566	White River	586880	1845330	PDC	Jan-2010
MVO1567	Bugby Hole	587400	1851433	Dome collapse	11-Feb-2010
MT20-MT37	Trants	589511	1852588	Dome collapse	11-Feb-2010
MVO1586	Trants	589511	1852588	Dome collapse	11-Feb-2010
MT06-MT11	Streatham ridge	586695	1850599	Dome collapse	11-Feb-2010

2.1.2 Estimation of macroscopic enclave volume fraction

Enclave abundance was estimated using both macroscopic point counting and image analysis in the phase V deposits. Nine lava blocks from the February 11th 2010 dome collapse deposits in the Trant's and Streatham areas (Fig. 2.2a) were analysed using both methods (results are shown in chapter 3; table 3.1).
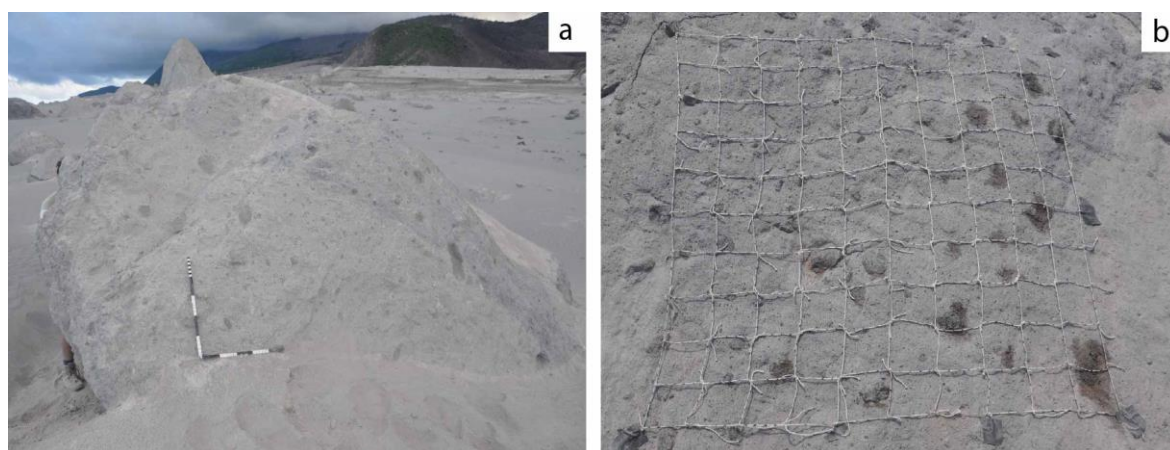
Figure 2.2: (a) A representative image of one of the andesitic blocks from the February 11 2010 dome collapse in the Trant's area chosen for point-counting (scale: 10 cm with 2 cm intervals). (b) An image of the net employed during point-counting of mafic enclaves. Net is 1 m^2, string is spaced at 10 cm intervals, with 2 cm tick marks.

Selection of the blocks was random, apart from requiring a relatively exposed and flat surface for analysis. Furthermore, to assess potential anisotropy in enclave fabric or abundance, two faces of a single block were analysed. For macroscopic point counting a grid of 1 m^2 with 2 cm intervals on each axis (Fig. 2.2b) permitted us to count up to a total of 2601 points per site. A similar method using a grid was employed by Feeley *et al.,* (2008), at the Mount Helen dome, Lassen Volcanic Center, USA where 441 points per site were counted, with a spacing interval of 5 cm. A lower spacing interval and thus higher point count was chosen in this study on the basis of that the average size of enclaves at SHV are <10 cm in diameter (Fig. 3.2), and therefore needed to capture full range of data. The minimum size of enclaves counted was 1 cm (smaller enclaves could not be distinguished from crystal clots/glomerocrysts in the field). In addition to enclave abundance, the size and shape of enclaves were also measured in the same 1 m^2 area by measuring the apparent diameter of the x and y axes (short and long axes) of each enclave; for the purpose of this thesis, the long axis of an enclave is referred to as the apparent diameter.

As well as point counting in the field, image analysis of the same blocks used for point counting was also carried out to compare the methodology. To do this, photographs of the same 1 m^2 area used for point counting were taken (Fig. 2.3a); subsequent images with enclave types marked on the blocks were also taken for later identification (Fig. 2.3b). Using the field images (Fig. 2.3b-c), enclaves and enclave types are digitally isolated from the andesite using adobe illustrator to create binary images (Fig. 2.d-f). The isolated area fraction occupied by the enclaves is calculated using ImageJ software, and compared to the point counting results. Image analysis yielded similar percentages, but consistently a little lower in comparison to the point counting method (by a mean of 1%). The slight underestimation of the image analysis method is due to our inability to resolve the small enclaves (<2 cm) in the images, but is within standard error. We refer to the values obtained by the point counting method for enclave abundances.
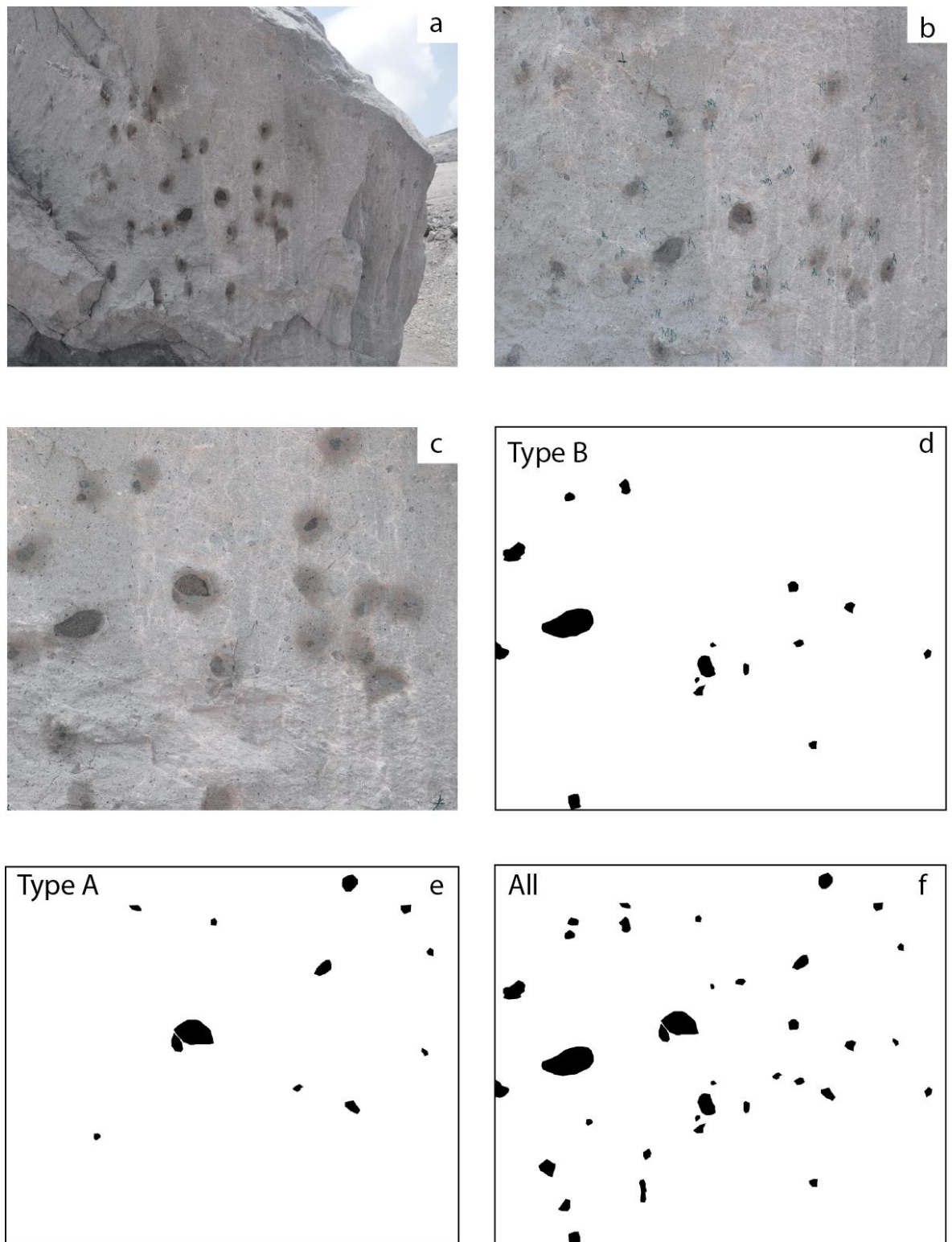
Figure 2.3: (a) A representative block used for image analysis located in Trants. (b) Enclave types were marked on the blocks for later identification (m=type A, a= type B and md= type C). (c) Images were then cropped to the same 1 m^2 used for point counting. (d-f). Examples of a series of binary images that were created using adobe illustrator to represent differing enclave types (types A and B; type C is not shown, but is included in (f)); the total enclave and enclave types area fraction was then calculated using ImageJ.

2.2 Laboratory Analytical Methods

2.2.1 Geochemical analysis

Seventy-four mafic enclave and andesite samples from phases III, IV and V (Table 2.1) were analysed using X-ray fluorescence (XRF). Alternating dark and fine-grained, and light and coarse-grained bands from within both MVO1535 and MVO1586 (see chapter 5 for explanation of dark and light bands) were separated and also analysed. Furthermore, in MVO1535, two dark bands (MVO1535b1 and MVO1535b2) were sampled and analysed. Samples were crushed and powdered for XRF analysis of major and trace elements at the University of East Anglia using a Bruker AXS S4 Pioneer. XRF major element standards used were SDO-1, GSP-2, W2a, AGV-2, AC-E; XRF trace element standards used were SDO-1, AC-E, MESS-2, STSD-2. All standards were analysed six times. The relative standard deviation of the measurements is <1% for all major oxides, apart from P_2O_5 which is <2 %. Trace element accuracy, based on calibration with a suite of standards, is <2 % relative apart from Ce and Sc, which are 4% and 7% respectively. The diameters of enclaves analysed ranged from 3.3–23.8 cm. Different splits of the same samples were analysed to rule out artefacts resulting from the relatively small sample size. Standard deviations are <1% for SiO_2, Al_2O_3, P_2O_5, Na_2O and Sr, all other major and trace element oxides are <5%. However, a single run of sample MT27 did produce anomalously high standard deviation values for K_2O and Ba of 15% and 31% respectively. The minimal deviations seen between different splits of the same sample were not great enough to explain the range of compositions as also concluded by Zellmer *et al.,* (2003a).

Trace element analyses using ICP Mass Spectrometry (ICP-MS) was carried out at Acme Labs, Vancouver, on 27 selected mafic enclave and andesite samples from eruptive phases III and V (see Table 4.1), and pseudotachylyte samples (see Table 5.2) using the same powders prepared for XRF analysis. Sample powders (0.2 g) were prepared using a lithium metaborate/tetraborate fusion and nitric acid digestion to analyse trace and rare earth elements. To minimise volatile loss, separate sample splits of 0.5g were prepared and leached in hot (95°C) Aqua Regia for base and precious metals analysis. Standards used were STD OREA545EA, DS9 and SO-18 and runs of these were repeated twice. Trace element and rare earth element (REE) accuracy (see Table 4.1 for all trace element

standard deviation percentages) based on calibration of the set of standards are all <6 %, except for Tm (8.7%), Li and Sc (11.1 %), U (15.9 %); detection limits for all trace and REE are also reported in Table 4.1. Standard deviations for the metals analysed in chapter 5 using the Aqua Regia method are Zn, Ni and Cu <1 %, Pb, Au, Ag <3 %, As and Cd <6%, and Mo <6.5 %. Detection limits for Cu, Pb, Ni, Mo, Cd are 0.1 ppm, As is 0.5 ppm, Zn is 1 ppm and Au is 0.5 ppb.

2.2.2 Petrological analysis

Thin sections of 40 samples were cut from dome rock and pumice to capture textural features of the enclosing andesite and mafic enclaves. In enclave sections, andesite-enclave margins were included, as well as the interior of large enclaves (>10 cm) to examine heterogeneity across enclaves. Secondary Electron Microscope (SEM) back scattered images (BSE) and element mapping (used in chapter 5) were collected using Jeol JSM-5900LV at the University of East Anglia using a 20 kV beam at a working distance of 10mm. Modal analyses of phenocrysts, vesicles and groundmass were performed on 21 thin sections that contained mafic enclaves. The number of points counted per section (441–1681 points, with a spacing of ~0.5 mm) was dependent on the size of mafic enclave captured in the selected thin section. These are reported in chapter 3 (Table 3.3; Fig. 3.8). Porosity (void space) and mineral abundances of the in the dark and light zones in the shear fracture samples (MVO1535c and MVO1586) in chapter 5 were determined from BSE images using ImageJ software.

Plagioclase phenocryst size, type, and rim and sieve-texture thickness were measured by analysing representative different mafic enclave types as defined by petrological, geochemical and textural analysis in Chapter 3 (Table 3.2). A total of six thin sections were used, one type A and the rest type B. A wider range of type B samples were analysed as a greater degree of inter-clast heterogeneity was initially observed in this enclave type. Results are reported in chapter 3 (Fig. 3.4). However, the results from the single type A clast were compared qualitatively with other type A samples to ensure that the sample chosen was representative. The positive correlation between rim width and the proportion of sieved inherited phenocrysts in different enclaves (see Fig 3.4) rules out the possibility of a 2D sampling artefact as the cause of variation in rim widths.

Electron probe analysis was undertaken at the University of Cambridge using a Cameca 5-spectrometer SX-100 instrument. Minerals (excluding glass, oxides, cristobalite and metals) were analysed using a 1-5 µm spot size, with a 15 kV, 10 nA electron beam; standard deviations for all measured elements are <1%. Glasses were analysed using a 10 µm spot size with a 15 kV, 2 nA and 10 nA beam for major and trace elements respectively; standard deviations are <0.9% for SiO_2 and Al_2O_3, and <0.4% for all other major and trace elements. Copper sulphides, cristobalite, quartz and oxides were analysed using a 1 µm, 20 kV, 20 nA focused beam; standard deviations for metals are <3% relative.

2.3 Appendix

Electronic appendices are also supplied within this thesis and contain the following information:

- Sample information and details of procedures carried out on the samples
- Electron microprobe mineral analyses results
- All geochemical analyses used in this thesis

Chapter 3: Characterisation of mafic enclaves

erupted in 2009−2010

The large bulk of this chapter has been accepted for publication as a paper entitled 'Characterisation of mafic enclaves in the erupted products of Soufrière Hills Volcano, Montserrat 2009-2010' in 'An overview of the Soufrière Hills Volcano from 2000-2010' which forms a Geological Society of London Memoir; due to be published in 2014. I am the first author of the paper, and undertook all fieldwork, laboratory analysis and interpretation of the results, and wrote the paper. My supervisors, Jenni Barclay, Madeleine Humphreys, Marie Edmonds and Richard Herd, and Thomas Christopher from the Montserrat Volcano Observatory are all co-authors on the paper; they discussed the interpretation of the results and provided edits, and assisted in part of the fieldwork. The following has been modified from the original paper to fit with the structuring and overall objectives of the thesis: (i) the methods are now moved to chapter 2 to avoid repetition; (ii) a small section on discontinuous streaked material is added along with a section on geothermometry of the mafic enclave mineral phases to provide further evidence for conditions of entrainment, (iii) the discussion section from the paper examining the change across the eruptive phases in relation to the mafic enclaves is now moved to chapter 6 and (iv) two additional figures are included (Figs. 3.3 and 3.5) to exemplify the characteristics of entrained phenocryst phases, and some images have been updated.

3.1   Introduction

The process of magma mingling, where two or more magmas mix incompletely during magma storage in the crust, is commonly associated with arc volcanism (*e.g.* Pallister *et al.,* 1992; Clynne, 1999) and results in the formation of banded pumice and magmatic mafic enclaves (*e.g.* Bacon, 1986; Clynne, 1999; Browne *et al.,* 2006b; Martin *et al.,* 2006b). More complete mixing of magmas is inhibited by large contrasts in viscosity and density, reflecting differences in temperature, composition and crystallinity, and the relative proportions of the incoming and host magmas (Eichelberger, 1980; Bacon, 1986; Sparks & Marshall, 1986). The textures of enclaves form in response to the local crystallisation conditions, and can yield information about the mingling processes or the dynamics of the intruding magma. For example, the presence of a diktytaxitic framework composed of elongate quench crystals and chilled enclave margins indicates rapid undercooling (Bacon, 1986). Lack of chilled margins and presence of more tabular framework crystals may indicate that enclaves were predominantly crystallised prior to incorporation into the host magma (solid-liquid mingling) (*e.g.* Eichelberger, 1980; Coombs *et al.,* 2002). Therefore such enclaves may represent the remnants of a fragmented vesiculated mafic layer from the silicic-mafic interface (Eichelberger, 1980; Thomas & Tait, 1997; Martin *et al.,* 2006a). Formation of a discrete layer of mafic magma is typically thought to be a product of slow and small volume material injection, where viscosity, density and temperature contrasts between the two magmas are strong (Sparks & Marshall, 1986). In contrast, enclaves that predominantly crystallised after incorporation into the host reflect direct injection of intruding magma into the host and therefore a more dynamic mingling relationship (Bacon, 1986; Sparks & Marshall, 1986; Clynne, 1999). For example, at Unzen, Japan, Browne *et al.,* (2006a) identified textural differences between enclaves to infer that enclaves sampled with medium-grained microphenocrysts in a glass matrix represent the slower cooling of the centre of an intrusion. In contrast, porphyritic enclaves with a glass and crystalline matrix represent the silicic-mafic interface where there is a high degree of undercooling.

As well as mafic enclaves, disequilibrium textures within both the host rock and enclaves can also be used to track mingling dynamics. Examples of these disequilibrium textures are sieve-textured plagioclase, reverse zoning in orthopyroxene, breakdown of

amphibole and clinopyroxene-rimmed quartz (*e.g.* Singer *et al.,* 1995; Tepley *et al.,* 1999; Nakagawa *et al.,* 2002; Browne *et al.,* 2006b). Disequilibrium may be caused by variable heating of the host magma from input of hotter magma (*e.g.* Tepley *et al.,* 1999), or incorporation of the host phenocrysts into the incoming magma (*e.g.* Ruprecht & Wörner, 2007), which may then be recycled back into the host magma via disaggregation (*e.g.* Clynne, 1989, 1999; Browne *et al.,* 2006b; Humphreys *et al.,* 2009). In the 1953-1974 eruption of Southwest Trident volcano, Katmai National Park, Alaska, USA, the presence of sieve-cored plagioclase phenocrysts with overgrowth rims in the host dacite are identified to have originated from an andesite intrusion and were transferred to the dacite via disaggregation of andesite enclaves (Coombs *et al.,* 2000). Combined textural, petrological and geochemical analysis of magmatic enclaves and coexisting phenocrysts can therefore provide insights into the nature of the mixing magmas, the dynamics of the mingling process, and changes that may be occurring during mixing.

Soufrière Hills has provided a unique opportunity to study the process of magma mingling in an active system. Magma intrusion at depth appears to have been quasi-continuous throughout the eruption, based on excess sulphur emissions (Edmonds *et al.,* 2001, 2010) and ground deformation patterns (Mattioli & Herd, 2003; Elsworth *et al.,* 2008). A higher proportion in the abundance of mafic enclaves compared to earlier extrusive phases may hint at changes in the magma mingling dynamics in phase III (Barclay *et al.,* 2010). Phases IV (July 2008 – Jan 2009) and V (Oct 2009 - Feb 2010) marked a change at SHV: eruptive phase length reduced from years to months and the average extrusion rate increased (Wadge *et al.,* 2014). We present geochemical, textural and petrological analyses of mafic enclaves from phase IV and V, alongside results from fieldwork. This work provides a window into syn-eruptive magma mingling processes.

3.1.1 Previous work at SHV (Phases I-III)

SHV andesite is porphyritic (30–40%) and is described in detail in previous studies (Devine *et al.,* 1998; Barclay *et al.,* 1998; Murphy *et al.,* 2000; Couch *et al.,* 2001; Humphreys *et al.,* 2009). Within the andesite at SHV mafic enclaves have been ubiquitous (Murphy *et al.,* 1998, 2000; Harford *et al.,* 2002; Barclay *et al.,* 2010). The phenocryst assemblage of the andesite is plagioclase + hornblende + orthopyroxene + Fe-Ti oxides

and minor quartz and rare zircon crystals, whereas the groundmass assemblage is plagioclase + orthopyroxene + clinopyroxene + Fe-Ti oxides, and interstitial glass is rhyolitic in composition. The andesite temperature, as bracketed by quartz and amphibole stability is ~830-870 °C (Barclay *et al.,* 1998). As quartz is only stable at >830 °C this may indicate that the andesite chamber was thermally zoned prior to mafic intrusion (Murphy *et al.,* 2000). Orthopyroxene phenocryst reverse zoned rims that record higher temperatures (880-1050 °C) than their cores (~858 °C), reverse zoned dusty sieve-textured plagioclase phenocrysts, embayed quartz crystals with clinopyroxene rims in the andesite are all cited as evidence of reheating by a mafic magma intrusion (Murphy *et al.,* 2000). However, heterogeneity of these phenocryst disequilibrium textures indicates that reheating is non-uniform and perhaps localised by proximity to the mafic intrusion (Murphy *et al.,* 2000). Geochemically, SHV andesite compositions have been modelled as the result of fractional crystallisation of equal proportions of amphibole and plagioclase from the South Soufrière Hills basalt (erupted in the south of the island around 130 ka; Zellmer *et al.,* 2003a; Harford *et al.,* 2002). A more detailed explanation of the geochemistry of the erupted material from Soufrière Hills and South Soufrière Hills is outlined in chapter 4. No evidence for the widespread disaggregation of mafic enclaves into the andesite was found in phases I and II andesite (Murphy *et al.,* 2000; Mann, 2010), but using a new imaging method, clear evidence for this process in the form of plagioclase microlites derived from the mafic enclaves has been seen in phase III and IV andesite samples (Humphreys *et al.,* 2012). Additionally, a suite of high K_2O melt compositions in the andesite from phases I-III similar to that observed in mafic enclaves are interpreted to be the result of the mingling of mafic melt transferred by the disaggregation of partially crystallised mafic enclaves (Humphreys *et al.,* 2010). This implies that the disaggregation and mixing of mafic material into the andesite may be more prevalent than previously established and its resulting effect on bulk andesite compositions over the eruptive phases, which will be examined in more detail in chapter 4.

Mafic enclaves make up <1–12 wt % of the lava erupted at SHV through phases I-III (Murphy *et al.,* 2000; Mann, 2010, Barclay *et al.,* 2010). Prior work on enclave petrology has focussed predominantly on phases I to III (prior geochemical work is outlined in chapter 4). The petrology and textures of mafic enclaves from phases I-III are indicative of rapid cooling. Diktytaxitic groundmass and chilled and crenulated margins are all identified features associated with rapid cooling rates. High anorthite framework

plagioclase cores (An$_{70-89}$) and high TiO$_2$ concentrations in titanomagnetite crystals are taken as evidence for higher temperatures associated with the mafic magma than the andesite (Murphy *et al.,* 2000). Mafic enclave temperatures are not well constrained as crystals and melt record the quench crystallisation temperature and not the magmatic temperature, but two pyroxene thermometry suggests a temperature of around ~1100 °C (Humphreys *et al.,* 2009). Early work from phase I identified that large crystals of plagioclase, amphibole, orthopyroxene and quartz present in the mafic enclaves were derived from the andesite (Murphy *et al.,* 2000), and were further identified in phases II-III (Mann, 2010; Humphreys *et al.,* 2009). Three types of enclaves were suggested from the phase II deposits by Mann (2010) on the basis of petrological and geochemical analyses: (1) T1: identified by the presence of inherited phenocrysts (2) T2: identified by the presence of phenocrysts (3) T3: identified by higher Rare Earth Element concentrations. Mann, (2010) surmises that the T1 enclaves were formed at the interface between the andesite and mafic magmas, the T2 enclaves deeper with the mafic intrusion, and T3 enclaves from a shallower magma source, which intruded as dyke into the andesite. In a study of phase III deposits by Barclay *et al.,* (2010), a further four enclave types were identified in the field: (1) Diktytaxitic: porphyritic with a visible interlocking groundmass (2) Andesite: similar in appearance to the SHV andesite (3) Waxy: porphyritic, but groundmass not visible (4) Mixed: mixed zones of (1) and (3). Therefore, there is a need to reconcile field-based observations with detailed petrological, textural and geochemical analyses, and to have better constraints on enclave type conditions of formation *i.e.* temperature.

The presence of mafic enclaves in SHV andesite is ascribed to the interaction between mafic magma and the andesitic host magma, which may have been the trigger and driver for the 1995–2010 eruption (Devine *et al.,* 1998; Murphy *et al.,* 1998; Murphy *et al.,* 2000; Couch *et al.,* 2001). It has been proposed that the initial intrusion of mafic magma underplated the andesitic magma (Murphy *et al.,* 2000). A strong viscosity contrast exists between the highly crystalline andesite magma and phenocryst-poor mafic magma, so mechanical mixing is likely to be inhibited significantly (Sparks *et al.,* 2000). Enclaves may have formed when fragmented dykes and blobs of less dense mafic material were injected into the overlying andesite (Murphy *et al.,* 2000). The remobilisation of the andesitic magma may have taken place via initial conduction of heat across the mafic-andesite boundary followed by the development of instabilities and convection in the andesitic magma (Couch *et al.,* 2001). An alternative model suggests that the

remobilisation of the andesite (essentially a crystal mush) takes place by 'gas sparging', involving the upward migration of a hot fluid volatile phase derived from the mafic intrusion (Bachmann & Bergantz, 2006). This fluid transports heat by advection, which is more efficient over shorter time-scales than conduction and may occur alongside limited mafic-silicic mingling, making this model consistent with observations of 'cryptic' mafic component of ~6% by volume in phase III products (Humphreys *et al.,* 2009; 2012) and of excess gas (Edmonds *et al.,* 2014).

Questions still remain concerning the dynamics of the mingling between the two magmas at SHV. Although different enclave types have been recognised in earlier eruptive phases (Barclay *et al.,* 2010; Mann, 2010), there has been little attempt to decipher the differing petrological and textural features between types. Eruptive phase length has altered in phases IV and V (Wadge *et al.,* 2014), and therefore an additional aim of the work is to evaluate any changes in enclave petrology relative to the early stages of the eruption that might allow us to infer changes in magma reservoir conditions.

3.2   Results

We present in this chapter, the results of the extensive fieldwork of the erupted phase V products, and characterise the suite of phase IV and V samples collected through petrological and textural analyses. Sample locations are shown in table 2.1 and figure 2.1; methods employed during fieldwork are outlined in chapter 2.
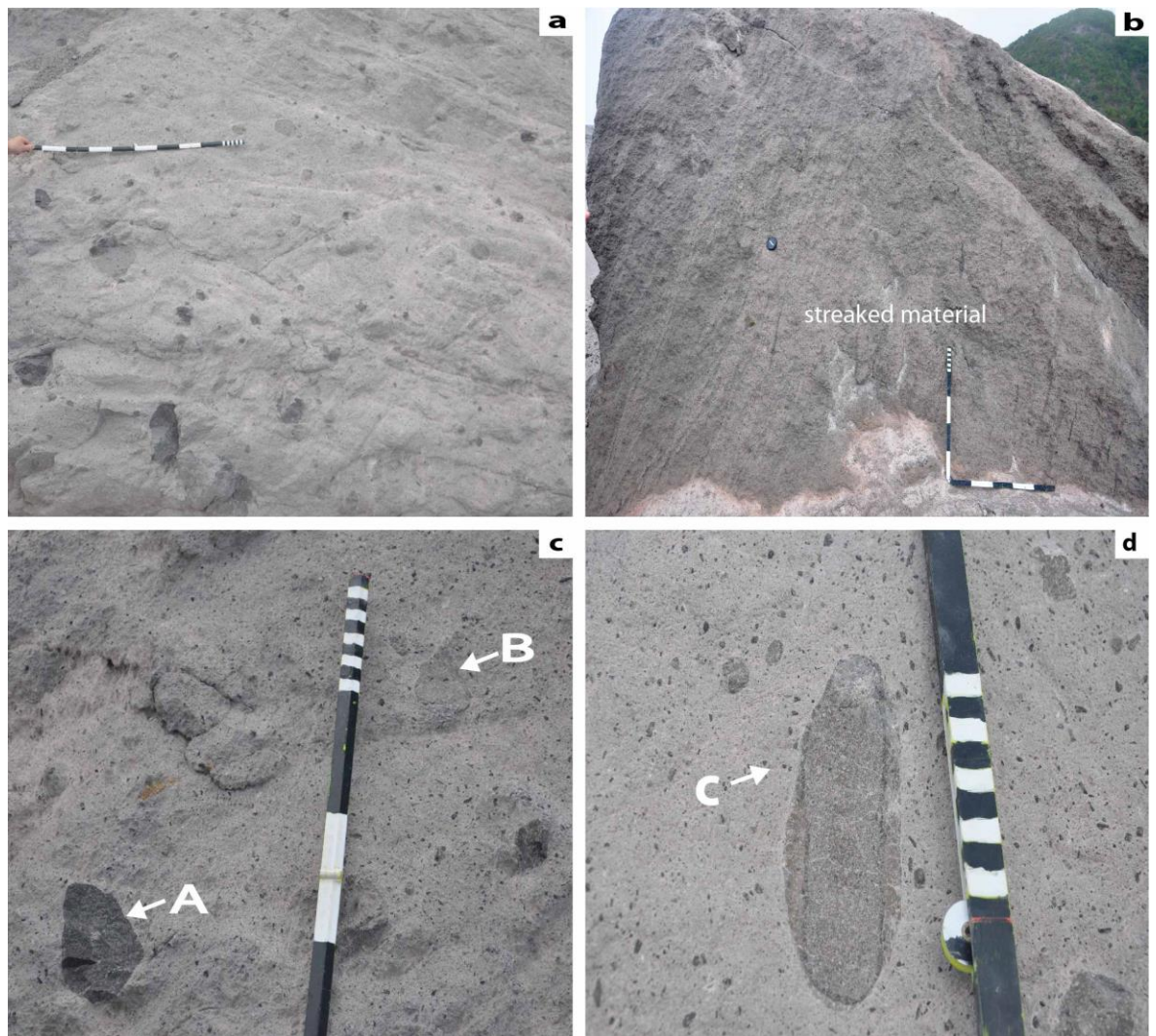
Figure 3.1: (a) A representative image of an andesitic block from Feb 11 2010 dome collapse (scale: 10 cm with 2 cm intervals). (b) Image of an andesite block from the Trants area (Fig. 2.1) with distinctive streaks within. Continuous white streaks are predominantly made up of plagioclase, discontinuous black streaks represent those in figure 3.10. (c) Image of type A and B enclaves seen in the field. Note distinct colour difference and the clearly distinct margins in A as opposed to B. (d) Image of a type C enclave observed in the field, with two distinct portions to the enclave. Type C enclaves have variable textures therefore this is not necessarily a typical example.

41

The andesite erupted in phase V of the eruption is porphyritic with a fine-grained groundmass, and contains mafic enclaves as in earlier phases (Fig. 3.1) (Murphy *et al.,* 1998, 2000; Harford *et al.,* 2002; Barclay *et al.,* 2010). Some andesite blocks contain distinctive streaked, highly crystalline layers of amphibole and plagioclase (Fig. 3.1), and rare cumulate nodules. Pumice is porphyritic with a fine-grained groundmass and often contains mafic enclaves.

The abundance of the mafic enclaves in the field was measured in the phase V deposits using the method outlined in chapter 2. Total measured mafic enclave abundances within andesitic phase V blocks range from 2.9 % to 8.2 % from point counting, with a mean of 5.6 % (Table 3.1). The size of individual enclaves ranges from 1 to 80 cm; however, ~95 % of the enclaves were <10 cm in apparent diameter (Fig. 3.2). We categorised phase V enclaves into three broad types that were readily identifiable in the field using characteristics such as phenocryst proportions, the nature of the margin between enclave and andesite, vesicularity, enclave size and shape, and groundmass size and colour (Table 3.2). The classification scheme applied by Barclay *et al.,* (2010) is insufficient to describe the large textural diversity of the phase V enclaves.
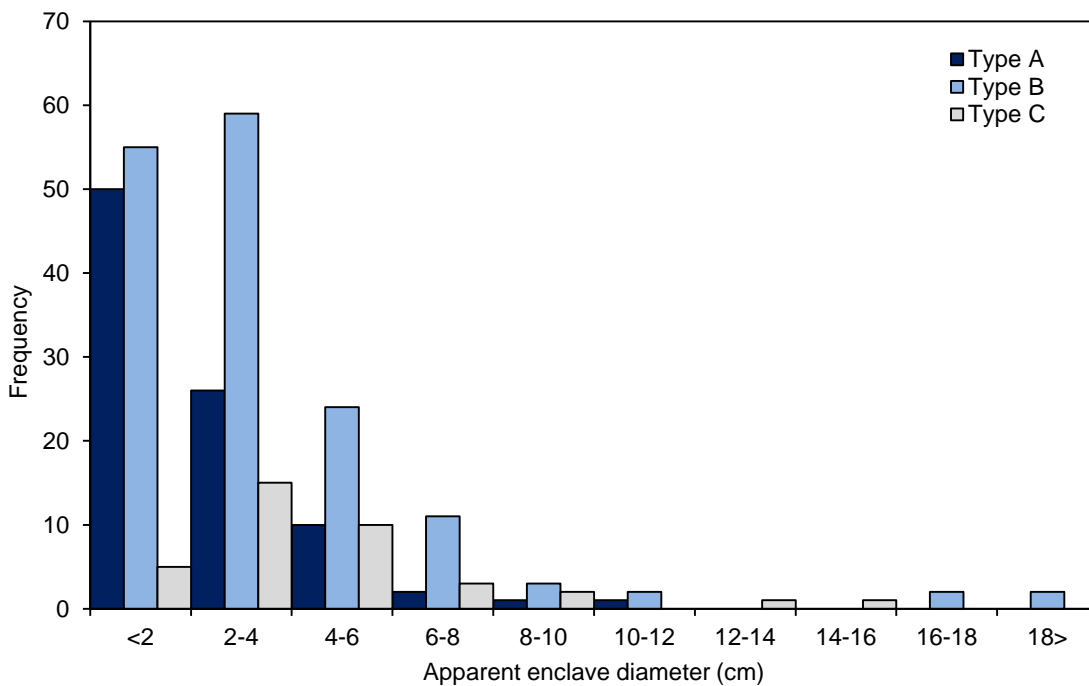
Figure 3.2: Frequency size distribution of measured enclave apparent diameters from andesitic blocks used to evaluate mafic enclave abundance in Table 3.2.

Type A enclaves are characterised as phenocryst-poor, vesicle-rich, with dark grey groundmass and chilled margin (Table 3.2, Fig. 3.1). In the field these enclaves are readily identified by their dark grey colour caused by the fine-grained groundmass. Type A enclaves are typically ellipsoidal to sub-angular in shape, with occasional fingers of the enclave material protruding into the andesite. Commonly the smaller (1–5 cm) angular enclaves without evident chilled margins are clustered, suggesting that they are fragments of a larger enclave that disaggregated mechanically after formation. Type A enclave volume fraction reaches 46 % (with a mean of 22 %) of the total number of enclaves measured (Table 3.1). These have the smallest mean diameter of all the enclave types measured (2.3 cm), although large enclaves over 18 cm were also measured (Fig. 3.2).

Table 3.1: *Phase V mafic enclave proportional abundances*

Enclave type	Block 1a*	Block 1b*	Block 2	Block 3	Block 4	Block 5	Block 6	Block 7
Total points	1326	2550	2397	2397	2397	2397	2295	2601
Total enclaves points	47	155	137	196	125	115	67	126
Overall % of magmatic enclaves	3.54	6.08	5.72	8.18	5.21	4.80	2.92	4.84
Total number of enclaves measured	20	30	46	39	48	43	30	29
Type %								
A	0.00	30.32	13.14	4.59	27.20	27.83	46.27	29.37
B	100.00	60.65	77.37	80.61	54.40	31.30	52.24	52.38
C	0.00	9.03	9.49	14.80	18.40	40.87	1.49	18.25

*Block 1a and 1b is the same block, but two different faces were analysed
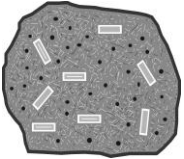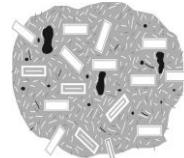
Type B enclaves are characterised as phenocryst-rich, vesicle-poor, with a light grey groundmass and indistinct margins (Table 3.2, Fig. 3.1). In the field, type B enclaves are a lighter grey than type A, and resemble most closely the host andesite in colour and texture (Fig. 3.1). They are generally ellipsoidal and well-rounded, although a few (<5 %) are angular in shape. Type B enclaves dominate across most of the analysed blocks, and represented 31% to 100% (with a mean of 64%) of the total enclaves measured. Their size distribution is strongly positively skewed from the norm with most <6 cm, (with a mean of 3.4 cm; Fig. 3.2).

Type C enclaves are composite and are characterised by distinct textural zones akin to types A and B (Fig. 3.1d; Table 3.2). Type C enclaves were present in all blocks examined except for block 5, with variable abundances of 0–41% (mean; 14%; Table 3.1).

The size distribution of type C enclaves shows a weaker positive skew from the norm towards smaller sizes, (with a mean of 4.4 cm; Fig. 3.2). Below 2 cm composite textures were difficult to identify, which may be a factor in the increased mean size in comparison to other enclave types.

Distribution of enclaves is not even through the blocks; enclaves tend to cluster together, particularly in the smaller size fractions. Heterogeneity is observed both between blocks and within a single block; *e.g.* for block 1a-b, where two faces of the same block were measured, block 1a had a lower abundance of enclaves (3.5%), relative to the other face, block 1b (6.1%, Table 3.1). Furthermore, type A was absent from block 1a, but type A enclaves constituted 30% of the total in block 1b (Table 3.1), and of those, 66% were <2 cm (Fig. 3.2). This suggests localised clustering both of enclaves and enclave types.

Table 3.2: *Summary of key features of enclave types A and B*

Type		Composition	Margin	Vesicularity (shown in black)	Framework crystals	Inherited phenocryst abundance	Inherited plagioclase phenocryst rim thickness
A		49-52 wt % SiO_2	Chilled	32% vol (mean)	High-Al amphibole present	<8% vol	132-230µm
B		53-57 wt % SiO_2	Unchilled to diffuse	13% vol (mean)	High-Al amphibole rare to absent	15-25% vol	27-113µm

3.2.1 Petrological and Textural Analysis: SHV andesite

Following the criteria set out in Murphy *et al.,* (2000), the term phenocryst is used for large crystals with major axis >300 µm, microphenocrysts 100–300 µm, and microlites <100 µm for the andesite and enclaves. The compositions of minerals from phase V andesite are similar to those from earlier eruptive phases, and there is no major change in andesite assemblage (Murphy *et al.,* 2000; Humphreys *et al.,* 2009; Thomas *et al.,* 2014). The andesite from phase V is crystal rich (29–38% phenocrysts; table 3.3) similar to the phases I-III (Murphy *et al.,* 2000; Humphreys *et al.,* 2009; Mann 2010). The andesite

phenocryst assemblage is plagioclase + hornblende + orthopyroxene + Fe-Ti oxides, with minor quartz, trace amounts of apatite and clinopyroxene, and rare zircon (Murphy *et al.,* 2000; Humphreys *et al.,* 2009; Mann 2010; this study). The andesite groundmass is plagioclase + orthopyroxene + clinopyroxene + Fe-Ti oxides + rhyolitic glass (Murphy et al., 2000; Humphreys et al., 2009; Mann 2010; this study). The phenocrysts have variable textures in all samples similar to those described previous studies of the phase I-III andesite (Murphy *et al.,* 2000; Humphreys *et al.,* 2009). Plagioclase crystal textures may display sieve-texturing, oscillatory zoning and some patchy zoning. The sieve-texture zones, which are made up of networks of calcic plagioclase and glass, are usually in a rim near the outer part of the crystal, but some (12–23 % of the total plagioclase population; table 3.3) have a sieve-texture throughout the crystal apart from the outer rim. Hornblende crystals (5–11 %; table 3.3) may be in part or completely replaced by opacite, have reaction rims of clinopyroxene, plagioclase, oxides and glass, or decompression rims. Only <1 crystals per thin section may show little sign of these textures, the vast majority show these textures extensively. These hornblende textures may indicate instability due to heating, rapid decompression or shallow storage in the dome (Garcia & Jacobson, 1979; Murphy *et al.,* 2000; Rutherford & Devine, 2003; Browne & Gardner, 2006; Buckley *et al.,* 2006; Plechov *et al.,* 2008). Orthopyroxene phenocrysts (1–4 %; table 3.3) may be unzoned, may show reverse zoning, or clinopyroxene overgrowth rims. Multiple Mg-rich zones in some orthopyroxene crystals have been interpreted as evidence for reheating episodes (Humphreys *et al.*, 2009). Quartz phenocrysts (<1 %; table 3.3) can be embayed, have clinopyroxene rims or be resorbed. The glass is rhyolitic, but may be partially devitrified in some samples as in earlier phases (Murphy *et al.,* 2000; Mann, 2010; Humphreys *et al.,* 2009, 2010).

Table 3.3: *Modal composition of the phase V SHV andesite*

	MT30	MT35	MT31	MVO1588
Plagioclase	245	150	209	199
Plagioclase sieve texture %	12.7	23.3	17.2	11.6
Hornblende	73	69	100	41
Orthopyroxene	7	18	37	20
Quartz	0	5	0	0
Oxides	5	4	7	7
Groundmass (including vesicles)	694	564	567	629
Total points	1024	810	920	896

3.2.2 Petrological and Textural Analysis: SHV mafic enclaves

Mafic enclaves have a diktytaxitic groundmass framework of elongate, randomly-oriented crystals (Fig. 3.3a). This groundmass consists of plagioclase ± clinopyroxene ± high-Al-amphibole ± orthopyroxene. Fe-Ti oxides are observed throughout, and are often more abundant near inclusion margins. Titanomagnetite is the most common oxide, but ilmenite is also present. Trace amounts of apatite are often observed as inclusions in titanomagnetite and plagioclase-inherited phenocrysts (see below). Variable amounts of interstitial rhyolitic glass (71–78 wt% SiO_2) are found within the enclaves. Clinopyroxene (Mg# ~75) occurs as either the breakdown product of amphibole, or as reaction rims on inherited orthopyroxene phenocrysts, or in the groundmass of the enclaves. The degree to which the framework is interlocked is usually inversely correlated with the amount of glass, disruption of vesicles and median size of the groundmass crystals.
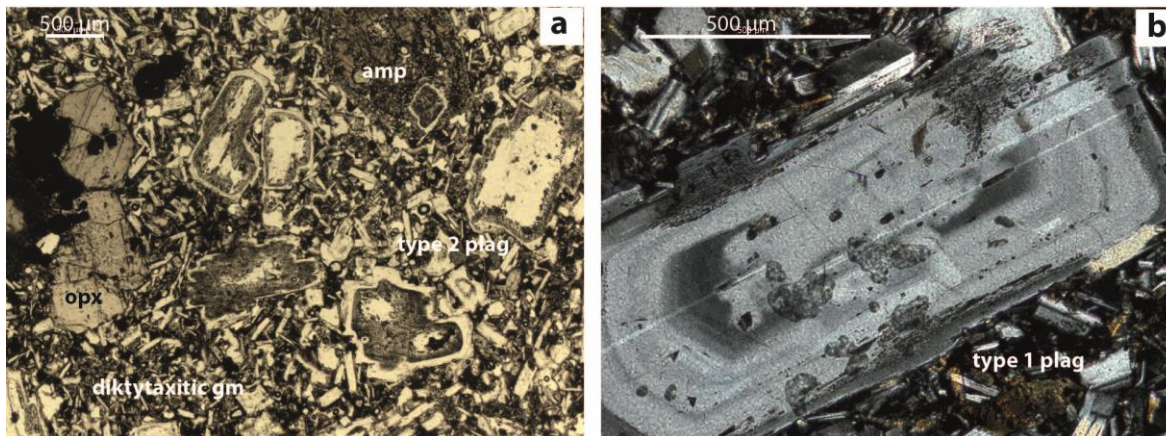
Figure 3.3: Inherited phenocryst types derived from the SHV andesite in mafic enclaves. Scale is 500μm. (a) Photomicrograph of mafic enclave with inherited phenocrysts of amphibole (amp), orthopyroxene (opx), type 2 plagioclase (type 2 plag) with varying degrees of pervasive sieve-texture, and a diktytaxitic groundmass (diktytaxitic gm) (b) Photomicrograph of a large inherited type 1 plagioclase crystal (type 1 plag) with oscillatory zoning.

Table 3.4: *Inherited phenocryst proportional abundances of phase V enclave types*

Inherited Phenocryst Type	Type A (%)	Type B (%)	Type C: inner (%)	Type C: exterior (%)
Plagioclase type 1	*0*	*0.5-10.9*	*0*	*1.9*
Plagioclase type 2	*0 -7*	*5 - 21*	*8.9*	*13*
Plagioclase Total	0 -7	8 - 21.2	8.9	14.9
Amphibole	0 - 2.9	1.2 - 8.5	3.3	6.7
Orthopyroxene	0 - 0.6	0.4 - 4.5	0	4.5
Total Range	**0-8**	**15.8 - 23.6**	**12.6**	**26.5**

Large crystals (~2-3 cm) of plagioclase, amphibole and orthopyroxene are present in the mafic enclaves (Fig. 3.3); most exhibit textural and compositional evidence that they have been inherited from the andesite (Murphy *et al.,* 2000; Humphreys *et al.,* 2009). We refer to these as 'inherited phenocrysts' as they are not antecrystic or xenocrystic in origin. Following Murphy *et al.,* (2000), the large inherited plagioclase phenocrysts in the enclaves can be split into two main types (Fig. 3.3). Type 1 comprise large, oscillatory-zoned, sodic phenocrysts (An_{49-57}) with calcic rims (An_{69-80}) 40–47 µm thick, similar to the type 1 and 2 plagioclases in the andesite (after Murphy *et al.,* 2000) (Fig. 3.3b). Type 2 are reverse-zoned, dusty, sieve-textured phenocrysts, where the sieve-texture (of thickness 70 µm to extending to the crystal core) is overgrown by a clear calcic rim (of thickness 0-230 µm) and comprises glass and high-anorthite (An_{70-90}) plagioclase (Fig. 3.3a). Smaller crystals (<1000 µm) have a pervasive sieve-texture. Rim width is typically largest where the degree of sieve texture is highest (Fig. 3.4).
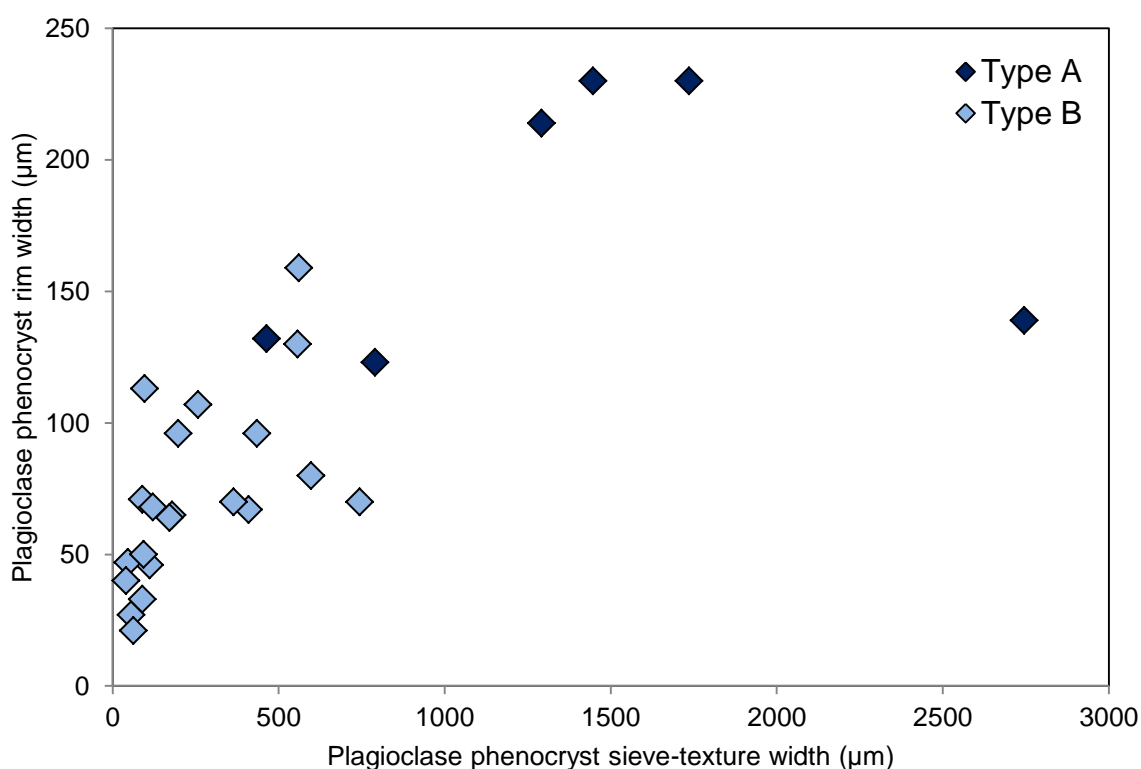
Figure 3.4: Inherited plagioclase phenocrysts overgrowth rim width (measured distance from crystal edge to sieve-texture) *vs.* sieve-texture width (where sieve-texture variable, the maximum width was measured). Increasing rim width is correlated with sieve-texture width. Note that where sieve-texture width is greater than 1000µm the sieve-texture pervades through to the crystal core.
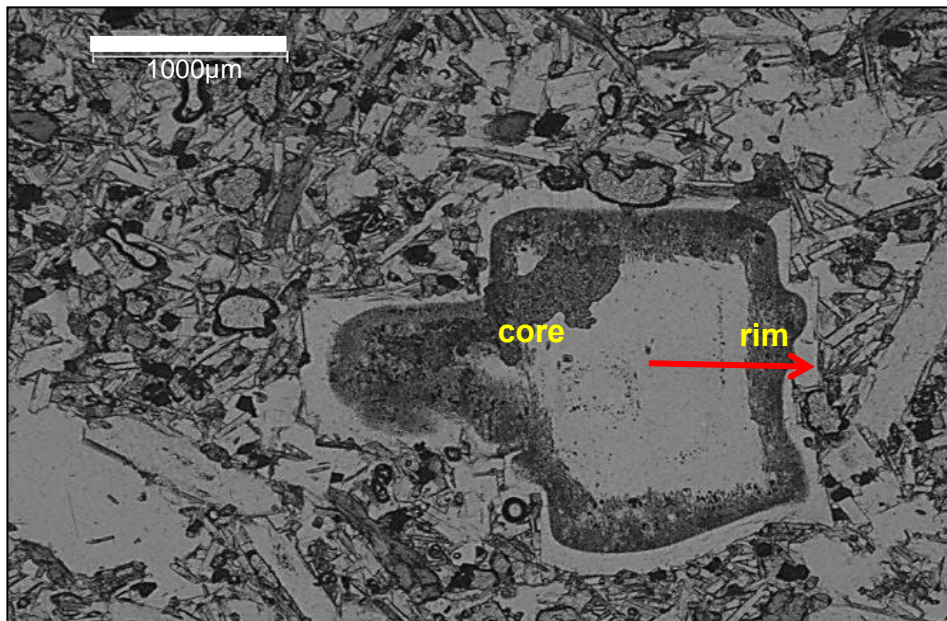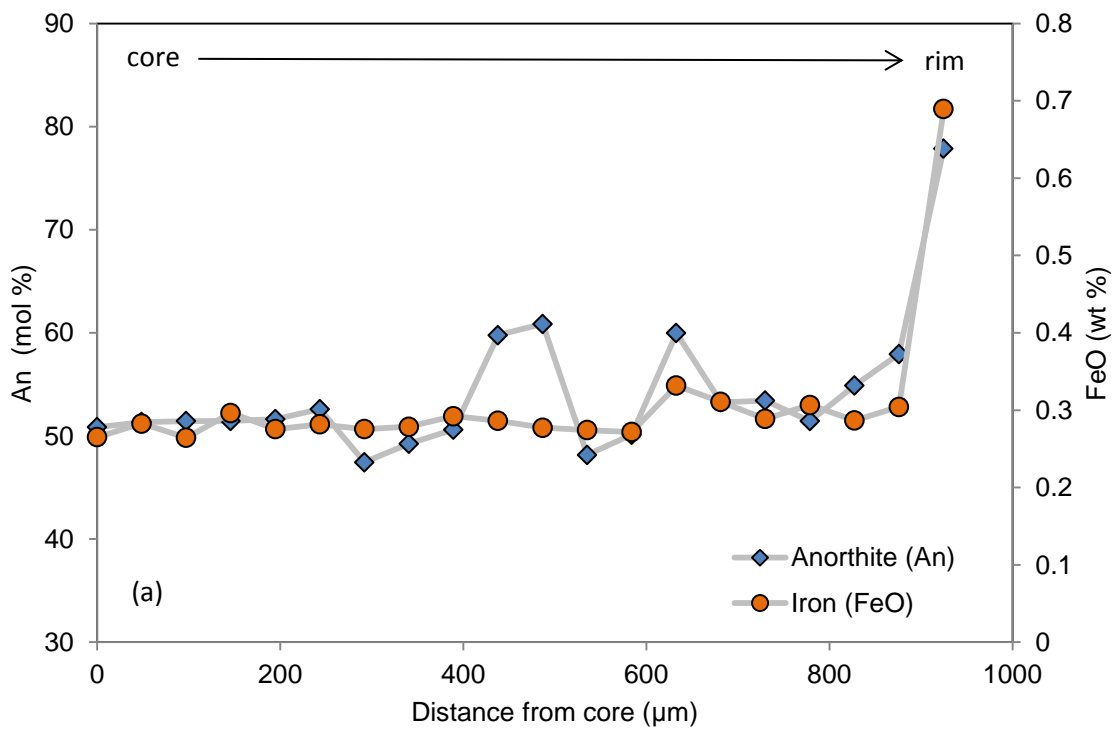
Figure 3.5a: Core to rim transects across inherited plagioclase crystals (MVO1588p27). Increase in An at rim is correlated with a sharp increase in FeO at the rim, indicating incorporation of phenocryst into high-calcium melt.
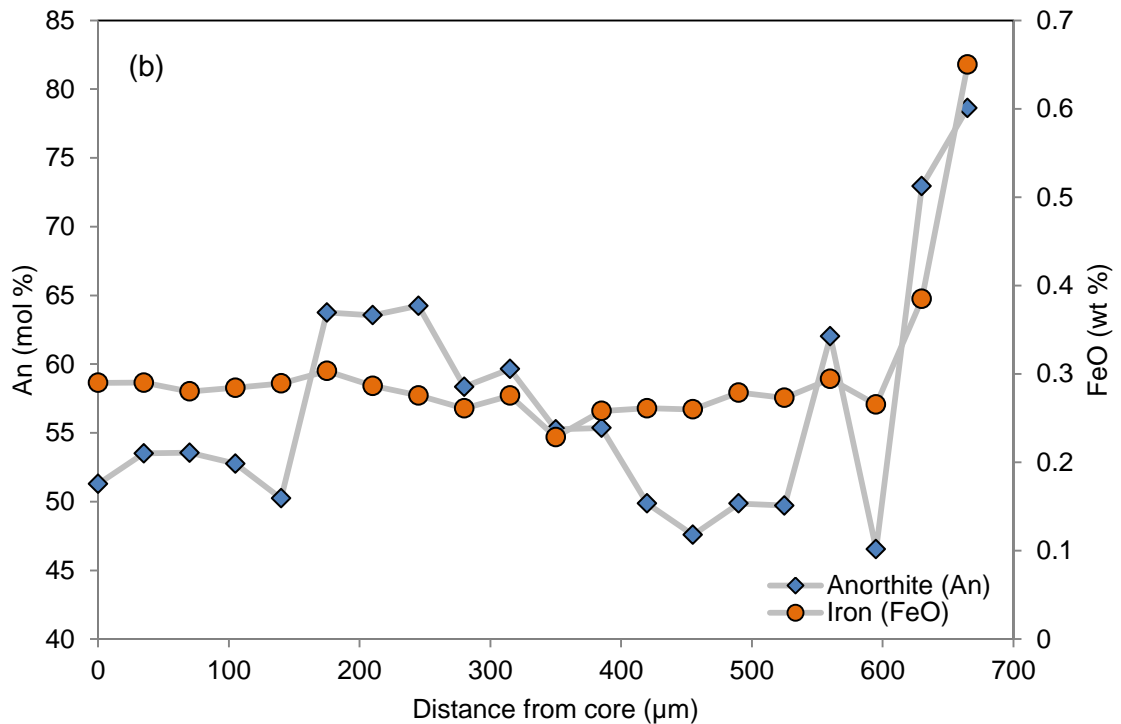
Figure 3.5b: Core to rim transects across inherited plagioclase crystals (MVO1591p16). Increase in An at rim is correlated with a sharp increase in FeO at the rim, indicating incorporation of phenocryst into high-calcium melt. Further analyses can be found in appendix 2.

Low anorthite compositions (An_{49-57}) of the cores in both plagioclase types are identical to andesite phenocrysts compositions observed throughout the eruptive phases (Murphy *et al.,* 2000; Humphreys *et al.,* 2009). Core-to-rim transects across inherited plagioclase phenocrysts show a sharp increase in X_{An}, FeO and MgO at the rim (Fig. 3.5), similar to observations by Humphreys *et al.,* (2009). Inherited amphibole phenocrysts are Mg-hornblende (Leake *et al.,* 1997), identical to low Al_2O_3 (6-8 wt %) amphibole phenocrysts in the andesite. They are often variably opaticised, or partially reacted, with plagioclase and clinopyroxene overgrowths, indicating instability due to heating, rapid decompression or shallow storage in the dome (Garcia & Jacobson, 1979; Murphy *et al.,* 2000; Rutherford & Devine, 2003; Browne & Gardner, 2006; Buckley *et al.,* 2006; Plechov *et al.,* 2008). Inherited orthopyroxene phenocrysts commonly have clinopyroxene overgrowths and Fe-Ti oxide inclusions, and are typically reverse-zoned, with Mg# 58-74 identical to the andesite orthopyroxene compositions (Murphy *et al.,* 2000; Humphreys *et al.,* 2009). Rare embayed quartz phenocrysts with rims of clinopyroxene were also observed. Rare zircon crystals are also present in some enclaves.

3.2.2.1 Type A enclaves

Type A enclaves (Table 3.2 and Fig. 3.6) are defined by a fine-grained groundmass, high vesicularity (19–40%, Fig. 3.7), chilled margins and low abundance of inherited phenocrysts (0–8.6%, Table 3.4, Fig. 3.8). The framework consists predominantly of plagioclase, with acicular amphibole and clinopyroxene also present. In the framework plagioclase disequilibrium features similar to a sieve texture can be seen developing in the cores of many microphenocrysts (Fig. 3.6 d). These are enclosed by rims of clear plagioclase of composition An_{77-89} (Table 3.5, Fig. 3.6d). The framework amphibole (~13-15 wt % Al_2O_3, Table 3.5) is magnesio-hastingsite to pargasite (Leake *et al.,* 1997), and typically has reaction rims of clinopyroxene that range from 5 μm thick to sometimes pervading the entire crystal (Fig. 3.6). In phase I the presence of framework amphibole was observed to correspond with larger enclave sizes (Murphy *et al.,* 2000); this appears not to be the case in phase V. Framework amphibole is present irrespective of the size of the enclave. Glass abundance is low (<5%), but is concentrated near vesicles and chilled margins. It contains on average 75 wt % SiO_2 and 3.8 wt % K_2O (Table 3.5 and Fig. 3.9), and we examine the glass geochemistry in more detail in section 2.2. Chilled margins are typically present, defined by a decrease in groundmass grain size towards the boundary, which is sharp to weakly gradational. Across large enclaves, inherited phenocryst abundances can be spatially extremely variable with densely clustered plagioclase phenocrysts associated with regions of increased enclave vesicularity. Type 1 plagioclase (with minor disequilibrium textures) is usually absent with predominantly type 2 (sieve-textured) dominating (Table 3.4). The rims on type 2 crystals range from 132–230 μm thick, which are the thickest rims measured in all the enclave types (Fig. 3.4). The rims of the inherited phenocrysts have high anorthite contents, of An_{80-90}. Inherited amphibole phenocrysts are commonly completely opaticised with very little amphibole remaining, or have been almost completely replaced by clinopyroxene and plagioclase reaction products. Inherited phenocrysts are rarely observed transecting the boundary in this enclave type.
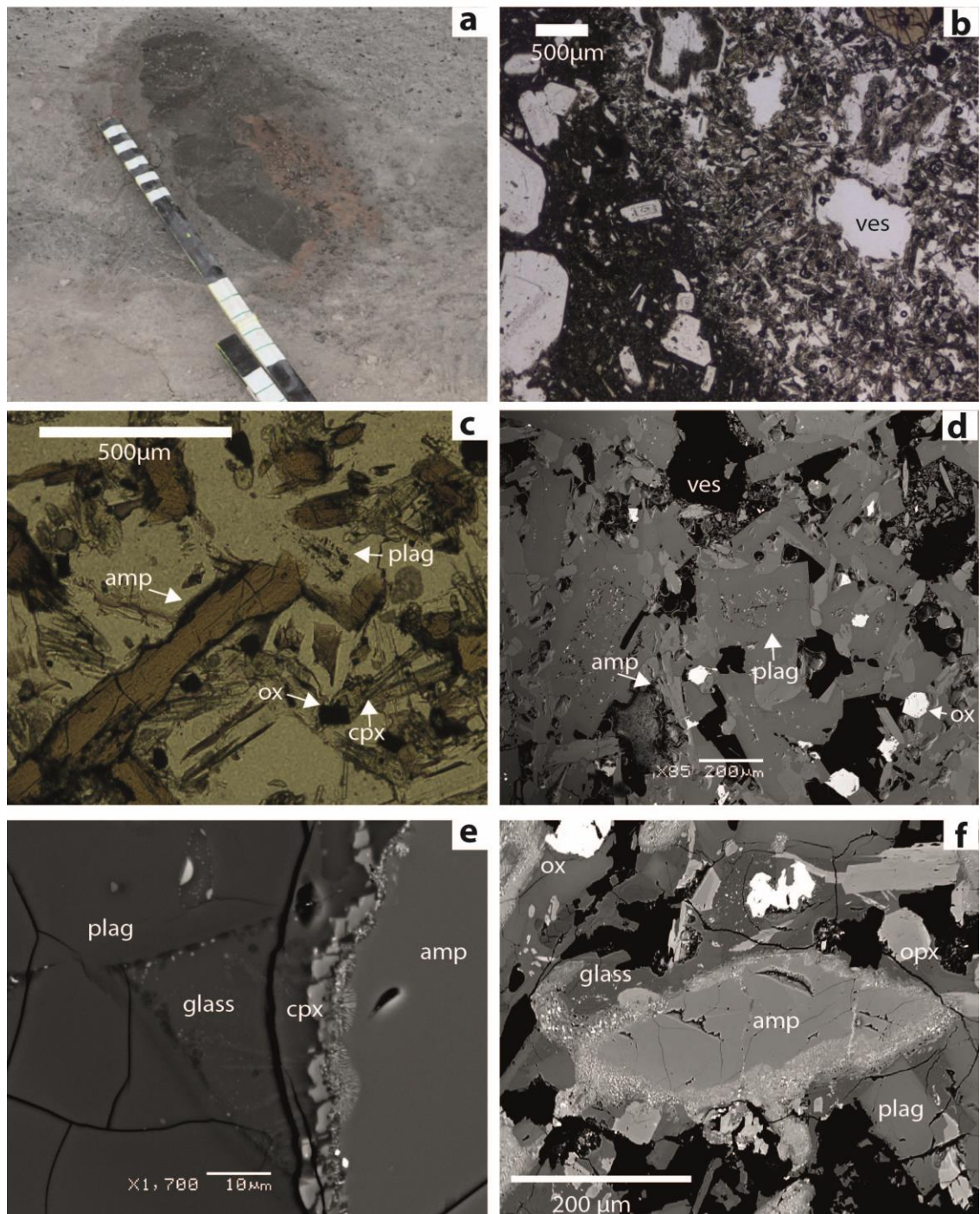
Figure 3.6: Images are representative of type A enclaves. (a) Large type A enclave from Feb 11 2010 dome collapse deposit. Darkening of andesite around the enclave is an artefact of water spray used to clean the outcrop (scale: 10 cm with 2 cm intervals) (b) Photomicrograph of a type A chilled margin shown by a reduction in framework crystal size; andesite is on the left and mafic enclave on the right (c) Photomicrograph of type A framework crystals, Fe-Ti oxides (ox) (d) BSE image of framework plagioclase with sieve-texture developing in the interior of the crystal. (e) BSE image of a clinopyroxene reaction rim developing on a high-Al amphibole microphenocryst. (f) Amphibole developing a cpx and oxide reaction rimS

Table 3.5: *Average framework microphenocryst compositions from mafic enclaves*

Plagioclase	Type A (core)	±1σ	Type A (rim)	±1σ	Type B (core)	±1σ	Type C Interior	±1σ	Type C Exterior	±1σ
n	19		12		18		9		7	
SiO_2	47.20	1.76	47.15	1.22	49.90	1.89	45.82	0.94	48.86	1.15
TiO_2	0.02	0.01			0.03	0.01	0.02	0.01	0.03	0.01
Al_2O_3	32.67	1.41	32.89	0.95	31.17	1.13	32.84	0.79	30.62	1.01
FeO	0.57	0.08	0.64	0.07	0.68	0.06	0.59	0.04	0.70	0.06
SrO	0.03	0.02	0.03	0.04	0.04	0.01	0.01	0.06	0.03	0.04
MgO	0.06	0.02	0.08	0.02	0.07	0.02	0.07	0.03	0.08	0.02
CaO	16.32	1.67	16.97	0.94	14.68	1.35	17.02	0.68	14.89	0.94
Na_2O	2.12	0.85	1.85	0.54	3.28	0.82	1.76	0.39	3.01	0.52
K_2O	0.03	0.01	0.03	0.04	0.06	0.02	0.02	0.02	0.06	0.02
Total	99.03		99.63		99.93		98.12		98.34	
X_{An}	80.79	7.62	83.39	4.79	71.03	7.06	84.12	3.46	72.98	4.66

Amphibole (core)	Type A	±1σ	Type B	±1σ	Type C Interior	±1σ	Type C Exterior	±1σ
n	18		10		5		na*	
SiO_2	41.27	0.74	41.88	2.20	40.21	0.43		
TiO_2	2.01	0.18	1.87	0.20	2.06	0.14		
Al_2O_3	14.77	1.10	13.81	2.59	14.97	0.40		
Cr_2O_3	0.01	0.01	0.01	0.01	0.00	0.02		
FeO	10.00	0.96	10.79	2.04	9.75	0.44		
MnO	0.12	0.03	0.18	0.14	0.11	0.05		
MgO	15.21	0.43	14.65	0.72	15.23	0.24		
CaO	11.96	0.21	11.66	0.42	11.96	0.19		
Na_2O	2.44	0.07	2.30	0.34	2.45	0.07		
K_2O	0.25	0.02	0.23	0.05	0.24	0.03		
Cl	0.06	0.01	0.07	0.03	0.08	0.05		
F	0.01	0.01	0.03	0.04	n.a.			
Total	98.09		100.25		99.88			

Clinoyroxene (core)	Type A	±1σ	Type B	±1σ	Type C Interior	±1σ	Type C Exterior	±1σ
n	9		9		5		8	
SiO_2	49.21	1.48	50.37	1.86	47.38	1.40	47.96	2.01
TiO_2	0.80	0.28	0.64	0.26	0.95	0.35	0.90	0.39
Al_2O_3	4.73	1.72	4.16	2.62	6.07	2.14	5.42	2.35
FeO	10.09	2.39	10.04	1.44	9.25	1.60	9.58	1.17
MnO	0.37	0.20	0.41	0.19	0.29	0.20	0.31	0.10
MgO	14.50	1.17	14.39	0.88	14.06	0.69	14.41	1.37
CaO	19.76	2.19	19.80	1.36	20.46	1.46	19.91	1.60
Na_2O	0.27	0.05	0.31	0.17	0.25	0.01	0.24	0.04
Total	99.75		100.87		98.76		98.82	

Table 3.5: *Average framework microphenocryst compositions from mafic enclaves*

Titanomagnetite (core)	Type A		Type B		Type C Interior		Type C Exterior	
		±1σ		±1σ		±1σ		±1σ
n	10		17		na		6	
SiO_2	0.10	0.02	0.44	1.12			0.32	0.62
TiO_2	9.33	2.53	9.26	2.92			9.40	1.83
Al_2O_3	4.15	1.02	2.16	0.25			2.31	0.33
FeO	79.69	1.66	81.75	3.52			81.18	2.37
MnO	1.65	0.26	1.24	0.36			1.57	0.13
MgO	0.39	0.04	0.52	0.09			0.54	0.05
CaO	0.05	0.04	0.07	0.07			0.07	0.06
Total	95.38		95.46				95.41	

Glass	Type A		Type B		Type C Interior		Type C Exterior	
		±1σ		±1σ		±1σ		±1σ
n	26		14		7		7	
SiO_2	75.05	1.38	77.05	1.29	74.46	0.40	75.52	0.90
TiO_2	0.63	0.14	0.39	0.05	0.64	0.10	0.51	0.05
Al_2O_3	12.21	0.65	11.50	0.43	12.07	0.27	11.75	0.28
FeO	2.20	0.30	1.63	0.23	2.42	0.11	2.26	0.28
MgO	0.23	0.18	0.11	0.04	0.31	0.05	0.15	0.12
MnO	0.05	0.06	0.06	0.04	0.06	0.04	0.12	0.07
CaO	1.18	0.41	1.01	0.32	1.42	0.12	1.52	0.14
Na_2O	4.16	0.47	3.61	0.16	4.00	0.17	3.91	0.11
K_2O	3.83	0.55	2.98	0.10	2.89	0.08	2.68	0.16
P_2O_5	0.13	0.11	0.11	0.25	0.22	0.08	0.22	0.09
Cl	0.35	0.17	0.46	0.11	0.52	0.08	0.47	0.08
Total	100.13		99.04		99.15		99.23	

*na: not available
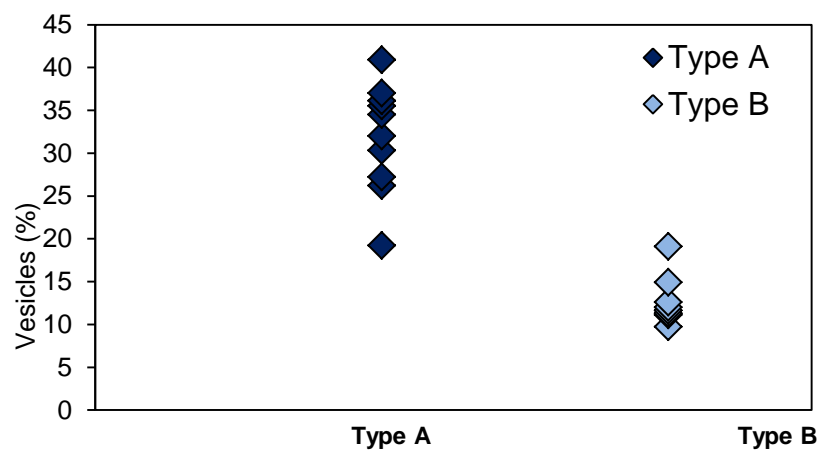
Figure 3.7: Vesicle size distribution of measured type A and B enclaves.
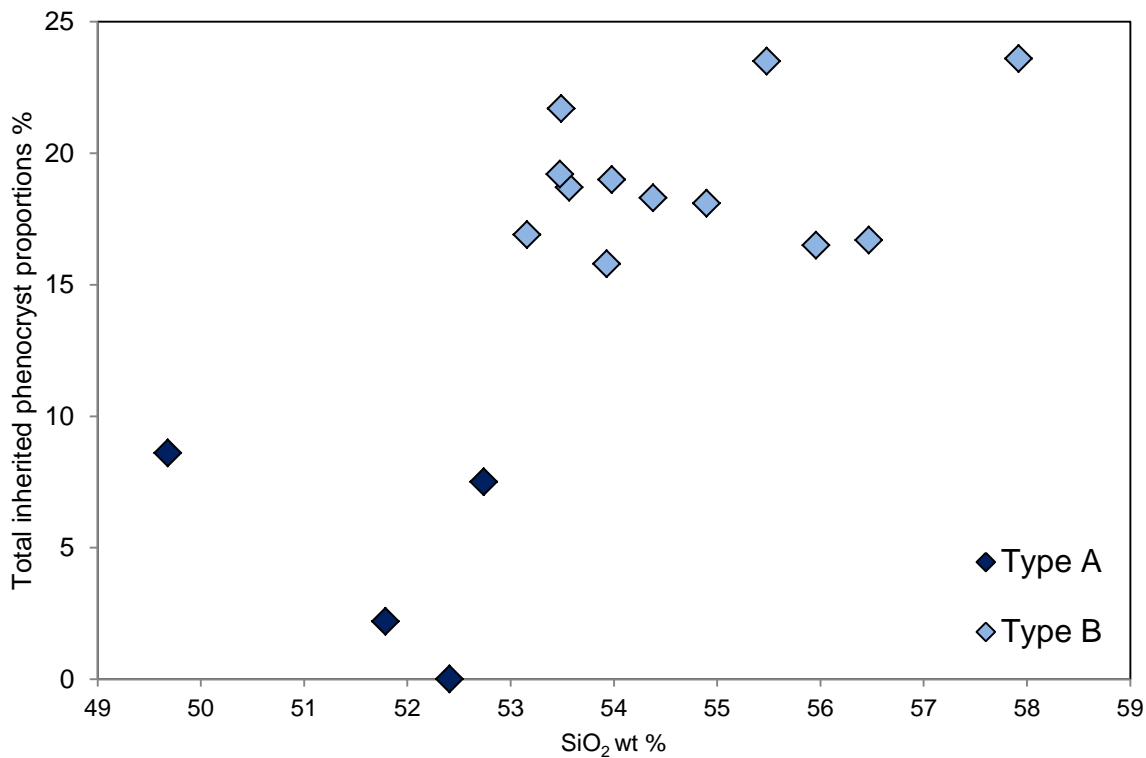
Figure 3.8: Total inherited phenocryst modal proportions by enclave type against SiO_2 composition. A total of 16 enclaves were used and we observe that enclave types A and B plot in two distinct fields. Details of the inherited phenocryst type proportions counting are shown in Table 3.4.

3.2.2.2   Type B enclaves

Type B enclaves (Table 3.2 and Fig. 3.9) are defined by a fine to medium-grained groundmass, low to medium vesicularity (9–19%, Fig. 3.6, Fig. 3.7), diffuse margins, and medium to high inherited phenocryst abundance (16.5–26%, Fig. 3.7, Fig. 3.8 and Table 3.4). As with all enclave types the framework is predominantly plagioclase (An_{65-75}), which have lower X_{An} values in comparison with type A framework plagioclase (An_{77-89}). High-Al framework amphibole is typically absent, but occasionally present in enclaves with lower abundances of inherited phenocrysts (i.e. those that are closest to the type A enclaves). Glass is rare (<5%), and contains on average 77 wt% SiO_2 and 2.9 wt% K_2O (Table 3.5), and is typically pooled near large vesicles where present (Fig. 3.9c). Orthopyroxene microlites (Wo_{2-4}, Fs_{38-40}, En_{56-60},) and calcic plagioclase microlites are sometimes observed growing outwards from vesicle walls (Fig. 3.9c). Some enclaves have large elongated vesicles, (~4 cm) with some vesicles disrupting the diktytaxitic framework, where crystals close to larger vesicles appear to have been bent after formation. Crystals

(microlites or inherited phenocrysts) are regularly seen transecting enclave margins. Type 2 inherited plagioclase phenocrysts dominate (Table 3.4); overall rim thickness (27–113 μm) is smaller in comparison to type A enclaves (see above) and is variable between different enclaves (Fig. 3.4). Inherited amphibole phenocrysts have variable disequilibrium textures: phenocrysts are either completely opaticised, broken down to clinopyroxene and plagioclase, or have undergone only minor disequilibrium. Rare inherited quartz with clinopyroxene overgrowth rims are also observed.

3.2.2.3   Type C enclaves

Type C enclaves are composite, with at least two distinct different textural zones with respect to colour, vesicularity, and inherited phenocryst assemblage. Sample MT08 for example has a dark grey interior surrounded by a lighter grey exterior (Fig. 3.9e-f). The dark grey interior is somewhat similar to the type A enclaves, with a diktytaxitic groundmass framework composed of plagioclase (~An_{84}; Table 3.5), amphibole (~14 wt % Al_2O_3; Table 3.5) and clinopyroxene, and a mean vesicularity of 23.9%. Inherited phenocryst abundance is low (12.6%); type 2 inherited plagioclase phenocrysts are dominant (Table 3.4). The lighter grey outer portion resembles type B enclaves, with a diktytaxitic framework of plagioclase (~An_{72}; table 3.5) and clinopyroxene (composition from table 3.5); this portion does not display the same degree of crystal interlocking as the darker interior portion. Sparse high-Al amphibole laths are also observed in the outer portion close to the margin with the interior portion, typically where the margin is more diffuse. Furthermore, at the most diffuse margins plagioclase microphenocrysts are often observed. Vesicularity is lower in the outer portion relative to the interior portion (~17.2%). Inherited phenocryst abundances are high (~26.5%), dominated by plagioclase type 2, but type 1 is also present (Table 3.4). Inherited amphibole and orthopyroxene are also present, which typically display more subtle disequilibrium textures than in the interior portion. The glass fraction is between 5 and 10%, and it is higher in the interior portion. Glass composition is similar to the type B enclaves in both portions, although the interior portion has a slightly lower mean (74 wt% SiO_2) to the exterior (75 wt% SiO_2; Table 3.5). The margin between the exterior portion and the host andesite is diffuse, with phenocrysts transecting the margin.
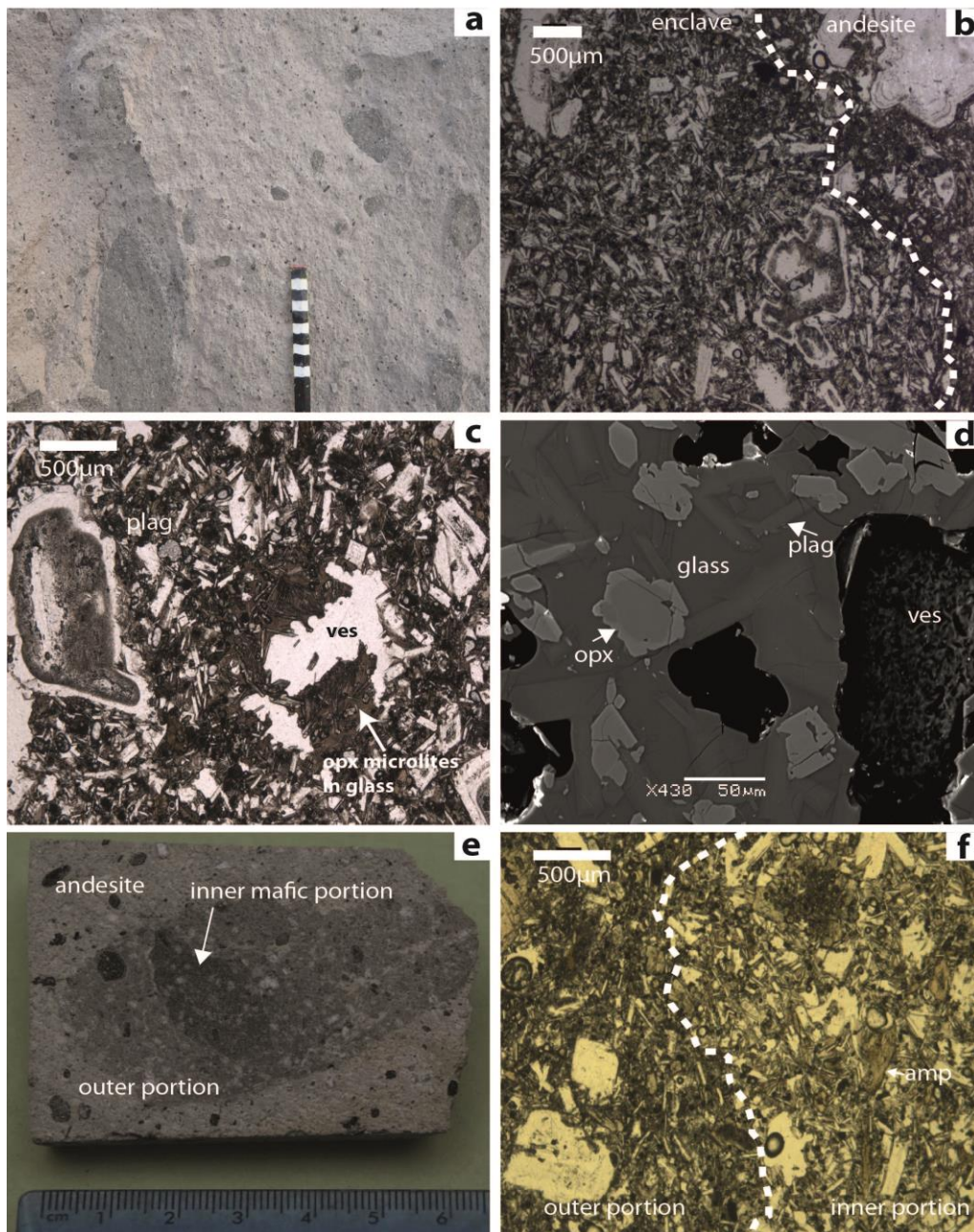
Figure 3.9: (a) to (d) are representative of type B enclaves; (e) to (f) are representative of type C. (a) Type B enclaves sized from 2 cm to >10 cm in a single andesite block from Feb 11 2010 dome collapse deposit (scale: 10 cm with 2 cm intervals). (b) Photomicrograph of a diffuse margin between the host andesite and type B enclave. (c) Photomicrograph of small orthopyroxene microlites growing outwards from vesicle walls in pools of glass. Concentrations of glass are often associated with larger coalesced vesicles. (d) BSE image of a type B groundmass. Note zoning of opx crystal to cpx from core to rim. (e) Hand specimen image of the type C enclave used for this study (MT08) with an inner mafic portion and a hybrid mafic exterior portion. (f) Photomicrograph of the margin between the inner and outer enclave portions. The interior to the right of the margin contains more glass and high-Al amphibole microphenocrysts than the exterior portion to the left of the margin.

3.2.2.4 Enclaves In Pumice

Enclaves in pumice are extremely vesicular compared to those in lava dome blocks. The margins of the enclaves are lined with large coalesced vesicles, inhibiting identification of the original (pre-decompression) margin texture. Large amphiboles in the enclaves sometimes display boudinage textures similar to those seen in the andesite pumice (Giachetti *et al.,* 2010). We do not include enclaves in pumice in our classification scheme owing to the large degree of textural overprinting of features by late-stage ascent processes.
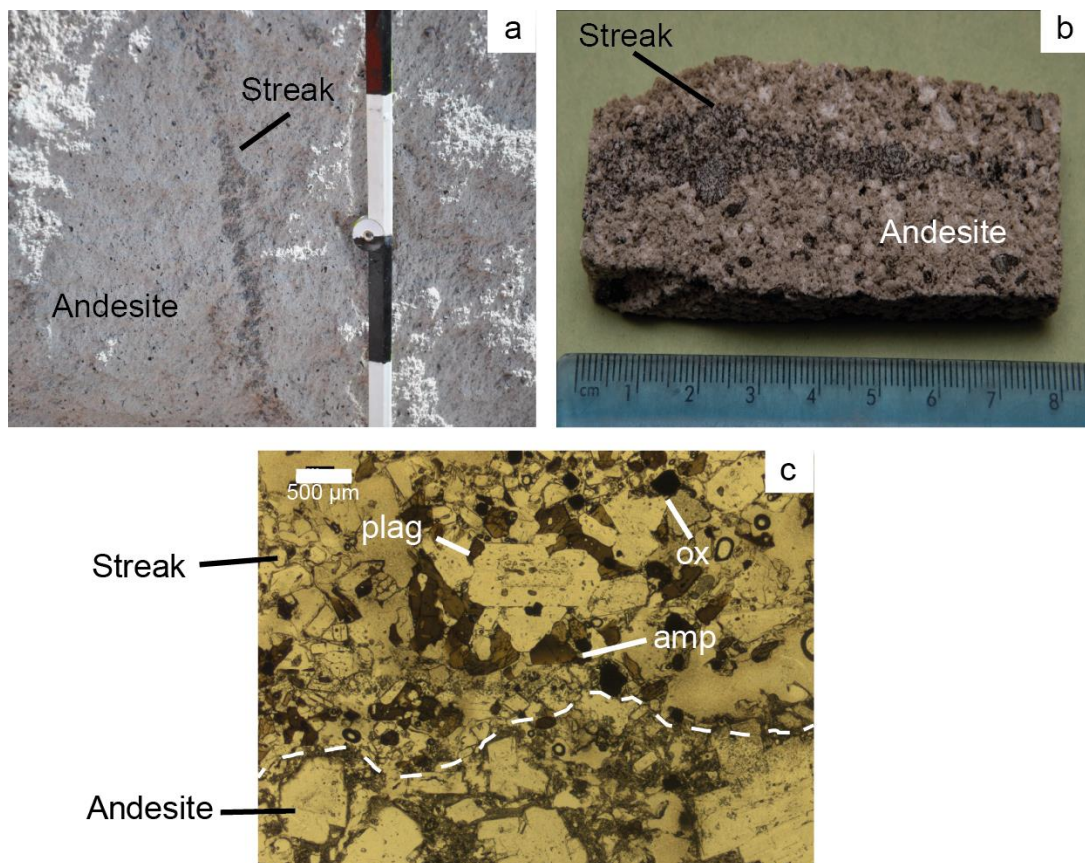
Figure 3.10: Discontinuous streaks in andesite. (a) Streak observed in an andesitic lava block ((scale: 10 cm with 2 cm intervals) (b) Hand specimen sample of a streak. (c) Photomicrograph of streak-andesite margin. Amphiboles and plagioclase are similar in composition to the andesite, but amphiboles show less apparent disequilibria than in the andesite or mafic enclaves.

3.2.2.5   *Discontinuous streaks in andesite blocks*

The discontinuous crystalline streaks found in some andesite blocks (Fig. 3.10) consist of predominantly plagioclase and amphibole, with minor glass. Bulk geochemical results of both major and trace elements from XRF and ICP-MS indicate a composition close to the andesite (Table 3.6). Petrological analyses of the mineral phases present show that the amphibole are of a similar (edenitic) composition to the andesite phenocryst assemblage. We therefore rule out that these streaks are disaggregated mafic enclaves, instead suggest that these may be akin to the banded material described in Murphy *et al.,* (2000). It should also be noted that these streaks reported here are not the same as the psueotachylitic/cataclastic veins presented in chapter 6.

3.2.3 *Geochemistry*

We present whole rock major and trace element geochemical data in table 3.6 for the mafic enclave types discussed above and andesite from phases III, IV and V, and examine geochemical differences between the enclave types, as defined on the basis of their texture and petrology. Trace element geochemical data are examined in more detail in chapter 4, where the range of mafic enclaves compositions are modelled to examine whether mixing or fractional crystallisation models are capable of reproducing the observed range of data.

We first compare phases IV and V major and trace element composition with the earlier phases of the eruption. Phases IV and V mafic enclaves and host andesite continue to fall on similar major element trends to most previous phases (Fig. 3.11) (Murphy *et al.,* 2000; Zellmer *et al.,* 2003a; Mann, 2010). Although phase V andesite SiO_2 is slightly lower on average than earlier phases, values still lie within the range of data from the previous phases (Fig. 3.11). However, the compositional gap in SiO_2 between the mafic enclaves and the andesite observed in phases I-III, no longer exists in phase V (Fig. 3.11). Phase V andesite and mafic enclaves do not continue the trend of increasing MgO and decreasing Fe_2O_3 established between phases I to III (Barclay *et al.,* 2010) (Fig. 3.11), but instead remain similar in composition to phase III.

The different categories of enclaves, as defined by their textural and petrological features, are also distinct in terms of bulk geochemistry. Although the type A and B enclaves fall on a single linear array with the andesite, each type plots in a distinctive field for all major elements (Fig. 3.12). Type A enclaves occupy a narrow compositional range (49.7–52.4 wt % SiO_2), whereas type B enclaves have a much broader range (53–58 wt % SiO_2) (Fig. 3.12). Trace element distributions in these enclaves are consistent with previous studies. For example, Zr is positively correlated with SiO_2, whilst V is negatively correlated (Fig. 3.12). Type A enclaves have systematically higher compatible trace element contents, and lower incompatible trace element contents, than the type B enclaves (Fig. 3.12).

In the composite type C enclaves, interior portions are less evolved (52.7 to 55.4 wt% SiO_2) and the outer portions are more silicic (55.8 to 58.1 wt% SiO_2), with one analysis lying in the host andesite field. The relative difference in SiO_2 between the two portions is typically about 3 wt %, irrespective of absolute SiO_2 values. However, type C enclave bulk compositions plot entirely within the field for type B enclave points (Fig. 3.12).
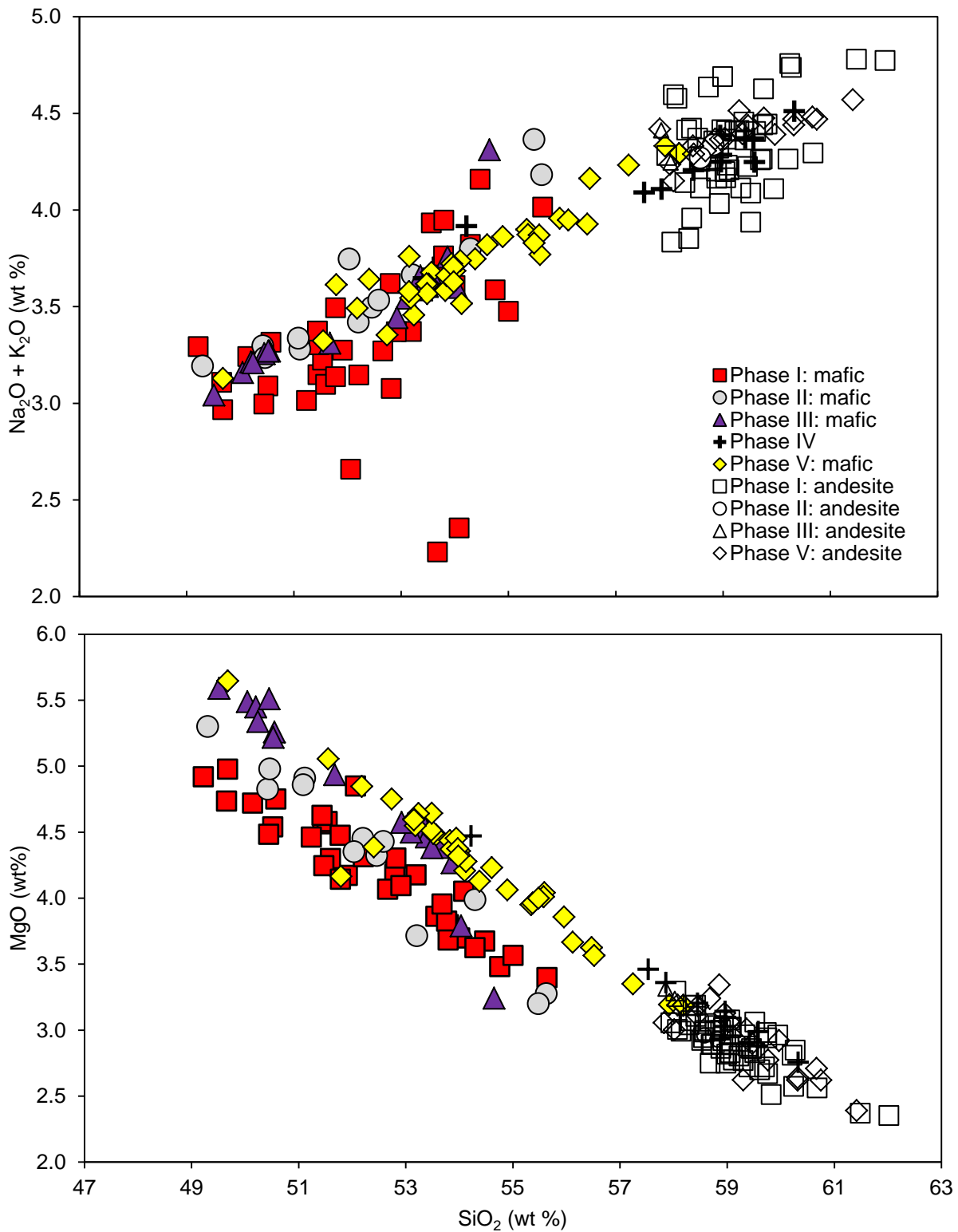
Figure 3.11: Comparison of XRF bulk geochemistry of mafic enclaves and host andesite across the first five phases of extrusive activity. Open symbols are SHV andesite and closed symbols are mafic enclaves. phase I (Murphy et al, 2000; Zellmer et al, 2003); phase II (Mann 2010; Zellmer et al, 2003); phase III (Barclay et al, 2010; this study); phases IV to V (this study).
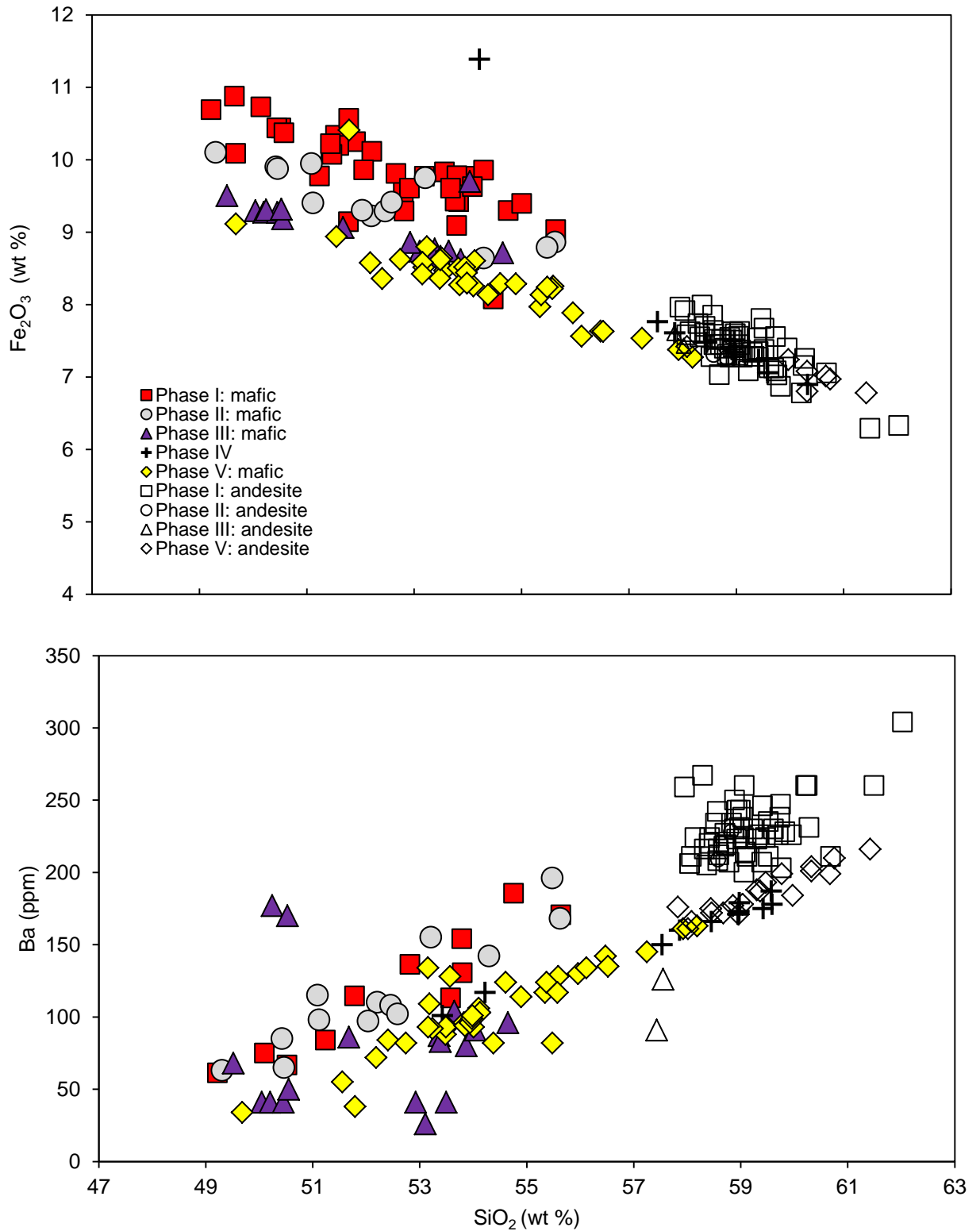
Figure 3.11 continued: Comparison of XRF bulk geochemistry of mafic enclaves and host andesite across the first five phases of extrusive activity. Open symbols are SHV andesite and closed symbols are mafic enclaves. phase I (Murphy et al, 2000; Zellmer et al, 2003); phase II (Mann 2010; Zellmer et al, 2003); phase III (Barclay et al, 2010; this study); phases IV to V (this study).
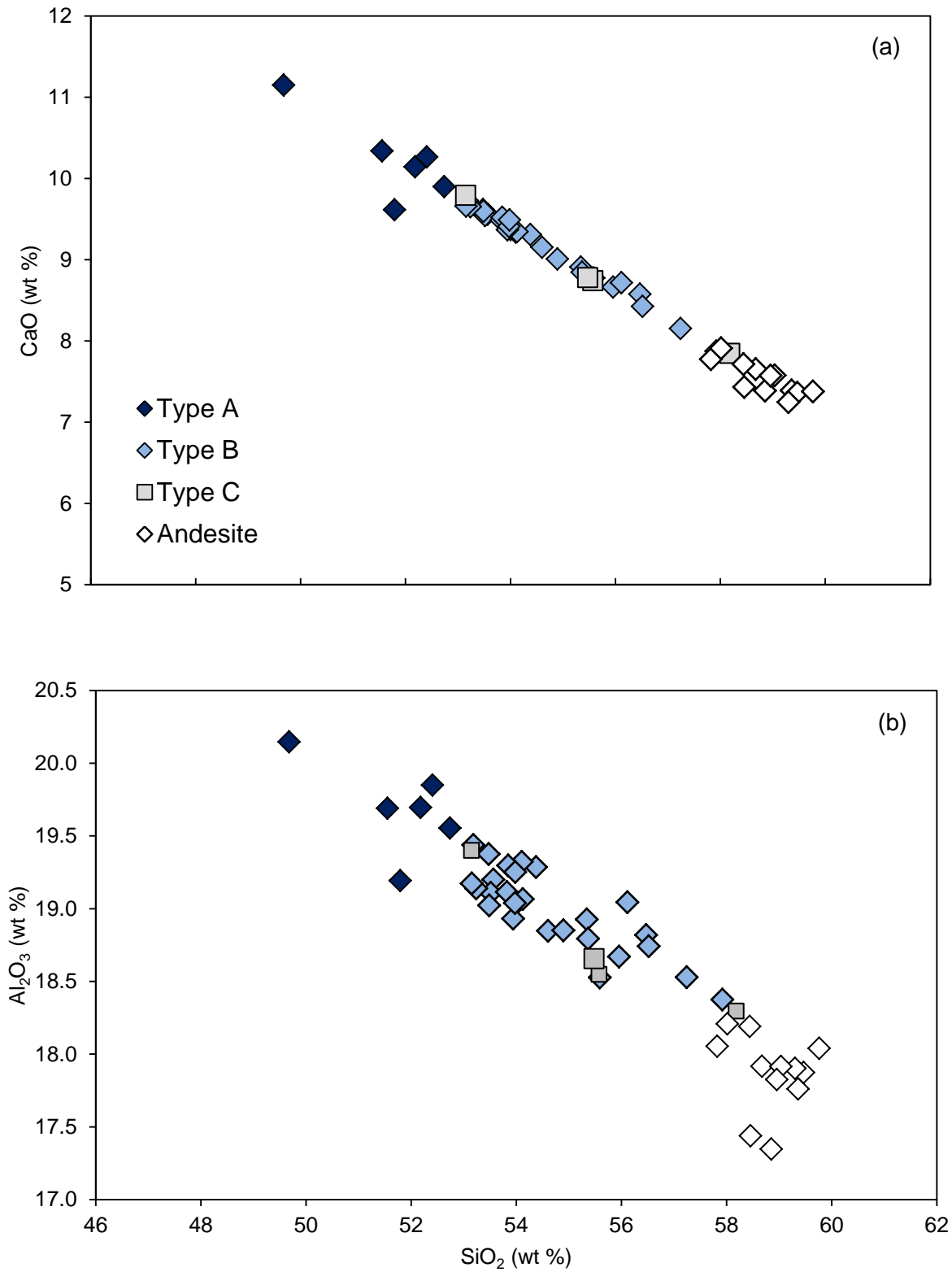
Figure 3.12: Comparison of mafic enclave types A, B and C from phase V using representative XRF bulk geochemistry data.

Table 3.6: *Phases III, IV and V major element analyses*

Phase	Phase III								
Sample no:	**M001**	**M002**	**M003**	**M004**	**M005**	**M006**	**M007**	**M008**	**M009**
Type	maf	maf	and	maf	maf	maf	maf	maf	maf
SiO_2	54.12	53.1	57.43	51.19	52.99	53.63	53.76	48.98	53.35
TiO_2	0.63	0.77	0.64	0.84	0.76	0.76	0.74	0.9	0.75
Al_2O_3	19.11	18.97	17.86	19.48	19.04	18.99	18.5	19.93	18.99
MnO	0.18	0.18	0.18	0.16	0.17	0.18	0.21	0.17	0.18
MgO	3.21	4.51	3.29	4.89	4.43	4.25	3.77	5.53	4.36
Fe_2O_3	8.63	8.67	7.55	8.98	8.7	8.58	9.65	9.4	8.69
CaO	8.71	9.55	7.81	10.13	9.49	9.3	9.14	10.89	9.41
Na_2O	3.8	3.09	3.61	2.81	3.01	3.14	2.93	2.6	3.07
K_2O	0.47	0.55	0.77	0.47	0.55	0.6	0.65	0.41	0.53
P_2O	0.17	0.12	0.13	0.11	0.12	0.13	0.14	0.11	0.12
LOI	na	na	na	na	na	na	na	na	na
Total	99.03	99.51	99.27	99.06	99.26	99.56	99.49	98.92	99.45
Phase	**Phase III**								
Sample no:	**M010**	**M011**	**M012**	**M013**	**M014**	**M015**	**M016**	**M017**	**M018**
Type	and	maf	maf	maf	maf	maf	maf	maf	maf
SiO_2	57.55	52.76	52.41	52.98	49.59	49.84	49.89	50.08	49.78
TiO_2	0.63	0.77	0.78	0.74	0.87	0.88	0.88	0.85	0.86
Al_2O_3	18.09	19.24	19.15	19.06	19.8	19.76	19.45	19.75	19.83
MnO	0.17	0.17	0.18	0.17	0.17	0.17	0.17	0.17	0.17
MgO	3.21	4.47	4.53	4.34	5.44	5.41	5.45	5.21	5.29
Fe_2O_3	7.37	8.68	8.77	8.58	9.21	9.21	9.17	9.1	9.22
CaO	7.82	9.63	9.68	9.48	10.77	10.72	10.54	10.56	10.64
Na_2O	3.45	3.01	2.88	2.95	2.74	2.77	2.77	2.78	2.77
K_2O	0.76	0.51	0.53	0.62	0.39	0.42	0.45	0.46	0.41
P_2O	0.13	0.11	0.12	0.12	0.11	0.1	0.12	0.11	0.11
LOI	na	na	na	na	na	na	na	na	na
Total	99.18	99.35	99.03	99.04	99.09	99.28	98.89	99.07	99.08

maf = mafic enclave, and = andesite, A= type A enclaves from phase V, B = type B enclaves from phase V, C = type C enclaves from phase V (see text for an explanation of enclave types from phase V), na = analysis not available, LOI = loss on ignition.

Table 3.6: *Phases III, IV and V major element analyses cont.*

Phase	*Phase III*	*Phase IV*							
Sample no:	M019	MVO 1532a	MVO 1532b	MVO 1532dm	MVO 1532df	MVO 1534-a	MVO 1535-a	MVO 1535-b	MVO 1535d
Type	maf	and	and	and	and	and	and	and	maf
SiO_2	50.06	58.38	58.03	59.27	57.52	59.04	59.57	59.01	53.85
TiO_2	0.84	0.64	0.65	0.6	0.66	0.62	0.6	0.62	0.97
Al_2O_3	19.7	17.93	18.2	17.75	18.12	17.84	17.71	17.91	16.17
MnO	0.17	0.17	0.18	0.17	0.18	0.18	0.18	0.17	0.24
MgO	5.17	3.2	3.37	2.9	3.46	3.1	2.88	3.03	4.44
Fe_2O_3	9.23	7.47	7.63	7.22	7.76	7.35	7.25	7.29	11.31
CaO	10.56	7.75	7.98	7.35	8.06	7.55	7.3	7.54	8.21
Na_2O	2.8	3.42	3.37	3.52	3.35	3.5	3.54	3.56	3.29
K_2O	0.44	0.78	0.75	0.84	0.74	0.79	0.83	0.83	0.6
P_2O	0.11	0.14	0.14	0.13	0.13	0.14	0.14	0.14	0.24
LOI	na	na	na	na	na	na	na	na	na
Total	99.08	99.88	100.3	99.75	99.98	100.11	100	100.1	99.32

Phase	*Phase IV*				*Phase V*				
Sample no:	MVO 1535e	MVO 1535g	MVO 1535h	MVO 1535f	MT29	MT35	MVO 1567d	MVO 1566b	MT27
Type	maf	and	and	and	A	A	A	A	A
SiO_2	53.47	59.12	59.61	60.19	51.6	52.01	51.5	51.96	49.54
TiO_2	0.77	0.64	0.62	0.58	0.8	0.8	0.82	0.79	0.88
Al_2O_3	19.17	17.75	17.95	17.52	19.12	19.63	19.67	19.68	20.09
MnO	0.17	0.18	0.18	0.17	0.23	0.16	0.17	0.21	0.16
MgO	4.54	3.15	2.99	2.75	4.15	4.83	5.05	4.35	5.63
Fe_2O_3	8.61	7.53	7.06	6.88	10.37	8.55	8.93	8.29	9.09
CaO	9.6	7.49	7.25	7.05	9.58	10.11	10.33	10.18	11.12
Na_2O	3.11	3.47	3.45	3.62	3.18	2.93	2.78	3.16	2.71
K_2O	0.54	0.79	0.8	0.88	0.42	0.55	0.54	0.45	0.41
P_2O	0.11	0.14	0.13	0.13	0.18	0.1	0.11	0.08	0.09
LOI	na	na	na	na	-0.33	-0.29	-0.28	0.1	-0.11
Total	100.09	100.26	100.04	99.77	99.63	99.67	99.9	99.15	99.72

maf = mafic enclave, and = andesite, A= type A enclaves from phase V, B = type B enclaves from phase V, C = type C enclaves from phase V (see text for an explanation of enclave types from phase V), na = analysis not available, LOI = loss on ignition.

Table 3.6: *Phases III, IV and V major element analyses cont.*

Phase	*Phase V*								
Sample no:	MT18	MT20	MT26	MT22	MT25a	MT25b	MT31b	MT33	MVO 1566a
Type	B	B	B	B	B	B	B	B	B
SiO_2	53.93	53.68	53.46	58.57	58.04	57.22	55.49	55.21	54.47
TiO_2	0.76	0.77	0.77	0.63	0.63	0.66	0.72	0.71	0.76
Al_2O_3	19.01	19.09	19.16	18.23	18.41	18.52	18.66	18.88	18.8
MnO	0.17	0.18	0.17	0.17	0.17	0.17	0.18	0.17	0.17
MgO	4.35	4.66	4.47	3.12	3.2	3.35	4	3.94	4.22
Fe_2O_3	8.48	8.65	8.45	7.29	7.39	7.53	8.24	7.95	8.27
CaO	9.36	9.63	9.54	7.73	7.89	8.15	8.78	8.89	9.13
Na_2O	3.12	3.06	3.12	3.55	3.55	3.49	3.16	3.26	3.2
K_2O	0.56	0.52	0.55	0.79	0.79	0.74	0.67	0.63	0.61
P_2O	0.12	0.12	0.11	0.14	0.13	0.13	0.12	0.12	0.12
LOI	-0.24	-0.35	-0.14	-0.25	-0.23	-0.36	-0.39	-0.25	0.07
Total	99.86	100.36	99.8	100.22	100.2	99.96	100.02	99.76	99.75

Phase									
Sample no:	MVO 1566c	MVO 1566e	MVO 1567a	MVO 1567b	MVO 1590	MVO 1591	MVO 1593	MVO 1588	MT10
Type	B	B	B	B	B	B	B	B	B
SiO_2	52.97	54.14	53.77	54.04	54.03	53.83	54.72	53.62	53.27
TiO_2	0.76	0.74	0.76	0.76	0.77	0.75	0.73	0.76	0.78
Al_2O_3	19.36	19.2	18.87	19.06	19.03	19.29	18.79	19.04	19.02
MnO	0.17	0.16	0.18	0.18	0.17	0.17	0.18	0.17	0.18
MgO	4.53	4.11	4.44	4.38	4.27	4.37	4.05	4.42	4.47
Fe_2O_3	8.48	8.1	8.49	8.45	8.59	8.27	8.26	8.47	8.6
CaO	9.69	9.27	9.34	9.42	9.33	9.52	8.98	9.45	9.5
Na_2O	3.02	3.13	3.13	3.11	2.93	3.11	3.24	3.01	3.06
K_2O	0.51	0.6	0.58	0.6	0.58	0.55	0.61	0.56	0.54
P_2O	0.11	0.11	0.12	0.12	0.12	0.11	0.12	0.12	0.12
LOI	0.1	0.12	-0.42	-0.33	0.14	0.12	0.08	0.11	-0.11
Total	99.6	99.56	99.68	100.12	99.82	99.97	99.68	99.62	99.54

maf = mafic enclave, and = andesite, A= type A enclaves from phase V, B = type B enclaves from phase V, C = type C enclaves from phase V (see text for an explanation of enclave types from phase V), na = analysis not available, LOI = loss on ignition.

Table 3.6: *Phases III, IV and V major element analyses cont.*

Phase	*Phase V*								
Sample no:	MVO 1587	MT08a	MT08b	MT36a	MT36b	MT37a	MT37b	MVO 1537-b	MVO 1538-b
Type	B	C	C	C	C	C	C	and	and
SiO_2	53.99	52.88	55.58	57.72	55.33	56.61	52.84	60.32	60.75
TiO_2	0.74	0.78	0.73	0.66	0.73	0.66	0.8	0.57	0.58
Al_2O_3	19.28	19.3	18.55	18.02	18.78	18.77	19.59	17.84	17.3
MnO	0.17	0.17	0.18	0.18	0.17	0.17	0.17	0.17	0.18
MgO	4.2	4.57	4.01	3.05	3.96	3.57	4.76	2.62	2.62
Fe_2O_3	8.24	8.38	8.22	7.87	8.13	7.64	8.64	6.8	6.97
CaO	9.32	9.74	8.74	7.76	8.84	8.44	9.92	7.02	6.78
Na_2O	3.15	3.02	3.23	3.62	3.23	3.39	2.74	3.56	3.57
K_2O	0.58	0.54	0.64	0.79	0.64	0.78	0.62	0.88	0.9
P_2O	0.12	0.11	0.13	0.15	0.12	0.13	0.11	na	na
LOI	0.09	-0.06	-0.01	-0.11	-0.1	-0.25	1.06	na	na
Total	99.79	99.49	100.01	99.82	99.93	100.16	100.19	99.78	99.65

Phase	*Phase V*					
Sample no:	MVO 1539-a	MVO 1537A	MV0 1538A	MV0 1539B	MT09b	MVO 1594
Type	and	and	and	and	streak	streak
SiO_2	59.97	58.08	60.67	60.32	57.95	59.57
TiO_2	0.62	0.64	0.59	0.59	0.64	0.61
Al_2O_3	17.56	18.28	17.49	17.63	17.88	18
MnO	0.18	0.17	0.18	0.18	0.18	0.2
MgO	2.92	3.19	2.71	2.64	3.23	2.87
Fe_2O_3	7.24	7.42	7.01	7.08	7.66	7.67
CaO	7.13	7.81	6.9	6.94	7.69	7.36
Na_2O	3.52	3.37	3.58	3.6	3.48	3.77
K_2O	0.87	0.78	0.9	0.87	0.76	0.82
P_2O	na	na	na	na	0.14	0.16
LOI	na	na	na	na	0	0.05
Total	100.01	99.74	100.03	99.85	99.61	101.03

maf = mafic enclave, and = andesite, A= type A enclaves from phase V, B = type B enclaves from phase V, C = type C enclaves from phase V (see text for an explanation of enclave types from phase V), na = analysis not available, LOI = loss on ignition.
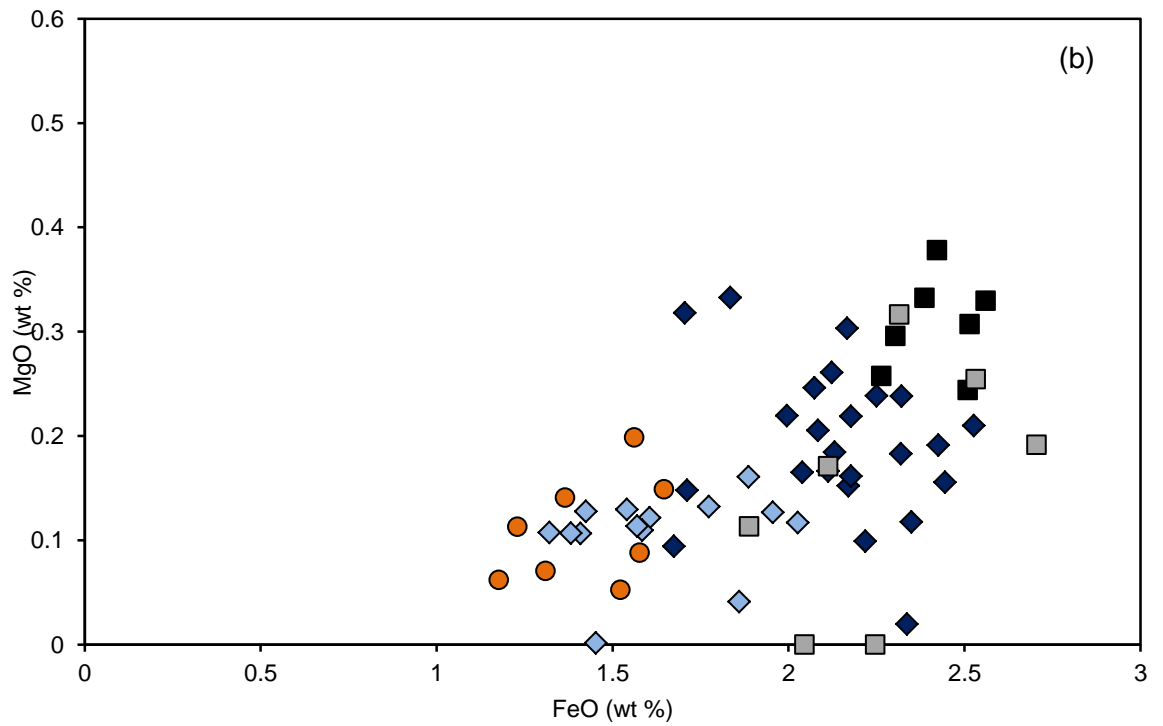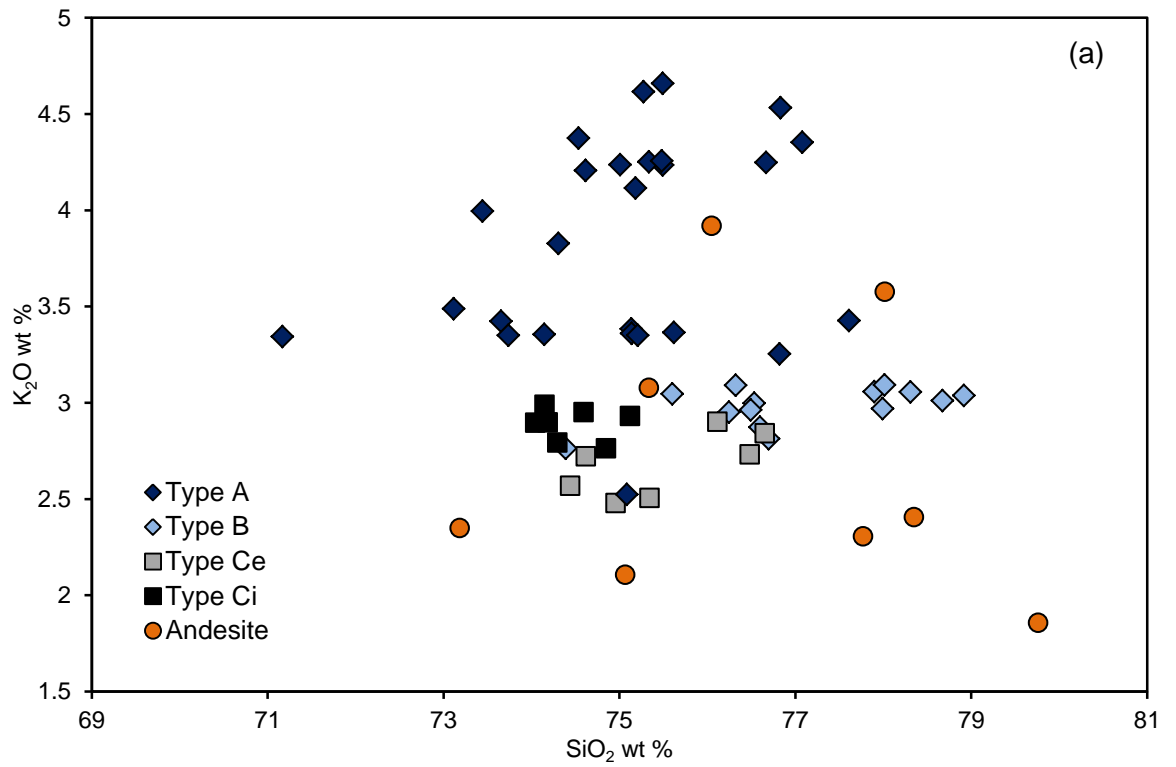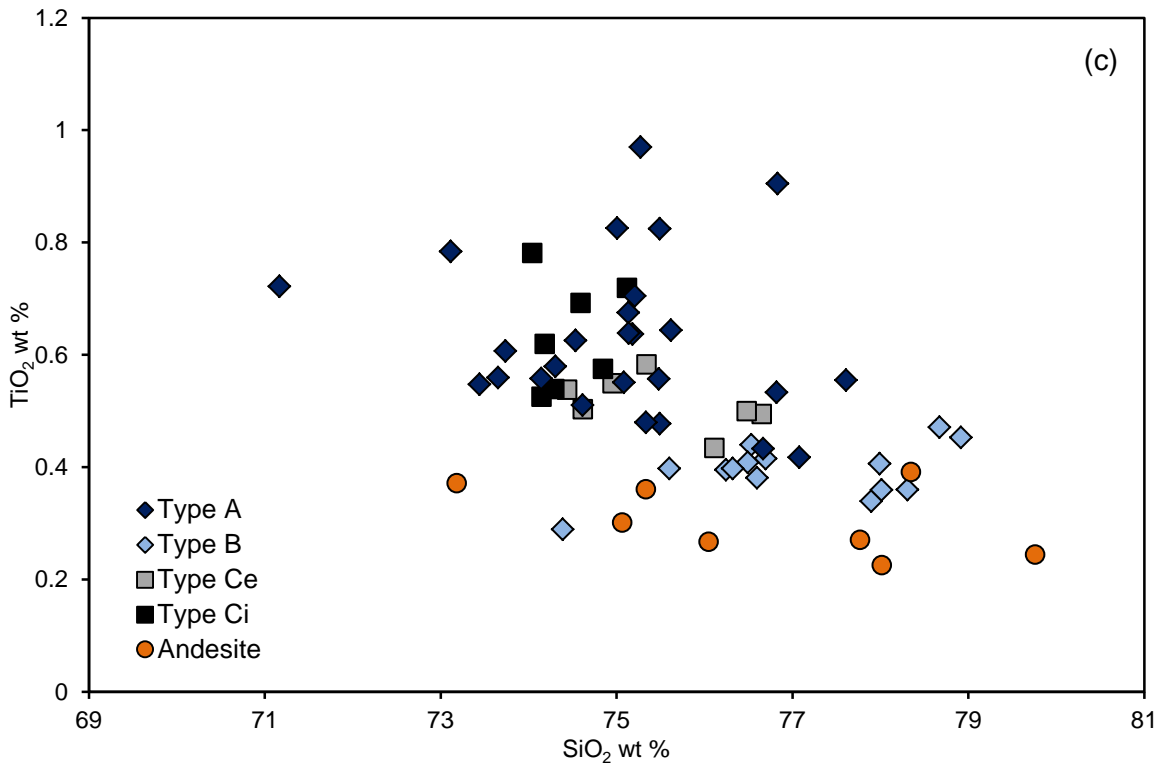
Figure 3.13: Groundmass glass compositions of enclave types from electron probe analyses. (a) SiO_2 vs. K_2O. Type Ci (interior of portion of composite enclave), Type Ce (exterior portion) (b) FeO*tot vs. MgO (c) SiO_2 vs. TiO_2.

Glass compositions are rhyolitic (71–79 wt% SiO_2, table 35) for the mafic enclaves similar to prior eruptive phases and lie within established trends (Humphreys *et al.,* 2010; Murphy *et al.,* 2000). There are some notable differences between the enclave types of phase V. Type A enclaves have a wide scatter of K_2O contents in comparison to types B and C, but higher absolute contents on average (Fig. 3.13a). Type A enclaves also have on average higher FeO, MgO and TiO_2 contents (Fig. 3.13b,c). In contrast type B enclaves have low FeO, MgO and TiO_2 contents (Fig. 3.13b,c). Type C inner and outer enclave portions glass compositions were measured. In most elements measured there is an observed difference between the two portions. The inner portion compositions plot within the type A field in FeO, MgO and TiO_2, whereas the outer portion compositions tend to plot within the type B field in K_2O (Fig. 3.13a). There are however considerable overlaps between the fields in FeO and MgO (Fig. 3.13b). Andesite glass compositions are rhyolitic (73–80 wt % SiO_2) and overlap with the mafic enclave compositions (Thomas et al., 2014; appendix 2). The phase V andesite glass has variable high and low K_2O concentrations (Fig. 3.13a) as established in earlier eruptive phases (Humphreys et al., 2010). The andesite

68

glass FeO and MgO concentrations overlap with those seen in the type B enclaves (Fig. 3.13b). TiO_2 concentrations are on average lower than seen in the mafic enclave glass, although overlap with the type B enclave concentrations (Fig. 3.13c).

3.3 Discussion

In general, the low crystallinity and inherited phenocryst content, chilled margins, and relatively restricted primitive geochemical composition suggests that the type A enclaves are closer to an end-member mafic magma that quenched rapidly on contact with the andesite. In contrast, type B enclaves, with their much higher inherited phenocryst content, lack of chilled margins and more evolved compositions, are significantly hybridised. Type C enclaves are composite, with a more mafic interior indicating dynamic mingling between types A and B. Below we discuss in detail the constraints on the formation of these three enclave types and implications for the nature of magma mixing at Soufrière Hills Volcano.

3.3.1 Geochemical constraints on end-member magma compositions

The type A enclaves are the least evolved of the enclave types, with low incompatible trace element concentrations; we therefore interpret them to be closest to a hypothesised low SiO_2 mafic magma end-member. However, the presence of inherited phenocrysts indicates that even these least evolved enclaves are already hybridised. The type B enclaves are more evolved in comparison to type A, but reflect a broad range of compositions. The strongly linear compositional arrays in major elements (Al_2O_3, CaO *etc.*) and trace elements (Zr, Ba *etc.*) through the mafic enclaves to the host andesite in phase V (Fig. 3.12), suggests a mixing relationship between the mafic and andesite end-members in phase V. However, this would mark a change from the fractional crystallisation model suggested by Zellmer *et al.,* (2003a) to fit the phase I mafic enclave data. We explore this potential change in the control on the mafic enclave compositional range in detail in chapter 4. If mixing were the control on the range of mafic enclave compositions this would suggest that type B enclaves reflect a continuum of degrees of mixing. Nonetheless, we also observe that there is bimodal distribution between the total inherited phenocryst fraction between types A and B, and we also examine the effect of the incorporation of the inherited phenocrysts on the bulk mafic enclave compositions in chapter 4.

The relatively homogeneous rhyolitic composition of glass in the mafic enclaves could indicate that felsic melt from the andesite has infiltrated into the mafic enclaves, or may simply be the result of extensive crystallisation of a mafic melt. Engulfment of inherited phenocrysts must also be accompanied by liquid assimilation from the andesite host, which will affect the bulk composition of the mafic enclaves. If this is the case, type B melt compositions may reflect a localised hybrid starting composition before framework crystallisation in contrast to the type A melt. At Narugo Volcano, Japan compositional similarity between glasses in the host magma and mafic inclusions is interpreted as evidence of infiltration of the host magma melt into a boundary layer before enclave formation (Ban *et al.,* 2005). Although glass compositions of the andesite and enclaves are both rhyolitic and overlap at SHV, there is a clear difference between the types A and B glass in K_2O (Fig. 3.13a). Type B is somewhat similar to the andesite (Humphreys *et al.,* 2010) and less variable than type A glass. This may imply that the melt in Type B enclaves is more homogenised in comparison to Type A allowing K_2O time to re-equilibrate with the andesite host (Humphreys *et al.,* 2010). The diffusive timescale of K has been calculated to be 32 days for rhyolitic compositions across a length-scale of 1 cm (Humphreys *et al.,* 2010). Therefore, preservation of the higher K_2O glass composition of the type A enclaves may be attributed to a shorter timescale of mixing than type B.

3.3.2 *Petrological and textural mingling constraints*

The presence of chilled margins, lower inherited phenocryst abundance, higher plagioclase anorthite compositions and ubiquitous presence of high Al-amphibole in the framework crystals of type A enclaves relative to the type B enclaves all suggest that controls on the formation differed between the enclave types.

Engulfment of phenocrysts from the host magma by an incoming magma has been observed elsewhere *e.g.* Unzen, Kameni, Chaos Crags (Clynne, 1999; Browne *et al.,* 2006a; Martin *et al.,* 2006a; Feeley *et al.,* 2008). Previous work on inherited plagioclase phenocrysts from SHV demonstrates a positive correlation between iron and anorthite content at the phenocryst rim (Fig. 3.5; Humphreys *et al.,* 2009). The disequilibrium textures and rim growth on the plagioclase was therefore probably caused by the incorporation of the inherited phenocrysts into a high-calcium melt (Ruprecht & Wörner, 2007; Humphreys *et al.,* 2009) rather than by decompression and degassing (Coombs *et al.,*

2000). The presence of inherited phenocrysts in the type A enclaves, where chilled margins would significantly inhibit mass exchange between the enclave and andesite (Blake & Fink, 2000), indicates that the majority of phenocryst incorporation must have taken place before chilled margin formation. The higher inherited phenocryst fraction in the type B enclaves (16.5–26%) in comparison to the Type A enclaves (0–8.6%) indicates a greater interaction with the andesitic melt prior to enclave formation (Fig. 3.8). Differing rim and sieve-texture disequilibria widths of the inherited plagioclase phenocrysts in individual enclaves may reflect differing time-scales of engulfment or conditions of residence in the mafic melt (Fig. 3.4). In contrast, at Unzen, Japan, uniformity of calcic rim widths and sieve-textures of inherited plagioclase phenocrysts are interpreted as indication of a single episode of engulfment of phenocrysts into enclaves (Browne *et al.,* 2006b).

The effect of adding inherited phenocrysts on the viscosity of the mafic magma was estimated using the Einstein-Roscoe relation for effective viscosity, with melt viscosity calculated using the empirical model of Giordano *et al.,* (2008). We find that the addition of the inherited phenocrysts increases the effective viscosity of the mafic magma and dominates over the effect that the associated temperature reduction would have (Fig. 3.14). However, even with the maximum observed volume of 25 % inherited phenocryst fraction in the type B end-member a relative viscosity contrast between the andesite (45–55 vol% phenocrysts) still exists. Prior to mafic magma crystallisation, the viscosity will be lower than the andesite viscosity. However, after quench crystallisation, where crystal content can be >90% vol, enclave viscosity will be greater than andesite viscosity and this will inhibit mixing (Sparks & Marshall, 1986). The inherited phenocryst content also contributes to a viscosity contrast between types A and B, which implies that mixing would be inhibited between the two types (Fig. 3.14).
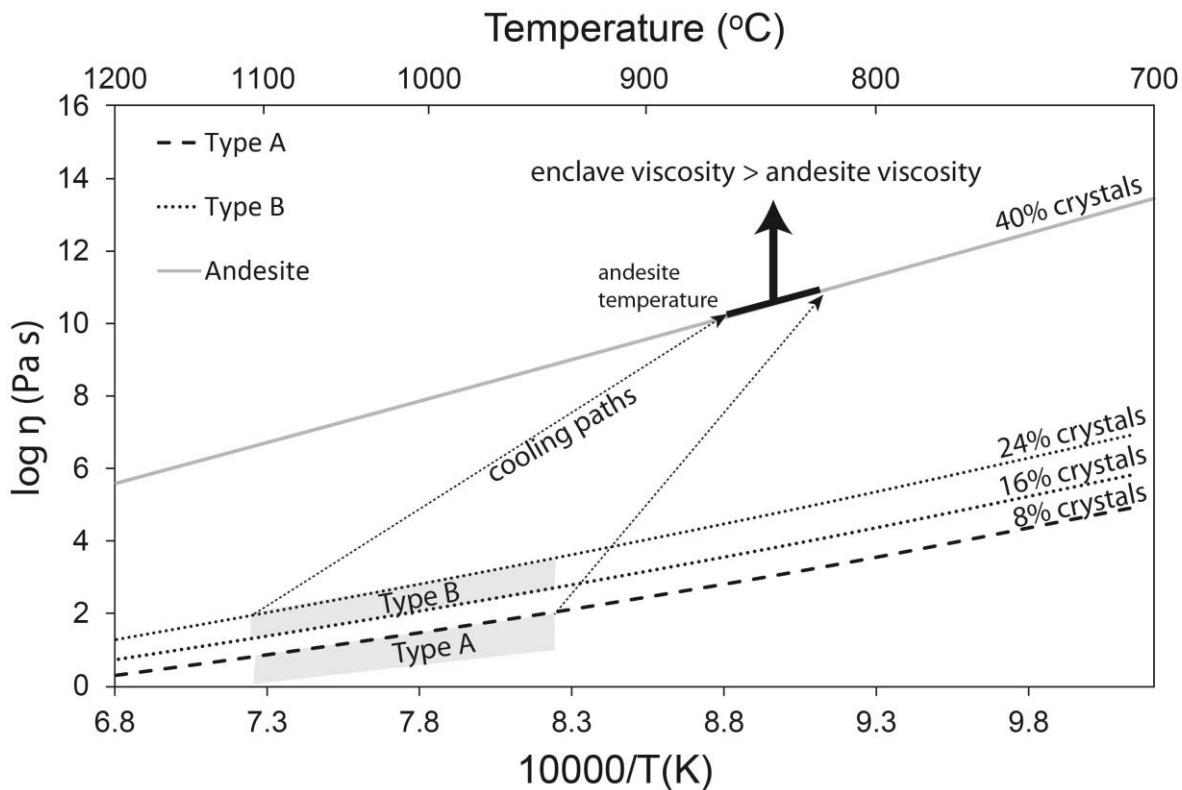
Figure 3.14: Simplified modelled effective viscosity of SHV host andesite and mafic enclaves against temperature. Melt viscosity was modelled using the method of Giordano *et al.,* (2008) and effective viscosity using the Einstein-Roscoe relation. Andesite sample has 77 wt % SiO_2 40% crystals, 4% wt % H_2O. We use three enclave samples using measured bulk compositions, and assume modal inherited phenocryst proportions are mixed in prior to enclave formation. Type A (MT27) is the least evolved phase V sample with 49 wt % SiO_2, 8% inherited phenocryst volume, and 6 wt % H_2O. Type B end-members were modelled (1) 53 wt % SiO_2 and 16% inherited phenocrysts, 6 wt % H_2O (2) 58 wt % SiO_2, 24% inherited phenocrysts, and 6 wt % H_2O. We assume mafic magma temperatures of between 950-1100°C, and similar temperatures for Types A and B for the purposes of this model, H_2O contents from Edmonds *et al.,* (2014) and andesite temperatures from Barclay *et al.,* (1998).

The diktytaxitic framework observed in both type A and B enclaves demonstrates that quench crystallisation took place during thermal equilibration with the andesite. This implies that a temperature contrast must exist between the andesite and even the most hybridised mafic melt prior to enclave crystallisation. However, textural and petrological differences show that this contrast was variable during formation of types A and B enclaves. An overall higher anorthite content of type A enclave inherited plagioclase phenocryst rims, microphenocrysts and microlites in comparison to type B enclaves, could be indicative of crystallisation under hotter conditions or more H_2O-rich conditions. Differing sized enclaves and types may take different times to equilibrate thermally (Bacon 1986), and therefore phenocryst disequilibrium is likely to be slightly different between

enclaves. However, inherited plagioclase phenocrysts' sieve-textures and rims in type A enclaves are consistently thicker (Fig. 3.4). This hints at higher temperatures, rather than a longer residence time of the inherited phenocrysts in comparison to type B enclaves, which may be consistent with inferences from the residual glass composition. Furthermore, this process would be limited by the rapid cooling that would take place as the enclave reached thermal equilibrium (Bacon, 1986; Sparks & Marshall, 1986). Chilled margins reflect rapid cooling caused by a significant temperature contrast between the enclave and host magma, with the enclave largely liquid during formation (Bacon, 1986; Sparks & Marshall, 1986; Clynne, 1999). We therefore infer that type A enclaves not only formed from a hotter melt than type B, but that formation was the result of injection into the andesite as a liquid, where rapid cooling drove crystallisation and formation of the chilled margins.

The lack of chilled margins in type B enclaves could result either from a smaller temperature contrast between enclave and andesite, in comparison to type A, or from mechanical abrasion of enclave margins caused by shear stress (Feeley & Dungan, 1996). We suggest that mechanical abrasion would be unlikely to remove all evidence of a chilled margin. A smaller temperature contrast would prevent strong decrease in crystal size at the chilled margin, and allows greater time for mass and chemical exchange during quenching (Bacon, 1986). A temperature difference of 15–50 °C has been experimentally constrained to produce similar textures to the type B enclaves during crystallisation in a layer at the silicic-mafic interface (Coombs *et al.,* 2002). Furthermore, variability in textures in the type B enclaves may be a function of crystallisation depth below a mafic-silicic interface, as slower cooling will take place further away from the boundary (Coombs *et al.,* 2002; Martin *et al.,* 2006a). This may indicate that quench crystallisation of the type B enclaves took place before incorporation into the andesite and subsequent disaggregation (Eichelberger, 1980; Martin *et al.,* 2006a).

Estimates of temperatures using the mineral phases in the mafic enclaves have proved unsuccessful. Many of the geothermometers and geobarometers may not apply to quench crystallisation where local equilibrium (both thermal and chemical) may not be achieved. Testing the empirical plagioclase-liquid thermometer derived by Putrika, 2008 eq. 26 (shown below), this may yield the temperature that plagioclase crystallised from a

silicate melt at a given pressure, using mafic enclave plagioclase and glass (liq) compositions.

$$\frac{10^4}{T\,(K)} = 10.86 - 9.7654\left(X^{liq}_{KO_{0.5}}\right) + 4.241\left(X^{liq}_{CaO}\right) - 55.56\left(X^{liq}_{CaO}X^{liq}_{AlO_{1.5}}\right)$$
$$+ 37.50\left(X^{liq}_{KO_{0.5}}X^{liq}_{AlO_{1.5}}\right) + 11.206\left(X^{liq}_{SiO_2}\right)^3$$
$$- 3.151\mathrm{x}10^{-2}\left(P(kbar)\right) + 0.1709\left(H_2O^{liq}\right)$$

In single enclaves, temperatures range from between 907 °C to 1016 °C. Although this is broadly what we might expect as a temperature for the mafic magma, this range mainly was probably controlled by the variable glass composition due to incomplete chemical equilibrium across the interstitial glass.

The ubiquitous presence of the high-Al amphibole laths in the type A as opposed to the type B enclaves might be a function of melt volatile content. In several plutonic centres such as the Cadillac Mountain Granite and the Pleasant Bay Intrusion, a positive correlation between more hybridised (higher SiO_2) enclaves, and the absence of hornblende and presence of clinopyroxene has been observed (Wiebe, 1993; Wiebe *et al.,* 1997). The change from a hydrous to anhydrous assemblage is attributed to the exchange of H_2O between stably stratified mafic and silicic layers (Wiebe *et al.,* 1997). Amphibole compositions suggest that the type A enclaves have 6.4–9.0 wt % H_2O calculated using the empirical method of Ridolfi and Renzulli (2011), although pressures attained using this thermometer would put the depth >25 km, which does not seem feasible with quench crystallisation. However, these H_2O contents are consistent with RhyoliteMelts modelling of a saturated water-rich mafic magma (>8 wt % H_2O), which reproduces the observed porosity and fraction of melt remaining in the type A enclaves (Edmonds *et al.,* 2014). The lower porosity and abundance of amphibole in the type B enclaves might suggest a lower melt volatile content in comparison to type A. The presence of some high-Al amphiboles laths in the least evolved type B enclaves implies that the H_2O content was sufficient to allow limited amphibole crystallisation. Variability in the volatile content of the mafic magma might also account for differences in the anorthite content of the plagioclase microphenocrysts between enclave types. Higher H_2O concentrations in the melt can lead to higher anorthite content as well as higher temperatures, which is

consistent with the type A enclaves (*e.g.* Couch *et al.,* 2003). Alternatively, the high-Al amphibole might have had more time in the type B enclaves to resorb, which also might explain their absence.

The plagioclase framework microphenocryst disequilibria observed in the type A enclaves (Fig. 3.6c) could be created by a number of processes, such as (1) strong undercooling where melt is trapped in the skeletal structure of the crystals as they grow rapidly; (2) decompression-induced disequilibrium (Nelson & Montana, 1992); (3) degassing-induced disequilibrium (Frey & Lange, 2011). As there is already evidence to suggest higher rates of cooling in the type A enclaves, the large temperature contrast could conceivably be the controlling process. However, destabilisation of some framework pargasitic amphibole rims indicated by breakdown to clinopyroxene may indicate decompression-induced disequilibria or shallow storage residence in the dome (Rutherford & Devine, 2003; Browne & Gardner, 2006; Buckley *et al.,* 2006).

The large coalesced vesicles in some of the type B enclaves suggest vesicle expansion caused by decompression or by longer timescales. Coalesced vesicles have been cited as evidence of overturn and subsequent breakup of a foam layer at the mafic-silicic interface (Martin *et al.,* 2006a). Bent framework crystals also imply vesicle expansion after crystallisation (Martin *et al.,* 2006a). This disruption to the enclave framework implies that the type B enclaves are perhaps disaggregated fragments of larger pieces (Martin *et al.,* 2006a; Edmonds *et al.,* 2014). This is further supported by the presence of clusters of small angular to sub-angular enclaves within andesite. In a sample of andesite from phase III, Humphreys *et al.,* (2012) calculated that the total cryptic abundance of material derived from disaggregation of mafic enclaves is approximately 6–7%, implying that this process is prevalent at SHV. Microlites or microphenocrysts of high-Al amphibole are very rarely observed within the andesite, which lends support to the idea that it is largely or even exclusively this hybridised layer that is experiencing this level of disaggregation.

3.3.3 Type C enclaves

Composite or mixed enclaves have been observed in previous eruptive phases (Barclay *et al.,* 2010) as well as phases IV and V. Composite enclaves are suggestive of

more complex hybridisation mechanisms. The inner portion of the enclave used for this study has retained a compositional and textural identity similar to the more mafic type A. The surrounding more silicic portion is texturally and compositionally similar to type B enclaves. The concentration of glass near the interior margin of the inner part of the enclave, together with the diktytaxitic framework present, suggests that hotter, more mafic magma is mingled into the cooler more silicic magma, whilst both are still fluid (Snyder *et al.,* 1997). The presence of a few high-Al amphibole laths in the more silicic portion near the inner margin demonstrates that there has been limited mechanical exchange of melt and groundmass material between the two portions of the enclave. The enclave-andesite margin, with fingers of andesitic material intruding into the enclave indicates weak cooling of the silicic portion in contact with the host andesite (Fig. 3.10). Composite enclaves may form as mafic magma 'pillows', surrounded by a thin film of hybrid material separating the mafic from the silicic magma (Blake & Ivey, 1986; Snyder *et al.,* 1997). The inner mafic portion will crystallise first, and then the surrounding hybridised portion preserving the interior mafic portion (Collins *et al.,* 2000).

3.3.4 *Phase V mingling model*

We propose that the textural and petrological variations of the type A and B enclaves are created by differing formation mechanisms, partly influenced by the degree of mingling between the host andesite and intruding mafic magma, which in turn controls temperature and viscosity contrasts. In addition, the nature and timing of incorporation of the enclaves into the andesite may also play a role in the differences between the enclaves. In our model for enclave formation (Fig. 3.15), volatile-saturated mafic magma is injected into the chamber as a plume, and mixes with the host andesite to varying degrees, engulfing the andesite-derived phenocrysts and creating a hybrid mafic magma with a broad range of compositions. Type A enclaves formed at high rates of cooling and therefore may have formed at the plume margin (Browne *et al.,* 2006a). The high viscositycontrast between the mafic and andesitic magma end-members would prevent effective mixing (Fig. 3.14), but viscous shearing of the plume margin could have taken place. Alternatively, blobs of less dense mafic magma might have detached from the plume during injection into the andesite as a 'spray' quenching upon incorporation into the andesite. Ponding of the intruding magma from plume collapse is likely to have occurred

either as a result of a decrease in the rate of injection (*e.g.* Eichelberger, 1980; Sparks & Marshall, 1986) or in the density contrast with the andesite (Feeley *et al.,* 2008). This leads to the formation of a mafic hybrid layer where at the mafic-silicic interface crystallisation-induced vesiculation occurred (Eichelberger 1980), from which type B enclaves are derived (Fig. 3.15b). For enclave flotation to occur due to lower density as a result of vesiculation, the H_2O content of the enclaves must be >6 wt % (Edmonds *et al.,* 2014). Disruption of the mafic-silicic interface may be result of (1) crystallisation-induced vesiculation, where the density of the hybrid mafic magma fell below that of the andesite enabling overturn or (2) an instability or plume of the mafic magma intruded through the hybrid layers destabilising and inducing breakup, reproducing the cycle

Composite enclaves may form from small plumes of vesicular, less dense, hotter mafic material which could buoyantly rise and mingle within the overlying cooler hybridised layers (Cardoso & Woods, 1999). The compositional and viscosity gap between types A and B end-members would limit mixing (Fig. 3.14) and perhaps allow the composite enclaves to form. These could form undercooled mafic pillows within the hybrid layer, which is then intruded into the overlying andesite (Fig. 3.15c). However, this does not explain adequately the presence of the inherited phenocrysts in the interior more mafic portion of the enclaves.

It is unclear if the timing of the processes forming the type A, B and C enclaves are similar. The presence of the composite enclaves could imply multiple injections of mafic magma, and suggest a temporal separation between types A and B. Differences in glass compositions (Fig. 3.9), also may indicate longer mingling time-scales for the type B enclaves in comparison to type A. In addition, differing degrees of inherited phenocryst disequilibria within single enclaves might suggest temporal variations of the engulfment of phenocrysts rather than a single intrusion. However, as SHV is a long-lived system with multiple extrusive phases with evidence for quasi-continuous intrusion at depth (*e.g.* Edmonds *et al.,* 2001; Elsworth *et al.,* 2008), it is likely to demonstrate dynamic mingling. We also cannot rule out that the differing enclave types may be due to turbulent mingling processes rather than suggesting temporal differences, although this unlikely in the highly crystalline andesite.
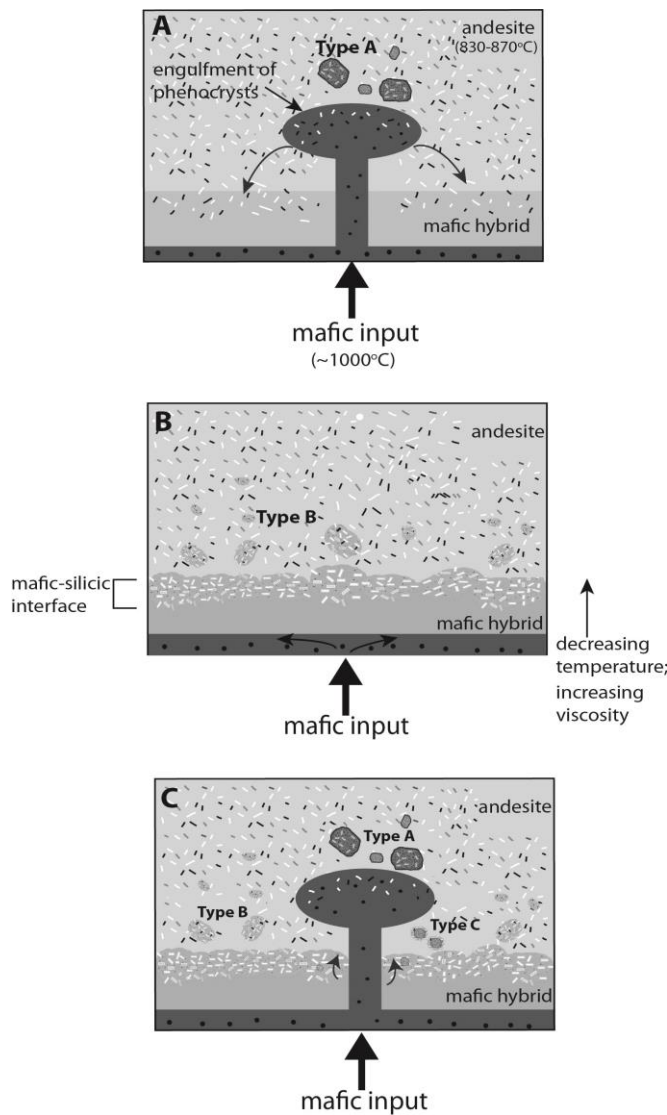
Figure 3.15: Proposed mingling model for phase V from petrological, textural and geochemical analysis of mafic enclave types. (A) Type A enclaves form during intrusion of a mafic magma plume either at plume margins or from 'spray'. Collapse of plume as indicated by arrows is driven by both density and gravity contrasts, or by a reduction in the rate of mafic injection. Andesite derived phenocrysts and melt are engulfed by the intruding mafic magma forming a hybrid mafic magma, which ponds towards the magma chamber base, with perhaps denser material at the base. (B) Hybridised mafic magma derived from the collapse of a plume; hybridised as a result of localised mixing with the andesite is shown at the base of the chamber. At the hybrid mafic-andesite interface crystallisation results due to cooling of the hybrid mafic layer. Type B enclaves are derived from this layer either as the result of blobs of magma detaching from the layer or breakup of the layer. Mafic material may also continue to pond at the base of the chamber beneath the mafic hybrid due to quasi-continuous input of mafic material. (C) Type C enclaves may be the result of multiple injections of mafic magma. Blobs of mafic magma may detach from the intruding magma as it intrudes through the mafic hybrid, mingling with the hybrid magma. Composite enclave textures are only likely to form where viscosity and temperature contrast is greatest between the mafic and mafic hybrid *i.e.* close to the mafic-silicic interface.

3.3.5 Gas escape from enclaves

The erupted mafic enclaves are highly crystalline and are variably vesicular (9–40 wt %). Results from rhyoliteMELTS modelling suggest that the mafic magma is H_2O-rich at >6% (Edmonds *et al.,* 2014). Therefore, an important question is how does the gas escape from the mafic magma and enclaves? Quench driven crystallisation of the intruding hotter mafic magma as it interacts with the cooler andesite will drive volatile concentrations in the mafic magma to saturation leading to rapid exsolution and vesiculation. Volatile release and transfer from the mafic magma to the andesite is invoked as mechanism to remobilise the cooler crystal-rich andesite, which may take place at the layer interface between the mafic and andesitic magmas (Bachmann & Bergantz, 2006). As discussed earlier, evidence (low porosity and lack of high-Al amphiboles) suggests that the type B enclaves could be derived from a hybrid layer, which may possibly have a lower melt volatile content than the modelled 6 wt % H_2O from Edmonds *et al.,* (2014). Therefore, the type B enclaves may have lost the majority of their volatiles in a hybrid layer prior to entrainment into the andesite. In addition, the absence of chilled margins in the type B enclaves would allow volatile escape via permeable flow into the andesite. However, in the type A enclaves, where a chilled glassy margin may be present, volatile escape via permeable flow to the andesite is less feasible. It should be noted although the type A enclaves display a variable range of chilled margins, where some are defined by a reduction in the groundmass crystal size and not only glass, thus making gas escape a viability. Recent work by Edmonds *et al.,* (2014) summarised below in examining this issue with the type A enclaves using the rhyoliteMELTS model suggest that up to 30–40% melt could be present within some enclaves after initial incorporation into the andesite. They conclude that this amount of melt would allow further volatile expansion and thus degassing to occur. During enclave rise through the andesite, decompression will lead further volatile expansion within the enclave, and the resulting overpressures may overcome any chilled margins present, leading to the disaggregation of the enclave. This mechanism is proposed to explain why extremely vesicular enclaves are generally absent in the erupted andesite (Edmonds *et al.,* 2014). It also implies that volatiles may be transferred to the andesite via enclave disaggregation in addition to being directly sourced from the intruding mafic magma at the base of the chamber. The preserved erupted type A enclaves, may have contained a lower degree of initial melt when first entrained into the

andesite thus reducing the effect of volatile expansion, or perhaps vesicles close to glassy chilled margins permitted some permeable flow to the andesite.

3.4 Conclusions

We provide a complete petrological, textural and geochemical description of three distinct mafic enclave populations in the Soufrière Hills andesite, from the eruptive products of phases IV and V of the current eruption. Type A are basaltic with a narrow range of compositions, and are recognised by the presence of chilled margins and high-Al amphiboles, high vesicularity and high inherited phenocryst abundance. Type B have a broad range of compositions (basaltic andesite), and are identified by a lack of chilled margins, low vesicularity and high inherited phenocryst abundance, and rare to absent high-Al amphiboles. Type C are composite with a more mafic interior zone, which is similar to the described type A, and an exterior zone akin to type B. Analysis of bulk compositions, textures, enclave petrology and viscosity demonstrates that differences between the enclave types are partially the result of the degree of mingling between the andesite and mafic magmas. This in turn has led to differing contrasts in temperature, viscosity, density and composition between the enclave types. We interpret type A to be close to a mafic end-member magma, while type B is significantly hybridised; type C represents an interface between the two types.

We observe linear compositional arrays between type A enclaves and the host andesite; with type B enclaves reflecting a broad range of compositions along these arrays (Fig. 3.11). In addition, the presence of inherited phenocrysts confirms that all enclaves are hybridised to some degree. The higher inherited phenocryst abundances in type B indicate a greater degree of interaction with the host andesite. All enclaves contain rhyolitic matrix glass due to crystallisation, which will be discussed further in chapter 4, but there are observable differences in composition between enclave types. Variations in K_2O may reflect differing time-scales for mingling and re-equilibration between the enclave types.

The absence of the high-Al amphibole, and lower anorthite content of plagioclase microphenocrysts in the type B enclaves may be due to a lower melt volatile content in type B relative to type A. The chilled margins in type A enclaves indicate that

crystallisation and formation was driven by rapid cooling with the andesite, while the more hybridised type B experienced slower cooling. Differences in the degree of mingling probably arose from variations in temperature, composition and viscosity contrasts between the andesite and mafic magmas. Thus the distinct textural, petrological and geochemical differences between enclave types reflect differing formation histories. The more mafic type A enclaves were formed from an injected plume of more primitive mafic magma, where limited mingling led to minor incorporation of inherited phenocrysts. Continued mixing of the intruding mafic magma resulted in a hybrid mafic magma, which ponded at the base of the chamber. The texturally broad type B enclaves represent differing fragments from within a disrupted hybrid layer formed at the mafic-silicic interface. Composite enclaves represent two-stage mingling between types A and B, where more mafic magma has intruded into the more hybrid magma layer reflecting temporal differences between them.

There is a suggestion that the degree of hybridisation has changed during the course of the current eruption, as reflected in the disappearance of the SiO_2 gap between the host and mafic enclaves bulk compositions in phase V. We explore that and the possibility whether type A and B enclaves may represent two separate magmas rather than simply differences in the degree of hybridisation in chapter 4. Differences in inherited phenocryst and vesicle abundances, glass compositions, and melt volatile contents could perhaps suggest that simple mixing with the andesite may not be the only compositional control between the two enclave types.

Chapter 4: Geochemical modelling of mafic enclave petrogenesis

4.1 Introduction

Mafic enclaves are a common feature of mingled and mixed magmas (*e.g.* Bacon 1986; Clynne 1999; Coombs *et al.,* 2000; Martin *et al.,* 2006), and their compositions and textures yield important clues as to the manner of interaction between magmas. Mafic enclaves often display a range of compositions, which may reflect hybridisation with the host magma and/or changes in end member magma composition (*e.g.* Bacon, 1986; Clynne, 1999; Browne *et al.,* 2006a). A key question is: can we use the range in mafic enclave compositions to better understand magma mixing? In particular, this chapter will investigate whether the geochemical trends in the SHV mafic enclaves are caused primarily by fractionation of a basaltic end-member magma, or by mixing with andesite, and if by mixing, in what proportion. Density, viscosity and temperature contrasts are key controls on the degree of mixing between magmas. In turn these variables are linked strongly to magma composition, and so the contrast in magma geochemistry between coexisting magmas plays an important role in determining their ability to mix. For example, Frost & Mahood (1987) concluded that homogenous geochemical mixing could only ever occur if the difference in SiO_2 contents between the two magmas is <10%. The more similar two magmas are, geochemically the more effective the mixing between them given relative similar proportions of the magmas (Frost & Mahood, 1987; Sparks & Marshall, 1986). Significant enclave disaggregation into the host magma may also modify the bulk composition of the host over time via crystal and melt transfer (Clynne, 1999). This may be important because changes in the mixing relationship between two magmas can influence eruptive behaviour. For example, a study by Coombs *et al.,* (2000) of the 1953-1974 eruptions at the Southwest Trident Volcano, Katmai, USA found that dacite lava flows with andesite enclaves were extruded for the first 7 years of the eruption. After this, a change from primarily effusive to vulcanian activity occurred where andesitic scoria was

83

primarily erupted. The increase in the ratio of andesite to dacite magma is interpreted to be a result of the waning in the supply of dacitic magma leading to the eruption of the andesitic scoria.

Although most mafic enclaves display evidence for a degree of hybridisation (*e.g.* Clynne, 1999*;* Browne, *et al.,* 2000a), the most primitive end-member may be geochemically the closest relation to the primary mantle-derived magma, and thus may provide a window into lower crustal processes at arc volcanoes. Variations in Rare Earth Element ratios (La/Yb and Dy/Yb) in arc magmas have been used determine the degree of 'cryptic amphibole fractionation' at mid-crustal levels (Davidson *et al.,* 2007). Amphibole contains H_2O, so a large degree of amphibole fractionation at depth could act as 'sponge' for water from mantle-derived melts. Alternatively, melting of deep, amphibole-rich cumulates could be a source for large volumes of hydrous melt, thus increasing the potential for explosivity in derived magmas (Davidson *et al.,* 2007). Therefore, understanding the geochemical controls on the composition of the enclaves will allow a better understanding of how they formed, and the long-term evolution of andesite magma bodies.

4.1.1 Influences on mafic enclave compositions

Commonly, suites of mafic enclaves display a range of compositions, which may reflect differentiation of the mafic magma, or the degree of mixing with the host magma. Strong linear trends in elements between magmas on variation diagrams are often cited as evidence for magma mixing (*e.g.* Langmuir, 1978). The presence of inherited phenocrysts derived from the host magma within mafic enclaves is further evidence for hybridisation of the intruding mafic magma (*e.g.* Bacon, 1986; Clynne, 1999; Browne *et al.,* 2006a). We might also expect phenocryst and melt transfer from the host magma to mafic magma to be a closely coupled process. If the enclave bulk composition is controlled by the degree of mixing with the host, we would expect that the net flux of melt and phenocrysts to the mafic magma to be systematically proportional to the hybridised bulk composition. This raises the question: to what degree does the transference of mass (crystals and melt) from the host magma and subsequent mingling influence bulk mafic enclave composition? The mafic enclave bulk composition can reflect a complex hybrid assemblage of groundmass crystals, melt and possibly host magma derived crystals. The composition of mafic enclave matrix glass may reflect the melt composition after enclave crystallisation. However, the

original mafic melt composition can be difficult to ascertain as the enclave crystal assemblage may be crystallised from a hybrid mixture of host and mafic melt. This chapter will focus on the influences on the mafic enclave compositions and assess whether the variations observed are controlled by differentiation or mixing, using trace element modelling of the bulk compositions. We use new whole rock trace element compositions for the mafic enclaves and andesite from phases III, IV and V and compare them to those from phases I and II (Murphy *et al.,* 2000; Zellmer *et al.,* 2003a; Mann, 2010) and the South Soufrière Hills (SSH) magmas (from Zellmer *et al.,* 2003a; Cassidy *et al.,* 2012).

4.1.2 Volcanic centres on Montserrat

Most of the volcanic centres on Montserrat are andesitic, with mafic enclaves ubiquitous in the lava domes and block and ash deposits (Rea, 1974; Zellmer *et al.,* 2003a). South Soufrière Hills (SSH) is the exception, and has erupted magmas of basaltic to basaltic andesite composition. All Montserrat erupted rock compositions are calc-alkaline and have undergone extensive differentiation from primitive magmas, as indicated by low Ni and Cr concentrations (<10 – 30 ppm) and Mg numbers (<0.6) (Zellmer et al., 2003a). Previous work on the SHV set out to establish the SHV andesite and mafic enclave petrogenesis, and if they could be geochemically related to the SSH volcanics.

4.1.3 Soufrière Hills andesite petrogenesis

The SHV andesite is likely to be derived from basaltic magmas generated by the partial melting of the mantle wedge, where melting was predominantly promoted by fluid addition from the subducting slab, indicated by elevated LILE and U concentrations in the SHV andesite relative to the sediment and mantle wedge (Zellmer *et al.,* 2003a). The focus of prior work on the SHV andesite petrogenesis by Zellmer *et al.,* (2003a) examined whether the SHV andesite erupted in phase I (1995-1999) could be generated by the fractional crystallisation of the mafic enclave magma (using enclaves from phase I) or the SSH magma. The lower abundances of Light Rare Earth elements (LREE) relative to Heavy Rare Earth elements (HREE) in the enclaves compared to the andesite indicate that the phase I andesite was not derived simply via multiphase fractionation from the SHV basaltic magma enclave composition (Zellmer *et al.,* 2003a). This is highlighted by the

lower LREE/MREE ratios in the mafic enclaves relative to SHV andesite; the most differentiated mafic enclave from phase I has evolved to higher Sm concentrations than the andesite (Fig. 4.1 recreated from Zellmer *et al.,* 2003a).
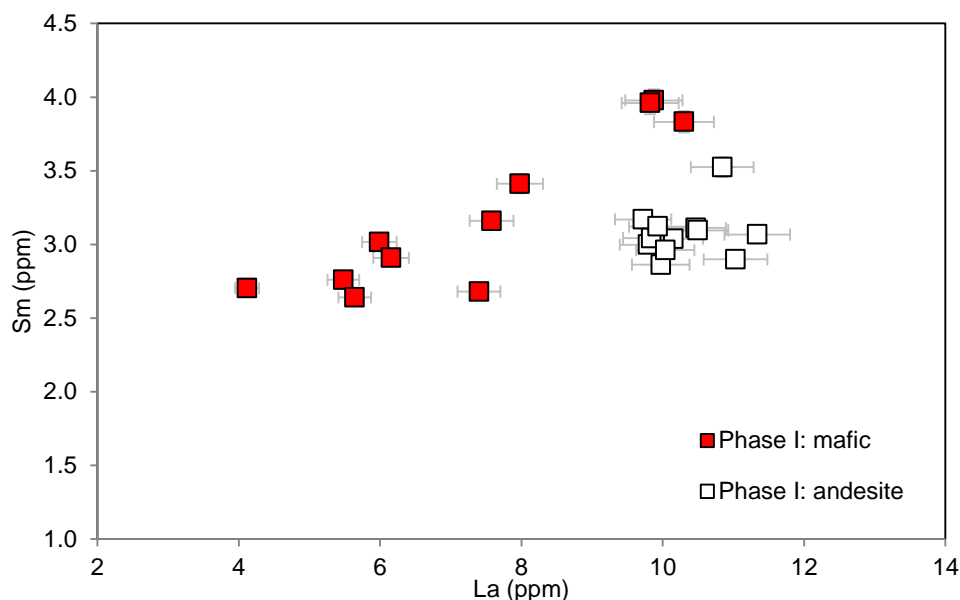
Figure 4.1: Sm vs. La plot of phase I mafic enclave and andesite compositions recreated from Zellmer *et al.,* 2003a. Phase I mafic enclave Sm concentrations evolve to above the SHV andesite suggesting that the mafic enclave magma is not parental to the SHV andesite (Zellmer *et al.,* 2003a).

Instead, on the basis of their trace element signatures, the SHV andesite was most closely linked to the basaltic magma erupted from the SSH volcano and generated by 50% fractional crystallisation of amphibole and plagioclase (Zellmer *et al.,* 2003a). The differentiation of basaltic SSH magma probably took place in an open system, with frequent recharge, highlighted by a drop in U/Th ratios with differentiation, as U and Th are both highly incompatible in most igneous minerals apart from magnetite, therefore U/Th ratios would be expected to remain constant in a closed-system (Zellmer *et al.,* 2003a). SSH basaltic andesite magmas were produced by 30% fractional crystallisation of an undetermined percentage of plagioclase and amphibole, whilst a mafic magma with lower LILE abundances and U/Th ratios continuously recharged the SSH magma with r = 0.9 (Zellmer *et al.,* 2003), where r is the ratio (mass/ unit time) of assimilating magma to fractional crystallisation (De Paolo *et al.*, 1981). However, recent work indicates that the SSH petrogenesis is more complex, and that the SSH magmas are isotopically distinct from SHV magmas, and the magmas associated with other volcanic centres on Montserrat (Cassidy *et al.,* 2012). The distinct geochemical signature of the SSH lavas may be caused

by a greater slab fluid contribution and lesser sediment addition, as indicated by their lower Ce/Pb and Th/Ce ratios. Furthermore, two distinct suites are now identified from trace elements: suite A has higher Zr/Er, and lower Ba/La and Sr/La than Suite B (Cassidy *et al.,* 2012). These differences are thought to be due to a higher subducted sediment contribution relative to slab fluid in suite A than B (Cassidy *et al.,* 2012). SSH magmas may have been generated from shallower depths in the mantle wedge than other Montserrat magmas prior to the onset of substantial partial melting of sediments from the downgoing slab (Cassidy *et al.,* 2012). This therefore calls into question whether the SHV andesite are derived from the SSH magma, as we would expect to observe a similar isotopic signature in both lavas if linked.

4.1.4 Soufrière Hills mafic magma petrogenesis

The mafic enclaves erupted in phase I of the SHV eruption are not related to the mafic SSH lavas by any simple differentiation (Zellmer *et al.,* 2003a) or mixing (Cassidy *et al.,* 2012) process. Instead they are influenced by two dominant processes: a) closed-system fractional crystallization of a parental "end member" magma involving up to 70% total crystallization, with 70% amphibole and 30% plagioclase (Zellmer *et al.,* 2003a) and b) hybridisation by mingling and mixing with the host andesite (Mann, 2010). In contrast to the interpretation that fractional crystallisation controls the compositions of phase I mafic enclaves (Zellmer *et al.,* 2003a), the range of compositions in the phase II mafic enclaves have been attributed primarily to differing degrees of mixing between a parental mafic magma with the andesite (Mann, 2010). The results of previous studies leave it unclear whether the mafic magma, which ranges from basaltic to basaltic andesite in composition (49–57 wt % SiO_2), has already undergone a degree of hybridisation at depth before interaction with the andesite in the shallow chamber, or if it represents a mafic end-member (Zellmer *et al.,* 2003a). Bulk major element concentrations in phase III mafic enclaves hint at a change in the mafic end-member in comparison to phases I and II, with for example decreasing Fe_2O_3 and increasing MgO contents, (Barclay *et al.,* 2010). The major element geochemistry presented in Chapter 3 also shows that the phase V suite of enclaves appear to lie on a parallel trend to the phase I and II enclaves, and fit a linear trend with the andesite (Fig. 3.11). The observed proportion of mafic enclave abundances has also apparently increased from 1 % in phase I to 12 % in phase IV (Murphy *et al.,* 2000; Mann, 2010, Barclay *et al.,* 2010; Komorowski *et al.,* 2010), suggesting a change in

the proportions of the end member magmas in the chamber, or in the dynamics of the mixing process. In this chapter, we examine whether the models proposed to explain the geochemical trends of the mafic enclaves from the earlier extrusive phases at SHV above could be applied to the phase III and V mafic enclaves, or if new models reflecting changing geochemical processes over time are required.

4.1.5 Summary of phase V mafic enclave types (Chapter 3)

Mafic enclaves sampled from phase V (2009-2010) are categorised into three types (A, B and C) on the basis of differences in bulk compositions, textures, enclave petrology and viscosity (described in detail in chapter 3). Type A enclaves are basaltic with a narrow range of compositions (~49–52 wt % SiO_2), and are recognised by their chilled margins and high-Al amphiboles, high vesicularity and low inherited phenocryst abundance. Type B enclaves have a broad range of compositions (53–57 wt % SiO_2), and are identified by a lack of chilled margins, low vesicularity and high inherited phenocryst abundance (~25%), and rare to absent high-Al amphiboles. Analysis from Chapter 3 demonstrates that differences between the enclave types such as differing modal abundances of inherited phenocrysts may reflect different mafic to andesite mixing ratios. Textural differences such as the presence of chilled margins in the type A enclaves *versus* the absence of these in the type B enclaves also suggest differing degrees of temperature contrast between the enclave types and the andesite. Elevated K_2O concentrations in some of the type A enclaves glass compared to type B (Chapter 3) also might suggest differing timescales for mixing between the enclave types and host andesite or differentiation trends, which will be discussed in section 4.4.4. Therefore, it is important to assess the degree to which the mafic enclave compositions are the result of mixing as this may yield information on enclave formation mechanisms. The clear differences in textures, petrology and geochemistry between the enclave types raises the question as to whether the enclaves types from phase V are generated from the same mafic end-member composition. This chapter will examine in detail the bulk geochemical differences between phase V enclave types to ascertain if the enclave types may be related to different mafic magma batches, or if the differences between the enclave types are simply controlled by the degree of mixing with the andesite.

Table 4.1: *Calculated bulk partition coefficients for phase III and V end-member compositions using equation [2]*

Element	Phase III (MO08:MO01)	Phase V (MT27: MT25)	Phase V (MT27: MT08b)	Phase V MT27: MT25 (NC)
Sc	2.55	n.a.	n.a.	n.a.
V	1.94	1.55	1.42	1.68
Cr	4.37	n.a.	n.a.	n.a.
Co	1.43	1.30	0.97	1.54
Ni	3.43	n.a.	n.a.	n.a.
Cu	0.02	n.a.	n.a.	n.a.
Zn	1.27	n.a.	n.a.	n.a.
Ga	0.77	1.10	1.09	1.31
Rb	0.60	-0.11	0.06	-0.11
Sr	0.75	1.05	1.09	1.02
Y	0.44	0.93	0.82	1.00
Zr	1.22	0.40	0.44	0.44
Nb	0.38	0.49	0.40	0.61
Cs	-0.78	-0.23	0.46	-0.22
Ba	-0.29	0.07	0.12	0.02
La	0.02	0.35	0.39	0.42
Ce	0.06	0.37	0.35	0.44
Pr	0.08	0.57	0.52	0.69
Nd	0.39	0.77	0.74	0.87
Sm	0.45	0.90	0.90	1.01
Eu	0.65	0.95	0.97	0.96
Gd	0.50	0.96	0.91	1.00
Tb	0.54	1.09	1.00	1.30
Dy	0.51	1.05	0.95	1.19
Ho	0.51	1.00	0.98	1.19
Er	0.61	0.93	1.01	1.06
Tm	0.17	1.00	0.91	1.19
Yb	0.38	0.99	0.84	1.13
Lu	0.43	0.93	0.76	1.05
Hf	0.80	0.18	0.24	0.21
Ta	1.00	n.a.	n.a.	n.a.
Pb	0.35	n.a.	n.a.	n.a.
Th	0.00	0.00	0.00	0.00
U	-1.61	0.22	0.07	n.a.

4.2 Geochemical modelling methodology

4.2.1 Fractional crystallisation model

The extent of fractional crystallisation is calculated from the bulk rock compositions from each individual phase using the Rayleigh equation:

$$C_L = C_0 F^{(D_i - 1)}$$ [1]

where C_L is the concentration of an element in the most evolved magma composition during fractional crystallisation from an individual phase, C_O is the concentration of the element in the least evolved magma composition from an individual phase, F is the fraction of melt remaining, and D_i is the bulk partition coefficient for elements i. D_{Th} was set to zero *i.e.* we assume that Th is perfectly incompatible in the crystallising assemblage. We then solve for F_{Th} by rearranging [1]:

$$F_{Th} = \frac{\log\left(C_L / C_0\right)}{\left(D_{Th} - 1\right)}$$ [2]

and then use this value of F_{Th} to calculate relative partition coefficients, D_i^{rel}, for each individual trace element i (following Zellmer *et al*. 2003). Calculated D_i^{rel} for all elements in all phases of the eruption are positive except for D_{Cs}^{rel} (Table 4.1 analytical precision is shown in table 4.3). For phases II to V, D_{Cs}^{rel} are systematically negative, which is impossible in nature. Caesium concentrations are low (between 0.1 and 0.3 ppm), and the detection limit for analysis is high (0.1), so the likely cause for these results is analytical uncertainty. The calculated D_i^{rel} are then compared to partition coefficients for each element i in each crystallising phase j (amphibole, plagioclase, etc.), D_i^{j}, and used to obtain the mineral proportions in the fractionating assemblage. D_i^{j} were obtained from the literature (Table 4.2; references within). Where no D_i was available for pargasitic amphibole, D_i for hornblende was used instead (Table 4.2). It should also be noted that

there is a large range of reported values for D_i^j, and choice of partition coefficient has a large impact on the calculated mineral proportions in the assemblage. For example, REE partitioning in pargasitic amphibole correlates negatively with pressure (Adam and Green, 1994), therefore without knowing exact pressures this can make the choice of partition coefficients problematic. Consequently, a range in D_i^j is also used to attain a more realistic range of mineral proportions in the fractionating assemblage (Table 4.2).

4.2.2 Magma mixing model

To assess the degree of mixing a simple mixing equation is used (*e.g.* Langmuir, 1978):

$$C_{mix}^i = X(C_{and}^i - C_{bas}^i) + C_{bas}^i \qquad [3]$$

where, C_{and}^i, C_{bas}^i, and C_{mix}^i are the concentrations of an element i in the andesite, mafic magma, and in the mixed magma respectively, X is the fraction of andesite in the resulting mixed magma. The least evolved mafic enclave composition and the most evolved andesitic composition are chosen to represent the end-members, on the basis of SiO_2 content, although clearly the choice of the end-member compositions is important and can

exert a large influence on the results. Mixing between the andesite and the basalt is evaluated for major and trace elements by using mass balance equations (Bryan *et al*. 1969):

$$m_0 = m_f \pm m_{i1} \pm \cdots m_{in} \qquad [4]$$

where, m_o is the initial composition, m_f is the final composition, m_i are the compositions added or subtracted from the initial composition. Least squares regression mixing equations from Byran *et al.,* (1969) are used, where the residual sum of squares (Σr^2) are used to determine the goodness of fit (where ideally values of <0.2 indicate a good fit; Bryan *et al*., 1969) for the major elements, and R^2 values are used for the trace elements.

Table 4.2: *Partition coefficients used in geochemical modelling*

	Pargasite	Ref.	**Hornblende**	Ref.	**Orthopyroxene**	Ref.
Sc	-	-	2.18-4.2	*4,5*	1.2	*3*
V	-	-	1.35-3.4	*3,9*	0.6	*3*
Co	-	-	1.35-1.77	*4*	3	*3*
Rb	0.2	*2*	0.1-0.29	*3,7,10*	0.022	*3*
Sr	0.298	*2*	0.35-0.46	*8,10*	0.04	*3*
Y	0.52-1.62	*1,2*	1	*10*	0.18	*3*
Zr	0.13-0.81	*1,2*	0.4-0.5	*3,10*	0.18	*3*
Nb	0.16-0.24	*1,2*	0.3-0.8	*6,10*	0.15	*10*
Cs	-	-	0.046-0.2	*4*	0.01	*11*
Ba	0.16	*2*	0.39-0.44	*4*	0.013	*3*
La	*0.05-0.28*	*1,2*	0.16-0.2	*4,5,6*	0.002	*6*
Ce	-	-	0.26-0.37	*4,5,6*	0.02	*14*
Pr	-	-	0.35	*6*	0.0048	*6*
Nd	0.25	*2*	0.33-0.7	*6,10,14*	0.03	*14*
Sm	-	-	0.76-0.93	*4,5,6*	0.05	*14*
Eu	-	-	0.88-1.08	*4,6,*	0.05	*14*
Gd	0.32-2.1	*1,2*	0.63-1.08	*5,6,10,14*	0.09	*14*
Tb	-	-	1.02-1.29	*4,5*	0.019	*6*
Dy	-	-	0.64-1.3	*6,10,14*	0.15	*14*
Ho	0.62	*2*	0.73-1	*6,10*	0.026	*6*
Er	0.57	*2*	0.68	*6*	0.23	*14*
Tm	0.51	*2*	0.9	*10*	0.04	*6*
Yb	-	-	0.49-0.8	*6,10,14*	0.34	*14*
Lu	0.43-1.72	*1,2*	0.51-0.8	*5,6,10*	0.42	*14*
Hf	0.33-1.07	*1,2*	0.5	*3*	0.05	*10*
Ta	0.27	*1*	0.25	*10*	0.15	*10*
Pb	0.04	*2*	0.1	*6*	0.0013	*6*
Th	0.039	*2*	0.05-0.5	*3,10*	0.13	*10*
U	0.0041	*2*	0.08-0.1	*3,10*	0.035	*10*

(1) Hilyard *et al.,* 2000; (2) La Tourette *et al.,* 1995; (3) Rollinson, 1993; (4) Matsui *et al.,* 1977; (5) Higuchi & Nagasawa, 1969; (6) McKenzie & O'Nions, 1991; (7) Green *et al.,* 1993; (8) Ronov & Yaroshevskiy, 1976; (9) Sisson, 1994; (10) Fujimaki *et al.,* 1984; (11) Bacon & Druitt, 1988; (12) Zack *et al.,*1997; (13) Foley *et al.,* 1996; (14) Arth, 1976; (15) Philpotts & Scnetzler, 1970; (16) Bindeman *et al.,* 1998; (17) Aigner-Torres *et al.,* 2007; (18) Villemant, 1998; (19) Dunn & Sen, 1994; (20) Lemarchand *et al.,* 1987; (21) Schock, 1979.

Table 4.2: *Partition coefficients used in geochemical modelling*

	Clinopyroxene	Ref.	**Plagioclase**	Ref.	**Magnetite**	Ref.
Sc	3.2	*3*	0.04	*18*	1.59	*20*
V	1.35	*3*	0.27-0.022	*16,19*	6.85	*22*
Co	2	*3*	0.07	*18*	4.61-7.4	*3,20*
Rb	0.031	*3*	0.071-0.15	*3,6*	0.32	*20*
Sr	0.06	*3*	1.74-2	*6,17*	-	-
Y	0.9	*3*	0.01-0.03	*3,17*	0.2	*3*
Zr	0.1	*13*	0.048	*3*	0.1	*3*
Nb	0.005	*3*	0.01	*3*	2.0-4.0	*3*
Cs	0.13	*12*	0.13	*18*	-	-
Ba	0.026	*3*	0.23-0.6	*4,15*	-	-
La	0.0435	*13*	0.06-0.27	*6,17*	1.5-3.0	*21*
Ce	0.15	*14*	0.05-0.2	*6,14,17*	1.3-3.0	*21*
Pr	0.124	*14*	0.17	*6*	-	-
Nd	0.31	*14*	0.04-0.14	*5,6,14*	1.0-3.0	*21*
Sm	0.5	*14*	0.067-0.11	*6,14,16*	1.1-2.2	*21*
Eu	0.51	*14*	0.34-0.97	*6,14,16*	0.6-1.5	*21*
Gd	0.61	*14*	0.05-0.07	*6,14,16*	-	-
Tb	0.364	*13*	0.06	*6*	0.26	*20*
Dy	0.68	*14*	0.02-0.055	*6,15*	1.0-2.0	*21*
Ho	0.378	*13*	0.048-0.05	*6,17*	-	-
Er	0.65	*14*	0.041-0.063	*6,14*	-	-
Tm	0.297	*13*	0.036	*6*	1.0-2.0	*21*
Yb	0.62	*14*	0.031-0.08	*6,14,17*	0.9-1.8	*21*
Lu	0.56	*14*	0.025-0.06	*6,14*	-	-
Hf	0.263	*3*	0.051	*3*	2.0-4.0	*21*
Ta	0.013	*3*	0.04`	*18*	1.0-10	*21*
Pb	-	-	-	-	-	-
Th	0.03	*3*	0.01	*3*	0.26	*20*
U	0.04	*3*	0.01	*3*	0.19	*20*

(1) Hilyard *et al.,* 2000; (2) La Tourette *et al.,* 1995; (3) Rollinson, 1993; (4) Matsui *et al.,* 1977; (5) Higuchi & Nagasawa, 1969; (6) McKenzie & O'Nions, 1991; (7) Green *et al.,* 1993; (8) Ronov & Yaroshevskiy, 1976; (9) Sisson, 1994; (10) Fujimaki *et al.,* 1984; (11) Bacon & Druitt, 1988; (12) Zack *et al.,*1997; (13) Foley *et al.,* 1996; (14) Arth, 1976; (15) Philpotts & Scnetzler, 1970; (16) Bindeman *et al.,* 1998; (17) Aigner-Torres *et al.,* 2007; (18) Villemant, 1998; (19) Dunn & Sen, 1994; (20) Lemarchand *et al.,* 1987; (21) Schock, 1979.

Table 4.3: *ICP-MS data from phases III and V used in geochemical modelling.*

	Eruptive phase Sample no.	Phase III							
		M001	M003	M005	M006	M008	M010	M013	M014
	Type	m	and	m	m	m	and	m	m
ppm	DL (ppm)	SD %							
Li	0.1	11.1	11.7	13.1	9.9	10	10.9	12.2	11	8.3
Sc	0.1	11.3	14	14.8	21.9	21.9	36.3	16	20.9	29.3
V	1	4.8	152	163	230	227	295	167	230	283
Cr	1	5.8	1	3	5	5	8	3	5	8
Co	0.2	3.9	27.3	20.9	29.7	29.7	35.6	22.7	36	35.4
Ni	0.1	1.0	2.7	4.3	7.2	7.1	12.1	4.6	7.6	11.7
Cu	0.1	0.3	157.4	34.9	28.2	40.7	85.8	33.5	29.3	80.9
Zn	1	0.6	62.5	63.5	65.1	67	73.8	70.2	67.9	66.2
Ga	0.5	4.8	22.8	21.6	20.8	20.7	19.8	18.8	18.2	19
Rb	0.1	1.4	8.3	14.7	9.8	10.4	6.5	15.4	11.4	6.3
Sr	0.5	0.5	353.7	303.8	303.6	316	303	306.3	309.8	306.2
Y	0.1	3.5	27.6	21.6	20.3	20.6	19.6	20.2	18.5	19.4
Zr	0.1	4	47.2	161.2	65.1	73.8	54.2	115.6	66.1	54.5
Nb	0.1	3.6	2.2	2.7	2.1	2.2	1.5	3	1.9	1.3
Cs	0.1	0	0.3	0.4	0.3	0.3	0.1	0.4	0.3	0.3
Ba	1	2.9	148	194	125	137	67	193	131	80
La	0.1	5.5	10.4	10.5	7.8	8.2	5.7	11	7.8	5.6
Ce	0.1	3.4	24.5	24	18	18.3	13.7	23.7	17.3	13.6
Pr	0.02	0.8	3.13	2.88	2.23	2.43	1.78	2.92	2.18	1.83
Nd	0.3	4.1	14.1	12.9	11	10.5	9.7	12.9	10.1	9.1
Sm	0.05	3.9	3.67	3.14	2.9	2.89	2.61	2.91	2.48	2.5
Eu	0.02	4	1.18	1	0.94	0.99	0.95	1.01	0.9	0.96
Gd	0.05	2.6	4.1	3.32	3.19	3.24	3.01	3.31	3.04	3.05
Tb	0.01	3.4	0.69	0.56	0.53	0.54	0.52	0.51	0.48	0.5
Dy	0.05	5.4	4.58	3.41	3.56	3.56	3.38	3.39	3.32	3.06
Ho	0.02	2.1	0.96	0.78	0.73	0.72	0.71	0.69	0.64	0.7
Er	0.03	3.4	2.85	2.29	2.18	2.17	2.24	2.11	1.89	2.08
Tm	0.01	8.7	0.5	0.36	0.35	0.33	0.3	0.33	0.31	0.3
Yb	0.05	3.8	2.91	2.5	2.19	2.51	1.99	2.17	2.29	1.9
Lu	0.01	5.5	0.47	0.39	0.35	0.36	0.33	0.38	0.37	0.28
Hf	0.1	5.2	1.7	3.6	1.8	1.9	1.5	3.3	1.9	1.6
Ta	0.1	3.2	0.2	0.2	0.2	0.2	0.2	0.2	0.1	0.1
Pb	0.1	2.9	1.9	1.8	1.7	2.4	1.3	2.3	2.3	1.7
Th	0.2	1.4	1.6	2.4	1.5	1.7	0.9	2.3	1.5	1.1
U	0.1	15.9	0.5	0.7	0.4	0.5	0.1	0.7	0.5	0.2

n.a. not analysed; *Data from Mann, 2010; and = andesite; m = mafic; A,B and C refer to the enclave types defined in chapter 3

Table 4.3: *ICP-MS data from phases III and V used in geochemical modelling.*

	Phase III			Phase V						
			MVO	MVO	MT	MT	MT	MVO	MVO	MVO
	M015	M018	1448	1567d	27	18	25b	1566e	1590	1591
	m	m	T1	A	A	B	B	B	B	B
ppm										
Li	8.4	7.9	n.a.	15.2	n.a.	8.5	11.7	10.7	9.7	8.9
Sc	33.5	28.9	n.a.	32.9	n.a.	21.7	15.5	23.5	23.8	26.1
V	288	278	219	289	283	230	172	222	214	221
Cr	7	7	17	9	n.a.	6	2	8	6	8
Co	33.3	33.1	n.a.	29.1	31.4	25.9	24.1	25.3	25	24.1
Ni	11.9	11.6	14	10.6	n.a.	6.6	4.7	8.9	7.2	8.6
Cu	79.1	84.4	n.a.	125.1	47.9	40.3	22.5	39.9	62.5	41.2
Zn	65.5	71.7	n.a.	69.2	n.a.	65	67.9	67.5	67.7	62.5
Ga	19.1	18.3	16.7	18.3	19.2	17.5	17.6	17.8	17.6	17.4
Rb	6.8	6.5	11.6	10.8	6	10.2	16.2	10.8	11	9.7
Sr	310.3	310.8	263.9	307.5	319.1	304.7	303.9	306.2	300.1	306.1
Y	20	19.2	20.21	19.7	17.9	19	19	17.6	19.8	18.5
Zr	57.2	58.6	78.2	59.4	51.4	66.8	88	74.9	75.1	67.9
Nb	1.4	1.6	2.1	1.4	1.4	1.9	2.2	1.6	1.8	1.8
Cs	0.2	0.2	n.a.	0.3	0.2	0.3	0.6	0.4	0.3	0.2
Ba	86	83	107	99	81	132	186	144	151	135
La	6.3	5.9	6.81	6.8	5.7	8.6	10.2	7.8	8.2	7.7
Ce	13.9	14.2	14.93	15.2	12.3	17.7	21.6	17.7	18.7	17
Pr	1.87	1.9	2.09	2.04	1.79	2.27	2.64	2.18	2.38	2.25
Nd	9.8	8.9	9.73	8.8	8.7	9.9	10.7	9.9	10.2	11.2
Sm	2.46	2.56	2.55	2.41	2.53	2.73	2.76	2.53	2.55	2.42
Eu	0.93	0.92	0.89	0.92	0.9	0.92	0.94	0.87	0.98	0.92
Gd	3.18	2.96	3.18	3.13	3	3.03	3.1	2.86	3.16	3.06
Tb	0.52	0.49	0.49	0.51	0.51	0.49	0.47	0.44	0.48	0.45
Dy	3.49	3.06	3.26	3.19	3.29	3.07	3.14	2.86	3.19	3.42
Ho	0.72	0.68	0.69	0.69	0.67	0.66	0.67	0.61	0.65	0.73
Er	2.14	2	2.07	2.26	2.03	2.1	2.16	1.86	1.97	1.98
Tm	0.31	0.32	0.31	0.3	0.3	0.32	0.3	0.27	0.28	0.3
Yb	1.96	1.78	2.11	2.13	2.02	1.98	2.04	1.87	2.11	1.92
Lu	0.32	0.3	0.32	0.3	0.31	0.32	0.33	0.31	0.35	0.31
Hf	1.6	1.8	1.42	1.6	1.3	2	2.7	2.1	2.2	1.9
Ta	0.1	0.1	0.44	<0.1	<0.1	0.2	0.2	0.2	0.1	0.1
Pb	1.92	1.79	2	1.9	0.2	2.2	2.1	2.5	2.7	2.5
Th	0.9	1	n.a.	1.3	0.9	1.7	2.2	1.6	1.6	1.6
U	0.3	0.2	n.a.	0.3	0.3	0.4	0.6	0.5	0.5	0.4

n.a. not analysed; *Data from Mann, 2010; and = andesite; m = mafic; A,B and C refer to the enclave types defined in chapter 3

Table 4.3: *ICP-MS data from phases III and V used in geochemical modelling.*

	Phase V								
	MVO 1588	MT 10	MT 08a	MT 08b	MVO 1537b	MVO 1538b	MVO 1537a	MVO 1538a	MVO 1539b
	B	B	C	C	and	and	and	and	and
ppm									
Li	n.a.	n.a.	8.6	9.7	13.6	14.4	n.a.	n.a.	n.a.
Sc	n.a.	n.a.	25.2	20.2	12.6	11.3	n.a.	n.a.	n.a.
V	213	217	267	221	136	116	152	104	107
Cr	n.a.	n.a.	7	5	4	4	n.a.	n.a.	n.a.
Co	24.7	25.7	38.4	32.2	19.4	18.6	31.4	19.6	17.3
Ni	n.a.	n.a.	8.4	5.1	3.3	2.1	n.a.	n.a.	n.a.
Cu	21.0	22.7	46.2	34.3	29.3	23.1	15.3	37	16.7
Zn	n.a.	n.a.	67.8	65.1	66.9	61.1	n.a.	n.a.	n.a.
Ga	16.9	17.7	17.9	17.9	16.7	16.6	17.1	15.2	15.8
Rb	10.1	9	9.4	12.1	17.2	18.3	14.4	16.7	15.5
Sr	313.7	312.4	308	298.7	295	294.7	298.3	286	281.5
Y	20.3	19.3	19.5	20.5	20.3	22.1	17.8	20.6	20.4
Zr	74.1	77.9	69.5	78.4	99.2	102.1	92.3	93.4	94.4
Nb	1.7	1.5	2.1	2.2	2.9	2.8	2.3	2.4	2.6
Cs	0.4	0.4	0.3	0.3	0.6	0.5	0.5	0.5	0.5
Ba	142	128	118	156	229	236	200	225	221
La	7.9	8	7.6	9	12.2	12.3	10	12	11.3
Ce	17	15.7	17	20	25.4	27.6	21	24.1	22.8
Pr	2.33	2.29	2.16	2.57	3.06	3.32	2.63	3.11	2.92
Nd	9.3	12.1	10.3	10.6	12.2	14.9	11.8	12.6	13.4
Sm	2.78	2.85	2.58	2.72	3.06	3.03	2.54	3.2	3.11
Eu	0.97	0.98	0.93	0.92	0.98	1.07	0.9	0.99	0.94
Gd	3.33	3.09	3.06	3.21	3.17	3.4	3.04	3.47	3.39
Tb	0.51	0.53	0.5	0.51	0.5	0.55	0.51	0.56	0.51
Dy	3.47	3.63	3.3	3.42	3.38	3.75	3.3	3.51	3.33
Ho	0.77	0.8	0.73	0.68	0.68	0.75	0.66	0.78	0.74
Er	2.19	2.12	2.14	2.01	2.04	2.41	2.05	2.31	2.21
Tm	0.32	0.32	0.3	0.32	0.33	0.36	0.33	0.38	0.34
Yb	1.99	2.03	2	2.27	2.26	2.53	2.28	2.43	2.51
Lu	0.35	0.35	0.31	0.37	0.38	0.38	0.33	0.39	0.38
Hf	2	2.2	1.9	2.3	2.9	2.9	2.5	2.5	2.6
Ta	0.1	0.1	0.4	0.3	0.2	0.2	0.3	0.3	0.3
Pb	0.2	0.2	2.2	2.4	3.6	2.9	0.1	0.4	0.2
Th	1.7	1.4	1.5	1.9	2.7	3	2.3	2.6	2.7
U	0.5	0.3	0.5	0.6	0.8	0.8	0.7	0.9	0.7

n.a. not analysed; *Data from Mann, 2010; and = andesite; m = mafic; A,B and C refer to the enclave types defined in chapter 3

4.3 Results

New whole rock trace element geochemical data (XRF and ICP-MS) for the mafic enclaves and andesite from phases III, IV and V are presented (Table 4.3) to add to the major element data presented in Chapter 3. Methods for data collection are presented in Chapter 2. The data are compared to geochemical data from phases I and II (Murphy *et al.,* 2000; Zellmer *et al.,* 2003a; Mann, 2010). South Soufrière Hills data (SSH) (see locality map Fig. 1.6) (from Zellmer *et al.,* 2003a; Cassidy *et al.,* 2012), as representative of mafic lavas found on Montserrat, are also compared to the Soufrière Hills data.

Trace element concentrations in the mafic enclaves and andesite are first normalised to normal mid-ocean ridge basalt (N-MORB; Sun & McDonough, 1989; Fig. 4.2). MORB-normalisation is commonly used to examine arc basalts as elements are arranged in order of fluid mobility (with the most mobile elements on the left of the diagram), and therefore used to assess the mantle wedge component. However, in section 4.3.3 where rare earth elements are examined in more detail, concentrations are chondrite-normalised; chondrite compositions are believed to reflect the primitive mantle source, and therefore fractionation trends may be assessed with a greater degree of accuracy than the MORB values.

4.3.1 Andesite geochemistry

New major and trace element, and REEs concentrations from phases III to V andesite are compared to phases I and II (Murphy *et al.,* 2000; Zellmer *et al.,* 2003a; Mann, 2010). SHV andesite composition is variable and ranges from 57 to 62 wt % SiO_2 across the five eruptive phases. Although the concentration of SiO_2 is slightly lower on average for phase V andesite than for earlier phases, it is still within the range displayed by andesite erupted during the previous phases (Chapter 3: Fig. 3.11). Major elements from phases III to V follow established linear trends from the earlier phases; for example Al_2O_3 is negatively correlated with increasing SiO_2 (Chapter 3: Fig. 3.11). The trend of decreasing FeO and increasing MgO concentrations in mafic enclave compositions from phases I to III is not mirrored in the andesite compositions, and there is no observed change in the composition of andesite erupted in phase V (Chapter 3: Fig. 3.11).

97
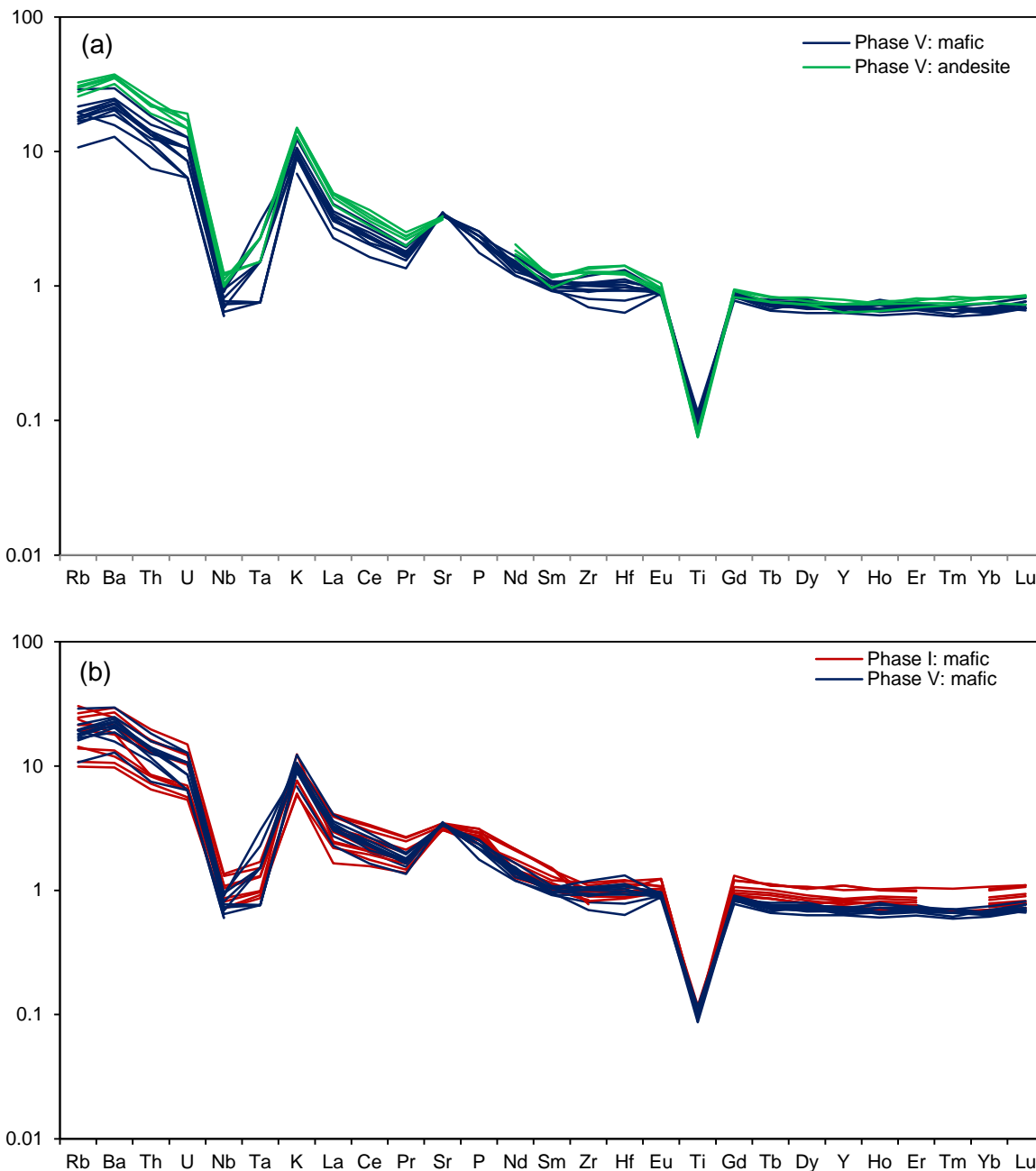
Figure 4.2: Trace element concentrations normalised to N-MORB values (Sun and McDonough, 1989) (a) Phase V mafic and andesite concentrations (b) Comparison of phase I and phase V mafic enclave trace element concentrations (phase I data from Zellmer *et al.,* 2003a and Mann, 2010).

The overall trace element patterns of the andesite across the eruptive phases are typical of subduction-related magmas in general (Fig. 4.2a). Large ion lithophile elements (LILE) such as Rb, K and Ba are enriched, whilst high field strength (HFS) elements such as Ti, Nb and Ta are depleted relative to rare earth elements (REE). Enrichment of LILE, which are fluid mobile, reflects the slab-derived aqueous fluids introduced into the mantle wedge during subduction of the downgoing slab and subsequent melt generation, whilst for

example Ti, Nb and Ta are both highly immobile in aqueous fluids and may be retained in minerals such as titanite, causing a relative depletion in these elements. Trace element concentrations in andesite erupted during phases III to V follow the trends established in the earlier phases, and the concentrations lie within the same range (Chapter 3: Fig. 3.11). Changes in mafic enclave REE patterns through phases I to V are not reflected in the andesite REEs; light rare earths continue to be enriched relative to middle and heavy rare earth elements, with REE abundances remaining stable (Fig. 4.3f).

4.3.2 Mafic enclave major and trace element chemistry, all eruptive phases

We first compare the major and trace element compositions of mafic enclaves in phases III, IV and V with those of the earlier phases of the eruption, which also serves as a summary of the major element results of Chapter 3. The compositions of mafic enclaves from phases IV and V fall on the same linear array on major element plots as the earlier phases (Chapter 3: Fig. 3.11; Murphy *et al.,* 2000; Zellmer *et al.,* 2003a). However, the compositional gap in SiO_2 between the mafic enclaves and the andesite observed in phases I-III no longer exists in phase V (Chapter 3: Fig. 3.11). The mafic enclaves erupted in phase V have compositions that do not continue the trend of increasing MgO and decreasing Fe_2O_3 concentrations established between phases I to III (Barclay *et al.,* 2010) (Chapter 3: Fig. 3.11), but instead remain similar in composition to phase III.

The overall trace element patterns of the mafic enclaves are similar to that of the andesite and typical of subduction-related magmas (Fig. 4.2a), although they are relatively depleted in elements from Rb to Hr (except for Sr) in comparison to the andesite (Fig 4.1a). Mafic enclave U/Th ratios remain constant with increasing differentiation in products from all eruptive phases, in contrast to the South Soufrière Hills basalt (Fig. 4.4). The same is seen for other high field strength elements such as Zr and Hf. The slightly higher degree of scatter in phases III and V (Fig. 4.4), can be largely attributed to the low analytical precision (0.22 ppm; table 4.3) and high error (15.9 %) for U/Th analysis of phases III and V. Nonetheless, the scatter in some phase III points is outside of error; but, this degree of scatter is not replicated in other incompatible element ratios such as Rb/Th. Many of the trace element distributions in the enclaves studied are consistent with previous
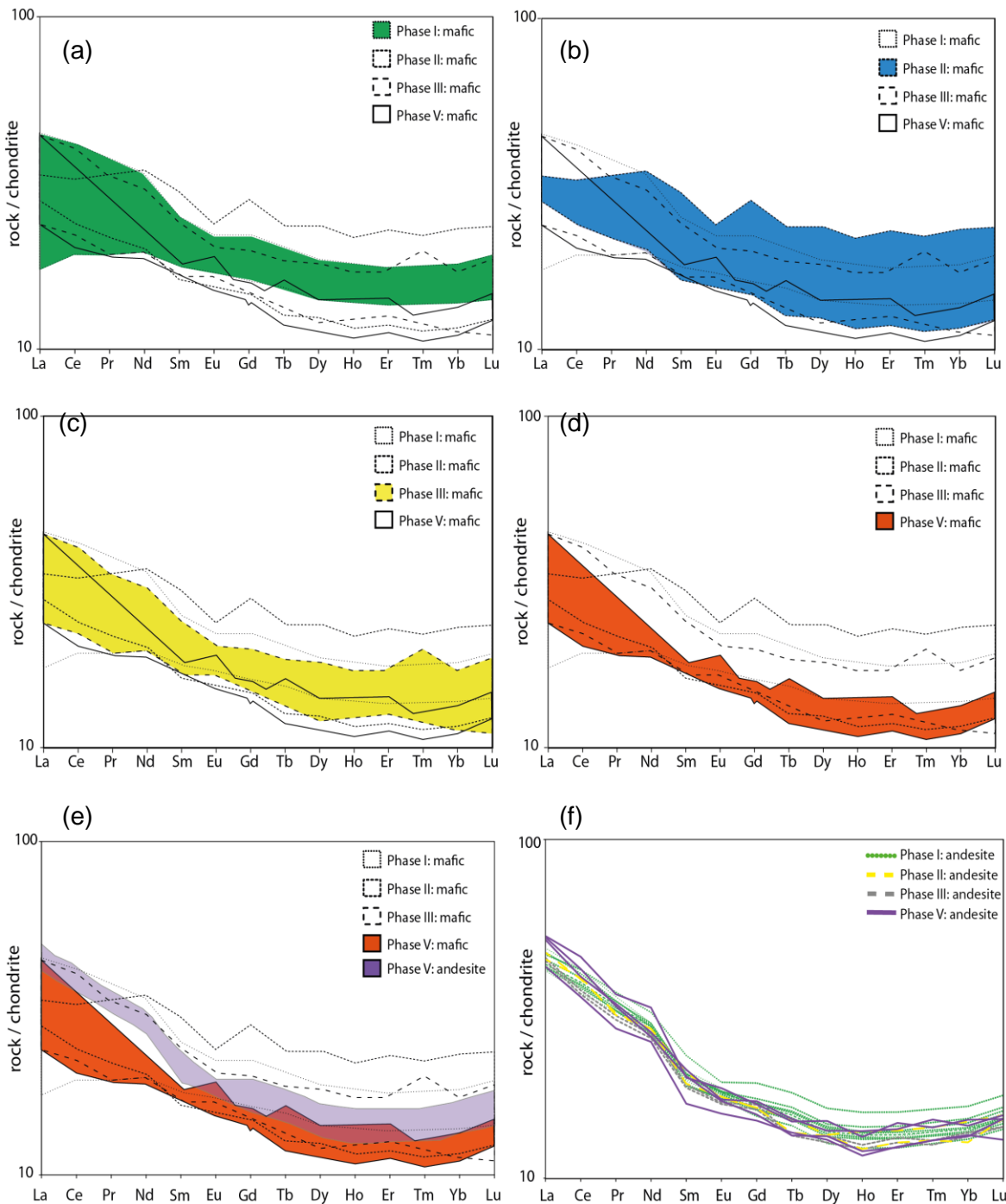
Figure 4.3: Chondrite-normalised rare earth element diagrams; (a) Phase I mafic enclave REE patterns highlighted in green (data from Zellmer *et al.,* 2003a) (b) Phase II mafic enclave REE patterns are highlighted in blue (data from Mann, 2010) (c) Phase III mafic enclave REE patterns (highlighted in yellow) which broadly still follow phases I and II (d) Phase V mafic enclave REE patterns (highlighted in red), these follow the established patterns from the eruptive phases, but have a more pronounced trough in the MREE to HREE patterns (e) Phase V mafic and andesite REEs (highlighted in red and purple); phase V andesite remains consistently similar to phase I, however, the mafic enclave MREE to HREE concentrations now lie below the andesite field. (f) Phases I to V andesite; REE concentrations all plot within the same field.

studies (Murphy *et al.,* 2000; Zellmer *et al.,* 2003a; Mann, 2010). However, vanadium and scandium concentrations in phases III and V mafic enclave compositions are systematically higher in comparison to phases I and II concentrations (Fig. 4.5), and decrease more sharply in concentration against increasing La; the difference between the phases is more pronounced in the least evolved mafic enclave compositions (Fig. 4.5), and is well outside analytical error (Table 4.3; Fig. 4.5).
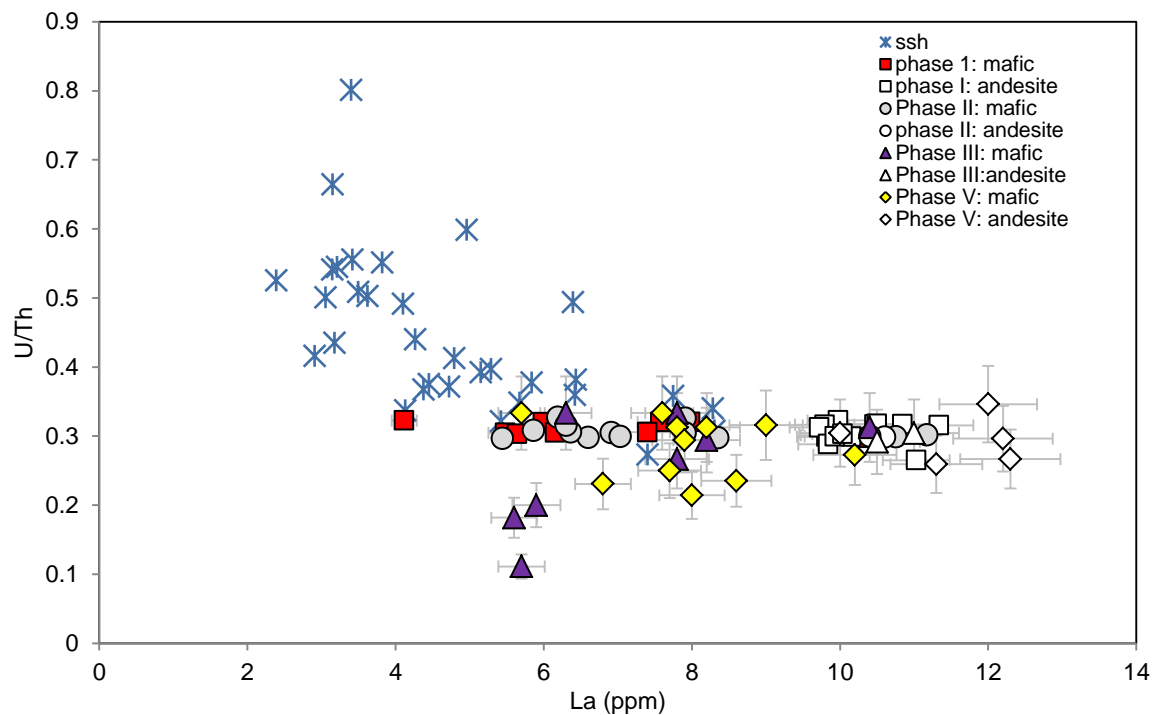
Figure 4.4: U/Th *vs* La; incompatible ratio elements demonstrate that mafic enclave compositions remain constant across the eruptive phases at SHV reflecting likely closed-system differentiation, unlike SSH compositions where open-system processes are inferred to control the SSH geochemical trends (Zellmer *et al.,* 2003). SSH data from Zellmer *et al.,* 2003; Cassidy *et al.*, 2012, phase I data from Zellmer *et al.,* 2003, phase II data from Mann, 2010.

4.3.3 Mafic enclave rare earth element chemistry, all eruptive phases

Rare earth element (REE) data from all phases have been chondrite-normalised using values from Sun & McDonough (1989) following Zellmer *et al.,* (2003a), and are presented in Fig. 4.3 and in table 4.3. The mafic enclaves in phases III-V continue the established pattern of enriched light rare elements (LREE) relative to the middle rare earth elements (MREE) and heavy rare earth elements (HREE) observed in phase I through to

101

phase V, typical of subduction-related magmas. However, REE concentrations and ratios have not remained constant throughout the eruption, and these changes are outside the range of the analytical uncertainty (Table 4.3). Decreasing REE concentrations are observed from phases I to V (Fig. 4.3) An increase in LREE/HREE ratios are observed between phases I to III (Ce_N/Yb_N = 1.4-2.3) and phase V (Ce_N/Yb_N = 1.7-2.9), which is also outside analytical error (Fig. 4.6a). Individual sample patterns for phase V are shown in figure 4.7, and are discussed in more detail in section 4.3.4. LREE/MREE ratios also increase from phase I (La_N/Sm_N 1.0−1.8) to phase V (La_N/Sm_N = 1.5−2.4) (Fig. 4.6b). This is also evident in a plot of Sm *vs*. La (Fig. 4.8), where in phases I-III the more differentiated mafic enclaves evolved to higher Sm concentrations than the host andesite (Zellmer *et al.,* 2003a). In contrast, Sm concentrations in phase V enclaves only increase weakly with increasing La, with the most evolved enclave compositions now lying within the andesite field, which is outside of analytical error (Fig. 4.8). A similar pattern is also observed for Y/La concentrations (Fig. 4.9).
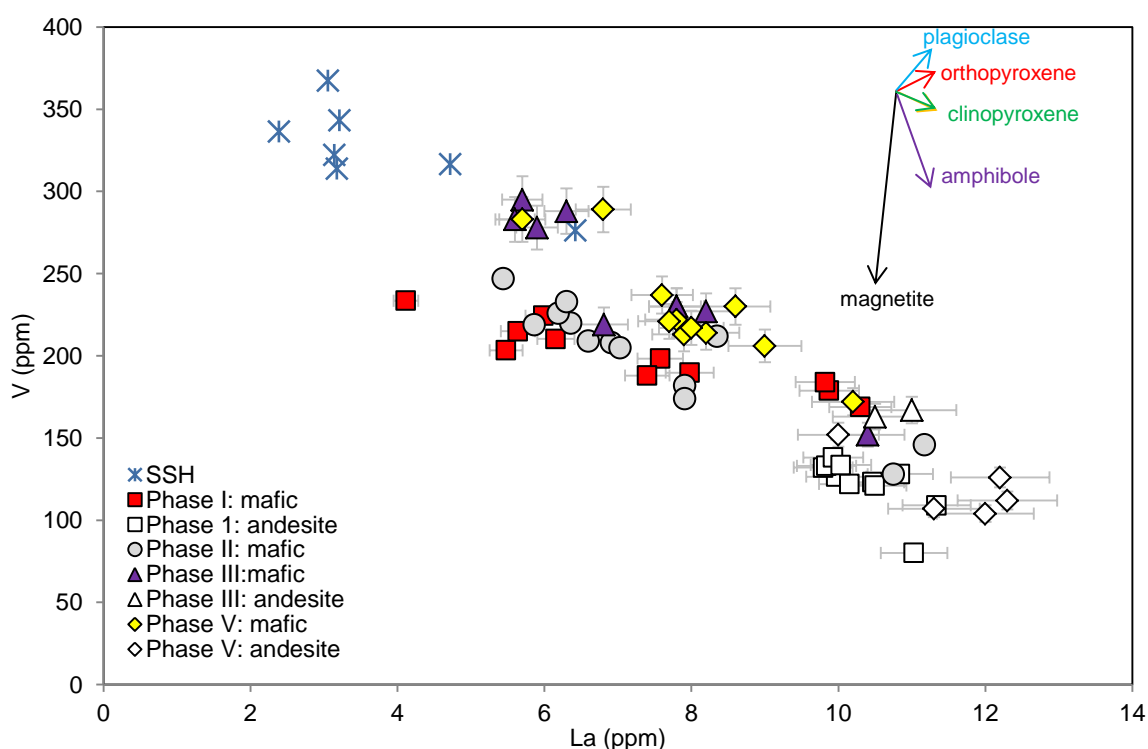
Figure 4.5: V *vs*. La; mineral vectors are indicative of 20% fractional crystallisation using partition coefficients from table 4.2. The least differentiated mafic enclave compositions of phases III and V have higher V concentrations than phases I and II, and form a steeper decreasing trend with differentiation. SSH data from Zellmer *et al.,* 2003; Cassidy *et al.*, 2012, phase I data from Zellmer *et al.,* 2003, phase II data from Mann, 2010.
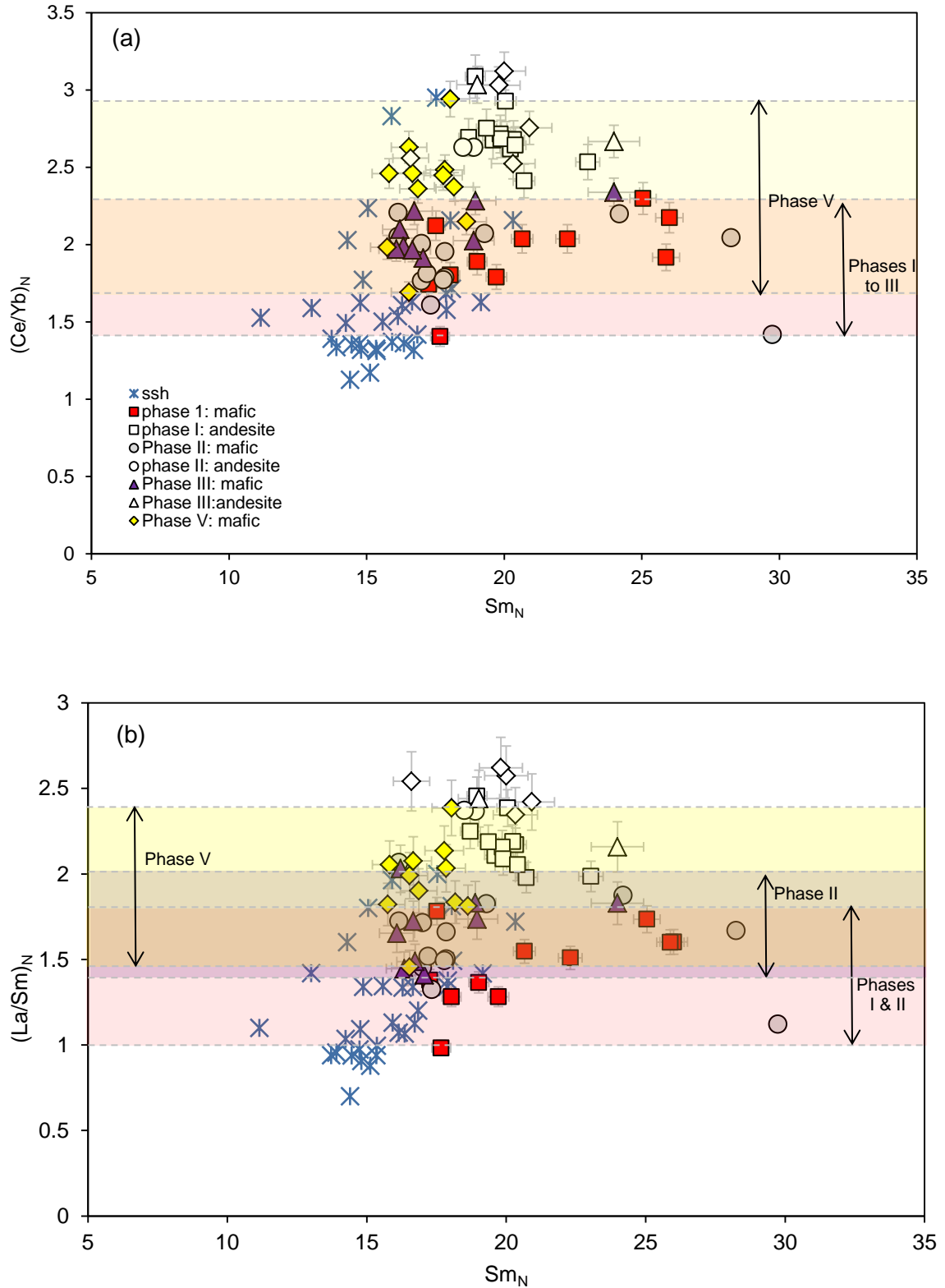
Figure 4.6: Bivariate plots examining the slopes of the REEs from all eruptive phases (a) Ce/Yb$_N$ *vs.* Sm$_N$; where Ce/Yb represents the slope of the overall slope of REE diagrams in fig. 4.4, and Sm as a measure of REE concentrations. An increase in the LREE/HREE ratios is observed in phase V from phases I to III. (b) La/Sm$_N$ *vs.* Sm$_N$; where La/Sm represents the slope of the LREE-MREEs. A progressive increase in the LREE/MREE ratios from phase I to V is observed. SSH data from Zellmer *et al.,* 2003; Cassidy *et al.*, 2012, phase I data from Zellmer *et al.,* 2003, phase II data from Mann, 2010.

The MREE-HREE concentrations are variable from phases I to III, but all plot within broadly the same field. However, phase V MREE-HREE concentrations exhibit a more pronounced trough-shaped pattern more akin to the SHV andesite patterns, and now have lower MREE-HREE concentrations than the SHV andesite from phase V (Fig. 4.3). For example, the phase V Yb_N concentrations have a lower and narrower range than earlier phases (Phase I = 12.3–19.2; phase II = 11.6–23; phase III = 10.5–17; phase V = 11.2–13.4; Fig. 4.10). To summarise, phase V mafic enclaves show higher LREE/HREE ratios, lower MREE/HREE ratios and lower MREE-HREE concentrations than earlier phases.
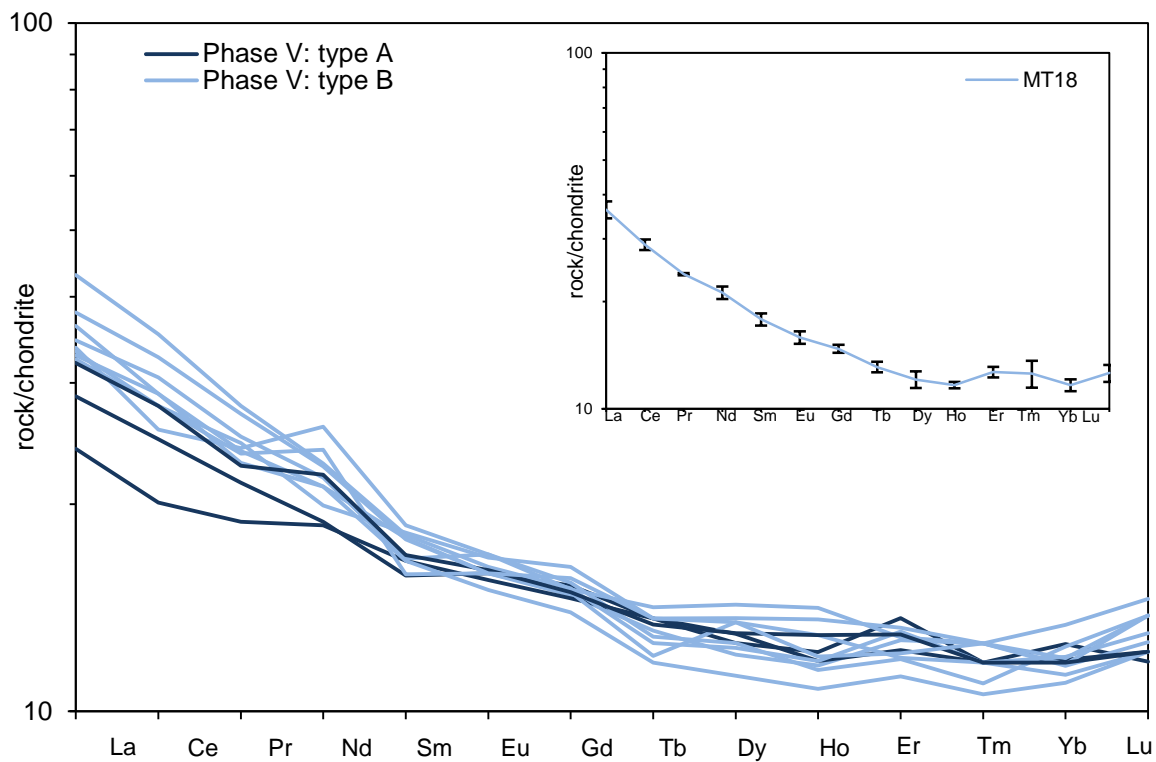
Figure 4.7: Individual sample REE patterns for phase V types A and B. Example error for phase V using an average mafic enclave composition (sample MT18) is shown in inset. Phase V samples do not display the same parallel REE patterns as phase I, with scatter in composition outside of error except for Tm and Dy.

4.3.4 Geochemical differences between phase V mafic enclave types

As presented in Chapter 3, the different enclave types (A, B and C) are also distinct in terms of bulk rock major- and trace element geochemistry, where although all enclave types fall on a single linear array with the andesite with no compositional gaps, each type plots in a distinctive field for all major elements (Chapter 3: Fig. 3.12). Type A enclaves occupy a lower SiO_2 range (49.7–52.4 wt% SiO_2) than the type B enclaves (53–58 wt% SiO_2) (Chapter 3: Fig 3.12). Type A enclaves have systematically higher compatible trace element contents (*e.g*. V, Ti), and lower incompatible trace element contents (*e.g*. Zr), than the type B enclaves (Chapter 3: Fig. 3.12).

Figure 4.8: Samarium *vs*. Lanthanum; mineral vectors are indicative of 20% fractional crystallisation using partition coefficients from table 4.2. Sm concentrations still increase with increasing La in phase V mafic enclaves, but no longer to above the SHV andesite. SSH data from Zellmer *et al.,* 2003; Cassidy *et al.*, 2012, phase I data from Zellmer *et al.,* 2003, phase II data from Mann, 2010.

Type A enclaves are depleted in LILEs such as Rb and Ba relative to type B. LREE extend to slightly higher concentrations, and MREE-HREE ratios in type A enclaves are somewhat flatter than type B (Fig. 4.7), although this is not statistically significant. This follows the pattern from the phase I enclaves of slightly more distinct trough-shaped REE patterns in the more differentiated enclaves compared with the less differentiated enclaves (Zellmer *et al.,* 2003a). Otherwise there are no significant differences in the REEs between the two enclave types. In the composite type C enclaves, where the interior portions are less evolved (52.7–55.4 wt% SiO_2) and the outer portions are more silicic (55.8–58.1 wt% SiO_2), the more mafic portion has a slightly flatter MREE-HREE ratio than the silicic portion, which is consistent with the types A and B patterns. Phase V mafic enclave glass composition data are presented in Chapter 3. To summarise, the glasses are rhyolitic (71–79 wt% SiO_2) and lie within established trends from the prior eruptive phases (Humphreys *et al.,* 2010; Murphy *et al.,* 2000). However, differences between the enclave types in K_2O, FeO and MgO are observed, and are discussed in Chapter 3.
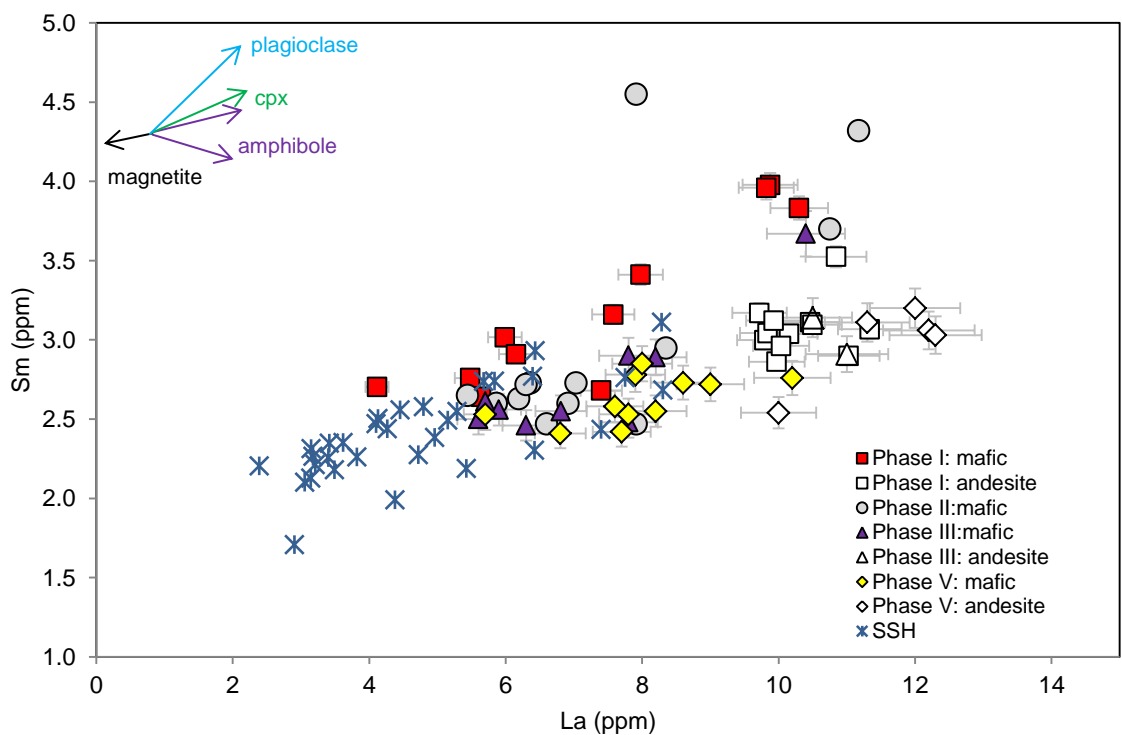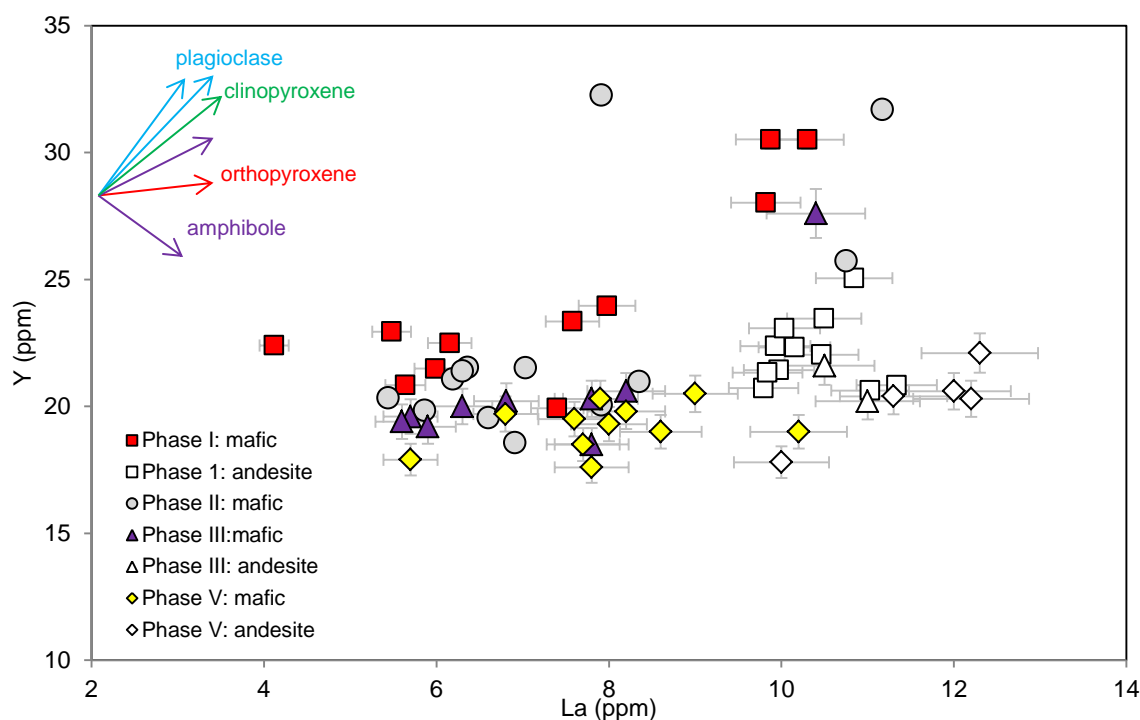

Figure 4.9: Yttrium *vs.* Lanthanum; mineral vectors are indicative of 20% fractional crystallisation using partition coefficients from table 4.2. Similar to Sm patterns in figure 4.8, Y concentrations no longer increase to above the SHV andesite. Phase I data from Zellmer *et al.,* 2003, phase II data from Mann, 2010
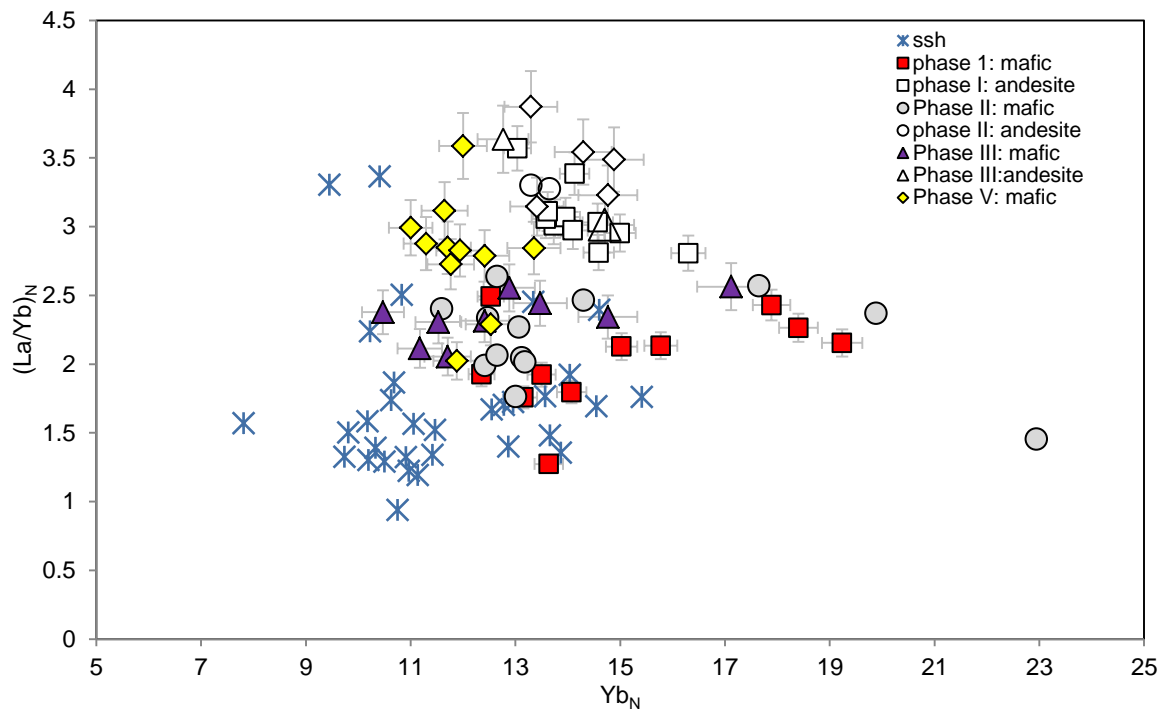
Figure 4.10: (La/Yb)$_N$ *vs.* Yb$_N$; REE data is chondrite-normalised using values from Sun & McDonough. As with Ce/Yb ratios in figure 4.5, La/Yb ratios increase from phase I to phase V. Yb values in phase V mafic enclaves no longer increase with increasing differentiation, with a considerably narrower range of concentrations than in phases I to III. SSH data from Zellmer *et al.,* 2003; Cassidy *et al.*, 2012, phase I data from Zellmer *et al.,* 2003, phase II data from Mann, 2010.

4.4 Discussion

Temporal changes in major and trace element concentrations, and REE concentrations and ratios in the mafic enclaves from phase II onwards suggest changes in the processes affecting generation and/or differentiation of the mafic enclave magma, or a change in the mixing relationship with the SHV andesite. In summary, increasing LREE/HREE ratios coupled with decreasing MREE/HREE ratios are observed in mafic enclaves from phases I to V. Parallel linear trends in the mafic enclaves between eruptive phases exist in some major elements such as FeO and MgO, but phases III and V compositions lie on the same major element trends. Clear differences in major element chemistry between the phase V enclave types are only reflected in lower LILE and higher LREE concentrations. Andesite compositions from phases I to V remain similar. Several key questions may be answered using the new trace element data presented here:

(i) Has the end-member mafic composition changed throughout the course of the eruption?

(ii) Can the range in enclave compositions be explained by fractional crystallisation, mixing or both?

(iii) Are type A and type B mafic enclave compositions (as defined in chapter 3) related by fractional crystallisation or mixing/assimilation of andesite, or do they represent distinct melts intruding the system?

(iv) Can the erupted andesite composition be explained by fractionation from PIII-V enclave composition?

4.4.1 Changes in the mafic enclave magma end-members?

An important question is whether the end-member magma compositions have changed through the course of the current eruption. On the basis of FeO and MgO data, Barclay *et al.* (2010) suggested that from phase I to III a change in the mafic magma end-member composition occurred. However, Thomas *et al.* (2014) suggest that the reduction in scatter in the composition of mafic enclaves from phases I to III in certain elements may be due to the diminishing effect of assimilation of a cumulate residue into the intruding mafic magma as the eruption progresses over time without a change in the mafic end-

member. New trace element data (*e.g.* vanadium) in this chapter as well as the parallel linear trends in major elements (e.g. MgO) between eruptive phases I-III highlight that a change in the end-member composition has occurred since phase I. This could be due to progressive deeper tapping of a single compositionally stratified mafic magma source, or perhaps evidence for different batches of mafic melt over the course of the eruption. However, the progressive change in the end-member compositions in some elements from phases I-III has halted in phase V (Fig. 4.5) suggesting that phases III and V might share a similar mafic magma source.
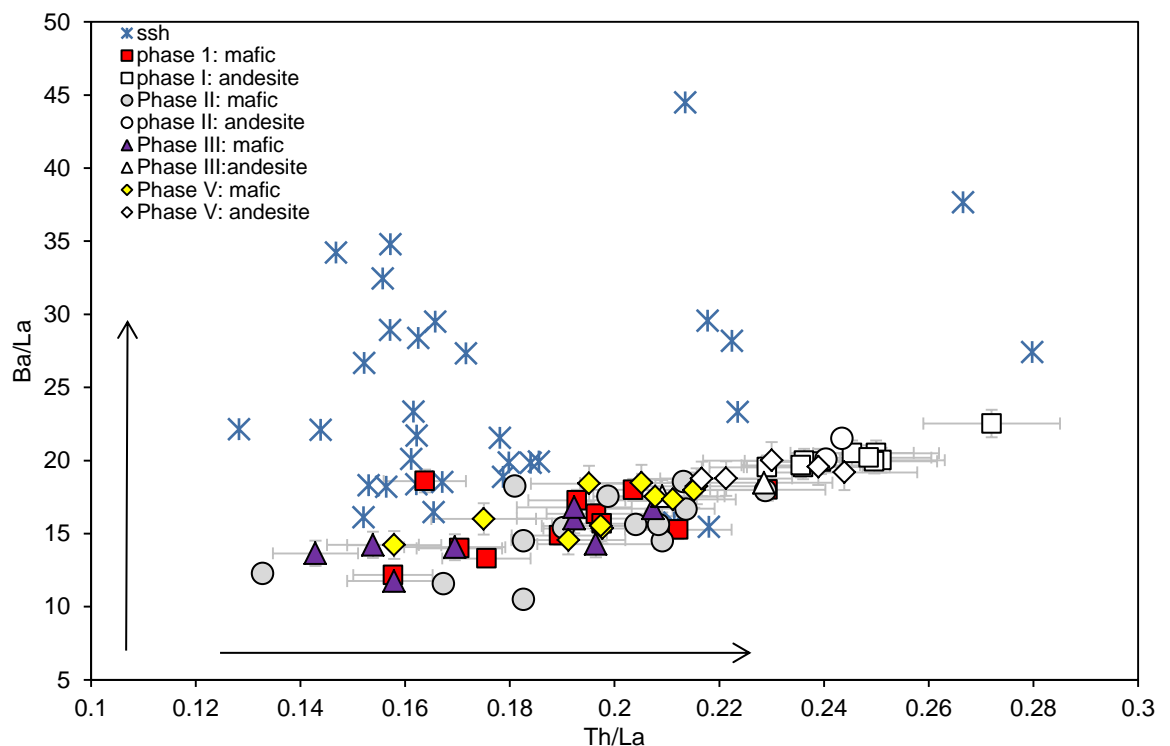
Figure 4.11: Plot of Ba/La *vs.* Th/La; ratios remain consistent across the eruptive phases indicating that there has been no change in the 'subduction component' of the parental SHV mafic magma. SSH data from Zellmer *et al.,* 2003; Cassidy *et al.*, 2012, phase I data from Zellmer *et al.,* 2003, phase II data from Mann, 2010.

The change in mafic enclave major elements concentrations from phases I-III has been suggested as perhaps a shift towards the SSH mafic compositions (Barclay *et al.,* 2010). To evaluate if there are any apparent changes in the parental magma source composition during the current eruption, similar to that of the SSH lavas, we examine the unique trace element signature of the SSH volcanics. Ba/La *vs.* Th/La ratios have been used to assess the relative effect of slab fluid *vs.* sediment addition on the erupted Montserrat products

(Cassidy *et al.,* 2012). Ba is fluid-mobile, so higher Ba/La ratios indicate a greater slab fluid contribution, as inferred for the SSH lavas (Cassidy *et al.,* 2012). Th/La in arc magmas can be additionally inherited from subducting sediment, where a relative increase or decrease of this ratio would signify a greater or lesser contribution from partial melting of sediments (Plank, 2005). Lesser Antilles sediments have Th/La of ~0.32 and the Antilles mantle <0.1, whilst the Th/La range across the Lesser Antilles arc basalts is ~0.15–0.28 reflecting different ratios of mantle to sediment component during subduction across the arc (Plank, 2005). Figure 4.11 shows that there is no apparent variation in the Ba/La and Th/La ratios of mafic enclaves during the course of the eruption. Therefore, there is no indication of a change in the parental mafic enclave magma source composition towards that of the SSH lavas, as the sediment addition/slab fluid geochemical signature remains consistent across the eruptive phases (Fig. 4.11; Cassidy *et al.,* 2012). This implies that the geochemical variations observed in the range of mafic enclave compositions across the eruptive phases may be controlled by either changes in fractionating assemblage, changing ratios of basalt to andesite mixing, or differing melts intruding the system over time.

4.4.2 Influence of fractional crystallisation on mafic enclave compositions

In this section we evaluate whether the trends in the mafic enclave compositions are controlled by fractional crystallisation, and if changes in the fractionating assemblage across the eruptive phases could be responsible for the changes observed in the mafic enclave trends. The constant U/Th ratios across all phases of the eruption (Fig. 4.4) suggest that the range of mafic enclave compositions could be controlled simply by closed-system differentiation of the magma represented by the mafic enclaves. If open-system processes were significant, we would expect to see decreasing U/Th ratios with differentiation, as observed in the SSH lavas (Fig. 4.4; Zellmer *et al.,* 2003a). Geochemical modelling of the phase I bulk mafic enclave compositions indicates that they are controlled by 70 % fractional crystallisation with ~70 % amphibole and ~30 % plagioclase (Zellmer *et al.,* 2003a). Increasing Lu/Gd and La/Gd ratios with differentiation are also cited as evidence for significant amounts of amphibole fractionation from the phase I mafic magma prior to intrusion into the andesite (Fig. 4.12; Zellmer *et al.,* 2003a). The same trend is observed in phases II-V enclave compositions (Fig. 4.12). However, several key trace element patterns

in phases III-V imply that significantly more amphibole fractionation is involved in differentiation of phase V mafic enclave magma in comparison to phases I and II: (i) a lower and narrower range in Yb_N concentrations in phase V (Fig. 4.10) coupled with the more distinctive trough-shaped REE patterns (Fig. 4.3), which are outside the range of analytical uncertainty (ii) sharply decreasing vanadium and scandium concentrations against La in phases III and V in comparison to phases I and II (Fig. 4.5) (iii) less strong Sm enrichment against increasing La concentrations in phase V (Fig. 4.8) also indicates that amphibole might have an increasing importance. A change in the extent of amphibole fractionation at depth might be caused by a number of factors. For example, small changes in the activity of H_2O in the melt, caused by increased H_2O in primary melts from the mantle wedge, or changes in the composition of co-existing vapour (in terms of H_2O/CO_2) can lead to increased amphibole and oxide fractionation. An increase in the apparent degree of amphibole fractionation between phases I-II and III-V further implies that the mafic magma end-member composition may have changed. We assess whether fractional crystallisation is still the dominant control on mafic enclave bulk compositions, and to what degree the fractional crystallisation model applied to the phase I enclaves is required to change in the latter phases.
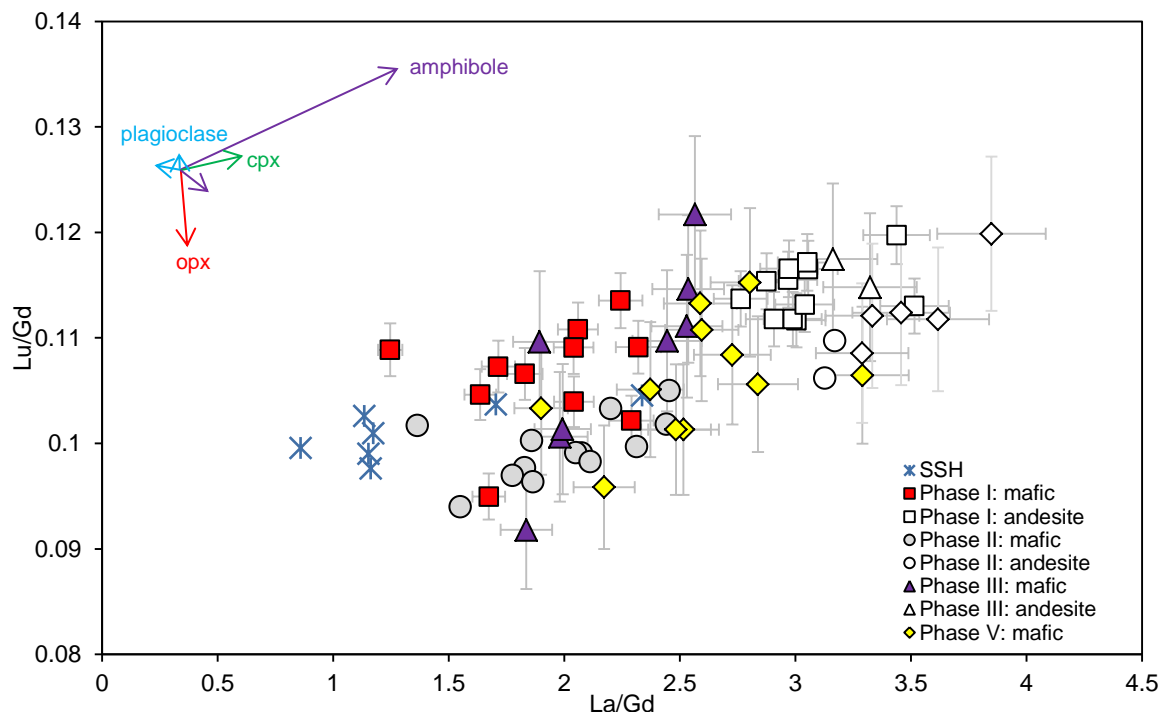
Figure 4.12: Lu/Gd *vs.* La/Gd; mineral vectors indicate 20 % fractional crystallisation using partition coefficients from table 4.2 SSH data from Zellmer *et al.,* 2003; Cassidy *et al.*, 2012, phase I data from Zellmer *et al.,* 2003, phase II data from Mann, 2010.

4.4.2.1 Phase III

The differentiation trends in phase III are first examined using the method described in section 4.2.1 to assess whether the trends are controlled by fractional crystallisation. Sample (MO08) is the least evolved composition (C_O) on the basis of SiO$_2$, and sample (MO01) the most evolved mafic enclave composition (C_L) from phase III. Assuming Th is perfectly incompatible, the calculated fraction of melt remaining, F_{Th}, is 0.54. Using this value of F to calculate the remaining bulk partition coefficients D_i^{rel} yields negative values for uranium and barium (Table 4.3). The least evolved end-member sample (MO08) has an unusually low uranium content of 0.1 ppm, and therefore with a detection limit of 0.1, the negative value is within error. On the other hand, the negative D value for barium may simply be the result of anomalously low Ba value (67 ppm) for MO08 in comparison to other similar mafic enclave compositions (~80 ppm). This may suggest that the selection of end-member is incorrect, but trying other different potential end-member samples, such as MO14 did not solve the problem, and actually yielded a greater number of negative D calculated values.
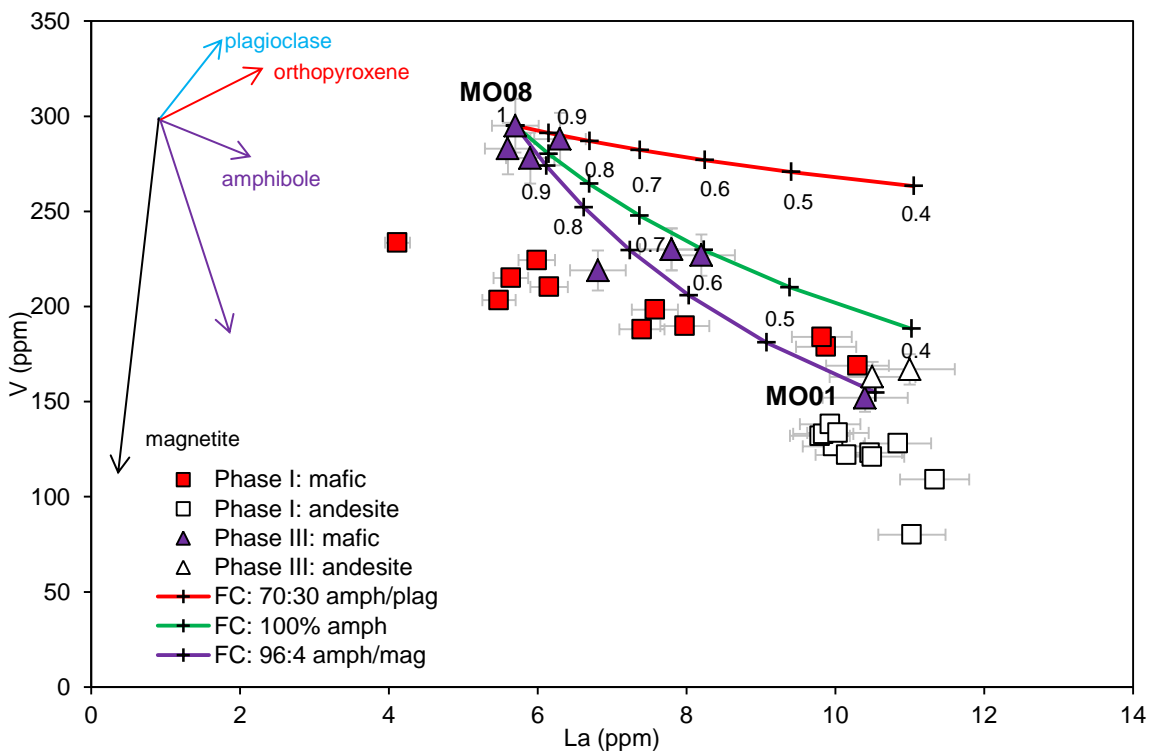
Figure 4.13: Samarium *vs.* Lanthanum phase III model; fractional crystallisation model using 70 % amphibole and 30 % plagioclase, 65:35 amphibole/plagioclase and 75:35 amphibole/plagioclase for Phase III mafic enclave compositions. Mineral vectors indicate 20 % fractional crystallisation.

Although the REE concentrations in phase III are lower than in phase I, forward modelling of the phase III data with 60% fractional crystallisation, using a 70:30 ratio of amphibole:plagioclase fits the range of mafic enclave REEs concentrations well in phase III (Fig. 4.13), although there is significant scatter to higher La contents for a given Sm concentration (Fig. 4.13). However, for certain elements (V and Sc) the 70:30 amphibole:plagioclase model fits poorly. This can be seen in the vanadium *vs.* lanthanum plot; the FC model cannot match the steep decrease in V with increasing La unless fractionation involves at least 96 % amphibole and 4 % magnetite (Fig. 4.14), which is not physically reasonable given the observed mineral assemblages in the enclaves (Chapter 3). This suggests that a change in enclave petrogenesis has taken place in phase III.
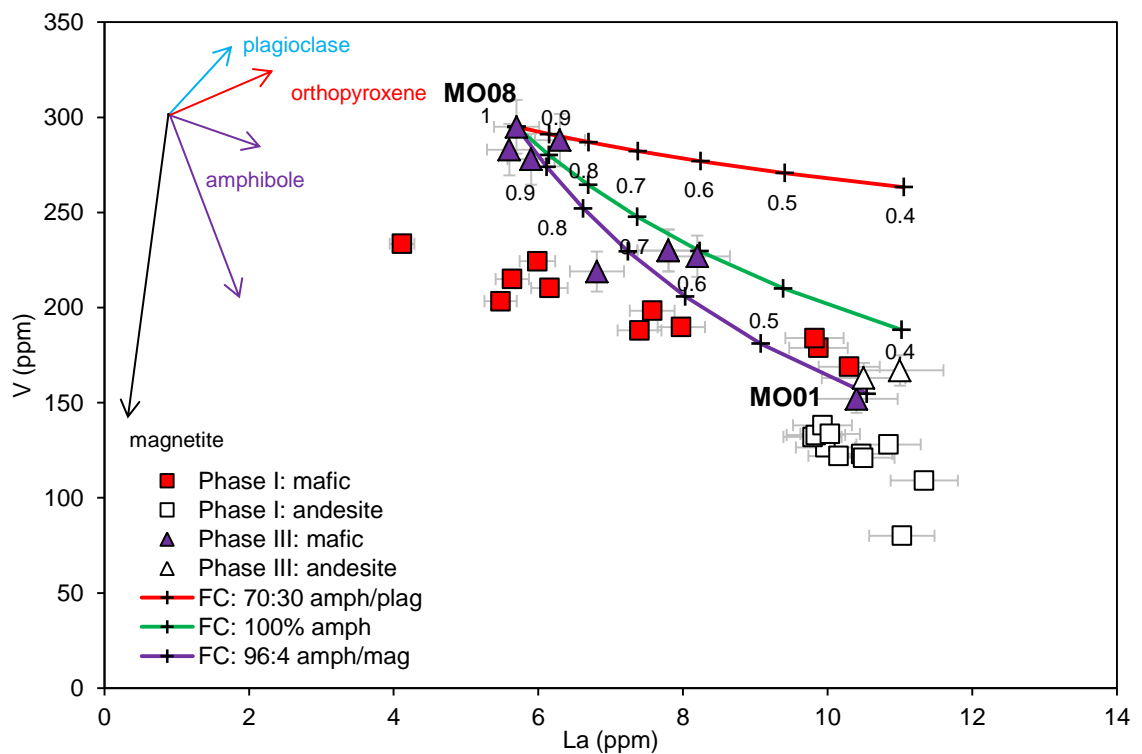
Figure 4.14: Vanadium *vs.* Lanthanum phase III FC models; the introduction of more amphibole (~25 %) and minor magnetite into the crystallising assemblage is needed to fit the phase III mafic enclave trends. Mineral vectors indicate 20 % FC. Phase I data from Zellmer *et al.,* 2003a.

4.4.2.2 *Generation of distinct phase V mafic enclave types*

A novel contribution has been the identification of texturally and petrologically distinct types of enclaves erupted in phase V. An important question is whether these different end-member types could be geochemically related to one another by fractional
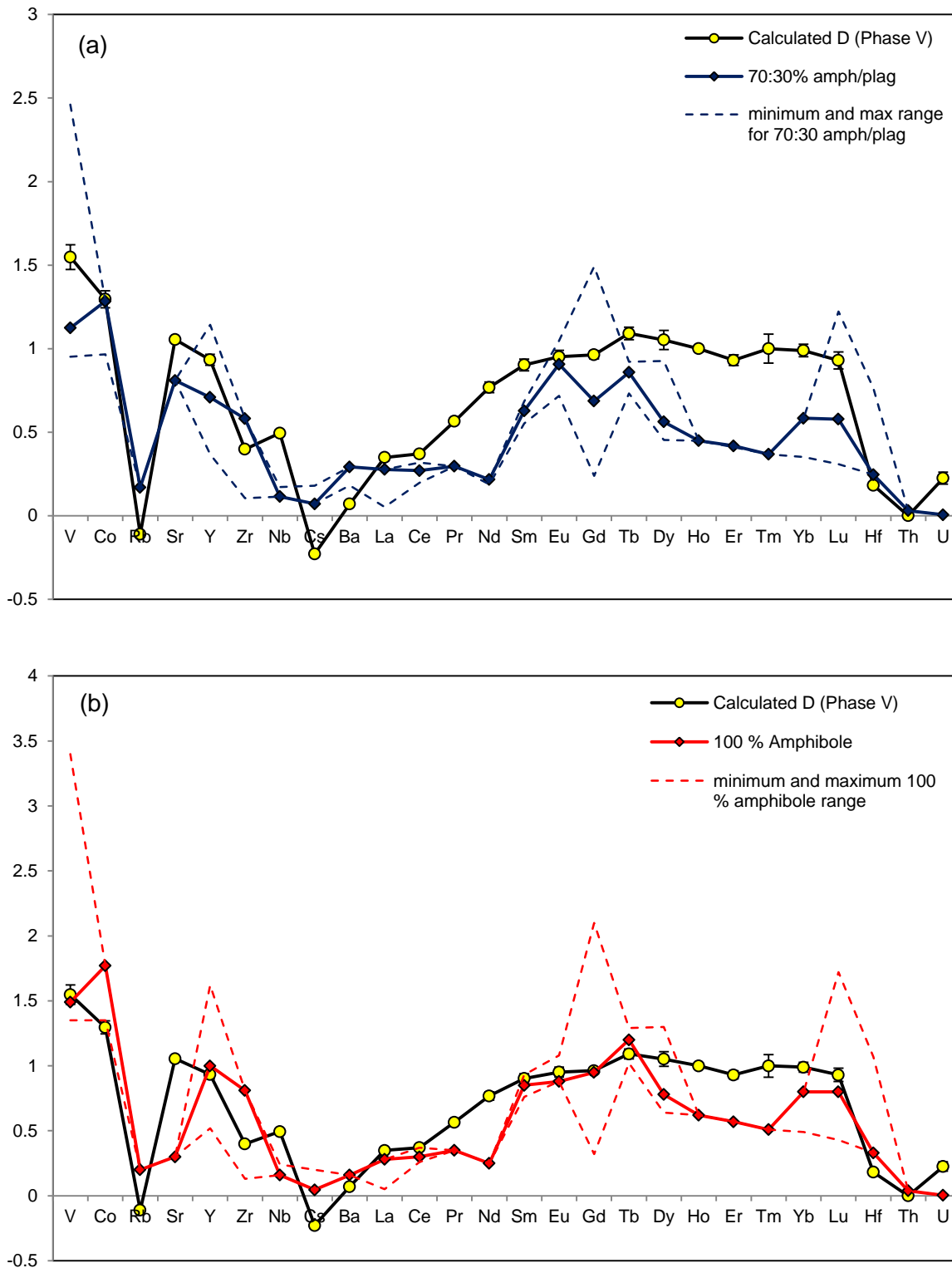
Figure 4.15: Comparison of calculated trace element D values against forward modelling D values. Calculated D values are from table 4.3 (error is from table 4.1). Minimum and maximum range of D values used is also shown using the partition coefficients from table 4.2. (a) FC model using 70% amphibole and 30 % plagioclase; model is a poor fit for most REE data. (b) FC model using 100 % amphibole; model is a better fit, but still outside of error for some elements.

crystallisation (FC), or whether they are derived from different parental sources, or by different degrees of hybridisation (see later). The shift in REE patterns in phase V and the crossover of individual sample REE patterns in the phase V mafic enclave compositions (Fig. 4.7) is inconsistent with fractionation controlling differentiation trends between the enclave types. Testing whether types A and B enclaves in phase V are related by fractional crystallisation uses the type A end-member (MT27) and type B end-member (MT25). The same fractional crystallisation modelling outlined earlier was used to calculate $F = 0.41$ for $D_{Th} = 0$ (Table 4.3). Using this value of F to calculate the remaining bulk partition coefficients D_i^{rel} yields negative values for Rb and Cs (Table 4.3). The resulting bulk partition coefficients for each element are then inverted to calculate fractionating mineral proportions (Fig. 4.15). An indication of errors in the modelling is given by the maximum and minimum values of D_i, calculated by the range of D_i^j in table 4.2 (Fig. 4.15).
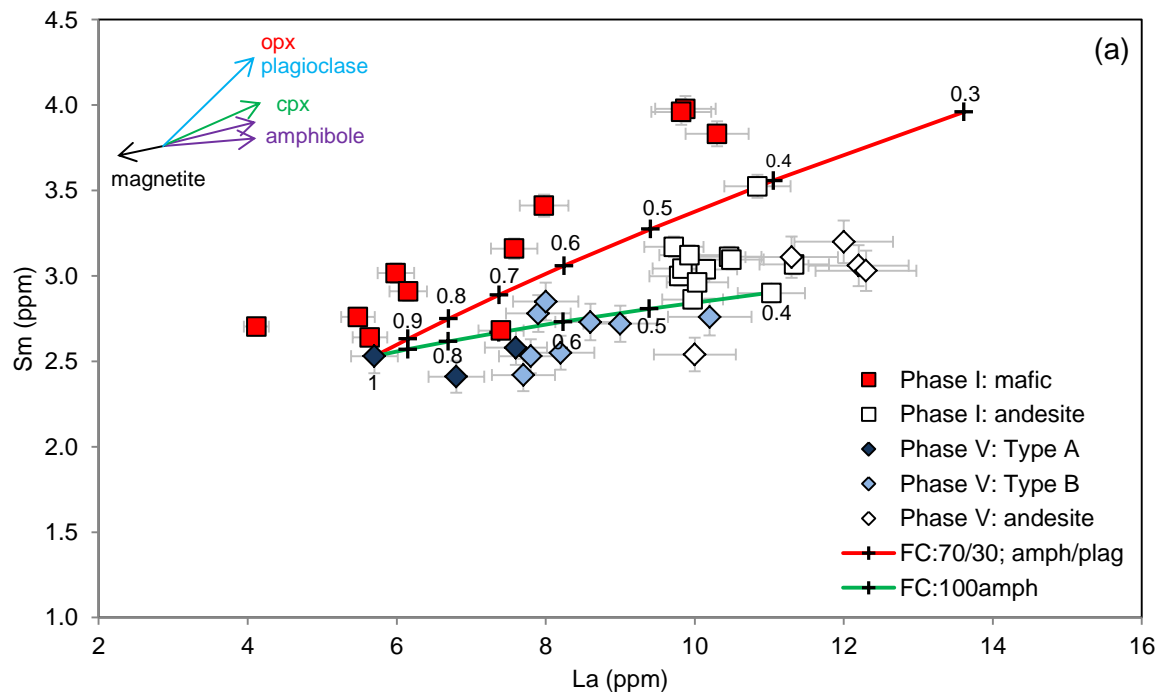
Figure 4.16: Phase V fractional crystallisation models using 70 % amphibole:30 % plagioclase, and 100 % amphibole (a) Samarium *vs.* Lanthanum; the 100 % amphibole FC model proves a better fit than the 70/30 amphibole/plagioclase model applied to phase I enclaves. Continued on next page.
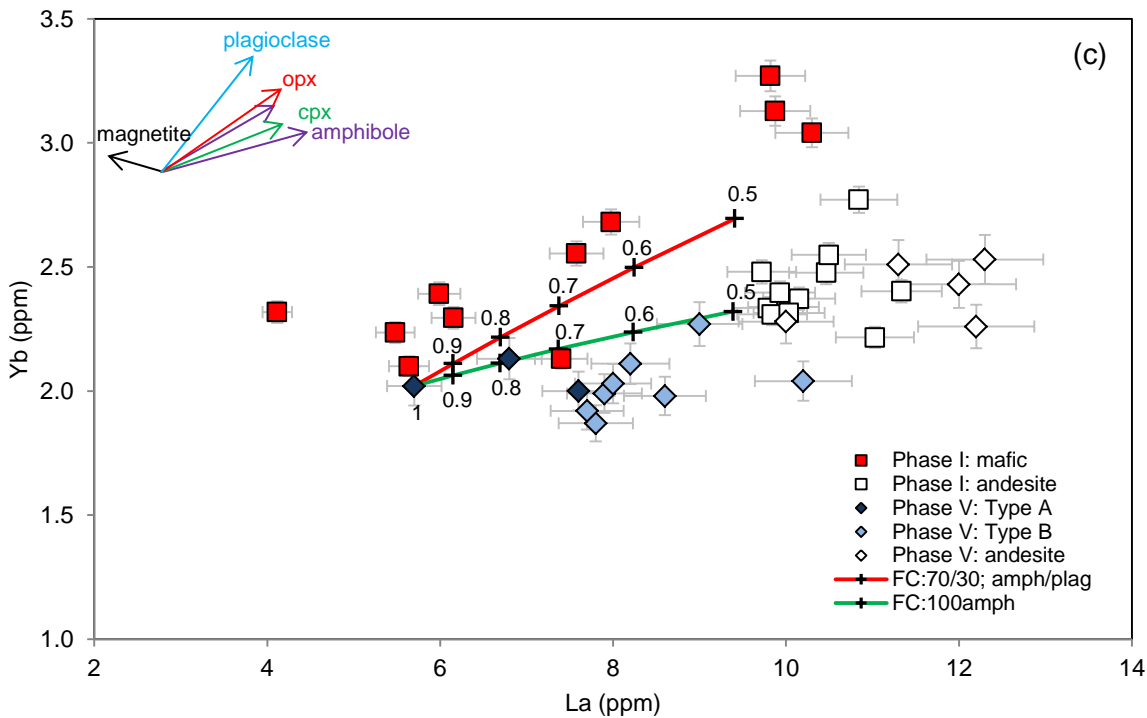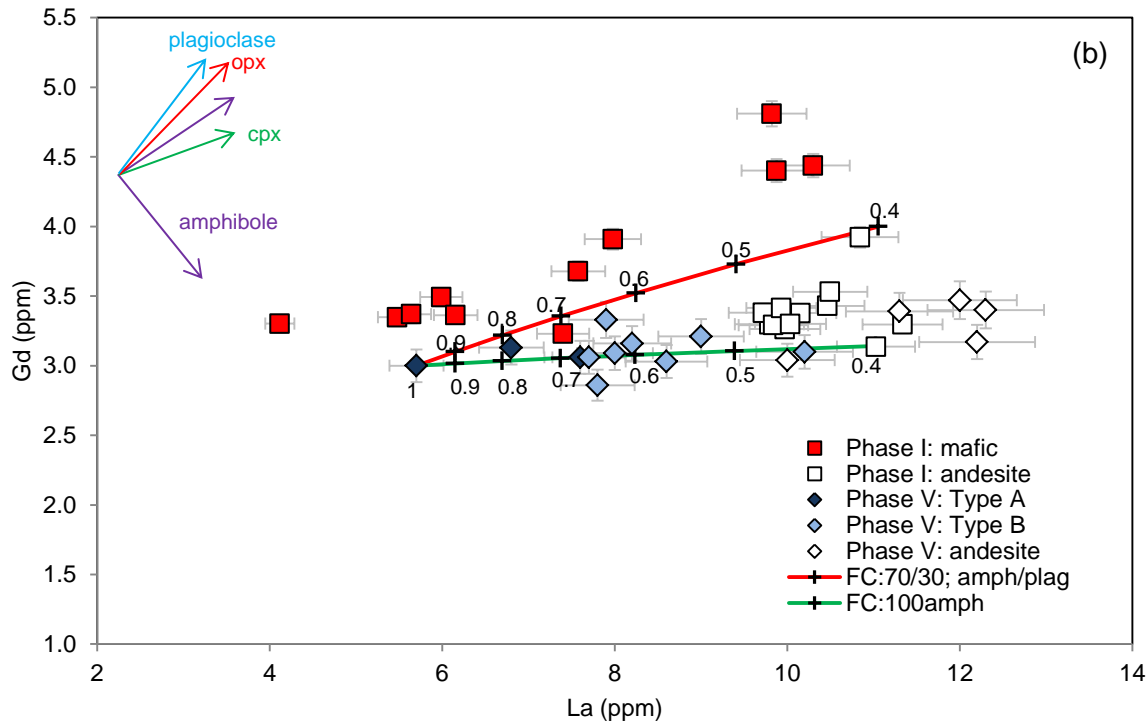
Figure 4.16: Phase V fractional crystallisation models using 70 % amphibole:30 % plagioclase, and 100 % amphibole (a) Samarium *vs.* Lanthanum; the 100 % amphibole FC model proves a better fit than the 70/30 amphibole/plagioclase model applied to phase I enclaves (b) Gadolinium *vs.* Lanthanum; the 100 % amphibole FC model fits the phase V enclave data well (c) Ytterbium *vs.* Lanthanum; the 100 % amphibole FC model does not fit the phase V enclave trend well, but is a better fit than the 70/30 amphibole/plagioclase model. Phase I data from Zellmer *et al.,* 2003.
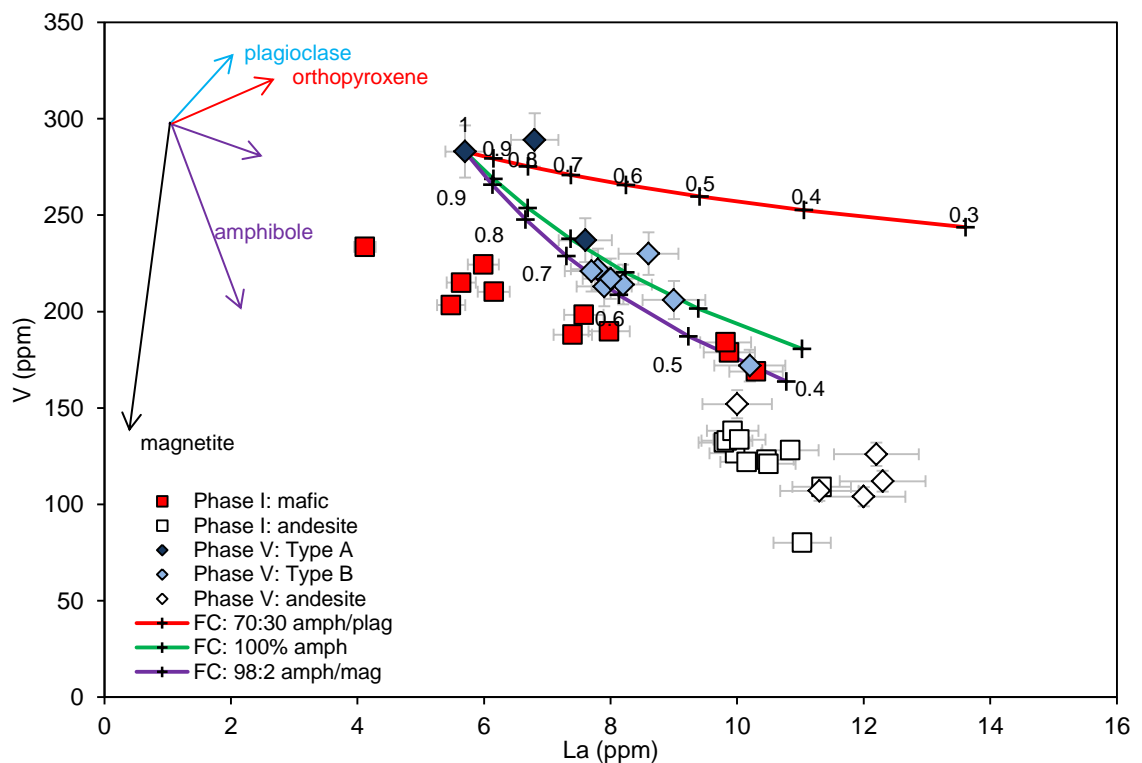
Figure 4.17: Vanadium *vs.* Lanthanum phase V FC modelling; mineral vectors are indicative of 20 % FC. The phase I model does not fit the phase V enclave trends, instead again an increase of amphibole is required to reproduce the trends. The addition of minor magnetite provides a slightly better fit between the type A end-member and type B end-member. Phase I data from Zellmer *et al.,* 2003.

The calculations show that the fractional crystallisation model cannot explain the full range of phase V mafic enclave compositions, in particular LREE and MREE (Fig. 4.15; Table 4.3). Forward modelling of the mineral proportions demonstrate that a 70:30 amphibole:plagioclase ratio will not fit the REE trends (Fig. 4.16), unlike the earlier phases. In the Sm *vs.* La plot (Fig. 4.16) it could be argued that a different end-member starting composition could reproduce the phase I model, but this is only limited to Sm. Close to 100% amphibole fractionation could reproduce most type B LREE-MREE compositions from type A by fractional crystallisation (Fig. 4.16), but this cannot account for the HREE data, as seen in the Yb *vs.* La plot (Fig. 4.16, Fig. 4.15). If we compare the forward-modelled D_i^j to the calculated D_i^{rel}, increasing amphibole fractionation to 100 % fits to many of the D_i^{rel} calculated, but that some elements such as Sr, Nd, Ho, Er remain outside of the modelled range (Fig. 4.15). Furthermore, this interpretation does not fit with other trace element trends such as V *vs.* La, which indicate as with the phase III mafic enclave trends that minor magnetite may also have been fractionated (Fig. 4.17). To reproduce

those trace element concentrations by fractional crystallisation, the crystallising assemblage is required to be ~98 % amphibole, ~2% magnetite (Fig. 4.17). However, the introduction of magnetite into the fractionating assemblage then provides a poorer match for the REE patterns. These results imply that simple fractional crystallisation cannot link type A and B phase V enclaves.

4.4.3   Influence of andesite on phase V mafic enclave compositions

The presence of inherited phenocrysts from the andesite in the mafic enclaves in all eruptive phases (Murphy *et al.,* 2000; Zellmer *et al.,* 2003a; Barclay *et al.,* 2010; Humphreys *et al.,* 2009; Mann 2010) is irrefutable evidence that mixing between the mafic and andesitic magmas has occurred. However, mixing between the andesitic and mafic enclave magmas in phase I cannot explain the trends in mafic enclave compositions, because the mafic enclave and andesite compositions are not co-linear in certain elements such as Sm, Y and V (Figs. 4.1, 4.5, 4.8 and 4.9). In phase V, the enclaves and andesite are co-linear, apparently as a result of the lower MREE and higher V, Sc concentrations of the enclaves (*e.g.* Fig. 4.5, Fig. 4.8). In phases II and III, some enclaves plot on the Sm-enriched trend from phase I, but others fall on the co-linear trend from phase V. Mann (2010) suggests that a mix of 58 % of the least evolved phase II mafic enclave composition and 42 % host andesite can produce a hybrid composition (54 wt% SiO_2) after differentiation. In phase V, the disappearance of the compositional SiO_2 gap between the andesite and the mafic enclave compositions, suggests that the andesite might exert a control on at least the most evolved mafic enclave compositions (type B). Additionally, the linear trends between the mafic and andesite compositions in REEs such as Sm and Gd (Fig. 4.15) present in phase V might be influenced by greater mixing between the two magmas. In section 4.4.2 FC modelling could not adequately explain all of the geochemical trends in phase V and III, and therefore the influence of magma mixing needs to be constrained and assessed in phase V and III.

The model was used first to evaluate whether type B enclave compositions may be reproduced by mixing between phase V type A end-member and the andesite. Major element mixing of 33% mafic and 67% andesite, using the type A end-member composition (MT27) and the andesite end-member composition (MVO1538-b), achieves the most evolved type B (MT25) composition, with a relatively good fit with a (Σr^2) 0.2 for
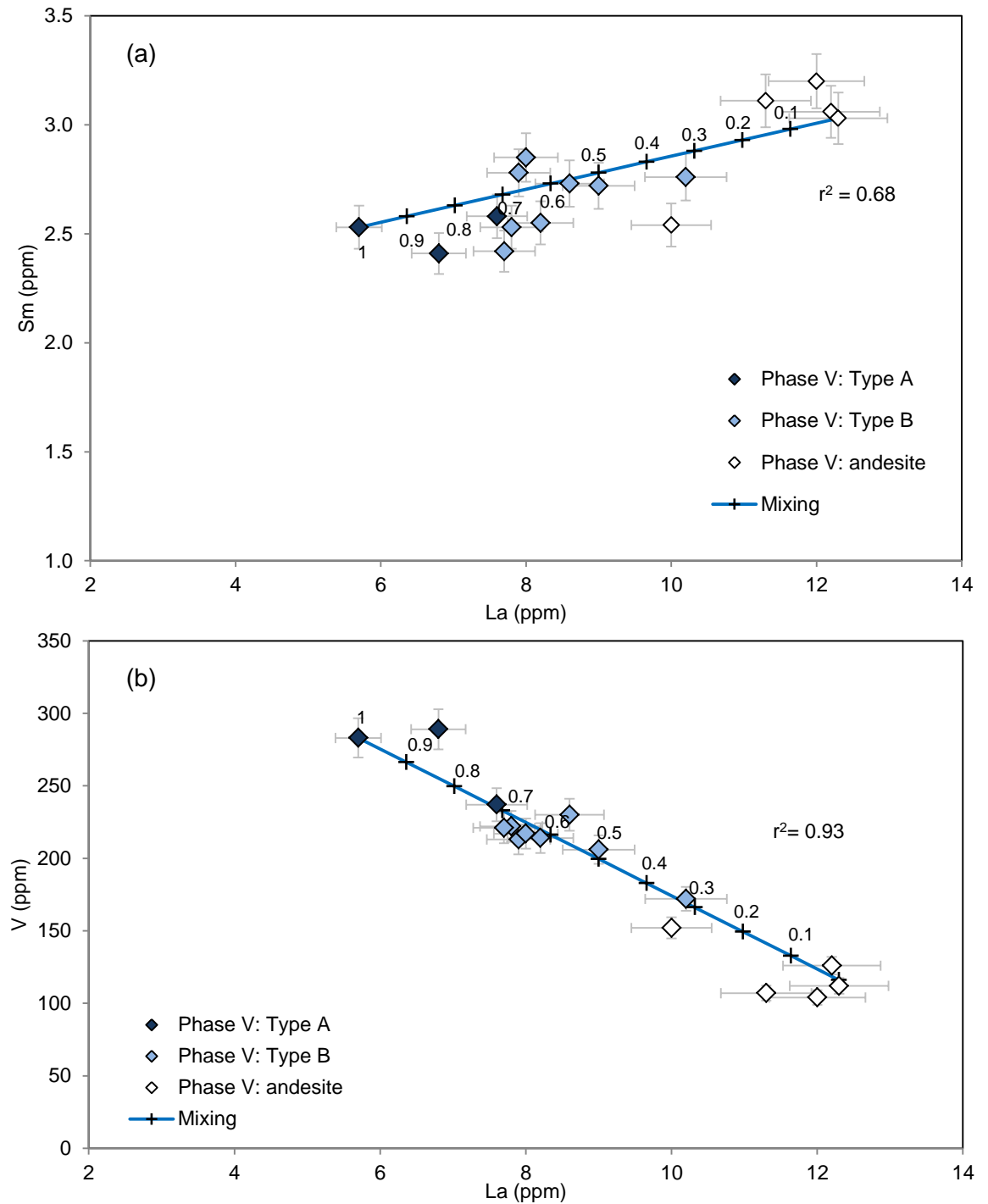
Figure 4.18: Phase V mixing models; (a) Samarium *vs.* Lanthanum (b) Vanadium *vs.* Lanthanum. Mixing lines represent mixing between phase V mafic end-member (MT27) and andesite (MVO1538b). To reproduce phase V type B end-member 67 % andesite and 33 % mafic magma is modelled. (continued on next page)
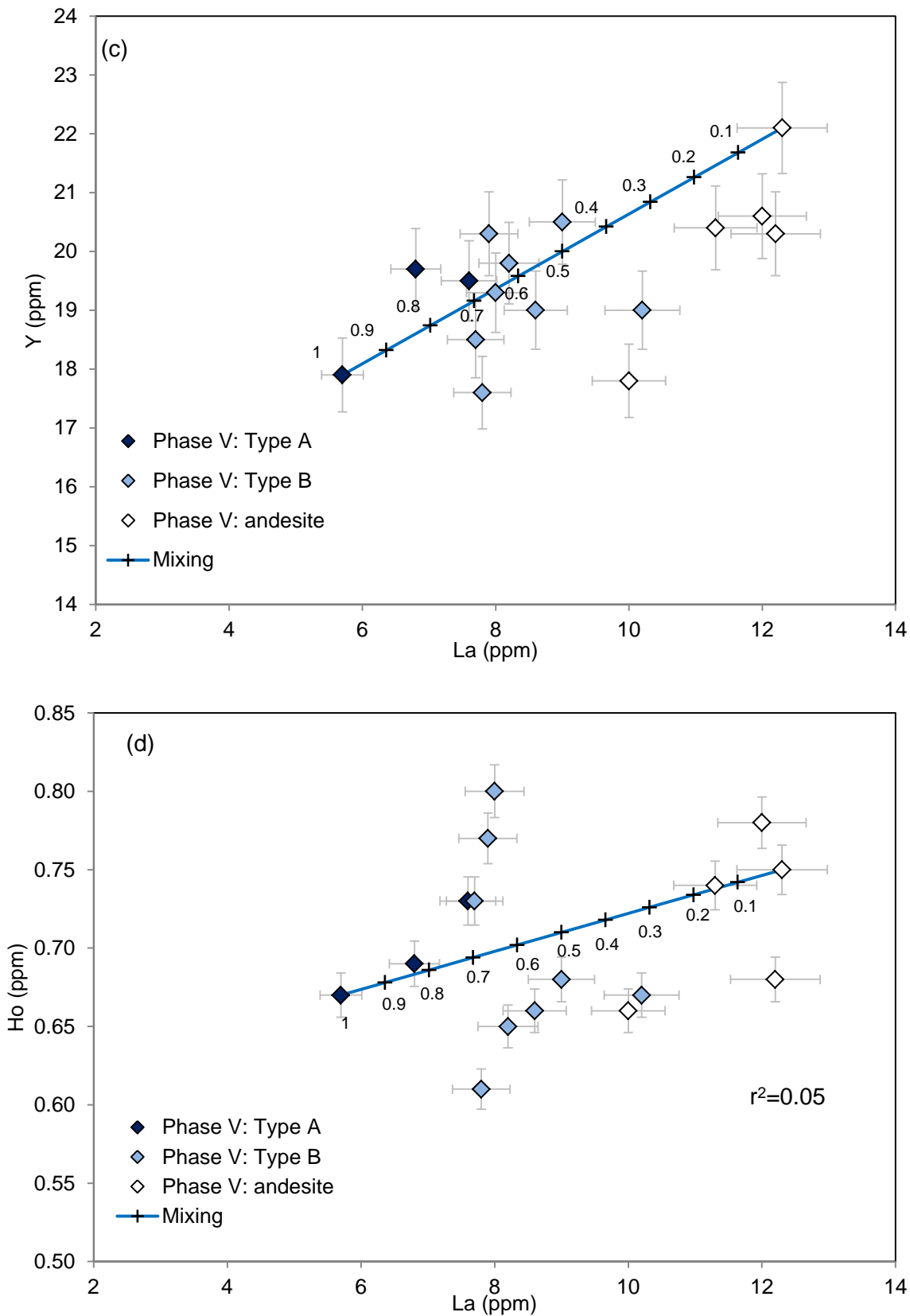
Figure 4.18: Phase V mixing models; (c) Y *vs.* La; R^2 value indicates that mixing is less good, and is outside of analytical error. (d) Ho *vs.* La: mixing between the mafic magma and andesite is poor for this element, indicated by the low R^2 value, and is outside of analytical error.

all trace elements. (Table 4.4; Fig. 4.18). Major element fits are also good, as expected given that the major element trends between types A, B and the andesite are linear (Fig. 3.9). Linear regression modelling of the entire compositional range between the phase V andesite and least evolved mafic composition was also carried out for all trace elements, using La as a differentiation index (*e.g.* Fig. 4.18). R^2 values for all trace elements are calculated from the lines of best-fit for mixing between the andesite and mafic compositions and are summarised in figure 4.19. Analysis of the R^2 data in figure 4.19 shows that for the phase V data range certain elements such as V, Ba and Zr have high R^2 values, whilst some of the REEs such as Ho have extremely low R^2 values indicating mixing is poor fit for those data. This is a result of strong scatter in these elements (Fig. 4.18d). The mixing calculations show that a high percentage of andesite (67%) is required to achieve the most evolved Type B composition. This is qualitatively consistent with the observed high percentage of inherited phenocrysts (15–25 %), and undoubtedly a proportion of rhyolitic melt from the andesite must have been mixed into the mafic magma during phenocryst incorporation. If the mafic enclave starting composition were the most evolved type A, this would then require at least 40 % melt from the andesite to be mixed into the mafic enclave magma to produce the most evolved type B composition. The equivalent treatment of phase III enclaves provides very similar results to phase V (Fig. 4.40), given the close correspondence of major and trace element compositions to phase V this is unsurprising.

Overall the calculations demonstrate that a mixing model gives a good match to the major element trends between the phase V andesite and mafic magma, and certain trace element trends, such as vanadium, La and Sm also fit with a mixing model. However, other trace element data such as Ho and Y (Fig. 4.18b,c) with a higher degree of scatter fit a mixing model less well. It seems likely that the geochemical trends cannot be explained by one simple model and that the degree of scatter in some elements could reflect multiple processes such as concurrent fractionation and mixing. In conclusion, phase V enclave types A and B bulk compositions are simply related and controlled by differing degrees of mixing between the andesite and a mafic magma end-member, with fractional crystallisation exerting a weaker influence on the range of enclave bulk compositions than in prior extrusive phases.
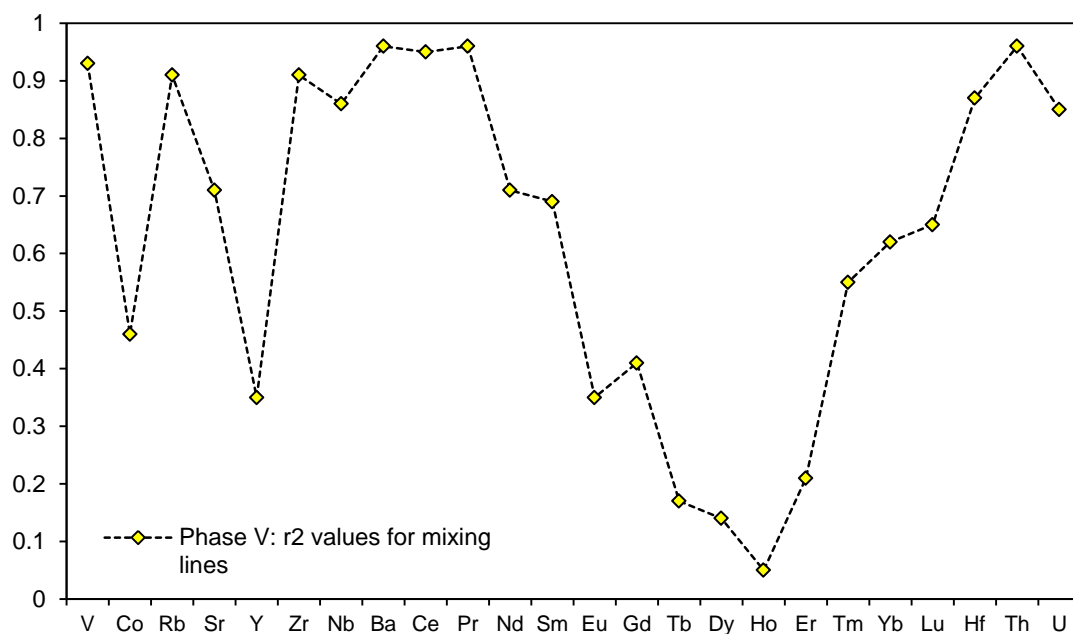
Figure 4.19: Summary of r^2 values for best-fit mixing lines between all phase V mafic enclaves and andesite data (see fig. 4.18 for example mixing lines) where La is used on the x-axis as independent variable as in figure 4.18. Standard deviation errors from table 4.3 are shown. R^2 values are variable with REEs in particular showing lowing r^2 values.

Another question is whether the resulting range of phase III-V enclave compositions are simply the result of mafic enclave magma from the earlier phases (I-II) mixing with the andesite. To test this mafic enclave magma end-members from phases I-II were mixed with the andesite to see if the phase V enclave compositions could be reproduced. We found that phases I and II mafic end-members cannot generate the range of phase V enclave compositions when mixed with the andesite in a number of major and trace elements. We conclude that the range of phase V enclave compositions is unlikely to be the result of mixing between the earlier mafic enclaves and the andesite adding further evidence that the PIII-V mafic end-member magma has changed from phases I-II.

Table 4.4: *Mixing calculations between phase V type A enclaves and andesite*

	Type A end-member (MT27)	Andesite end-member (MVO1538-b)	Type B end-member (mt25b)	Calculated	Residuals
SiO$_2$	49.72	60.96	57.32	57.38	-0.06
TiO$_2$	0.88	0.58	0.66	0.68	-0.02
Al$_2$O$_3$	20.16	17.36	18.55	18.27	0.28
Fe$_2$O$_3$	9.12	6.99	7.54	7.68	-0.14
MnO	0.16	0.18	0.17	0.17	0.00
MgO	5.65	2.63	3.36	3.60	-0.25
CaO	11.16	6.80	8.16	8.21	-0.05
Na$_2$O	2.72	3.58	3.50	3.31	0.19
K$_2$O	0.41	0.90	0.74	0.75	0.00
			Type A	*33 %*	
			Andesite	*67 %*	
			r^2	*0.99*	
			Σr^2	*0.20*	
V	283	112	185	182.63	-5.25
Co	31.4	18.6	24.1	23.86	-1.04
Ga	19.2	16.6	17.6	17.45	0.01
Rb	6	18.3	16.2	16.07	-1.83
Sr	319.1	294.7	303.9	299.96	2.79
Y	17.9	22.1	19	18.83	1.88
Zr	51.4	102.1	88	86.92	-1.55
Nb	1.4	2.8	2.2	2.25	0.09
Cs	0.2	0.5	0.6	0.67	-0.27
Ba	81	236	186	183.62	1.23
La	5.7	12.3	10.2	10.15	-0.02
Ce	12.3	27.6	21.6	21.40	1.15
Pr	1.79	3.32	2.64	2.69	0.13
Nd	8.7	14.9	10.7	10.64	2.21
Sm	2.53	3.03	2.76	2.81	0.06
Eu	0.9	1.07	0.94	1.01	0.00
Gd	3	3.4	3.1	3.14	0.13
Tb	0.51	0.55	0.47	0.55	-0.01
Dy	3.29	3.75	3.14	3.18	0.42
Ho	0.67	0.75	0.67	0.74	-0.02
Er	2.03	2.41	2.16	2.21	0.07
Tm	0.3	0.36	0.3	0.38	-0.04
Yb	2.02	2.53	2.04	2.09	0.27
Lu	0.31	0.38	0.33	0.41	-0.05
Hf	1.3	2.9	2.7	2.75	-0.37
Th	0.9	3	2.2	2.25	0.05
U	0.3	0.8	0.6	0.67	-0.04
			r^2	*0.99*	

4.4.3.1 Modelling the effect of contamination by inherited phenocrysts

As stated earlier, the presence of the inherited phenocrysts in the mafic enclaves is a clear indication that even the most primitive mafic enclave compositions are effectively a hybrid between the parental mafic enclave magma and the SHV andesite. Differing modal proportions of inherited phenocrysts incorporated into the mafic enclaves may also potentially cause a degree of scatter in the linear trends; for example, Lu/Gd and La/Gd values are strongly affected by amphibole fractionation, so mixing in different proportions of inherited amphibole phenocrysts to the mafic enclaves could therefore affect these ratios observed in the mafic enclaves. To establish the effect of the inherited phenocryst population (amphibole, plagioclase and orthopyroxene) on the phase V enclave bulk trace element compositions, modal proportions (Table 3.3, chapter 3) were subtracted from the bulk composition, using mineral-melt partition coefficients D_i^j, to derive an initial melt composition:

$$C_i^{rock} = \left(\emptyset^{opx} C_i^{opx} \right) + \left(\emptyset^{plag} C_i^{plag} \right) + \left(\emptyset^{amp} C_i^{amp} \right) + \left(\emptyset^{gm} C_i^{gm} \right) \qquad [5]$$

where, C_i^{rock} is the bulk element composition, $\emptyset^{min}$ is the phenocryst modal proportion, C_i^{min} is the element composition for that mineral using D_i^j from table 4.2., where hornblende D_i^j are used in these calculations, $\emptyset^{gm} C_i^{gm}$ is the remaining groundmass and melt composition. It should be noted that this method does not take into account any andesite melt that may also may have been incorporated into the enclaves, and assumes that the phenocrysts are evenly dispersed and homogeneously distributed. The gap in the modal proportions of inherited phenocrysts between types A and B from eruptive phase V is one of the parameters used to define the differing enclave types (see chapter 3). Therefore by removing the inherited phenocrysts, we can assess the degree to which the type B bulk compositions are controlled by mixing with the andesite, and if types A and B really have distinct end-members. Removing the relatively small fraction of inherited phenocrysts (0–8%) in type A enclaves leads to compositions that are only slightly more primitive (*e.g.* Fig. 4.21); these compositions still do not plot inside the range of phase I enclaves in terms of elements such as V and Sc (Fig 4.21). This suggests that phase V type A enclave magma is an end-member distinct from that erupted in phase I. The removal of the larger fraction of inherited phenocrysts from type B enclaves has a more pronounced
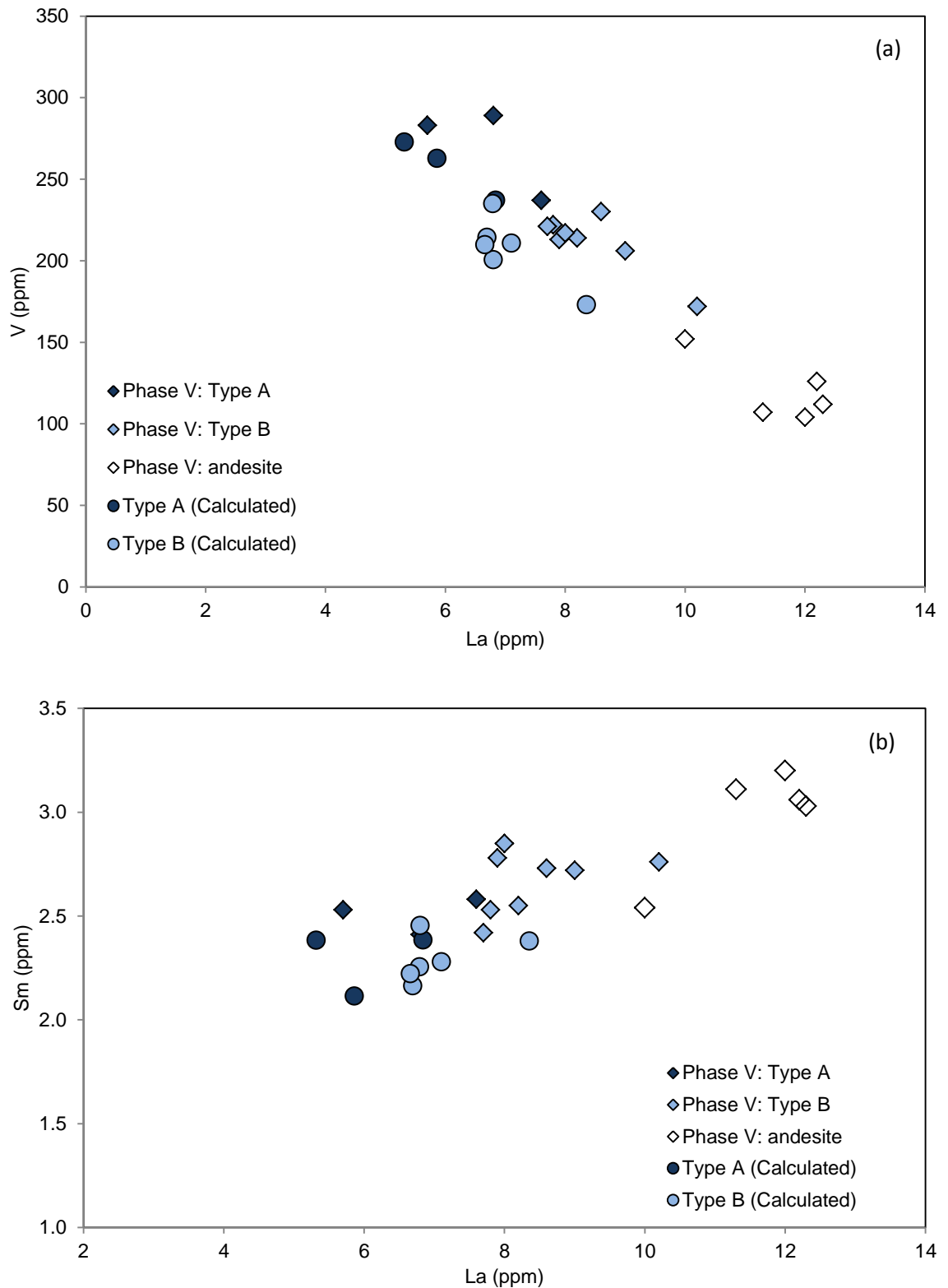
Figure 4.20: Phase III mixing models; (a) Sm vs. La (b) V vs. La. Mixing lines represent mixing between phase III mafic end-member (MO08) and andesite (MO10). Mixing lines fit well for V, but have a slightly less good fit for Sm, similar to phase V enclave trends.
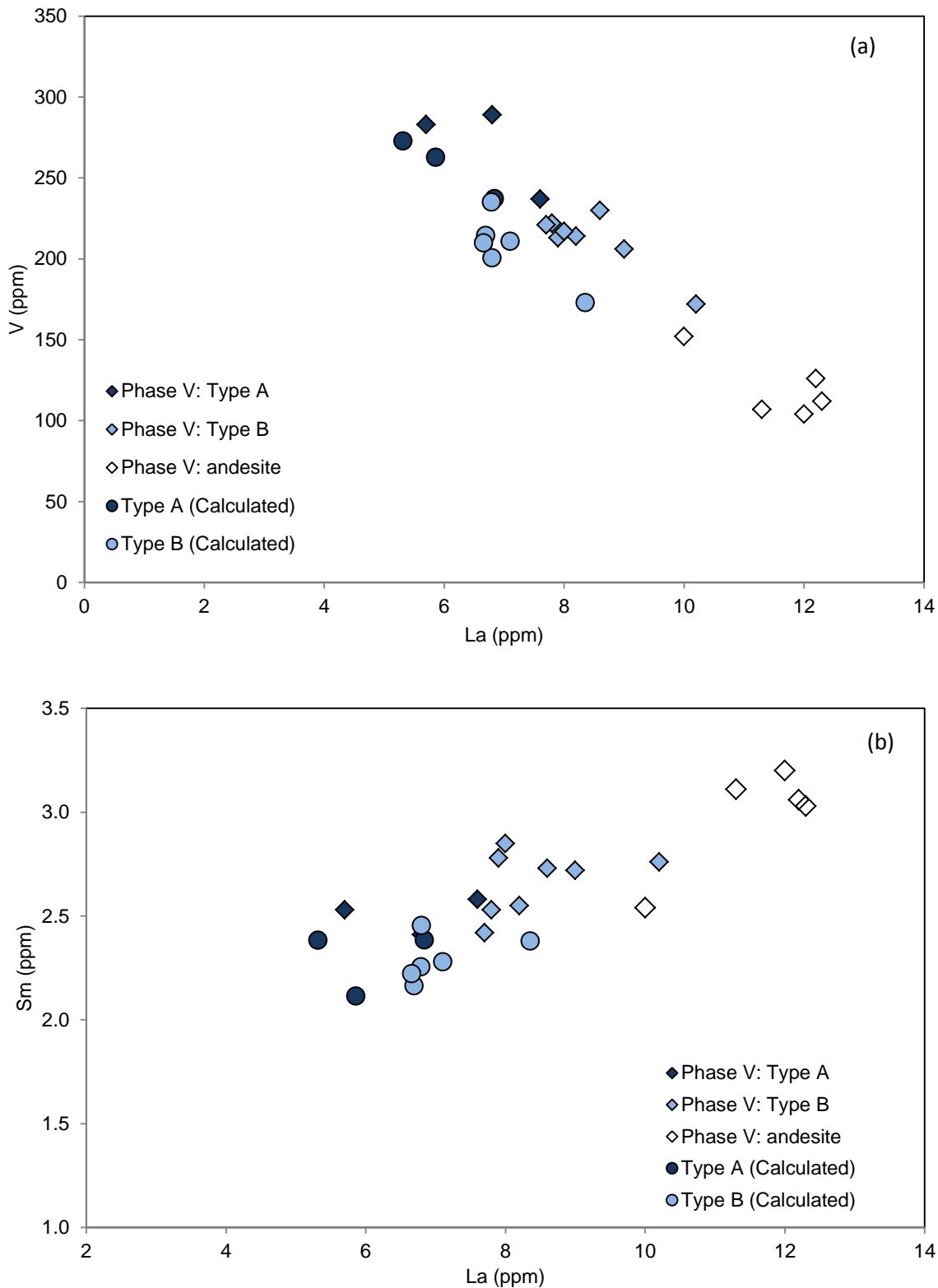
Figure 4.21: Plots showing the results of removing inherited phenocrysts from the bulk compositions of phase V enclaves referred in the plots as 'calculated' (see text for explanation of method). Both plots demonstrate that the effect of removing the inherited phenocrysts strongly affects the type B enclaves than type A but the overall linear trends do not vary significantly after removal.

effect on some element concentrations, with compositions plotting away from the andesite field, although on the same linear trend as type A enclaves (Fig. 4.21). This result agrees with the prior mixing calculations, which demonstrated that type B compositions are likely to be controlled by simple mixing of type A and the andesite.

To ensure that the effect of the inherited phenocryst compositions on the bulk compositions of types A and B are negated, the same fractional crystallisation tests in section 4.4.3 were applied to the calculated inherited phenocryst free compositions using the type A end-member (MT27) and type B end-member (MT25) compositions (phenocrysts subtracted). Removing the effect of the phenocrysts has had very little effect on the phase V FC models, to replicate the REE geochemical trends an increase in amphibole fractionation to ~100 % is required to achieve FC from type A to B as before. This suggests that it is difficult to relate types A and B by FC, but that amphibole appears to have a stronger influence on the fractionating assemblage than in earlier phases even after inherited phenocryst removal. The results of removing the inherited phenocrysts concur that mixing is a strong control on the phase V geochemical trends, but that a changing fractionating assemblage may also play a role. Removing the phenocrysts provides no strong evidence that type B enclaves are derived from a distinct separate melt than type A, but do suggest that they may be more differentiated prior to mixing in relation to type A.

4.4.4   Origin of rhyolitic matrix glass in enclaves

The matrix glass in both enclave types is rhyolitic, and the question still remains as to how much influence has mixing with the host andesite melt has had on the mafic enclave glass compositions. The phase I fractional crystallisation model of 70 % amphibole and 30 % plagioclase not only fits the range of mafic enclave compositions, but also could generate the residual melt composition of between 71–79 wt% SiO_2 (Zellmer *et al.,* 2003a). However, for the phase V REE bulk compositions to be produced by FC requires ~100% amphibole fractionation. This generates a residual melt composition of ~51–53 wt% SiO_2 after 63% fractionation, even if minor magnetite and plagioclase (5 %) are added into the fractionating assemblage, and this is clearly inconsistent with the measured rhyolitic glass compositions in phase V mafic enclaves (Chapter 3: table 3.4).

The results from the mixing calculations (section 4.4.3) suggest that up to 40 % melt from the andesite could be mixed into the mafic enclaves. Late-stage mixing of the melt into the enclaves could perhaps enable the preservation of the rhyolitic composition of the incorporated melt from the andesite. However, this cannot explain systematic differences in the melt compositions observed between the enclave types and the andesite, in particular in K_2O and TiO_2 content (section 3.2.3; see also Humphreys *et al.,* 2010). It is likely that the distinctive high-K_2O rhyolitic glass compositions in the type A enclaves are generated from the differentiation of the residual melt from entrainment-crystallisation of mafic enclaves involving an assemblage of plagioclase, ±amphibole, ±clinopyroxene and magnetite. Using a simple fractionating assemblage of plagioclase 80 % and amphibole 20 %, to represent roughly the appropriate modal proportions of a type A enclave diktytaxitic framework assemblage, a rhyolitic melt of ~76 wt% SiO_2 can be generated after 58 % crystallisation from the phase V mafic end-member composition. Varying the modal proportions of the framework assemblage, substituting clinopyroxene for amphibole, and amount of crystallisation would generate a range of melt compositions (~70–80 wt% SiO_2) that may fit the observed range in the enclaves. The slightly average lower MgO and CaO in the type B enclaves are perhaps consistent with more cpx crystallisation in these enclave types compared to type A. The low K_2O melt compositions in the mafic enclaves, which are similar to that in the andesite are evidence for the mingling of andesitic melt into the enclaves. However, with evidence for low and high K_2O melts in the same enclave this would suggest that the low K_2O melts are representative of late-stage mixing during enclave crystallisation.

4.4.5 Controls on SHV andesite composition

Andesite compositions remain similar throughout the eruptive phases, although there is a hint that changes in FeO and MgO may reflect those observed in the mafic enclaves (Thomas *et al.,* 2014). The slight decrease in SiO_2 concentrations seen in phase V andesite could hint of a growing influence of the addition of mafic material to the andesite over the course of the eruption. However, despite an increasing mafic enclave population in the erupted andesite since phase I to V (1–8 wt %), there is no clear evidence this is influencing the andesite composition. Further detailed work on the mafic enclave derived

crystal population density present in the andesite (Humphreys *et al.,* 2012) in all eruptive phases is required to ascertain the influence of mafic material.

The SHV andesite is suggested to have been generated by differentiation from a composition similar to the SSH magma (Zellmer *et al.,* 2003a). The mafic enclave compositions from phase I were ruled out as a parental magma to the SHV andesite on the basis of lower LREE/MREE ratios where Sm evolved to higher concentrations than the andesite (Zellmer *et al.,* 2003a). However, higher LREE/MREE ratios in the phase V enclaves (Fig. 4.3) could suggest that the mafic enclave compositions trends from phase V could be extrapolated to generate the SHV andesite. This does not take into account the influence of mixing on the mafic enclave bulk composition, which has been shown to be significant in phase V.

4.5 Conclusions

There is no evidence for a change in the parental mafic enclave source conditions from the subducting component (Fig. 4.12). Constant incompatible element concentrations (*e.g.* U/Th; Fig. 4.4) in the mafic enclave compositions across the phases indicate that closed system fractionation of the parental mafic enclave magma appears to be the mechanism for differentiation. The fractional crystallisation model by Zellmer *et al.,*(2003) produced for the phase I mafic enclave compositions fits the phase III REE data well, but for elements such as vanadium an increasing amount of amphibole and minor magnetite is needed to reproduce their trends. The change in vanadium concentrations and trend in phase III along with changes in selected major elements is further evidence that mafic end-member composition has changed between phases I and III, which has followed through to phase V. Although it could be argued that the MREE to HREE concentrations in phase V are now similar to the SSH magma, this is not observed in the LREEs which are depleted in the SSH magma compared to the phase V enclave magma. Furthermore, other phase V elements do not replicate the SSH concentrations (*e.g.* Fig. 4.5; 4.6; 4.9).

The FC model used to explain the range of phase I mafic enclave data range cannot be fitted to the phase V mafic enclave trace element data. To reproduce the phase V mafic enclave compositional trends (from type A to B), amphibole is required to play an unreasonably strong role (at least 94 %) in the fractionating assemblage. Furthermore, the FC model from phase I cannot explain the behaviour of trace elements such as V, Sc. Instead, the linear trends defined for many elements between the andesite and mafic enclaves can be reproduced by differing degrees of mixing between the type A enclaves and andesite. Scatter in the compositions outside of analytical error is likely to be the result of the combined processes of differentiation and magma mixing. The rhyolitic glass compositions also suggest that differentiation of residual liquid during crystallisation of the mafic enclave framework assemblage as enclaves are formed also plays a role in driving trends in bulk composition. In conclusion, the trends in the phase V enclave compositions may be perhaps influenced by a fractionating assemblage with greater amphibole content than in phase I, but mixing to differing degrees with the andesite after intrusion into the magma chamber from depth is the dominant control of compositional trends from type A to B. A similar conclusion may be drawn for phase III mafic enclave composition trends, although a better fit using the FC model from phase I of REE data suggest that FC might have a stronger role in phase III mafic enclave compositions than in phase V.

The change from a FC to mixing dominated trend in the mafic enclave compositions from phase I to V implies that conditions for mixing between the andesitic and mafic magmas have become more favourable. This could be due to a number of factors affecting the relative temperature, viscosity, density and/or composition of the mafic magma and the andesite (Sparks & Marshall 1986). Given that there are clear geochemical changes in the mafic enclave compositions, and that the andesite compositions are relatively consistent from phase I to V, it is inferred that the major influence on mixing characteristics is related to factors affecting the mafic magma, and that this is not being effectively reflected in the trace element geochemistry of the andesite.

Chapter 5: Geochemical evidence for relict degassing pathways preserved in andesite

The large bulk of this chapter has been accepted for publication as a paper entitled 'Geochemical evidence for degassing pathways preserved in andesite' in Earth and Planetary Science Letters. I am the first author on the paper and undertook all fieldwork, laboratory analysis, interpretation of the results, and wrote the paper. My supervisors Marie Edmonds, Madeleine Humphreys, Jenni Barclay and Richard Herd are co-authors; they discussed interpretations of the results and edited drafts of the paper. The following has been modified to fit with the structure of the thesis: (i) the methods section are moved to chapter 2 to avoid repetition within the thesis (ii) a small section calculating the shear and strain rates at Soufrière Hills Volcano in phase V has been added.

In the previous chapters, the dynamics of the interaction between the mafic and andesitic magmas were explored. In this chapter, the mechanisms that allow volatile escape from the shallow magmatic system (conduit and dome) are explored. New petrological and geochemical evidence for gas escape in andesitic shear fractures is presented in this chapter.

5.1   Introduction

SHV, similar to other andesite dome-forming volcanoes, emits large fluxes of volcanic gases (dominantly H_2O, CO_2, SO_2, HCl) (*e.g.* Edmonds *et al.,* 2001). The transfer of fluids rich in H_2O, CO_2 and sulphur from the intruding mafic magma at depth or mafic enclaves (Edmonds *et al.,* 2014) into the andesite is a key component of the volatile budget. The gas is largely decoupled from the flux of magma to the surface, indicating efficient magma-vapour segregation (Edmonds *et al.,* 2001). Effective outgassing during andesitic eruptions moderates explosivity and controls eruption style (Sparks, 2003). In andesites, shallow segregation and escape of gas in the volcanic system may take place through a

permeable bubble network (Eichelberger *et al.,* 1986), through the conduit walls (Jaupart, 1998; Jaupart & Allegre, 1991; Stasiuk *et al.,* 1996), or through networks of brittle fractures created by shear deformation of ascending magma at low pressures (Gonnermann & Manga, 2003; Edmonds & Herd, 2007; Castro *et al.,* 2012; Cabrera *et al.,* 2011). Observations, experiments and theory show that while magma behaves in a ductile way at low strain rates, it can fail in a brittle manner at high strain rates (Walker, 1969; Neuberg *et al.,* 2006; Dingwell, 1996; Lavallée *et al.,* 2012). Repeated brittle failure at the conduit walls during the 2004–2008 eruption of Mount St Helens produced a layer of cataclasite on the surfaces of lava spines, which channelled gases (Iverson *et al.,* 2006; Cashman *et al.,* 2008; Pallister *et al.,* 2012) and this process may lead to frictional melting (Grunewald *et al.,* 2000; Schwarzkopf *et al.,* 2002; Tuffen & Dingwell, 2005; Kendrick *et al.,* 2012). Evidence for repeated episodes of fracture and healing in rhyolite magma have been identified in an eroded conduit in Iceland (Tuffen *et al.,* 2003). At SHV, swarms of low frequency earthquakes have been attributed to the generation of shear fractures at the conduit walls (Neuberg *et al.,* 2006), and cyclic activity during lava dome growth at SHV may be linked to stick-slip motion of magma in the conduit controlled by pressure accumulation and relaxation at the conduit walls (Lensky *et al.,* 2008). Recent experimental work indicates that shear localisation and development of permeable fracture zones at the conduit edges may induce the rapid ascent of the less-sheared and non-degassed magma toward the conduit centre thus causing explosive volcanism (Okumura *et al.,* 2013). Closure and healing of permeable pathways for gas transport can occur via foam collapse, or welding of particulate matter in fractures perhaps assisted by frictional heating (Tuffen & Dingwell, 2005). The development (and closure) of permeable pathways for gas transport may therefore have important implications for eruption style.

A few studies of tuffisite-bearing rhyolite (Cabrera *et al.,* 2011; Castro *et al.,* 2012; Berlo *et al.,* 2013) have considered the implications of these high permeability zones for the channelling of magmatic volatiles. Sedimentary structures within tuffisite veins are consistent with transport of a fluidised gas-particle mixture (e.g. Heiken *et al.,* 1998; Stasiuk *et al.,* 1996; Tuffen *et al.,* 2003; Tuffen and Dingwell 2005). Decreases in H_2O concentrations towards tuffisite veins in obsidian probably indicate degassing of magmatic water into the fractures (Castro *et al.,* 2012; Cabrera *et al.,* 2011). Changes in metal concentrations within and next to rhyolitic tuffisite veins have also been suggested to be linked to vapour transport (Berlo *et al.,* 2013). Elevated carbon dioxide concentrations in

pyroclastic obsidians from Mono craters (USA) may result from equilibration with high-CO_2 fluids concentrated via magma degassing at the conduit walls (Rust *et al.,* 2004), although it remains unclear whether the degassing of the pyroclastic material was inhibited kinetically (Gonnermann & Manga, 2005). The paucity of geochemical and petrological evidence for gas pathways formed by brittle failure could be because gas transport zones are commonly being overprinted or destroyed during eruption, or perhaps because the transport zones themselves are not usually erupted.

In this chapter rare samples of some narrow bands found in andesite lava blocks from SHV are examined from events during the two latest extrusive phases of activity; Phases IV (28 July 2008 – 3 January 2009) and V (9 October 2009 – 11 February 2010). The bands are interpreted to represent the loci of shearing and brittle failure, and that they record clear evidence of relict pathways for magmatic gases in the highly viscous magma at low pressures in the volcanic system. The results from the petrology and geochemistry are presented and discussed, with the implications for eruption style and mineralisation.

5.2   Background

Sample MVO1535 is a ballistic clast associated with pumice fallout ejected during a vulcanian explosion that occurred on 3rd January 2009 in Phase IV (Komorowski *et al.,* 2010) (Fig. 5.1). Phase IV activity was characterised by increased average lava extrusion rates (6.8 m^3s^{-1}) in comparison to earlier extrusive phases (Wadge *et al.,* 2014) generating a total volume of 39 x 10^6 m^3 lava extrusion in Phase IV. A series of four vulcanian explosions on 3 January 2009, preceded by increased cyclic tremor amplitude indicating an increase in pressure (~ 25 MPa) (Chardot *et al.,* 2010), marked the end of Phase IV. The largest explosion generated an 11 km-high plume, with an estimated conduit excavation depth of 1.9 km (Chardot *et al.,* 2010). Large blocks of pumice and dome rock (20 – 40 cm in dimension) were ejected during the explosion. The deposits had a total volume of ~0.95 Mm^3 DRE (Komorowski *et al.,* 2010).
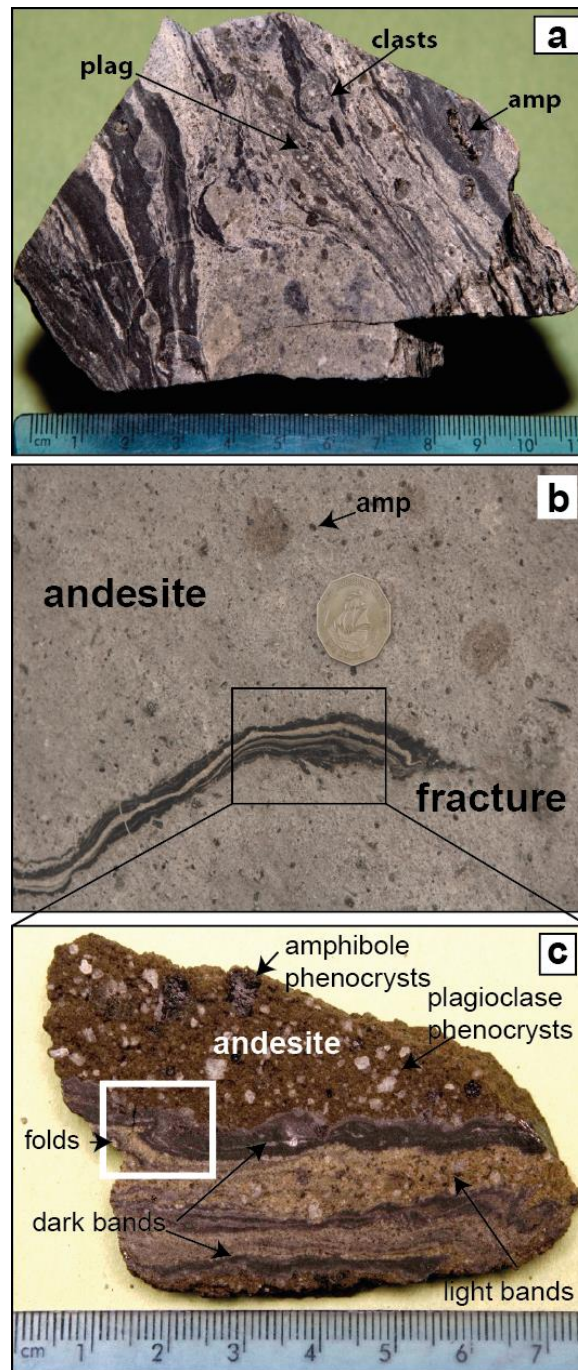
Figure 5.1: Field and hand specimen images of samples used in this study. (a) MVO1535, collected from the vulcanian explosion of January 3rd 2009. Alternating dark and light bands entirely comprise the hand specimen. Visible plagioclase crystals are observed in the lighter bands. Darker bands are occasionally wrapped round clasts. (b) MVO1586, within andesitic block from February 11th 2010 dome collapse deposits, fracture is up to 2 m in length (coin scale: 2.7 cm). Amphibole phenocrysts are clearly visible in the host andesite (c) MVO1586 cut section with the host andesite with visible plagioclase and amphibole phenocrysts, note alternating dark fine-grained and lighter coarse-grained bands similar to (a). Subtle folding observed in the darker bands as highlighted in box.

Sample MVO1586 is from a large andesite block within pyroclastic density current deposits associated with the 11th February 2010 dome collapse marking the end of Phase V (Stinton *et al.,* 2014). High average extrusion rates in Phase IV were maintained during Phase V at 6.8 m^{3}s^{-1}, but dropped to an average of 0.1 ms^{-1} in the days preceding the dome collapse (Stinton *et al.,* 2014). However, it has been calculated that extrusion rates may have reached as high 35 m^{3}s^{-1} for short periods of minutes to tens of minutes (Odbert *et al.,* 2014). A total of 38 x 10^6 m^3 of lava was added to the dome volume, resulting in a total dome volume of 245 x 10^6 m^3 before dome collapse on 11 February 2010. The dome collapse (40–50 x 10^6 m^3) excavated material to a depth of 320 m (Stinton *et al.,* 2014), although vulcanian explosions during the collapse event may have sourced material from a greater depth. Extensive sampling of the dome collapse deposits and rockfalls from this eruptive phase yielded only this one sample displaying the shear textures described in this chapter.

5.3   Petrological, geochemical and textural results

The methods employed in collecting the results can be found in chapter 2. In the field the narrow elongate zones were clearly defined within the andesite blocks by the sharp contact with the andesite (Fig. 5.1). Both samples contain narrow zones of alternating dark and light coloured bands (Figs. 5.1; 5.2). MVO1535 is a block (5 x 5 x 10 cm) entirely composed of the bands (Figs. 5.1a; 5.2), whereas the bands of MVO1586 occupied a narrow zone 2-5 cm wide by 2 m long within a larger andesite block (~ 5 x 5 m) (Fig. 5.1b and c). The contact with the host andesite varies from being sharp to more diffuse in places along the fracture length, and there is no evidence of crystal or vesicle alignment, or heating in the host andesite adjacent to the shear fracture (Figs. 5.1; 5.2; 5.3; 5.6a). In hand specimen, the darker bands have a glassy/waxy appearance with few visible crystals and no apparent porosity, whilst in the lighter bands crystals are apparent. Broken phenocrysts and folding of bands (particularly within the dark, fine-grained bands) are visible (Fig. 5.4a). In addition, very thin (<1 mm) dark, fine-grained bands are occasionally wrapped around cm-sized phenocrysts. In both samples, band thickness is variable along the fracture length; however, the lighter coarser bands on average are thicker by a ratio of 2:1 than the dark fine-grained bands.
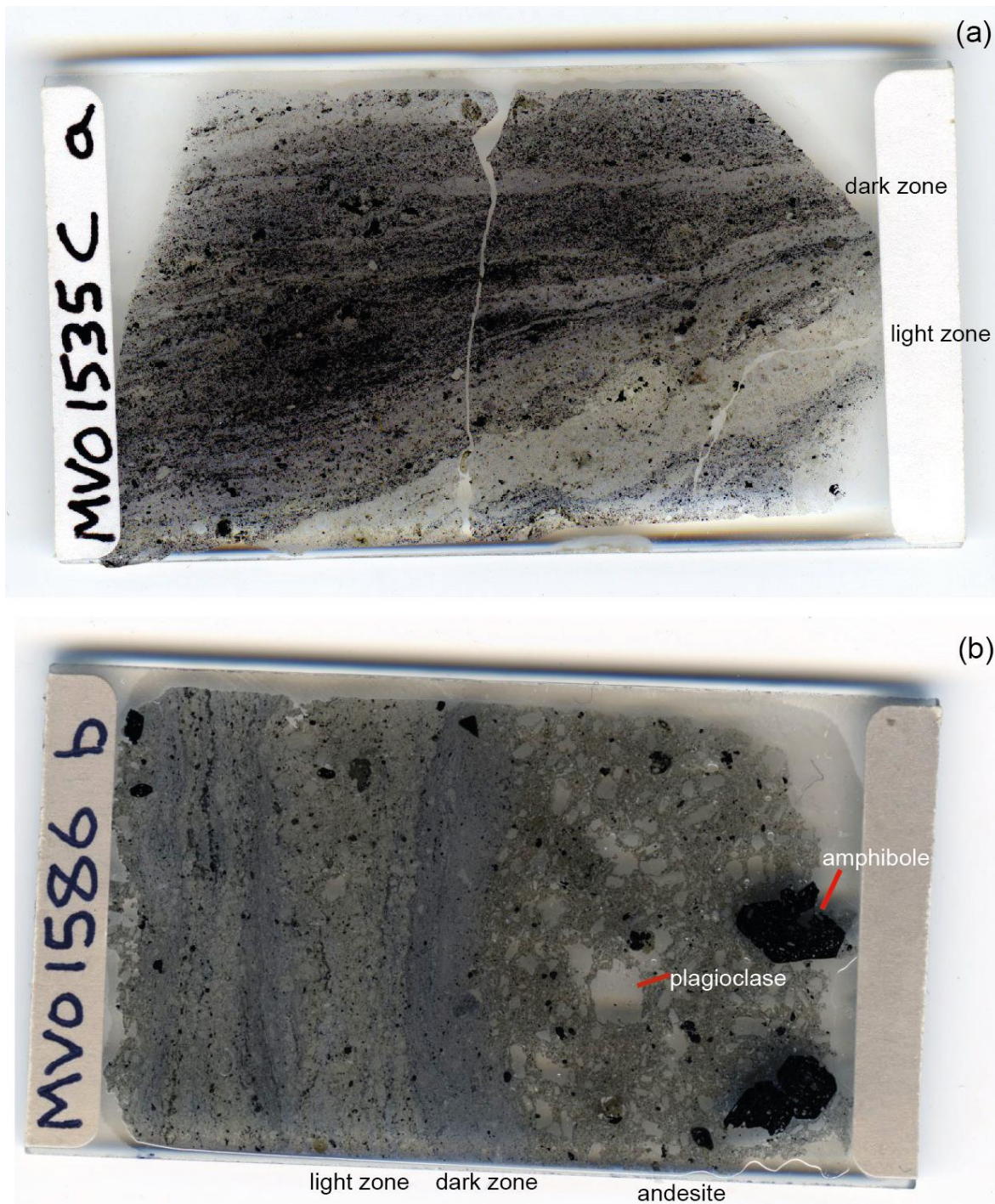
Figure 5.2: Whole thin sections from MVO1535 and MVO1586. (a) MVO1535: This thin section has predominantly more dark zones than light zones with the section. The dark zones contain oxides that contribute to the dark colouration (b) MVO1586: SHV andesite is present on the left side of the thin section with large amphibole and plagioclase phenocrysts set in groundmass of glass, microlites (plagioclase and orthopyroxene) and vesicles. On the right side of the thin section the dark and light zones are highlighted. In the lighter zone crystals are clearly visible, whereas in the darker zones the matrix is more fine-grained.
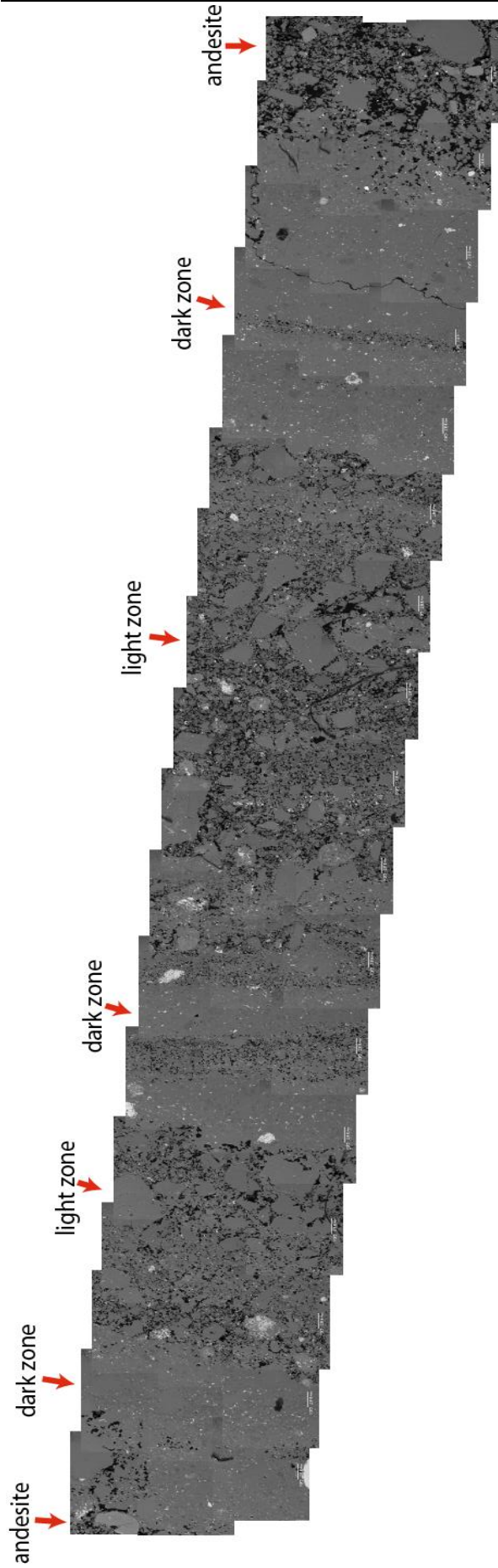
Figure 5.3: BSE composite cross-section of MVO1586 highlighting alternating dark and light zones. To the far right and left of the image andesite is present. Black indicates porosity, white indicates oxides, grey indicates minerals. The larger grey crystals throughout the figure are plagioclase. Within the dark zones more porous streaks are also observed. Note that the light zones look similar to the andsesite except that they are more crystalline with more angular larger crystals.

137

The dark, fine-grained bands (~30-70 μm) have low porosity (void space <1 %) (Figs. 5.3; 5.4). They have abundant zones and trails of anhedral Ti-magnetites (<8% vol), cristobalite and quartz (<20 % vol), pyroxene and fragments of sieve-textured plagioclase. The degree of sieve-texture in plagioclase phenocrysts is significantly more developed than that seen in identical plagioclase phenocrysts in the andesite host (Fisg. 5.5a; 5.6a,b), and small sieve-textured fragments are overgrown by a narrow, more albitic rim (Fig. 5.4b). Small (20–50μm) subhedral to hopper-shaped cordierite ($Mg_{1.3-1.7}Fe_{0.4-0.8}Al_{3.7-4.0}Si_{4.9-5.2}O_{18}$) microlites (Fig. 5.4b) are ubiquitous in the fine-grained dark bands in both samples. Some cordierite crystals may contain small inclusions of An-rich plagioclase as well as tiny melt inclusions, and appear to have more Mg-rich rims (Fig. 5.4). The magnesium number, X_{Mg} (Mg/Mg + Fe) of the cordierite varies between the samples; MVO1586 cordierite has lower but more variable X_{Mg} (0.49–0.62), and MVO1535 has a higher but narrower range of X_{Mg} values (0.64–0.68). Sieve-textured plagioclase comprises most of the groundmass. Glass content is variable (MVO1586 ~4–10 % vol and MVO1535 ~1–10 % vol). Small rounded to subhedral Ti-magnetite crystals (1-2 μm) are also present throughout the groundmass in these bands. Sparse ilmenite crystals are present in MVO1535, but are rarely found in MVO1586 (Table 5.1). Cristobalite is abundant within both samples with characteristic 'fish-scale' cracks (Fig.2c), which form due to cooling through the α-β cristobalite phase transition (~220°C; Darling *et al.,* 1997; Horwell *et al.,* 2012). Concentric cracks in the groundmass (glass and microlites) surrounding cristobalite crystals are also common (Fig. 5.4c), caused by the negative volume change of the cristobalite as it cools through the phase transition. Quartz is less abundant than cristobalite and forms discrete crystals (5-180 μm), often located between crystals of sieve-textured plagioclase and relict amphibole (Fig. 5.5). It is discriminated from the cristobalite by the presence of feldspar rims (<5 μm thickness), lack of 'fish scale' cracks and lack of concentric cracking around the crystals (Fig. 5.5). In MVO1535, small, localised quartz-rich lenses in the dark bands exhibit higher porosity in the form of voids between quartz crystals. Narrow zones (<600 μm) of small (<20 μm) elongate vesicles and tears are also present within the dark bands in MVO1586.
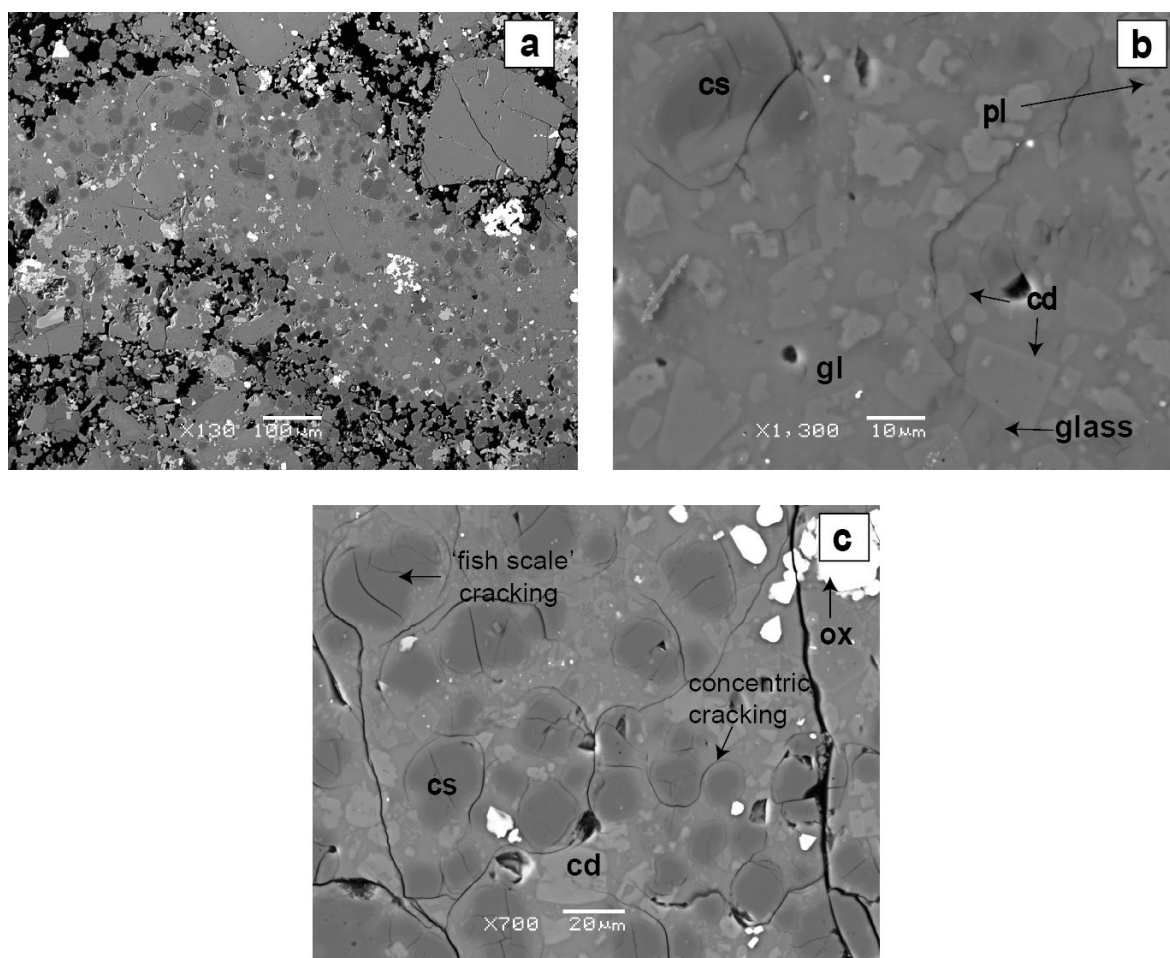
Figure 5.4: BSE images of dark fine-grained low porosity bands. Black represents void spaces (a) Thin low permeability dark fine-grained band that has been folded with large plagioclase crystals in the lighter coarser band (scale: 100 μm). (b) Image from dark low porosity band in MVO1586 with cordierite microlites and sieve-textured plagioclase. Concentric cracking is present in the groundmass of glass and microlites around cristobalite. 'Fish scale' cracking is present within the cristobalite crystals, where the fracture is constrained to within the crystal only (scale: 10 μm). Cordierite is distinguished from the plagioclase by its darker grey colour, and subhedral to hopper crystal shapes. Small melt and plagioclase inclusions are also present in the cordierite. Plagioclase fragments have narrow more albitic overgrowth rims. (c) Example of a dark low porosity band from MVO1586 (scale: 20 μm). Plagioclase (pl), oxides (ox), pyroxene (px), cristobalite (cs), glass (gl), and cordierite (cd).
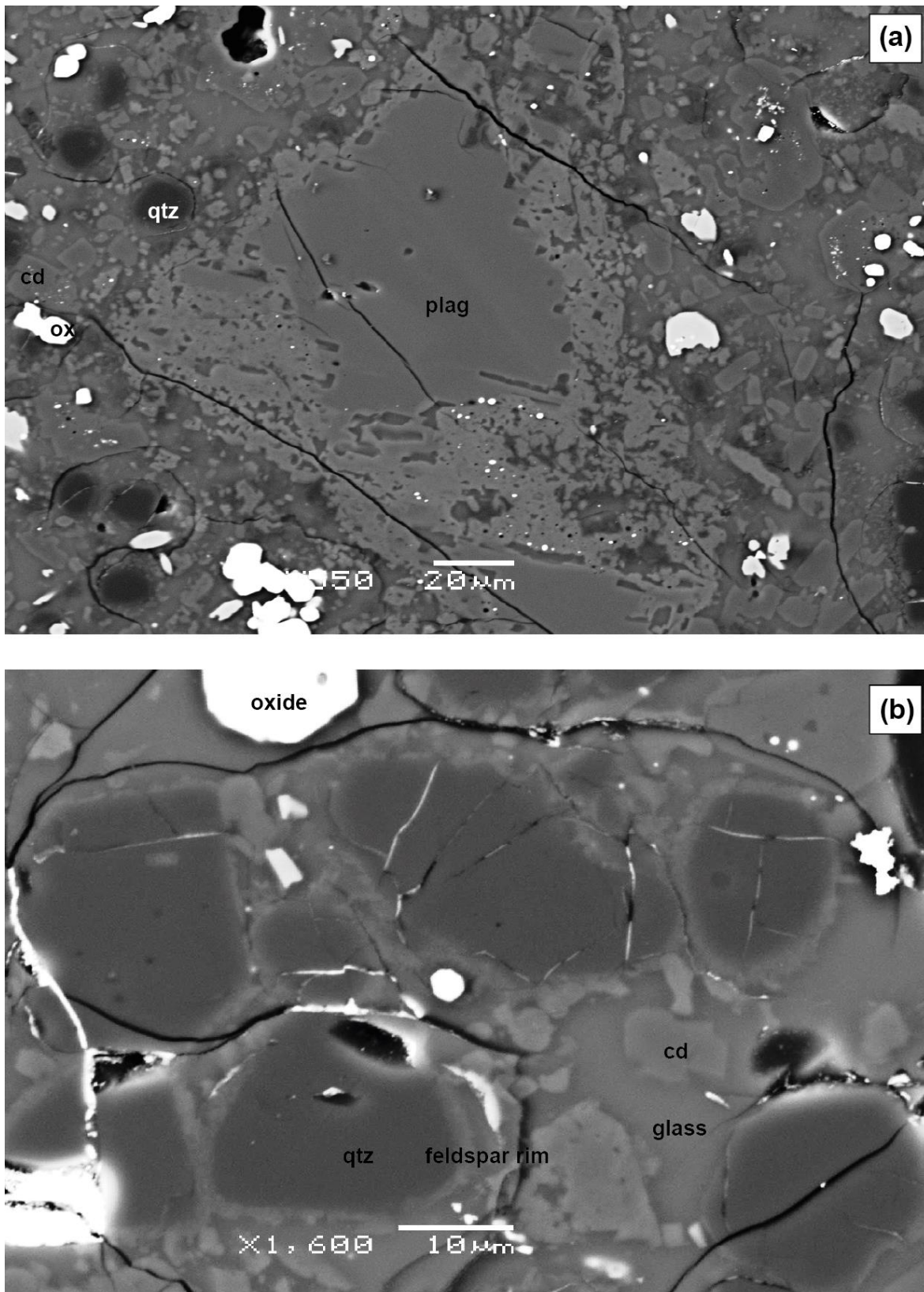
Figure 5.5: Back scattered images of dark fine-grained zones. (a) Image of a remnant plagioclase phenocryst with a corroded outer rim. The groundmass contains predominantly oxides, quartz, cordierite and glass. (b) Quartz microlites with feldspar rims.
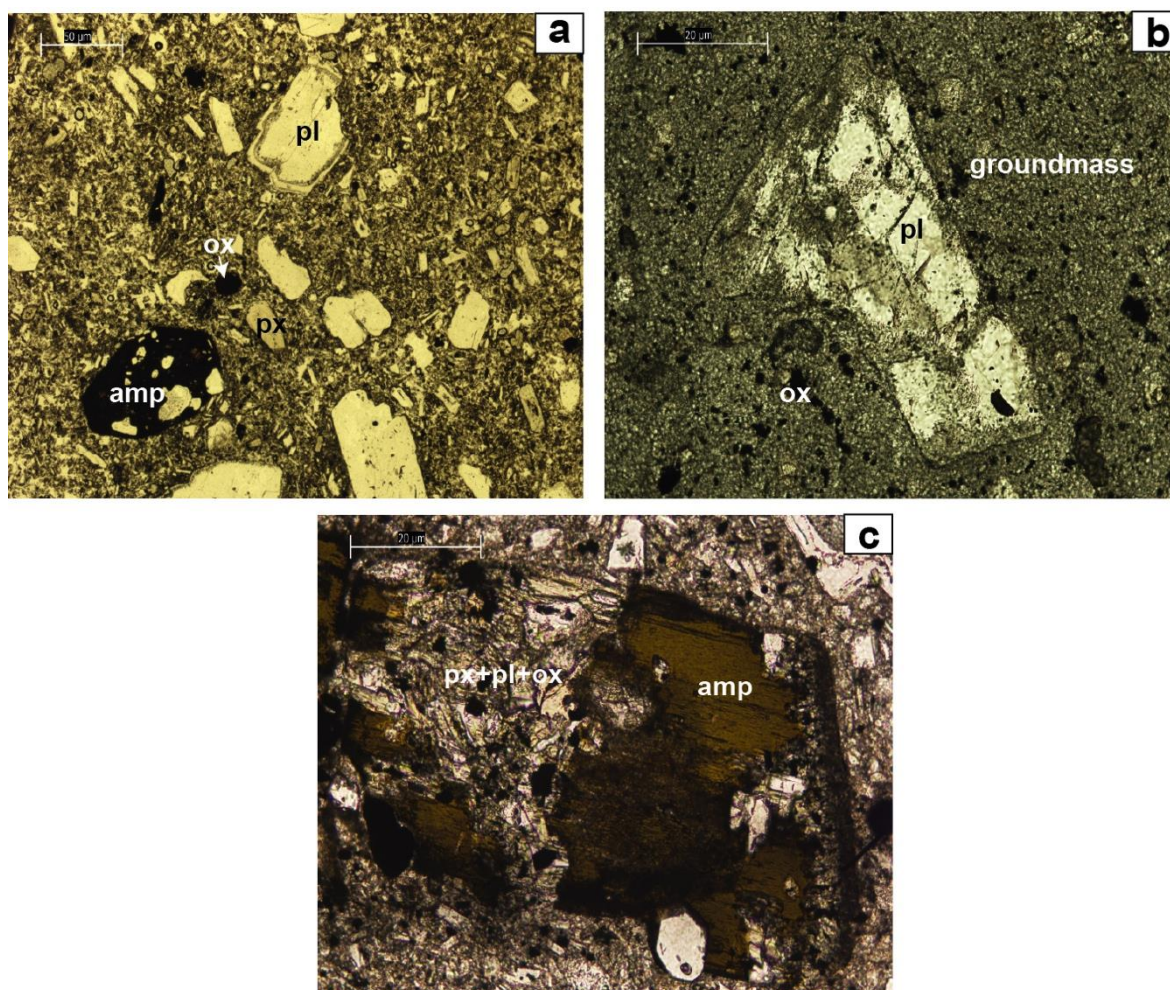
Figure 5.6: (a) is a photomicrograph of the host andesite adjacent to the shear zone in MVO1586. Note the limited sieve-texturing of the plagioclase. (scale: 50 µm) (b) Photomicrograph of MVO1586 dark band, with a partially sieved-textured plagioclase crystal surrounded by a crystalline groundmass with oxides (scale: 20 µm). (c) Example of an amphibole crystal from the light bands with replacement pyroxenes, plagioclases and oxides (scale: 20 µm).

The lighter coloured, coarse-grained bands (~100 – 350 µm grain size) consist of predominantly broken plagioclase crystals, orthopyroxene, clinopyroxene and sparse large amphibole phenocrysts (Fig. 5.7). Plagioclase phenocrysts are commonly fractured and some fractured pairs can be matched up, suggesting minimal displacement (Fig. 5.7a). Amphiboles are commonly partly broken down; they are reminiscent of thermal breakdown textures with an overprint of opacite (Fig. 5.6c), but it is difficult to be sure that this is not decompression breakdown. Porosity is variable and ranges from 7–19 %. Crystals are typically rounded with small patches (<5 µm across) of melt adhered to crystal edges (Fig. 5.7b). Glass is >3 % vol in both samples in the light coarse bands. Cristobalite is also present (Fig. 5.7). Total oxides make up <2.4 vol% and Ti-magnetite is less

abundant. Streaks of dark banded low porosity (<1%) regions occur throughout the coarse bands. Within these low porosity areas in MVO1535, some crystal alignment of intact and internally fractured tabular plagioclase microphenocrysts is observed.
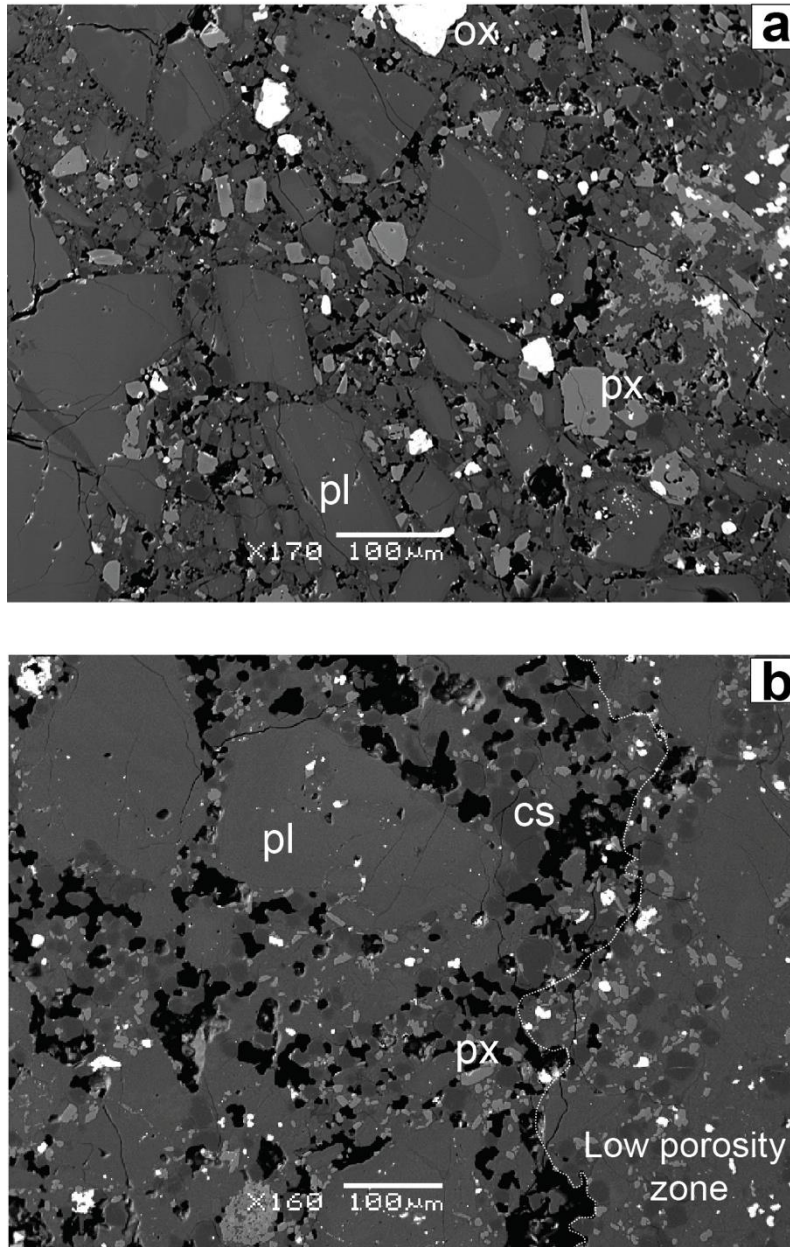
Figure 5.7: BSE images of light coarse-grained high porosity bands. (a) Example from MVO1535 of broken matched plagioclase pairs indicating minimal displacement (scale: 100 µm) (b) Example of rounded plagioclase crystals in the higher porosity zones with patches of melt adhered to the crystal edges (scale: 100 µm)

Table 5.1: *Mineral electron probe analysis of samples MVO1535 and MVO1586*

Mineral	Cordierite				Cristobalite				Clinopyroxene	
	MVO		*MVO*		*MVO*		*MVO*		*MVO*	
Sample	*1535*	±1σ	*1586*	±1σ	*1535*	±1σ	*1586*	±1σ	*1535*	±1σ
n	7		19		23		10		7	
SiO$_2$	49.4	0.6	49.3	1.2	97.5	0.9	97.1	0.8	50.6	1.4
TiO$_2$	cf	cf	cf	cf	0.1	0.0	0.0	0.0	0.6	0.2
Al$_2$O$_3$	33.1	0.2	33.0	0.9	0.2	0.3	0.3	0.3	3.2	1.5
FeO	5.5	0.4	7.1	1.2	0.2	0.1	0.0	0.1	10.3	0.6
MnO	0.2	0.0	0.3	0.1	cf		cf		0.4	0.2
MgO	11.1	0.7	9.8	0.8	0.0	0.0	0.2	0.0	16.0	1.3
CaO	0.4	0.8	0.2	0.5	cf		cf		18.8	0.8
Na$_2$O	0.1	0.2	0.1	0.1	cf		cf		0.2	0.0
K$_2$O	0.2	0.1	0.3	0.2	cf		cf		bd	
Total	100.0		100.2		98.0		97.8		100.3	

	Orthopyroxene				Ti-Magnetite				Illmenite		
	MVO		*MVO*		*MVO*		*MVO*		*MVO*		*MVO*
Sample	*1535*	±1σ	*1586*	±1σ	*1535*	±1σ	*1586*	±1σ	*1535*	±1σ	*1586*
n	5		4		18		7		4		1
SiO$_2$	52.3	0.4	51.4	0.7	0.1	0.1	0.2	0.1	0.1	0.0	0.2
TiO$_2$	0.3	0.1	0.2	0.1	6.5	0.8	10.5	2.6	43.4	1.7	46.7
Al$_2$O$_3$	1.4	0.5	2.6	0.8	4.2	0.2	4.3	1.2	0.3	0.1	0.1
FeO	21.2	2.0	23.4	0.4	79.7	1.5	76.3	3.3	49.9	1.6	46.8
MnO	1.1	0.3	0.9	0.2	0.4	0.0	0.5	0.1	0.5	0.1	0.7
MgO	23.6	1.5	22.1	0.8	1.3	0.1	1.5	0.2	2.6	0.2	2.6
CaO	1.5	0.3	0.5	0.3	bd		bd		bd		0.3
Na$_2$O	0.0	0.0	0.1	0.1	bd		bd		bd		bd
K$_2$O	0.0	0.0	0.0	0.0	bd		bd		bd		bd
CuO	cf		cf		0.1	0.1	0.0	0.1	bd		bd
ZnO	cf		cf		0.2	0.0	0.1	0.0	bd		bd
Total	101.5		101.3		92.6		93.6		96.8		97.4

	Plagioclase			
	MVO		*MVO*	
Sample	*1535*	±1σ	*1586*	±1σ
n	14		14	
SiO$_2$	50.3	2.2	52.4	4.1
TiO$_2$	cf			
Al$_2$O$_3$	30.7	1.3	29.04	2.4
FeO	0.7	0.1	0.6	0.2
MnO	0.02	0.03	0.01	0.03
MgO	0.1	0.06	0.03	0.02
CaO	14.1	1.6	12.4	2.9
Na$_2$O	3.3	0.9	4.1	1.6
K$_2$O	0.1	0.04	0.4	0.4
Total	99.4		99.1	

bd: below detection; cf: not analysed

With the exception of cordierite, mineral compositions in both the dark and light bands are within error of the established mineral compositions in the andesite, and mafic enclaves at SHV (Murphy *et al.,* 2000) (Table 5.1). However, Ti concentrations in Ti-magnetites in MVO1586 are systematically slightly higher than those in MVO1535 (Table 5.1). Bulk XRF analyses of the shear zones indicate that they have a similar composition to average andesite at SHV in major, minor and most trace elements, except for CaO, Na$_2$O

and Sr, which show minor depletion, and P_2O and K_2O, which show slight enrichment (Fig. 5.8; Table 5.2). However, some trace metals such as Cu, Zn, Ni, Pb and Au in both samples, and Ag and Mo in sample MVO1535, are enhanced in concentration in the shear zones relative to the surrounding andesite (Fig .5.5; Table 5.2).
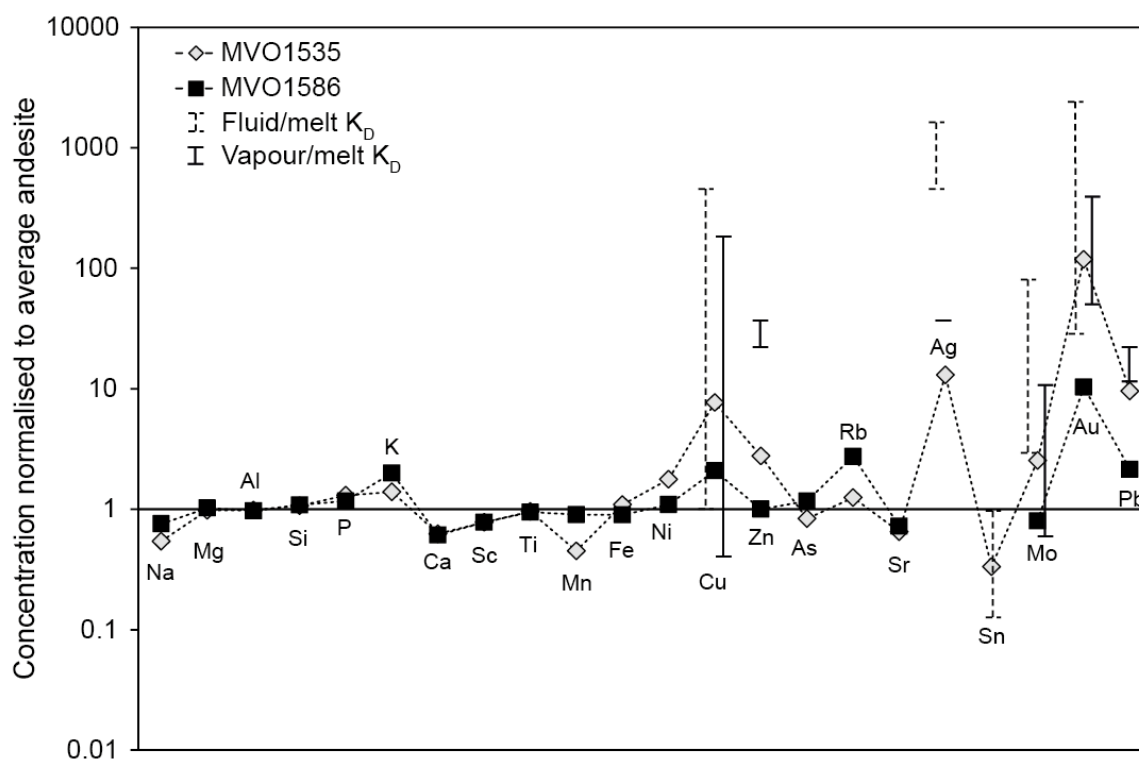
Figure 5.8: Enrichment and depletion of major and trace elements in atomic order of MVO1535 and MVO1586 relative to the average phase V (2009-2010) andesite composition at SHV (see Table 5.2 for geochemical data) compared to published metal partition coefficients (K_D). Fluid (Brine+vapour)/melt K_D (dashed line) and vapour/melt K_D (solid line). Enrichment and depletion trends of the metal contents of shear zones follow a similar to the published K_Ds for fluid and vapour (see Table 5.3 for data).

Copper concentrations (<200 ppm) in MVO1535 are up to ten times higher in the shear zones than in the andesite. Gold is typically below detection in the host andesite, but has been detected at levels of up to 88 ppb in both shear zones (Fig. 5.7; Table 5.2). The two separate dark bands from MVO1535 have almost identical concentrations in major and trace elements (Table 5.2) indicating little geochemical variation between the dark bands in the shear zone, and that sampling was robust. In both samples, Cu is typically hosted as Cu-Fe sulphide inclusions (1-25 μm) within and between clusters of Ti-magnetite and is associated with sieved channels within plagioclase phenocrysts (Fig. 5.9), and is typically concentrated in the dark fine-grained bands. The Cu-Fe sulphide inclusions were analysed

using an electron probe, but the nature of the localised concentrations of Cu and Fe within an inclusion make identification difficult, and analytical totals were poor.
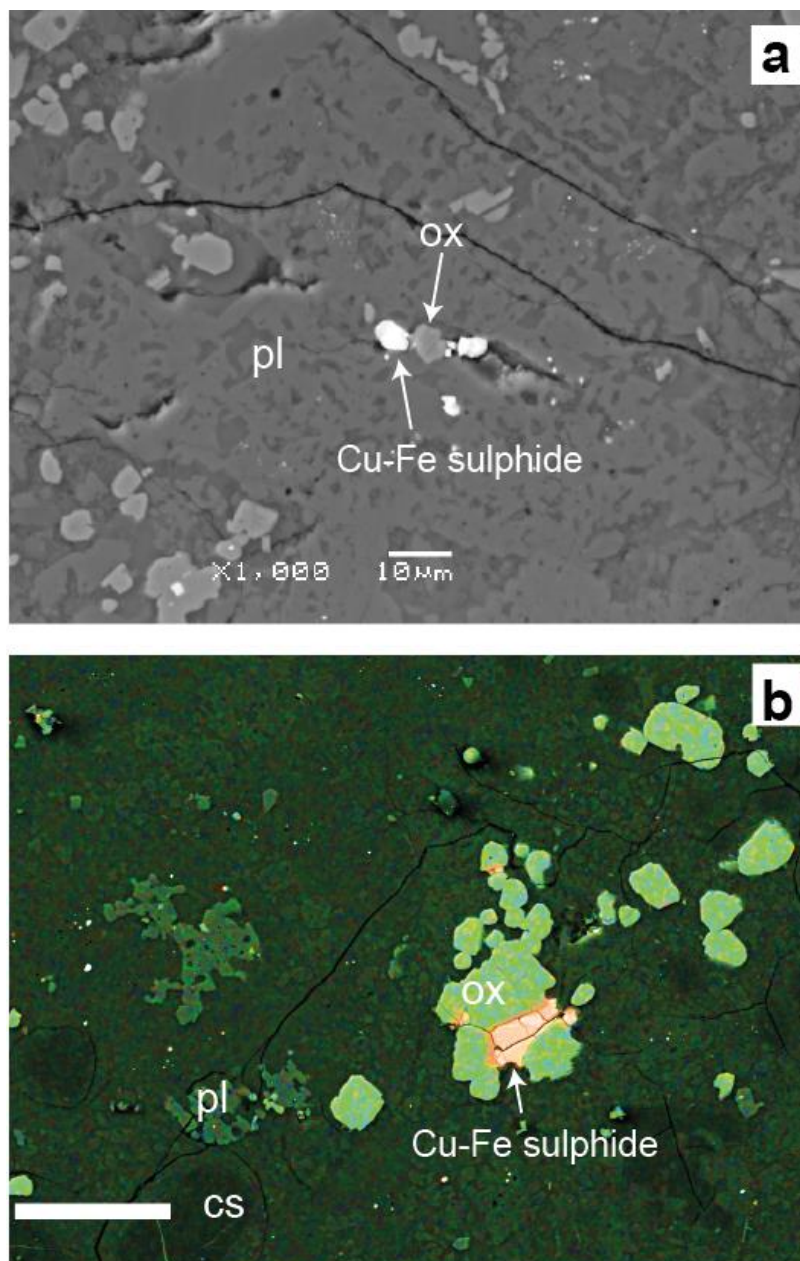
Figure 5.9: BSE images of Cu-Fe sulphide inclusions (a) BSE image within an MVO1535 dark low porosity band of a large highly sieve-textured plagioclase crystal with Cu-Fe sulphide inclusions (scale: 10 µm). (b) BSE image with superimposed false colour element mapping of a large Cu-Fe sulphide inclusion within a Ti-magnetite crystal within an MVO1535 dark low porosity band, where copper is shown in orange and iron in green (scale: 50 µm).

Table 5.2: *XRF and ICP-MS results for MVO1535 and MVO1586*

Sample	MVO1535b1	MVO1535b2	MVO1535c2	MVO1586	Phase V andesite	
	Dark fine-	*Dark fine-*	*Light coarse-*	*Light and dark*		
Area	*grained*	*grained*	*grained*	*area*	n=21	±1σ
SiO_2	62.7	63.0	62.8	63.9	58.9	0.9
TiO_2	0.6	0.6	0.6	0.6	0.6	0.03
Al_2O_3	17.6	17.5	17.7	17.4	17.9	0.3
MnO	0.1	0.1	0.1	0.2	0.2	0.01
MgO	2.6	3.2	3.0	3.1	3	0.3
Fe_2O_3	8.7	8.2	7.2	6.6	7.4	0.4
CaO	4.4	4.1	5.7	4.6	7.5	0.3
P_2O	0.2	0.2	0.2	0.1	0.1	0.01
K_2O	1.3	1.3	0.8	1.6	0.8	0.04
Na_2O	1.9	1.8	2.2	2.7	3.6	0.1
Total	**100.0**	**99.9**	**100.1**	**100.7**	**99.8**	
ppm						
Sc	12.0	12.0	11.0	13.0	15	1.6
V	136.0	131.0	127.0	112.0	121	26.8
Cu	200.4	180.5	148.6	47.9	23	12.1
Zn	65.0	60.0	41.0	20.0	20	5.5
Rb	25.0	25.0	14.0	44.0	15.5	1.2
Sr	168.2	172.8	222.5	208.7	288.6	8.7
Y	18.6	19.4	19.0	19.6	19.6	1.6
Zr	90.3	99.6	100.2	104.8	93.3	1.1
Ba	244.0	221.0	140.0	221.0	215.3	13.4
Ce	22.2	21.3	20.9	25.4	22.6	2.9
Be	3.0	bd	1.0	3.0	3	0
Co	25.0	21.5	21.7	18.7	22.8	7.5
Cs	0.5	0.4	0.2	1.1	0.5	0
Ga	16.0	16.3	16.0	15.8	16.1	0.9
Hf	2.0	2.3	2.5	2.6	2.5	0.05
Nb	2.2	2.7	2.7	2.9	2.4	0.15
Sn	2.0	1.0	1.0	bd	4	0
Ta	0.2	0.3	0.2	0.3	0.3	0
Th	2.4	2.5	2.2	2.8	2.5	0.2
U	0.8	0.9	0.8	0.9	0.7	0.1
La	10.3	10.9	10.4	11.9	11.1	1
Pr	2.8	2.6	2.7	3.1	2.8	0.2
Nd	12.0	12.0	13.4	14.0	12.6	0.8
Sm	2.8	2.8	2.9	2.9	2.9	0.4
Eu	0.9	0.9	0.9	0.9	0.9	0.04
Gd	3.1	3.0	3.1	3.2	3.3	0.2
Tb	0.5	0.5	0.5	0.5	0.5	0.02
Dy	3.3	3.0	3.2	3.3	3.4	0.1
Ho	0.7	0.7	0.7	0.7	0.7	0.06
Er	2.3	2.3	2.2	2.5	2.2	0.1
Tm	0.4	0.3	0.3	0.4	0.3	0.02
Yb	2.4	2.2	2.1	2.6	2.4	0.1
Lu	0.4	0.4	0.3	0.4	0.4	0.03
Mo[‡]	0.6	0.5	0.8	0.2	0.2	0.07
Pb[‡]	2.4	2.3	2.0	0.5	0.2	0.1
Ag[‡]	0.2	0.1	0.1	bd	bd	bd
Ni[‡]	1.2	1.3	1.4	0.8	0.7	0.2
As[‡]	bd	bd	0.5	0.7	0.6	0
*Au[‡]	62.4	62.3	88.3	6.2	0.6	0
Cd[‡]	0.2	bd	0.2	bd	bd	bd

*PPB; bd: below detection; ‡Aqua Regia preparation (see methods)

Table 5.3: *Published metal partition coefficients used in figure 5.5*

Source	Cu	Pb	Zn	Mo	Sn	W	Ag	Au	
Hedenquist & Lowenstern, 1994	*100-200*	*10 to 20*	*15 to 25*	*2 to 10*	*>1*	*4*			*Vapour/melt*
Zajacz *et al.,* 2012	*0.5 to 2*							*200*	*Vapour/melt*
Keppler & Wyllie 1991	1 to 83			0.75 to 7.2	0.01 to 0.07	0.37-4.1			Fluid/melt
Webster, 1997				8 to 80					Fluid/melt
Williams *et al.,* 1995	11 to 215								Fluid/melt
Frank *et al.,* 2011	*2.1 to 18*							*70 to 160*	*Vapour/melt*
Frank *et al.,* 2011	36 to 420							120 to 2400	Brine/melt
Simon *et al.,* 2008							*32*		*Vapour/melt*
Simon *et al.,* 2008							413 to 1151		Brine/melt
Candela & Holland, 1984	*9.1*			*2.5*					*Vapour/melt*
Audetat, 2010				17 to 20					Fluid/melt
Zajacz *et al.,* 2008				14.3 to 22.6					Fluid/melt
Schaefer *et al.,* 1999				14.35 to 14.97					Fluid/melt
Simon *et al.,* 2006	*63-316*								*Vapour/melt*
Simon *et al.,* 2006	240-443								Brine/melt
Frank *et el.,* 2002								40 to 830	Brine/melt
Hu *et al.,* 2008					0.13				Fluid/melt
Lowenstern *et al.,* 1991	*150*								*Vapour/melt*
Total range	*0.5 to 316*	*10 to 20*	*15 to 25*	*2 to 10*			*32*	*70 to 200*	*Vapour/melt*
	1.5 to 759			2.75 to 102	0.01 to 0.13	4	445-1183	40 to 2600	Fluid/melt

5.4   Discussion

5.4.1 Shear and fracturing during magma ascent

The textural evidence, particularly in the coarser-grained bands, is consistent with brittle failure of magma (*e.g.* broken crystals; Allen & McPhie, 2003). During magma ascent shear may occur at the conduit margins (*e.g.* Neuberg *et al.,* 2006; Okumura *et al.,* 2013) or along planes within the dome that may bound spines or lava lobes (*e.g.* Watts *et al.,* 2002, Cashman *et al.,* 2008) where strain rates are high (Dingwell, 1996; Sparks *et al.,* 2000). Magma viscosity is likely to be highest in the shallow parts of the volcanic system, due to pressure-dependent degassing of water during magma ascent and subsequent groundmass crystallisation (Cashman & Blundy, 2000). Magma flow may develop into a plug regime, resulting in high rates of shear strain at the conduit walls (Gonnermann & Manga, 2003), which in theory will readily exceed the critical strain rate for brittle failure even at the fairly modest ascent rates typical of SHV during lava dome-building (Edmonds & Herd, 2007). At a constant magma flux and conduit radius, brittle failure of the magma will occur once magma viscosity exceeds a threshold value. The strain rate τ of ascending magma is related to conduit radius r and magma flux Q by: (Gonnerman & Manga, 2003):

$$\tau = {4Q}/{\pi r^3}$$

and τ to the viscosity of the melt μ_{melt} by:

$$\tau \approx C G_\infty \mu_{melt}^{-0.9}$$

C is a fitting parameter (equal to $0.01^{-0.1}$) and G_∞ is the elastic modulus at an infinite frequency (10 GPa). The average magma flux Q was 6.8 m^3s^{-1} for both extrusive Phases 4 and 5 (Wadge *et al.,* 2012) and the conduit radius r is ~30 m (Neuberg *et al.,* 2006). An average strain rate of 3.2 x $10^{-4}\,s^{-1}$ is calculated for extrusive Phases 4 and 5, during which both fractures were formed. At a constant Q and r, brittle failure of the melt will occur once μ_{melt} exceeds a threshold value. Andesite at SHV typically has 5−25 % melt, 45−55 % phenocrysts and 20−30 % microphenocrysts and microlites (Murphy *et al.,* 2000), depending largely on the extrusion rate (Cashman & Blundy, 2000) and a bulk viscosity between 10^9-10^{14} Pa s (Sparks *et al.,* 2000), which is within the modelled criteria

for brittle failure for typical lava ascent rates (Tuffen *et al.,* 2003). Low frequency earthquake swarms recorded at SHV during lava extrusion phases may be generated by the repeated failure and healing of magma as it transitions from a ductile to brittle regime in the conduit at ~830 m (the depth at which the magma reaches a critical shear stress of 10^7 Pa based on an effective bulk viscosity with 30 vol % crystals; Neuberg *et al.,* 2006). However, stress localisation of the melt around crystals in the magma creates tears and the opening of pore space, which can lower the strain rate required to initiate brittle failure compared to a crystal-free melt (Smith *et al.,* 2001; Cordonnier *et al.,* 2012); furthermore 30 vol% crystals for magma at this depth is a likely underestimate given the significant decompression-driven crystallisation.

5.4.2 Frictional heating and partial melting

The textures in the dark bands (highly sieve-textured plagioclase phenocrysts with new overgrowth rims; Fig. 5.4) and the recrystallised assemblage (*e.g.* cordierite, Ti-magnetites) resemble experimental pseudotachylyte textures at the slip surface of the fracture (Lavallée *et al.,* 2012), which form as result of frictional heating, partial melting and subsequent crystallisation. Experimental work generating pseudotachylytes from granite demonstrate that pseudotachylytes are the product of initial fracture, followed by progressive comminution of grains leading to the generation of a melt (Spray, 2005). Therefore pseudotachylytes may form from fracture (extensional stress) and not merely only fusion (compressive stress). A series of experiments on lava dome material from Volcan de Colima, Mexico summarised below also shows that the development of fractures (extensional *vs*. shear fracturing) in magma is highly dependent on the degree of applied stress (Lavallée *et al.,* 2013). At lower applied stresses (28.5 MPa) at the ductile-brittle transition, extensional tensile fractures which formed first dominate and are followed by the development of shear fractures from compressive stress to a lesser degree (Lavallée *et al.,* 2013). However, at higher applied stresses (76 MPa) simulating deformation at the brittle end of the brittle-ductile regime, shear fractures that developed along shear planes at 20° from the applied compressional stress dominate with lesser extensional tensile fractures (Lavallée *et al.,* 2013). This series of experiments demonstrate that the extensional and shear fracturing modes are intrinsically linked and that a change from extensional to compressional stress may be governed by the degree of applied stress (Lavallée *et al.,* 2013). At high and sustained rates of shear along brittle fractures,

frictional heating may cause partial melting (*e.g.* Spray, 1987). Experimental data indicate that frictional heating will be at its greatest at the slip boundary and may increase by $100^\circ C$ per metre from the starting temperature with increasing shear stress (Lavallée *et al.,* 2012). Pseudotachylyte veins and slickenslides found on andesite block faces at SHV, generated as a result of flash melting of trapped pyroclastic matrix between large andesitic blocks during pyroclastic density current emplacement, are estimated to have reached temperatures of ~1200°C, based on the temperature required to generate a dry andesitic melt (Grunewald *et al.,* 2000). The SHV andesite temperature, as bracketed by quartz and amphibole stability is ~830-870°C (Barclay *et al.,* 1998). The absence of the amphibole in the dark bands is consistent with heating, as SHV amphibole becomes unstable at temperatures >875 °C (Barclay *et al.,* 1998). Sieve-textured plagioclase in the fine-grained dark bands indicate high temperature disequilibrium; similar textures were reproduced experimentally at temperatures of between 1200 °C to 1410 °C under dry conditions (Tsuchiyama, 1985). However, the development of sieve textures in the plagioclase is much more extensive than typically seen in plagioclase xenocrysts entrained in the mafic inclusions; this is also consistent with very high temperatures. The partial melting of the plagioclase, which contrasts with the complete melting of the amphiboles, is ascribed to differing melting points of the SHV phenocryst assemblage, as well as kinetic factors. From thin section analysis it is estimated that at least 50% of the bulk assemblage in the dark bands must have been melted. The time that the partial melt remained at elevated temperatures in the dark bands is unclear, although experiments at 1000 °C showed that complete plagioclase recrystallisation can occur in 25 hours at pH_2O = 5 kbar or >1000 hours in dry conditions (Johannes *et al.,* 1995); this would suggest hours rather than minutes. The presence of ilmenite within the zones also suggests high temperatures or lower fO_2; ilmenite-magnetite pairs (Table 5.1) using the Fe-Ti oxide thermometer (Ghiorso & Evans, 2008) yield temperatures of 950-1053°C at NNO +0.6, although these are similar to those obtained in the andesite (Humphreys *et al.,* 2009). The K/Na ratio of cordierite in equilibrium with granitic melt is dependent on temperature and aH_2O, while pressure has little effect (Thompson *et al.,* 2002). The elevated K_2O and low Na_2O trace concentrations measured in the cordierite microlites (Table 5.1) are consistent with experimentally determined temperatures of at least 1100 °C and aH_2O of <0.5, measured from low-Li and low-Be cordierites at a range of temperatures of 800-1000°C and pressures of 3-7 kbar (Thompson *et al.,* 2002). Low H_2O concentrations in cordierites are related to increasing temperature and decreasing pressures (Mirwald, 1982). Volcanic

cordierite from Tuscany and Lipari, Italy with volatile contents ~0.3 wt % formed at >950 °C and <2 kbar (Armbruster, 1985). Analytical totals close to 100% (Table 5.1) suggest that the SHV cordierites also have low H_2O and CO_2 contents, indicating high temperature formation. The abundance of melt and mineral inclusions in cordierite also suggests rapid growth.

This wealth of petrologic evidence for increased temperatures in the dark bands implies that these were the focus of slip events, where frictional heating would have been at its greatest. A large increase in temperature to over 1000 $^{\circ}$C would commonly be associated with a large amount of slip in "cold" fault systems, but studies of pseudotachylytes in hot volcanic environments suggest that the slip required to generate the same texture is much smaller (Lavallée *et al.,* 2012; Kendrick *et al.,* 2012). It is inferred that the coarser light bands did not undergo the same degree of frictional melting as the dark bands; amphiboles do not show clear evidence for thermal decomposition (Fig. 5.6), although it is assumed that some heat dissipation must have taken place from the partial melt generation. Rounded plagioclase crystals in the light bands might be related to heating or to mechanical abrasion. Evidence for broken crystals within both the light and dark bands (Fig. 5.7) suggest comminution and resembles cataclastic textures seen in tuffisite veins (*e.g.* Tuffen *et al.,* 2003). Furthermore the lack of both melt and a recrystallised assemblage indicates that the light coarse bands did not undergo the same degree of frictional melting as the dark bands.

5.4.3 *Degassing and metal transport*

The development of shear zones with transient high permeability over the typical SHV andesite (which has a permeability of 6 x 10^{-16} to 5 x 10^{-12} m^2; Melnik & Sparks, 2002), would facilitate gas transport. A mixture of gas and particles were transported through these permeable zones, where fracturing and comminution of crystals took place (Fig. 5.10). The observed enrichment of the metals (*e.g.* Cu, Ag, Au) within the shear zones suggests a vapour transport origin, given their vapour-melt partition coefficients of >1 at magmatic pressures and temperatures (Simon *et al.,* 2006) (Fig. 5.8; Table 5.3), and this is consistent with enrichment of metals such as Zn in volcanic gas and aerosols emitted from SHV (Allen *et al.,* 2000). At low pressures, the vapour phase is made up of ~90 mol% H_2O, with the remainder CO_2, S gases (SO_2 and H_2S) and HCl (Hammouya *et*

al., 1998), although the proportions of these species, particularly the Cl-bearing species, are likely to vary with eruptive activity (Edmonds *et al.,* 2002). Cu will partition in favour of vapour over the melt, and is preferentially stabilised in the vapour phase by high concentrations of sulphur (William-Jones & Heinrich, 2005), with published partition coefficients of 63-316 at 800°C (Simon *et al.,* 2006) and 100-200 at 825°C (Lowenstern *et al.,* 1991) (Table 5.3). In the dacite lavas erupted from Pinatubo in 1991, elevated concentrations of Cu (in the groundmass and in magnetite in mafic enclaves) and Zn were linked with fluid transport from basalt (Pallister *et al.,* 1991). Au will partition strongly in favour of the vapour phase in the presence of high H_2S, H_2O, NaCl and KCl (Zajacz *et al.,* 2010). Experimental Au vapour-melt partition coefficients were up to 200 in an andesitic melt at <NNO +0.5 (Zajacz *et al.,* 2012); however, they drop rapidly over the H_2S-SO_2 transition (>NNO+0.5) in the volatile phase (Zajacz *et al.,* 2012). This implies that changes in f_{O_2} during degassing could result in rapid deposition of metals (see below). Published partition coefficients for bulk fluid/melt and vapour/melt are plotted on Fig 5.5. The trend in their magnitudes matches the trend in the metal enrichments in the shear zones well, further substantiating the idea that the zones were the sites of vapour transport after brittle failure and consequent increase in permeability.

5.4.4 *Volatile resorption following partial melting*

The passage of gases through the fracture zones would have ceased once frictional melting reduced the permeability of the zone or gas supply ceased (Fig. 5.10). The high temperatures induced by the heating may have caused resorption of some of the volatiles back into the newly-formed partial melt. An increase of 100°C will increase sulphur solubility by a factor of 7 to 9 (Haughton *et al.,* 1974). Vapour-melt partition coefficients for metals may also decrease with increasing temperatures (William-Jones & Heinrich, 2005), leading to metal resorption into the melt, although changes in oxygen fugacity (f_{O_2}) may be more significant than temperature for metal volatile resorption, based on the experiments of Zajacz *et al.,* (2012). Volatile anions that have been resorbed into the melt may also affect metal vapour-melt partition coefficients by forming complexes with the metals (*e.g.* Au chloride or sulphide complexes; Botcharnikov *et al.,* 2010).
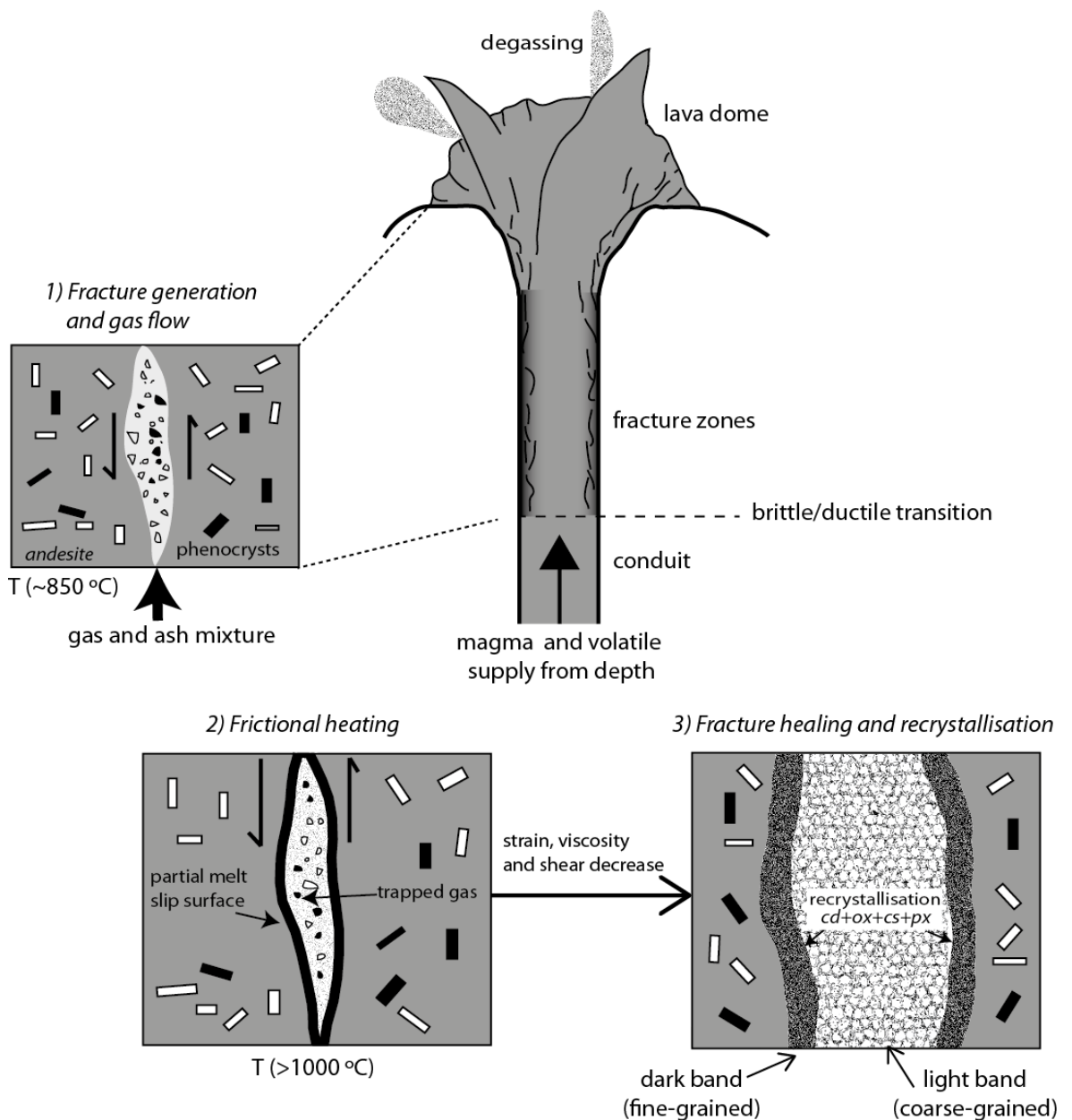
Figure 5.10: Schematic cartoon showing the evolution of the shear zones. 1) Fractures are generated by brittle failure at high strain rates at either the conduit walls or shallow dome as the magma transitions from brittle to ductile behaviour. The formation of the permeable fracture allows outgassing of a vapour and ash mixture. 2) Slip causes frictional heating at the slip surface to temperatures >1000 °C, and eventually partial melting (dark bands), which effectively stops gas flow and seals the fracture. Volatiles are resorbed into the partial melt, preserving the geochemical signature of the vapour phase. 3) Recrystallisation of the peraluminous partial melt takes place, with a crystallising assemblage of cordierite, cristobalite, plagioclase, cordierite, oxides, orthopyroxene and Cu-Fe sulphides in the dark fine-grained bands. The light coarser-grained bands with less melt (<3 % vol) are comprised of phenocrysts and crystal fragments (plagioclase, amphibole, orthopyroxene), and void space.

Water solubility is retrograde at low pressures and high temperatures (Liu *et al.,* 2005; Baker 2012), so heating during brittle failure would have the effect of lowering water solubility. However, the increase in melt fraction (>50 % wt) in the dark bands would also enable net H_2O resorption into the melt. Volatile concentrations will also be dependent on pressure in the magma, and the likely pressure changes during shearing are difficult to constrain. If the fractures were connected to the dome surface then the internal fracture pressure could drop to atmospheric pressure towards the surface as gas escapes, however, if the gas remained trapped in the fractures, pressure could increase to at least equal the magmastatic pressure, or even overpressure due to gas expansion. Cycles of magma fracturing and sealing could result in complex fluctuations in pressure. At any rate, the absolute mass concentration increase of volatiles in the partial melt will be proportional to the mass flux of vapour through the zone, which in turn will depend on fracture permeability and magmatic gas supply duration.

5.4.5 Recrystallisation of the partial melt

The fine-grained nature of the zones and the gross textures reproduce well those from experiments simulating frictional melting and recrystallisation (Lavallée *et al.,* 2012). We therefore infer that as they cooled, the partially melted shear zones recrystallised, preserving the bulk geochemical signature of the vapour and distributing the volatile species between minerals and (sparse) glass (Fig. 5.10). Although we do not rule out that the fractures might have acted as an open pathway to the surface, the presence of the Cu-Fe sulphides as part of the crystallising assemblage suggests that metal deposition is not the result of a fumarole type metal enrichment. Cu-Fe sulphide inclusions in plagioclase and between Ti-magnetite clusters and at the edge of crystals (Fig. 5.9) indicate that this was an early-crystallising phase, and that sulphide saturation was achieved in the melt, possibly due to sulphur resorption, efficiently sequestering Cu. Sulphide saturation is reached at sulphur concentration of <500-1000 ppm for rhyolitic melts with f_{O_2} buffered at NNO, and 1000-1500 ppm at NNO+0.5 (Liu *et al.,* 2007). The relative f_{O_2} of the pre-eruptive andesite has been estimated at NNO+1 (Devine *et al.,* 1998). Ti-magnetites are elevated in abundance (<8%) in the shear zones compared to the SHV andesite (0.3–2.5%; Humphreys *et al.,* 2009). The rapid, unbuffered crystallisation of abundant Ti-magnetite might cause more reducing conditions in the melt, resulting in a reduction of the sulphur concentration and sulphide saturation and hence precipitation of metal-bearing sulphides (Sun *et al.,*

2004). Titanomagnetite crystallisation may also prompt Fe-Cu sulphide saturation (which also sequesters Au) due to conversion of sulphate to sulphide in the melt (Sun *et al.,* 2004; Jenner *et al.,* 2010). Experiments demonstrate that after ~25% Ti-magnetite crystallisation, melts may lose up to 60% of their initial Au content and 35% of their initial Cu due to Cu-sulphide fractionation at 800 °C, 100 MPa and NNO (Simon *et al.,* 2008). Fresh pumice from Vulcán Popocatépetl is reported to contain metal-bearing minerals on vesicle walls crystallised from the trapping and condensing of magmatic gas (Larocque *et al.,* 2008). Sudden depressurisation can result in metal deposition *e.g.* Au in quartz veins; cavity expansions generates extreme reductions in fluid pressure and therefore generating a low density vapour leading to flash vaporisation coeval with silica deposition (Weatherley & Henley, 2013). The relative depletion of Ca and Na concentrations in the shear zones relative to the average andesite (Table 5.2) may reflect the partial destruction of plagioclase through melting within the zones. This could also enable Na to form complexes with chlorine vapour thus depleting Na from the melt as it partitions towards to the fluid (Shinohara, 1989), thus providing more evidence for vapour interaction. However, it is unclear whether these chloride complexes will form easily at low pressures (Shinohara, 1994). Although an enrichment of SiO_2 in the shear zones compared to the average phase V andesite is observed (Table 5.2), it should be noted that the bulk rock SiO_2 contents in erupted SHV andesite have been measured up to 62 wt % SiO_2. Deposition of silica sourced from hydrothermal or magmatic fluids may also account for high bulk silica content in the shear fractures (Edmonds *et al.,* 2003).

5.4.6 Cordierite crystallisation

The presence of cordierite, which is very unusual in a volcanic rock, is likely to be the result of crystallisation from a highly peraluminous hydrous partial melt generated by the frictional heating of the andesite crystal assemblage. Cordierite stability requires high activities of alumina, alkalis and silica, high Mg/(Mg +Fe) and low pressures (<5 kbar) (Douce, 1992; Clemens & Wall, 1998). Cordierite is absent from the normal andesite crystallising assemblage, with the average SHV rhyolitic glass composition depleted in the Al_2O_3 (~10 wt %), FeO (~1.5 wt %) and MgO (~0.05 wt %) needed for cordierite crystallisation (Humphreys *et al.,* 2010). Flash melting of SHV andesite within pyroclastic flows generated a resultant glass in pseudotachylyte veins with increased Al_2O_3 (~20 wt %), FeO (7 wt %) and MgO (2 wt %) concentrations in comparison to the average SHV

glass, but with no reported cordierite (Grunewald *et al.,* 2000). Preferential melting of plagioclase and amphibole could not only contribute the relative enrichment in Al, Fe and Mg that enables cordierite crystallisation, but would also provide the excess silica needed to form the quartz/cristobalite microlites grown in equilibrium with the cordierite (Douce, 1992). The major element geochemistry of the dark bands has an elevated alumina saturation index ASI (molecular ratio Al_2O_3/ CaO + Na_2O + K_2O) of 1.2-1.4 in comparison to the average SHV bulk andesite and rhyolitic glass composition of <1, as a result of a relative depletion in CaO and Na_2O with similar Al_2O_3 concentrations (Fig. 5.7) to the bulk andesite and glass. This indicates that a strongly peraluminous melt is likely to have existed in the dark bands, which allowed cordierite crystallisation along with the rest of the partial melt crystallizing assemblage (orthopyroxene, cristobalite, quartz, oxides and plagioclase). The distribution of the cordierite throughout the dark bands implies that the melt must have homogenised and chemically mixed to a degree, rather than just isolated pockets of 'protomelt' as observed in the pseudotachylyte veins (Grunewald *et al.,* 2000) and in 'dry' frictional melting experiments of andesite (Lavallee *et al.,* 2012). Prior to this study, volcanic cordierite has been previously observed only in a handful of settings. At Lipari, cordierite is associated with significant amounts of crustal contamination involving metapelites (Barker, 1987). At White Island Volcano, New Zealand, cordierite found in xenoliths ejected during phreatomagmatic explosions was part of the hydrothermal assemblage (Wood, 1994). Cordierite has been reported in the Krakatau 1883 pumice (Simkin and Fiske, 1983) and in the Mont Pelee 1902 lava dome (Lacroix, 1949). The finding of cordierite in both samples from differing extrusion phases at SHV suggests that the process of cordierite formation in these shear zones might be prevalent in similar andesitic shear zones.

5.4.7 *Healing of the fractures*

The recrystallisation of the partial melt in the dark bands signified the closure and healing of the fractures (Fig. 5.10). Frictional melts generated in faults have viscosities lower than the surrounding material and thus may act as a lubricant at the slip surface (*e.g.* Di Toro et al 2006a; Kendrick *et al.,* 2012). To calculate the melt viscosity for the shear fracture partial melt the empirical model of Giordano *et al.,* (2008) is used. The bulk shear zone compositions (Table 5.2) are used to reflect the partial melt composition (even though in detail, this assumption is probably incorrect as relict partially melted crystal cores

remain). Viscosities of 10^4 to 10^6 Pa s are obtained for a dry partial melt at slip surface for both fractures at temperatures of 1000-1200°C, where the change in melt composition (rhyolitic in the normal andesite, to andesitic in the shear zones), high temperatures, and melting of crystals leads to a lowering of both the melt and magma viscosity. Furthermore, using the assumption that a maximum of 2 wt % H_2O was resorbed into the partial melt or contributed by amphibole melting this lowers viscosity to 10^2 to 10^3 Pa s. This contrasts with estimated bulk viscosity for the andesite of 10^9 to 10^{14} Pa s (Sparks *et al.,* 2000) and suggests that the presence of partial melt at the slip surface could have resulted in a significant change in the slip behaviour in the shear zone. Relaxation or flow of the melt would eventually lead to healing of the fracture, analogous to the healing of tears in crystallising metal alloys (*e.g*. Farup *et al.,* 2001). The volatile signature must have been preserved during rapid quenching before overprinting could occur. These zones annealed to varying degrees after the cessation of slip, although effective and total healing across the whole fracture is unlikely in highly crystallised (>90%) magma (Okumura *et al.,* 2013). Folds within both fractures indicate that they went through the transition from a brittle to ductile regime post-welding, probably within the shallow dome before being erupted, suggesting that the shear zone viscosity returned to a similar level to the surrounding andesite. The shearing and frictional melting process is clearly uneven across the shear zones, giving rise to the alternating pale, coarser bands and the darker, fine-grained bands (Fig. 5.1). This may be the result of a single slip event forming a series of en-echelon fractures as brittle failure propagates across the shear zone analogous to strike-slip faulting. Bands of irregularly shaped vesicles 'tears' within the annealed dark fine-grained bands may also indicate multiple episodes of brittle failure within the fractures. The shear zones may also have originally been part of a larger branching network of sheared zones (as observed in Iceland; Tuffen *et al.,* 2003). Development of a low viscosity network of shear fractures lubricated by partial melt at the conduit walls could have the effect of increasing ascent rates, allowing the more viscous plug to rise faster in the conduit centre (Okumura *et al.,* 2013). Cycles of increased extrusion rates of >35ms^{-1} at SHV for short durations (minutes) in Phase V (Odbert *et al.,* 2014) could tentatively be linked to the sudden lowering of viscosity during the development of the shear zones.

5.4.8 Timescales

The duration that the fractures acted as pathways for vapour flux is unclear. If the fracture did not reach the surface, gas would have been unable to escape and could have been stored inside the fractures effectively pressurising and holding open the fracture after slip had ended (Molina *et al.,* 2004). Fracture depressurisation and subsequent gas loss may simply be the result of the fracture networks formed at conduit walls reaching the surface during lava extrusion. Variable SO_2 flux at SHV over short timescales (minutes to hours) has been attributed to the release of a SO_2-rich fluid stored in sealed fractures or pore space in the dome after rockfalls and pyroclastic density currents (Edmonds *et al.,* 2003). At Santiaguito, Holland *et al.,* (2011) propose that fractures are held open by trapped gas at pressures of ~3 MPa prior to explosion, with increased SO_2 emissions. At SHV, a transition from explosive to effusive activity in July 2003 was also correlated with increased SO_2 emissions (Edmonds and Herd, 2007). High overpressures (~25 MPa) preceding the vulcanian explosions in Phase IV (Chardot *et al.,* 2010) may suggest that gas was stored at depth prior to the explosion. Assuming that the fractures formed at the conduit walls at depth, it could be speculated that if the fractures were generated at a maximum depth of 1500 m (from seismic estimates, Neuberg *et al.,* 2006) with an average extrusion rate of 0.1 ms^{-1} in Phase V in the seven days preceding the dome collapse (Stinton *et al.,* 2014), a maximum time of ~ 4 hours can be calculated for the duration of time it would take for the fracture zones to reach the dome, where they would remain until erupted. However, this is an oversimplification as for example this does not take into account the effect of viscosity changes discussed above. It is likely though that both samples underwent brittle failure and healing relatively close (days to hours) to deposition, as we would expect textural overprinting if they remained in the dome for longer. The degree of partial melting in the plagioclase phenocrysts discussed in section 4.2, also suggests that the lifetime of the fractures was limited to hours rather than days. It cannot be completely ruled out that the fractures may have acted as an open channel for gas sourced from depth, with its lifetime depending on this supply (Lensky *et al.,* 2008). However, the association of the shear zones with large eruptive events might suggest that they were ripped off the conduit walls during a vulcanian explosion or dome collapse. Higher permeability rhyolitic tuffisite veins from Chaiten are calculated from diffusion profiles to have a life span of 30 minutes to hours with a high gas velocity, whereas a low permeability welded rhyolitic tuffisite vein from Torfajokull, Iceland could be as long

lived as a day or more (Berlo *et al.,* 2013). H_2O diffusion into healed obsidian faults from Lipari, Italy indicates faster timescales of 10-30 minutes (Cabrera *et al.,* 2011). The timescales from these studies are within the range of repeated swarms of low frequency earthquakes at SHV lasting hours to days (Neuberg *et al.,* 2006). Diffusion calculations for the shear zones from SHV are not viable, predominantly owing to the lack of constraints on pressure, and the H_2O content of the melt before diffusion takes place.

5.5   Conclusions

This is the first petrological and geochemical study to identify a preserved gas pathway in an erupted lava block from an andesite lava dome, and allows us to understand gas loss mechanisms as well as the behaviour of metals during magmatic degassing. In conclusion, the shear zones formed either at the shallow conduit walls or dome, where critical strain, viscosity and shear rates were reached allowing the magma to fail in a brittle manner. This development of permeable fractures has allowed the transient flux of magmatic gases within fractures until fracture healing. Geochemical evidence (enrichment of the zones in metals) shows that frictional melting, volatile resorption and consequent viscosity decrease is the mechanism at work for annealing the fracture networks, not merely a decrease in strain rate. The temperature increase required for frictional melting is substantial (a minimum of 300 °C), and the peraluminous partial melt thus produced has led to the highly unusual occurrence of volcanic cordierite. The transportation of gases through these zones may have implications in transitions in eruption style as these gas pathways shut off as volatile resorption takes place. Although both shear fractures in this study are correlated to extrusive phase ending activity, we suggest that they could be commonly found in deposits throughout the extrusive phases. Transitions from extrusive to explosive behaviour are common during extrusive phases lasting months to years at SHV, but owing to the dangerous nature of sampling during activity this will be difficult to ascertain.

Chapter 6: Conclusions

This thesis has sought to address the following questions about the flux of material in andesitic magmatic systems by using samples collected from erupted products of Soufrière Hills Volcano, Montserrat:

1. What diversity in petrological characteristics is present in the enclave population, and can this be used to constrain magma mingling processes?
2. What are the main controls on the geochemical composition of the enclaves (fractionation versus mixing) and has this changed through the course of the eruption?
3. Have these mixing and mingling mechanisms changed in their character through the course of the eruption?
4. Given that the system appears to be extremely volatile-rich, how important is the mafic magma for supplying volatiles to the system?
5. Given that the bulk of the mafic magma does not erupt; is there textural evidence in the andesite that gives insights into the mechanisms of outgassing of volatiles sourced from mafic magma occurs?

6.1 Magma mingling processes

The study of mafic enclave textures, petrology and geochemistry may be used as a window into magma mingling processes. At SHV, previous work has focussed on the early eruptive phases I to III (Murphy *et al.,* 2000; Humphreys *et al.,* 2009; Mann, 2010; Barclay *et al.,* 2010), but a change in eruptive phase length in phases IV and V leads us to examine erupted products from phase V to examine question (1): **What diversity in petrological characteristics is present in the enclave population, and can this be used to constrain magma mingling processes?** To answer this question, detailed textural, petrological and geochemical analyses coupled with field observations were used in chapter 3 to define a

classification scheme for enclave types to elucidate magma mingling processes during phase V. In summary, type A enclaves are defined by low inherited phenocryst proportions (>8 wt%), presence of high-Al amphiboles, chilled margins and are basaltic in composition (49–52 wt % SiO_2), indicating limited mingling with the andesite prior to enclave formation. Type B enclaves are defined by a high proportion of inherited phenocrysts (16–26 %), rare to absent high Al-amphiboles, lack of chilled margins and have a broad range of bulk compositions (53–58 wt % SiO_2), implying an increased degree of interaction between the andesite and mafic magmas prior to enclave formation compared to type A enclaves. This allows us to reconstruct the mingling processes of enclave formation during phase V. The low degree of hybridisation and evidence for a rapid cooling indicate that type A enclaves formed after intruding mafic magma was injected directly into the andesite, perhaps via a plume of mafic magma (Fig. 6.1). Type B enclaves are likely to be disrupted fragments of a vesiculating hybrid layer, which underwent slower cooling against the andesite and was therefore able to mingle more effectively (Fig. 6.1). Type C enclaves, which are composite in nature, with inner portions akin to type A and outer portions akin to type B, are evidence of the complexity of the mingling processes between the two magmas. This may reflect multiple mixing events, where more mafic magma (type A) has intruded into a more hybridised mafic layer (type B) (Fig 3.15).

Classification of enclave types such as at Unzen, Japan (Browne *et al.,* 2006) have been used to define temporal mingling dynamics, but the broad range of textures and petrology (*e.g.* differing rim sieve-texture widths in plagioclase phenocrysts within the same enclave) imply a more dynamic and complex set of mingling conditions existed at SHV during phase V. The classification and interpretation of the enclave types from this study indicates that physical transfer of mafic material to the andesite was not simply via a single mingling model. Evidence for enclave disaggregation is observed in phase III and IV andesite (Humphreys *et al.,* 2012), although this has not been examined in phase V andesite, qualitative observations in the field of small clustered enclave fragments imply that this process took place in phase V. This leads to the question as to why a significantly higher proportion of type B *vs.* type A enclaves are erupted in phase V. It could be simply that the majority of enclaves have been sourced from a hybridised mafic layer, implying that this is the predominant method of transfer of mass and volatiles from the mafic to andesite magma at SHV. However, Edmonds *et al.,* (2014) suggest that some SHV

enclaves with high initial melt contents (<40%) after entrainment into the andesite, may disaggregate via 'auto-fragmentation' as gas expands leading to volatile overpressure which 'bursts' the enclaves, thus transferring volatiles and crystals to the andesite (Fig. 6.1). This process could be a reason why very highly vesicular enclaves (type A) are less prevalent in the erupted andesite (Edmonds *et al.,* 2014). However, the lack of high-Al amphiboles in the andesite is puzzling (Murphy *et al.,* 2000, Couch *et al.,* 2001; Humphreys *et al.,* 2012), as we would expect to observe the amphibole, if type A enclaves are being preferentially disaggregated. Therefore, further work needs to be done to constrain the nature of disaggregated transferred material to the andesite in phase V, and therefore the proportion of enclave types formed. This raises implications in our understanding of mingling dynamics at SHV and other andesitic systems, as much of our assumed knowledge of magma mingling is defined by the study of the surviving erupted enclaves. The results from this study demonstrates the need for detailed studies of mafic enclaves, where the sample size needs to be wide enough to fully capture the diverse range of textures, petrology and composition of mafic enclaves.

A novel part of this study has been ability to compare to earlier eruptive phases at SHV, which will be discussed in more detail below. Mann (2010) suggests based on a classification scheme established for phase II enclaves, that 'type 3' enclaves (identified by high REE concentrations) may be derived from a shallower magma source than the other types. As such in this study we find no comparable enclave type from phase V, which may suggest that enclaves are no longer derived from this magma source. However, without a comparable standardised textural and petrological classification of enclaves from all eruptive phases it is difficult to ascertain the relative importance of abundances of the enclave types.

6.2 Controls on mafic enclave and andesite composition?

Detailed work on the petrogenesis of the mafic enclave and SHV andesite magmas thus far has been focussed on the erupted products from phase I (Zellmer *et al.,* 2003a). Therefore, after five phases of activity this thesis set out to answer question (2): **What are the main controls on the geochemical composition of the enclaves (fractionation *vs.* mixing) and has this changed through the course of the eruption?** In summary, geochemical data presented in chapter 4 show that whilst fractional crystallisation explains

well the range of phase I mafic enclave compositions, it cannot describe the range of phase III and V enclave compositions. Application of purely fractional crystallisation models using differing crystallisation assemblages to fit REE data require a significant increase in amphibole (~100 %), which proves to be unreasonable based on the petrography of the enclaves. Instead the dominant control on the range of enclave bulk compositions can be attributed to differing degrees of mixing between the andesite and mafic magmas from phases III to V.

Although mixing between the andesite and mafic magmas has become the dominant control in the bulk geochemistry of the mafic enclaves over the course of the eruption, the mafic end-member progressively changed in selected major (FeO and MgO) and trace (V and Sc) concentrations from phases I to III. Phase III and V mafic enclave compositions lie on the same linear trend implying that they have a similar mafic end-member. The reason for the change in the mafic end-member is not clear, but is perhaps due to progressive deeper tapping of a single compositionally stratified mafic magma source, or is maybe evidence for different batches of mafic melt over the course of the eruption. Differing mafic end-member compositions over the lifetime of a volcano, where magma mingling is prevalent, have been observed before such as at Unzen, Japan (Vogel *et al.,* 2008). Evidence for repeated intrusion of two distinct mafic magmas mingling with the host dacite over the lifetime of Unzen, Japan (550, 000 years), is inferred from differences in REE and trace elements highlighted by Polytopic Vector Analysis (Vogel *et al.,* 2008). However, the changes in the mafic end-member at SHV are over the course of the current eruption, and therefore on a much shorter timescale. The fractional crystallisation models in chapter 4 imply that the 'cryptic' crystallisation of amphibole at depth may be significantly more in phases III and V, than phases I and II. This is important as amphibole contains H_2O, and therefore this could signify changes in the H_2O of the parental mafic melts. Changes in the mafic end-member compositions therefore could lead to addition or reduction of volatiles to the andesite, which has implications for the driving forces of andesitic eruptions.

The bulk SHV andesite composition has remained relatively consistent over the course of the eruption. This relative consistency may be due to the proportion of mafic material mixed into the andesite and its composition. The total erupted mafic material in the form of macroscopic mafic enclaves is around 6 % (Fig. 1.7), but this is the surviving

164

mingled proportion, and therefore does not actually influence the measured andesite bulk chemistry. Disaggregated mafic material in the form of crystals, phenocryst overgrowth rims and crystal clots are included in the andesite bulk composition. In phases III and IV, this is estimated to be 6 % of the total erupted andesite (Humphreys *et al.,* 2012), but it is unlikely that this proportion will have a significant effect on the bulk andesite composition. For example, although plagioclase X_{An} contents in mafic enclaves can be significantly higher than observed in the andesite, it is questionable how much difference to the total bulk composition this would make. The disaggregation of an enclave for example with a bulk composition (crystals and melt) of 55 wt % SiO_2 into the andesite is not going to substantially alter the andesite bulk composition unless there are significantly high levels of enclave disaggregation. Although mafic enclave glasses can have higher K_2O and TiO_2 concentrations than the andesite melt, overall the glass compositions are very similar (Fig. 3.13), and therefore if melt transferred via disaggregation, it will not significantly alter the overall andesite melt composition. The generation of andesite compositions via magma mingling and subsequent enclave disaggregation is therefore highly dependent on the compositional contrast between the two magmas and the level of enclave disaggregation.

6.3 Mixing relationship changes over the course of the eruption

The results from chapters 3 and 4 show that the erupted material from phase V has a complex mixing history and that the bulk geochemistry appears to have changed from earlier phases. This leads to question (3): **Have these mixing and mingling mechanisms changed in their character through the course of the eruption?** Petrological, textural and geochemical analysis demonstrates a change in the mixing relationship between the andesite and mafic magmas over the course of the eruption. The high proportion of the hybrid type B enclaves observed in the field (Fig. 3.6), the loss of the compositional gap in SiO_2 between the andesite and mafic enclaves in phase V (Fig. 3.11), and geochemical modelling, all indicate that the mafic magma erupted in the form of enclaves has become more hybridised over the course of the eruption. This leads us to examine the possible reasons for the change in the ability of the two magmas to mix more efficiently.

6.3.1 Influence of bulk geochemistry change?

The bulk geochemistry of the mafic enclaves shows that the mafic-end member may have changed, but whether this compositional change has enabled greater mixing between the two magmas is unclear. The bulk Fe concentrations in the mafic enclaves have decreased to become closer to the andesite concentrations (Fig. 3.11), but Mg, V and Sc concentrations have all increased, thus moving away from the andesite (Figs. 3.11; 4.5). These changes in the trace and major element chemistry are probably not to a large enough degree to significantly alter the compositional contrast between the magmas and promote more efficient mixing. Compositional changes in the mafic end-member could only cause increased mixing between the magmas, if it was coupled with significant viscosity and temperature change. Therefore, it appears unlikely that compositional changes in the mafic enclaves across the length of the eruption have been solely the cause of increased mixing between the two magmas.

6.3.2 Influence of temperature change?

Increased mixing between the andesite and mafic magmas could have been promoted by a reduction in the temperature contrast between the magmas. A lower temperature contrast lowers the cooling rate and slows crystallisation of the intruding mafic magma thus allowing greater mixing (Sparks & Marshall, 1986). Any reduction in the temperature contrast between the two magmas would also have the effect of lowering the melt viscosity contrast. There is no strong evidence of a systematic temperature change in the intruding mafic magma from the mafic enclaves across the phases, but constraints on temperature from the mafic enclaves are poor. However, new results from Fe-Ti oxides geothermometry from phase V andesite, show a global temperature increase from 835°C in phase I to 845°C in phase V (Devine & Rutherford, 2014). This suggests that progressive heating of the andesite may have taken place over the course of the eruption since the initial mafic intrusion (Devine & Rutherford, 2014). The absence of quartz within the phase V andesite samples used in the above study is also cited as evidence for elevated heating (Devine & Rutherford, 2014); however, it should be noted that the results of this study show that quartz is not only present in the phase V andesite, but also in some mafic enclaves. A system wide increase in the temperature of the andesite magma over the course

of the eruption could lead to a lower viscosity. For example, the viscosity of the SHV andesite rhyolite melt (using the empirical model of Giordano *et al.,* 2008) can be calculated as 5.3 log Pa s (assuming 5 % wt H_2O) at 850 °C; a 10 °C increase reduces viscosity by 0.1 log Pa s; a 30 °C increase by 0.3 log Pa s. Any lowering of viscosity in the andesite would also increase the mobility of the gas phase through the andesite, thus advecting heat more efficiently (Bachmann & Bergantz, 2006) leading to more convection. Although the high crystal content of the andesite will limit the effect of any melt viscosity changes to the effective viscosity (melt + crystals).

Evidence of a global increase in the andesite temperature using Fe-Ti geothermometry after repeated mafic intrusions (Devine & Rutherford, 2014) may result in a reduced temperature contrast between the magmas. This could promote more efficient magma mixing, which tallies with the observation of a more hybridised mafic magma in phase V. Nonetheless, a 10 °C increase in the andesite temperature is clearly not sufficient to reduce the temperature and viscosity contrast enough to alter magma interaction from mingling to mixing, as demonstrated by the continuing presence of mafic enclaves in the erupted andesite. Whether the andesite magma body as whole would have been uniformly heated is debatable. Murphy *et al.,* (2000) suggest that the pre-eruptive andesite magma chamber could have been zoned in respect to temperature before eruptive activity commenced in phase I. It could be possible that chamber may have become more strongly zoned in respect to temperature with continuing transfer of heat from a mafic layer. Conversely, although decreasing the temperature contrast between the magmas would lead to more efficient mixing, it could also lead to slower reheating rates (Bachmann & Bergantz, 2006).

The transition between explosive and extrusive behaviour at arc volcanoes may be in part linked to temperature changes in the host magma caused by mafic magma intrusion (Ruphrect & Bachmann, 2010). The differing eruption styles of the effusive 1846-47 and plinian 1932 eruptions at Quizapu, Chile have been attributed to the host magma temperatures (Ruphrect & Bachmann, 2010). The effusive 1846-47 eruption showed evidence for magma mixing, where the intrusion of a hotter mafic magma led to significant reheating of host magma, elevating temperatures from 830 to 1000 °C (Ruphrect & Bachmann, 2010). The increase in the host magma temperature is interpreted to have enhanced magma degassing, but reduced rapid magma expansion and explosive behaviour

(Ruphrect & Bachmann, 2010). In contrast, the plinian 1932 eruption showed no evidence for magma reheating by mafic intrusion; therefore, it is concluded that the gases were trapped longer in magma during ascent, leading to explosive behaviour (Ruphrect & Bachmann, 2010). However, despite an apparent increase in the global andesite temperature at SHV (Devine & Rutherford, 2014), phases IV and V were as explosive as earlier phases, with some of the largest vulcanian explosions to date (Wadge *et al.*, 2014).

6.3.3 Influence of mafic magma supply change?

Over the course of the eruption the proportion of mafic enclaves observed in the erupted deposits has increased since phase I (1 to 8 %; Murphy *et al.,* 2000; Komorowski *et al.,* 2010, Mann, 2010; Barclay *et al.,* 2010; this study). This may indicate that perhaps the volume of the intruding mafic magma has increased significantly. In the 'gas sparging' model proposed by Bachmann & Bergantz, (2006), it is suggested that remobilisation of the andesite mush via advection from gas requires 0.5 km^3 of gas at magma chamber pressures sourced from ~2–3 km^3 of mafic magma. Thus far from 1995 to 2010, only ~0.06 km^3 of mafic magma in the form of mafic enclaves has been erupted suggesting a large volume of the mafic magma remains unerupted at depth, which is corroborated by continuing 'excess' sulphur emissions to date (*e.g* Edmonds *et al.,* 2014). There is no clear evidence from gas emissions or geophysical data to suggest an overall increase in the rate of mafic magma supply. The higher proportion of mafic enclaves could just reflect a portion of eruptible melt reservoir containing more enclaves is being progressively accessed. In section 6.1 the possibility that type A enclaves may be more susceptible to disaggregation after formation than the more hybridised type B enclaves was discussed. Therefore, perhaps as the mafic magma becomes more hybridised over the course of the eruption, the increased volume of mafic enclaves erupted is just a function of a lesser susceptibility to disaggregation. To test this hypothesis, future work examining the proportion of disaggregated mafic material in the andesite in phases I and II is required.
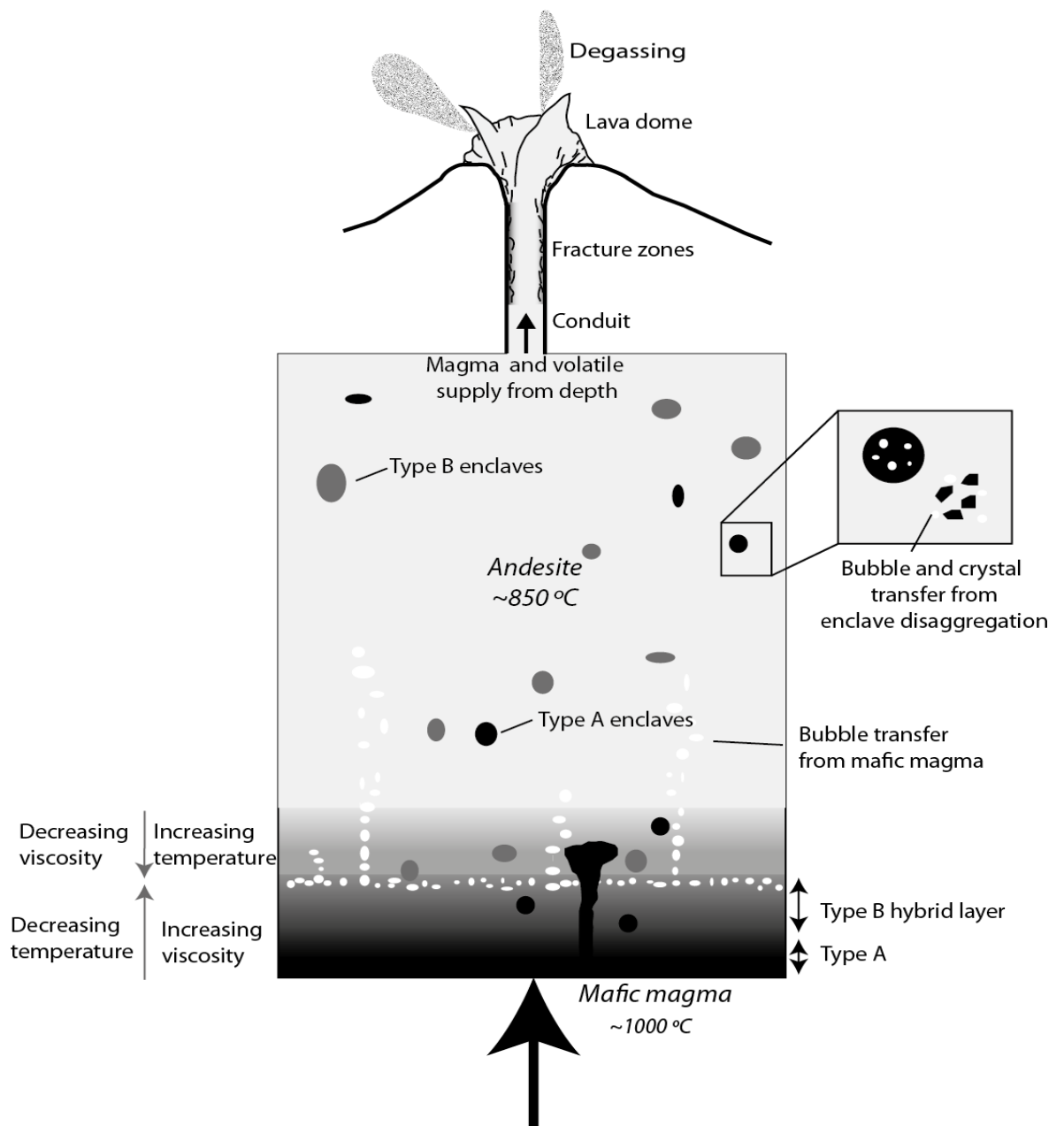
Figure 6.1: Schematic summary model of mafic-andesite interaction and flux of material at SHV (not to scale). Mafic magma intrusion at depth remobilised the andesite mush. Transfer of heat either via advection or bubble transfer led to convection and remobilisation of the andesite (Bachmann & Bergantz, 2006). Mafic magma may be mingled into the andesite via mafic plumes (type A enclaves) and detachment from or breakup of a vesiculating hybridised layer (type B enclaves). Progressive mafic magma intrusion has resulted in more hybridised enclaves (type B) over the course of the eruption as mafic-andesite interaction has changed. Fluids rich in H_2O, CO_2 and S are transferred from persistent mafic intrusion at depth (*e.g.* Edmonds *et al.,* 2001) and disaggregation of enclaves (Edmonds *et al.,* 2014). The decoupled metal-rich vapour phase may be degassed through shear fractures in the shallow conduit or dome.

6.4 Significance of volatile transport in the andesite

The transfer of volatiles (such as H_2O, CO_2 and sulphur) from the intruding mafic magma to the andesite can increase the mass and volume of the vapour phase in the host magma. This leads to question (4): **Given that the system appears to be extremely volatile-rich, how important is the mafic magma for supplying volatiles to the system?** Work carried out by Edmonds *et al.,* (2014) shows that volatile transfer may also occur not only directly from the intruding mafic magma, but also via the disaggregation of enclaves. Questions remain over the volatile content of the intruding mafic magma, differing modelling using MELTS and rhyoliteMELTS have yielded variable H_2O contents ranging from 2–8 wt % H_2O (Humphreys *et al.,* 2012; Edmonds *et al.,* 2014). The results from this thesis also suggest that differences in the petrology between enclave types may be linked to different mafic melt volatile contents. The possible increase in 'cryptic' amphibole fractionation at depth could imply an increase in H_2O in the parental mafic magmas over time. These results still leave unanswered questions about the mafic magma volatile contents and transfer to the andesite. Quench-driven crystallisation of the mafic magma as it interacts with the cooler andesite drives gas exsolution and subsequently volatile transfer to the andesite. However, the depth at which the intruding mafic magma interacts with the andesite also influences gas exsolution and escape. Therefore, better constraints on the depths at which the andesite and mafic magmas interact are required at SHV.

Continuing 'excess' sulphur emissions at SHV indicate the presence of mafic magma at depth (*e.g.* Edmonds *et al*., 2001), but this leads to question (5): **Given that the bulk of the mafic magma does not erupt; is there textural evidence in the andesite that gives insights into the mechanisms of outgassing of volatiles sourced from mafic magma occurs?** In chapter 5 geochemical, petrological and textural evidence presented indicate that shear fractures generated in the shallow dome or conduit can be used as a pathway for gas transport (Fig. 6.1). Brittle failure of the magma generated by high strain rates in the shallow conduit or dome led to the formation of the shear fractures. The rapid increase in permeability allowed a transient flux of magmatic gases flow through the fractures until recrystallization of the partial melt at the slip surface effectively sealed the fractures. The enriched concentrations of metals such as gold and copper within the fractures, which are transported in a sulphur- and chlorine-rich vapour was used a tracer

for the presence of magmatic vapours. The generation of these shear fractures involved a substantial temperature rise, which led to the development of a highly aluminous partial melt and lowering of viscosity. The significant increase in the melt fraction at the slip surface led to the resorption of volatiles, thus preserving the geochemical signature of the magmatic gas. The subsequent recrystallization of the partial melt led to the unusual presence of cordierite and Fe-Cu sulphides. Although it is unclear how long the fractures were open and therefore the mass flux of gas of gas through the fractures, the sudden changes in permeability as the fractures open and close may affect the efficiency of volatile escape as magma ascends in the conduit.

The development and closure of these fractures may be important not only as a mechanism to allow volatile escape in the shallow magmatic system, but also could have implications for conduit modelling. The development of fracture networks could act as transient low viscosity shear zones at the conduit walls effectively lubricating magma ascent towards to the centre of the conduit (Okumura *et al.,* 2013), whilst the closure of the networks may have the opposite effect. This has implications for conduit modelling of stick-slip behaviour as an ascending magma rises in the conduit, where cyclic activity in lava domes can lead to transitions between explosive and effusive activity. Questions remain about the how widespread these fractures are within the dome and conduit, but as the samples studied in this thesis are from two separate eruptive phases this suggests that these could be a relatively common occurrence. This work has important implications therefore for hazard assessment at lava dome-forming eruptions, not just at Soufrière Hills.

6.5 Remaining questions at Soufrière Hills

SHV has been extensively studied since the eruption start in 1995 by many researchers, but many questions still remain about the processes driving the current eruption, and some of these are discussed in the above sections. The work in this thesis highlights that interaction between the mafic and andesite magmas has changed through the course of the eruption. However, as discussed in section 6.4, the volatile content of the intruding mafic magma is still unclear. A change in the mafic end-member composition coupled with an apparent increase in the 'cryptic' amphibole fractionation at depth could imply that the mafic magma volatile contents could have changed over time. Therefore, an

area to explore further is whether volatile contents have changed and what effect a more H$_2$O-rich mafic magma may have on the interaction between the mafic and andesite magmas. The source depth of the mafic magma intrusion is still unclear, as is the depth at which the andesite and mafic magmas interact. The difficulty in obtaining accurate depth estimates from existing geobarometers using quench-formed crystals in the mafic enclaves has already been discussed in chapter 3. Questions remain about whether two distinct magma chambers exist (Elsworth *et al.*, 2008) and how these might be connected. As yet there is no petrographical evidence to help contribute to the answers raised by these questions. At the time of writing SHV is presently in its longest pause of the current eruption. If the pre-eruptive andesite temperature continues to progressively increase, this could have wide implications for the eruption dynamics as discussed in section 6.3.2. Nonetheless, the supply of mafic magma is widely accepted as the driving force of the current eruption, and this thesis has shown that the nature of the supply has been variable over the course of the eruption. If the mafic supply were to cease, we would presume that the andesite would eventually begin to cool and return to a rigid crystal-rich mush state. Therefore, it remains to be seen how eruptive activity will behave and develop in future eruptive phases.

6.6 Broader implications for andesite systems

The work in this thesis highlights that in long-lived andesitic dome-forming eruptions the complex relationship between the mafic and andesite magmas may evolve over the course of an eruption. This thesis has shown that even in an apparent 'steady state' of continuing magma mingling and dome-forming activity, that detailed analyses of the erupted products highlight that a 'steady state' is inherently complex, and is anything but 'steady'. At SHV, the mafic magma composition has clearly changed over time from the well-documented phase I eruptive products. The ability of magmas to mix can also alter over the course of the eruption, where at SHV this has resulted in more hybridised mafic enclave compositions Thus, it is crucial to continue to monitor petrologically and geochemically the erupted products from andesite volcanism in ongoing eruptions. The volatile budget in andesite volcanism is complex, where volatiles derived from mafic magmas contribute and mix with pre-existing volatile phases in the andesite. This thesis has provided an insight into one of the mechanisms that is associated with how volatiles

may be transported through the andesite. Many of the andesite dome-forming eruptions around the world often transition between effusive and explosive behaviour. Therefore, the evidence that gases can be transported through shear fractures generated in the shallow conduit or dome can contribute to our understanding of the mechanisms behind abrupt switches in eruptive style. Finally, this type of detailed study is important to develop our understanding of the complexities of active volcanic systems, as it can feed into hazard assessment of andesite dome-forming eruptions, where magma mixing is the driving force behind eruptive activity.

6.7 Future work

Specifically to SHV, further work on constraining the temperature of the mafic magma is required and ideally to elucidate whether there has been a change over time. However, as highlighted earlier in the thesis many of the geothermometers and geobarometers used in petrology are not adequately calibrated for crystals formed during quench crystallisation. Therefore, the development of thermometers that be can be used in relation to mafic enclaves would provide better constraints on mafic magma temperatures and depth of mixing between the two magmas not just at SHV, but also for other magma mixing systems. A detailed approach to examining the differences in enclave textures could alternatively be used to investigate the relative differences in temperature. For example, Mollo *et al.,* (2012) correlated plagioclase morphology with temperature. Crystal size distribution analysis used by Coombs *et al.,* (2002) in mafic enclave experiments highlighted differences in enclaves caused by the degree of cooling, which could be similarly utilised.

Further detailed work is needed in further in constraining the quantity of mafic material disaggregated into the andesite throughout the eruptive phases as discussed in section 6.1. This would give a better measure and indication of the variability of the contribution of total mafic material that has been mixed into the andesite over the course of the eruption. The results from this thesis show that the mafic end-member may have changed and that the mixing relationship between the magmas has evolved. Further work quantifying this change across the phases would be useful to help understand what is affecting these changes. Electron microprobe analyses of the framework amphibole and

clinopyroxene microphenocrysts in the mafic enclave indicate a change in some element concentrations (such as Al and Fe) from phases I to V. Therefore, as changes in the Al contents of amphibole can be an indication of crystallisation pressure, temperature or fO_2 change, this could provide an insight into not only mafic end-member changes, but also enclave formation.

As highlighted in this thesis the transport of volatiles is vitally important in playing a role in eruption dynamics. The composition of the volatile phase transported through the shear fractures is unclear. Cordierite, which can trap H_2O and CO_2 in channels within its structure, could be potentially used to quantify the proportion of these volatiles with the gas phase. Questions arise about how the metal-rich fluids from the mafic magma mix with the pre-existing vapour phase in the andesite, where the two magmas may have differing fO_2. Therefore, further quantifying the nature of volatile transfer between the two magmas could yield further information on the potential for ore mineralisation in arc volcanism.

Bibliography

Adam, J., & Green, T. H. (1994). The effects of pressure and temperature on the partitioning of Ti, Sr and REE between amphibole, clinopyroxene and basanitic melts. *Chemical Geology*, 117, 219-233.

Aigner-Torres, M., Blundy, J., Ulmer, P., & Pettke, T. (2007). Laser Ablation ICPMS study of trace element partitioning between plagioclase and basaltic melts: an experimental approach. *Contributions to Mineralogy and Petrology*, *153*, 647-667.

Allen, A.G., Baxter, P.J., Ottley, C.J., (2000) Gas and particle emissions from Soufrière Hills Volcano, Montserrat, West Indies: characterization and health hazard assessment. *Bull.Volcanol*. 62, 8-19

Allen, S.R., McPhie, J., (2003) Phenocryst fragments in rhyolitic lavas and lava domes. *J. Volcanol. Geotherm. Res.* 126, 263-283

Anderson, A. T., Swihart, G. H., Artioli, G., & Geiger, C. A. (1984). Segregation vesicles, gas filter-pressing, and igneous differentiation. *The Journal of Geology*, 55-72.

Annen, C., Blundy, J. D., & Sparks, R. S. J. (2006). The genesis of intermediate and silicic magmas in deep crustal hot zones. *J. Petrol*. 47, 505-539.

Armbruster, T. (1985) Fe-rich cordierites from acid volcanic rocks, an optical and x-ray single-crystal structure study. *Contrib. Mineral. Petrol*. 91, 180-187

Arth, J. G. (1976). Behavior of trace elements during magmatic processes—a summary of theoretical models and their applications. *J. Res. US Geol. Surv*. 4, 41-47.

Aspinall, W. P., Miller, A. D., Lynch, L. L., Latchman, J. L., Stewart, R. C., White, R. A., & Power, J. A. (1998). Soufrière Hills eruption, Montserrat, 1995–1997: Volcanic earthquake locations and fault plane solutions. *Geophys. Res. Lett.* 25, 3397-3400.

Audétat, A., (2010) Source and evolution of molybdenum in the porphyry Mo (-Nb) deposit at Cave Peak, Texas. *J. Petrol.* 51, 1739-1760

Bachmann, O. & Bergantz, G. W. (2006) Gas percolation in upper-crustal silicic crystal mushes as a mechanism for upward heat advection and rejuvenation of near-solidus magma bodies. *J. Volcanol. Geotherm. Res.*149, 85-102.

Bacon, C. R. 1986. Magmatic Inclusions in Silicic and Intermediate Volcanic Rocks. *J. Geophys. Res. Lett.* 91, 6091-6112

Baker, D.R., Alletti, M., (2012) Fluid saturation and volatile partitioning between melts and hydrous fluids in crustal magmatic systems: The contribution of experimental measurements and solubility models. *Earth-Sci. Reviews.* 114, 298-324

Ban, M., Takahashi, K., Horie, T. & Toya, N. (2005) Petrogenesis of Mafic Inclusions in Rhyolitic Lavas from Narugo Volcano, North eastern Japan. *J. Petrol.* 46, 1543-1563.

Barclay, J., Herd, R. A., Edwards, B. R., Christopher, T., Kiddle, E. J., Plail, M. & Donovan, A. (2010) Caught in the act: Implications for the increasing abundanceof mafic enclaves during the recent eruptive episodes of the Soufrière Hills Volcano, Montserrat. *Geophys. Res. Lett.* 37, L00E09. doi:10.1029/2010GL042509.

Barclay, J., Rutherford, M.J., Carroll, M.R., Murphy, M.D., Devine, J.D., Gardner, J. & Sparks, R.S.J. (1998) Experimental phase equilibria constraints on pre-eruptive storage conditions of the Soufrière Hills magma. . *Geophys. Res. Lett.* 25, 3437-3440

Barker, D.S., (1987) Rhyolites contaminated with metapelite and gabbro, Lipari, Aeolian Islands, Italy: products of lower crustal fusion or of assimilation plus fractional crystallization? *Contrib. Mineral. Petrol.* 97, 460-472

Berlo, K., Tuffen, H., Smith, V., Castro, J.M., Pyle, D.M., Mather, T., Geraki, K., (2013) Element variations in rhyolitic magma resulting from gas transport. *Geochim. Cosmochim. Acta.* 121, 436-451

Bindeman, I. N., Davis, A. M., & Drake, M. J. (1998). Ion microprobe study of plagioclase-basalt partition experiments at natural concentration levels of trace elements. *Geochimica et Cosmochimica Acta*, 62, 1175-1193.

Blake, S. & Fink, J. H. (2000). On the deformation and freezing of enclaves during magma mixing. *J. Volcanol. Geotherm. Res.* 95, 1-8.

Blake, S. & Ivey, G. N. (1986). Magma-mixing and the dynamics of withdrawal from stratified reservoirs. *J. Volcanol. Geotherm. Res.* 27, 153-178.

Botcharnikov, R.E., Linnen, R.L., Holtz, F. (2010). Solubility of Au in Cl- and S-bearing hydrous silicate melts. *Geochim. Cosmochim. Acta*. 74, 2396-2411

Browne, B. L. & Gardner, J. E. (2006). The influence of magma ascent path on the texture, mineralogy, and formation of hornblende reaction rims. *Earth Planet. Sci. Lett.* 246, 161-176.

Browne, B. L., Eichelberger, J. C., Patino, L. C., Vogel, T. A., Dehn, J., Uto, K. & Hoshizumi, H. (2006a). Generation of Porphyritic and Equigranular Mafic

Enclaves During Magma Recharge Events at Unzen Volcano, Japan. *J.Petrol.* 47, 301-328.

Browne, B. L., Eichelberger, J. C., Patino, L. C., Vogel, T. A., Uto, K. & Hoshizumi, H. (2006b). Magma mingling as indicated by texture and Sr / Ba ratios of plagioclase phenocrysts from Unzen volcano, SW Japan. *J. Volcanol. Geotherm. Res.*154, 103-116.

Bryan, W. B., Finger, L. W., & Chayes, F. (1969). Estimating proportions in petrographic mixing equations by least-squares approximation. *Science*, 163, 926-927.

Buckley, V. J. E., Sparks, R. S. J. & Wood, B. J. (2006). Hornblende dehydration reactions during magma ascent at Soufrière Hills Volcano, Montserrat. *Contrib. Mineral. Petrol.* **151**, 121-140. DOI 10.1007/s00410-005-0060-5

Burgisser, A., & Bergantz, G. W. (2011). A rapid mechanism to remobilize and homogenize highly crystalline magma bodies. *Nature*, *471*(7337), 212-215.

Cabrera, A., Weinberg, R. F., Wright, H.M.N., Zlotnik, S., Cas, R.A.F., (2011). Melt fracturing and healing: A mechanism for degassing and origin of silicic obsidian. *Geology*. 39, 67-70

Candela, P.A., Holland, H.D., (1984). The partitioning of copper and molybdenum between silicate melts and aqueous fluids. *Geochim. Cosmochim. Acta.* 48, 373-380

Cardoso, S. S. S. & Woods, A. W. (1999). On convection in a volatile-saturated magma. *Earth Planet. Sci. Lett.* 168, 301-310.

Cashman, K., Blundy, J., (2000). Degassing and crystallization of ascending andesite and dacite. *Philos. Trans. R. Soc. Lond. A.* 358, 1487-1513

Cashman, K.V., Thornber, C.R., and Pallister, J.S., (2008). From dome to dust: Shallow crystallization and fragmentation of conduit magma during the 2004 –2006 dome extrusion of Mount St. Helens, Washington, in A Volcano Rekindled: The First Year of Renewed Eruption at Mount St Helens, 2004– 2006, edited by D. R. Sherrod, W. E. Scott, and P. H. Stauffer, *U.S. Geol. Surv. Prof. Pap.*, 387-413, Professional paper 1750

Cassidy, M., Taylor, R. N., Palmer, M. R., Cooper, R. J., Stenlake, C., & Trofimovs, J. (2012). Tracking the magmatic evolution of island arc volcanism: Insights from a high-precision Pb isotope record of Montserrat, Lesser Antilles. *Geochemistry Geophysics Geosystems*, 13, Q05003.

Castro, J.M., Cordonnier, B., Tuffen, H., Tobin, M.J., Puskar, L., Martin, M.C., Bechtel, H.A., (2012).The role of melt-fracture degassing in defusing explosive rhyolite eruptions at volcán Chaitén. *Earth Planet. Sci. Lett*. 333-334, 63-69

Chardot, L., Voight, B., Foroozan, R., Sacks, S., Linde, A., Stewart, R., Hidayat, D., Clarke, A., Elsworth, D., Fournier, N., Komorowski, J.-C., Mattioli, G., Sparks, R.S.J., Widiwijayanti, C., (2010). Explosion dynamics from strainmeter and microbarometer observations, Soufrière Hills Volcano, Montserrat: 2008-2009. *Geophys. Res. Lett.* 37, L00E24 doi.org/10.1029/2010GL044661

Christopher, T., Edmonds, M., Humphreys, M. C., & Herd, R. A. (2010). Volcanic gas emissions from Soufrière Hills Volcano, Montserrat 1995–2009, with implications for mafic magma supply and degassing. *Geophys. Res. Lett* 37, L00E04

Christopher, T., Humphreys, M.C.S., Barclay, J., Genareau, K., De Angelis, S.H.M., Plail, M., Donovan, A., (2014) Petrological and geochemical variation during the Soufrière Hills eruption (1995-2010). In Wadge, G., Robertson, R. and Voight, B. (eds). The eruption of Soufrière Hills Volcano, Montserrat from 2000 to 2010. *Geol. Soc. Lon. Memoir*

Clemens, J.D., Wall, V.J., (1998). Controls on the mineralogy of S-type volcanic and plutonic rocks. *Lithos.* 21, 53-66

Clynne, M. A. 1989. The disaggregation of quenched magmatic inclusions contributes to chemical diversity in silicic lavas of Lassen Peak, California. Bull New Mexico *Bureau of Mines and Mineral resources,* 131, p. 54

Clynne, M. A. (1999). A Complex Magma Mixing Origin for Rocks Erupted in 1915, Lassen Peak, California. *J. Petrol.* 40, 105-132.

Cole, P.D.C., Smith, P.J., Stinton, A.J., Odbert, H.M., Bernstein, M.L., Komorowski, J.C., Stewart, R. (2014). Vulcanian explosions at Soufriere Hills Volcano, Montserrat between 2008 and 2010. In Wadge, G., Robertson, R. and Voight, B. (eds). The eruption of Soufrière Hills Volcano, Montserrat from 2000 to 2010. *Geol. Soc. Lon. Memoir*

Collins, W. J., Richards, S. R., Healy, B. E. & Ellison, P. I. (2000). Origin of heterogeneous mafic enclaves by two-stage hybridisation in magma conduits (dykes) below and in granitic magma chambers. *Geolog. Soc. America Spec. Papers* 350, 27-45.

Collins, W. J., Wiebe, R. A., Healy, B. & Richards, S. W. (2006). Replenishment, Crystal Accumulation and Floor Aggradation in the Megacrystic Kameruka Suite, Australia. *J. Petrol.* 47, 2073-2104.

Coombs, M. L., Eichelberger, J. C. & Rutherford, M. J. (2000). Magma storage and mixing conditions for the 1953-1974 eruptions of Southwest Trident volcano, Katmai National Park, Alaska. *Contrib. Mineral. Petrol.*140, 99-118.

Coombs, M. L., Eichelberger, J. C. & Rutherford, M. J. (2002). Experimental constraints on mafic enclave formation in volcanic rocks. *J. Volcanol. Geotherm. Res.* 119, 125-144

Cordonnier, B., Caricchi, L., Pistone, M., Castro, J., Hess, K.-U., Gottschaller, S., Manga, M., Dingwell, D.B., Burlini, L., (2012).The viscous-brittle transition of crystal-bearing silicic melt: Direct observation of magma rupture and healing. *Geology*. 40, 311-314

Costa, A., Melnik, O., & Sparks, R. S. J. (2007). Controls of conduit geometry and wallrock elasticity on lava dome eruptions. *Earth Planet. Sci. Lett.* 260, 137-151.

Couch , S., Harford, C.L., Sparks, R. S. J. & Carroll, M. (2003). Experimental constraints on the conditions of highly calcic plagioclase microlites at the Soufrière Hills Volcano, Montserrat. *J. Petrol.* 44, 1455-1475

Couch, S., Sparks, R. S. J. & Carroll, M. R. (2001). Mineral disequilibrium in lavas explained by convective self-mixing in open magma chambers. *Nature* 411, 1037-1039.

Darling, R.S., Chou, I-M., Bodnar, R.J., (1997). An Occurrence of Metastable Cristobalite in High-Pressure Garnet Granulite. *Science.* 276, 91-93

Darnell, A. R., Barclay, J., Herd, R. A., Phillips, J. C., Lovett, A. A., & Cole, P. (2012). Geographical information system approaches for hazard mapping of dilute lahars on Montserrat, West Indies. *Bull. volcanol*. 74, 1337-1353.

Davidson, J. P., Hora, J. M., Garrison, J. M., & Dungan, M. A. (2005). Crustal forensics in arc magmas. *J. Volcanol. Geotherm. Res.* 140, 157-170.

De Angelis, S. H., Larsen, J., & Coombs, M. (2013). Pre-eruptive Magmatic Conditions at Augustine Volcano, Alaska, 2006: Evidence from Amphibole Geochemistry and Textures. *J. Petrol. 54*, 1939-1961.

DePaolo, D. J. (1981). Trace element and isotopic effects of combined wallrock assimilation and fractional crystallization. *Earth and planetary science letters*, 53, 189-202.

Denlinger, R. P., & Hoblitt, R. P. (1999). Cyclic eruptive behavior of silicic volcanoes. *Geology*, 27, 459-462.

Devine, J. D., Murphy, M. D., Rutherford, M. J., Barclay, J., Sparks, R. S. J., Carroll, M. R., Young, S. R. & Gardner, J. E. (1998). Petrologic Evidence for Pre-Eruptive Pressure-Temperature Conditions, and Recent Reheating, of Andesitic Magma Erupting at the Soufrière Hills Volcano, Montserrat, W.I. *Geophys. Res. Lett.* 25 3669-3672.

Devine, J.D., Murphy, M.D., Rutherford, M.J., Barclay, J., Sparks, R.S.J., Carroll, M.R., Young, S.R., Gardner, J.E., (1998). Petrologic evidence for pre-eruptive pressure-temperature conditions, and recent reheating, of andesitic magma erupting at the Soufriere Hills Volcano, Montserrat, W.I. *Geophys. Res. Lett*. 25, 3669-3672

Devine, J.D., Rutherford, M.J. (2014) Magma storage region processes of the Soufriere Hills Volcano, Montserrat. In Wadge, G., Robertson, R. and Voight, B. (eds). The eruption of Soufrière Hills Volcano, Montserrat from 2000 to 2010. *Geol. Soc. Lon. Memoir*

Di Toro, G., Hirose, T., Nielsen, S., Pennacchioni, G., Shimamoto, T., (2006). Natural and experimental evidence of melt lubrication of faults during earthquakes. *Science*. 311, 647-649

Dingwell, D.B. (1996). Volcanic dilemma: Flow or blow? *Science* 273, 1054-1055

Douce, A.E.P., (1992). Calculated relationships between activity of alumina and phase assemblages of silica-saturated igneous rocks. Petrogenetic implications of magmatic cordierite, garnet and aluminosilicate. *J. Volcanol. Geotherm. Res.* 52, 43-63

Druitt, T. H., Young, S. R., Baptie, B., Bonadonna, C., Calder, E. S., Clarke, A. B., Cole, P.D., Harford, C.L., Herd, R.A., Luckett, R., Ryan, G., Voight, B. (2002). Episodes of cyclic Vulcanian explosive activity with fountain collapse at Soufrière Hills Volcano, Montserrat. *Geological Society, London, Memoirs*, *21*(1), 281-306.

Dungan, M. A., & Davidson, J. (2004). Partial assimilative recycling of the mafic plutonic roots of arc volcanoes: An example from the Chilean Andes. *Geology*, *32*, 773-776.

Dunn, T., & Sen, C. (1994). Mineral/matrix partition coefficients for orthopyroxene, plagioclase, and olivine in basaltic to andesitic systems: a combined analytical and experimental study. *Geochimica et Cosmochimica Acta*, 58, 717-733.

Edmonds, M., Pyle, D., Oppenheimer, C., (2001). A model for degassing at the Soufrière Hills Volcano, Montserrat, West Indies, based on geochemical data. *Earth Planet. Sci. Lett.* 186, 159-173

Edmonds, M., Pyle, D., Oppenheimer, C., (2002). HCl emissions at Soufrière Hills Volcano, Montserrat, West Indies, during a second phase of dome building: November 1999 to October 2000. *Bull.Volcanol*. 64, 21-30

Edmonds, M. Oppenheimer, C., Pyle, D.M., Herd, R.A., Thompson, G., (2003) SO_2 emissions from Soufrière Hills Volcano and their relationship to conduit permeability, hydrothermal interaction and degassing regime. J. *Volcan. Geotherm. Res*. 124, 23-43

Edmonds, M., Herd, R. A., (2007). A volcanic degassing event at the explosive-effusive transition. *Geophys. Res. Lett.* 34, L21310

Edmonds, M., Aiuppa, A., Humphreys, M., Moretti, R., Giudice, G., Martin, R. S., Herd, R. A. & Christopher, T. (2010). Excess volatiles supplied by mingling of mafic magma at an andesite arc volcano. *Geochem. Geophys. Geosyst.* 11, Q04005. doi:10.1029/2009GC002781.

Edmonds, M., Humphreys, M. C. S., Hauri, E., Herd, R., Wadge, G., Rawson, H., Ledden, R., Plail, M., Barclay, J., Aiuppa, A., Christopher, T., Giudice, G. & Guida, R. (2014). Pre-eruptive vapour and its role in controlling eruption style and longevity at Soufrière Hills Volcano. In Wadge, G., Robertson, R. and Voight, B. (eds). The eruption of Soufrière Hills Volcano, Montserrat from 2000 to 2010. *Geol. Soc. Lon. Memoir*

Eichelberger, J. C. (1980). Vesiculation of mafic magma during replenishment of silicic magma reservoirs. *Nature* 288, 446-450.

Eichelberger, J.C., Carrigan, C.R., Westrich, H.R., (1986). Non-explosive silicic volcanism. *Nature* 323, 598-602

Eichelberger, J. (1995). Silicic volcanism: ascent of viscous magmas from crustal reservoirs. *Annual Review of Earth and Planetary Sciences*, 23, 41-64.

Eichelberger, J. C., Chertkoff, D. G., Dreher, S. T., & Nye, C. J. (2000). Magmas in collision: rethinking chemical zonation in silicic magmas. *Geology*, *28*(7), 603-606.

Elsworth, D., Mattioli, G., Taron, J., Voight, B. & Herd, R. (2008). Implications of Magma Transfer Between Multiple Reservoirs on Eruption Cycling. *Science* 322, 246-248.

Farup, I., Drezet. J.-M., Rappaz, M., (2001). In situ observation of hot tearing formation in succinonitrile-acetone. *Acta Materialia* 49, 1261-1269

Feeley, T. C. & Dungan, M.A. (1996). Compositional and dynamic controls on mafic-silicic magma interactions at continental arc volcanoes: Evidence from Cordon El Guadal, Tatara-San Pedro complex, Chile. *J. Petrol.* 37, 1547-1577

Feeley, T. C., Wilson, L. F. & Underwood, S. J. (2008). Distribution and compositions of magmatic inclusions in the Mount Helen dome, Lassen Volcanic Center, California: Insights into magma chamber processes. *Lithos* 106, 173-189.

Frank, M.R., Candela, P.A., Piccoli, P.M., Glascock, M.D., (2002). Gold solubility, speciation, and partitioning as a function of HCl in the brine-silicate melt-metallic gold system at 800°C and 100 MPa. *Geochim. Cosmochim. Acta*. 66, 3719-3732

Frank, M.R., Simon, A.C., Pettke, T., Candela, P.A., Piccoli, P.M., (2011). Gold and copper partitioning in magmatic-hydrothermal systems at 800°C and 100 MPa. *Geochim. Cosmochim. Acta*. 75, 2470-2482

Frey, H. M. & Lange, R. A. (2011). Phenocryst complexity in andesites and dacites from the Tequila volcanic field, Mexico: Resolving the effects of degassing vs. magma mixing. *Contrib. Mineral. Petrol.*162, 415-445.

Frost, T. P., & Mahood, G. A. (1987). Field, chemical, and physical constraints on mafic-felsic magma interaction in the Lamarck Granodiorite, Sierra Nevada, California. *Geological Society of America Bulletin*, 99, 272-291.

Fujimaki, H., Tatsumoto, M., & Aoki, K. I. (1984). Partition coefficients of Hf, Zr, and REE between phenocrysts and groundmasses. *Journal of Geophysical Research: Solid Earth (1978–2012)*, 89, B662-B672.

Garcia, M. O. & Jacobson, S. S. (1979). Crystal clots, amphibole fractionation and the evolution of calc-alkaline magmas. *Contrib. Mineral. Petrol* 69, 319-327.

Ghiorso, M.S., Evans, B.W., (2008). Thermodynamics of Rhombohedral Oxide Solid Solutions and a Revision of the Fe-Ti Two-oxide Geothermometer and Oxygen-barometer. *American J. Science.* 308, 957-1039.

Giachetti, T., Druitt, T. H., Burgisser, A., Arbaret, L. & Galven, C. (2010). Bubble nucleation, growth and coalescence during the 1997 Vulcanian explosions of Soufrière Hills Volcano, Montserrat. *J. Volcanol. Geotherm. Res.* 193, 215-231.

Giordano, D., Russell, J.K. & Dingwell, D.B. (2008) Viscosity of magmatic liquids: A model. *Earth Planet. Sci. Lett.* 271, 123-134

Gonnermann, H.M., Manga, M., (2003). Explosive volcanism may not be an inevitable consequence of magma fragmentation. *Nature* 426, 432-435

Gonnermann, H.M., Manga, M., (2005). Nonequilibrium magma degassing. Results from modeling of the ca. 1340 A.D. eruption of Mono Craters, California. *Earth Planet. Sci. Lett.* 238, 1-16

Gonnermann, H. M., & Manga, M. (2007). The fluid mechanics inside a volcano. *Annu. Rev. Fluid Mech.*, *39*, 321-356.

Green, T. H., Adam, J., & Site, S. H. (1993). Proton microprobe determined trace element partition coefficients between pargasite, augite and silicate or carbonatitic melts. *EOS*, 74, 340.

Grunewald, U., Sparks, R.S.J., Kearns, S., Komorowski, J.C., (2000). Friction marks on blocks from pyroclastic flows at the Soufrière Hills Volcano, Montserrat: Implications for flow mechanisms. *Geology*. 28, 827-830

Hammouya, G., Allard, P., Jean-Baptiste, P., Parello, F., Sernet, M.P., Young, S.R., (1998). Pre- and syn-eruptive geochemistry of volcanic gases from Soufriere Hills of Montserrat, West Indies. *Geophys. Res. Lett*. 25, 3685-3688

Harford, C. L., Pringle, M. S., Sparks, R. S. J. & Young, S. R. (2002). The volcanic evolution of Montserrat using 40Ar/39Ar geochronology. *In*: Druitt, T.H. & Kokelaar, B.P. (eds). *The eruption of the Soufrière Hills Volcano, Montserrat from 1995 to 1999. Geolog. Soc. Lon. Memoir* 21, pp. 93-113.

Haughton, D.R., Roeder, P.L. & Skinner, B.J., (1974). Solubility of sulfur in mafic magmas. *Econ. Geol.* 69, 451-467

Hedenquist, J.W.,Lowenstern, J.B. (1994). The role of magmas in the formation of hydrothermal ore deposits. Nature 370, 519-527

Heiken, G., Wohletz, K., Eichelberger, J., (1988). Fracture filling and intrusive pyroclasts, Inyo Domes, California. *J. Geophys. Res.* 93, 4335-4350

Herd, R. A., Edmonds, M., & Bass, V. A. (2005). Catastrophic lava dome failure at Soufriere Hills volcano, Montserrat, 12–13 July 2003. *J. Volcanol. Geotherm. Res.* 148, 234-252.

Higuchi, H., & Nagasawa, H. (1969). Partition of trace elements between rock-forming minerals and the host volcanic rocks. *Earth and Planetary Science Letters*, 7, 281-287.

Hilyard, M., Nielsen, R. L., Beard, J. S., Patiñõ-Douce, A., & Blencoe, J. (2000). Experimental determination of the partitioning behavior of rare earth and high field strength elements between pargasitic amphibole and natural silicate melts. *Geochimica et Cosmochimica Acta*, 64, 1103-1120.

Holland, A.S.P., Watson, I.M., Phillips, J.C., Caricchi, L., Dalton, M.P., (2011). Degassing processes during lava dome growth: Insights from Santiaguito lava dome, Guatemala. *J. Volcanol. Geotherm. Res.* 202,153-166

Horwell, C.J., Williamson, B.J., Donaldson, K., Le Blond, J.S., Damby, D.E., Bowen, L., (2012). The structure of volcanic cristobalite in relation to its toxicity; relevance for the variable crystalline silica hazard. *Particle and Fibre Toxicology* 9, 44

Huber, C., Bachmann, O., & Dufek, J. (2010). The limitations of melting on the reactivation of silicic mushes. *J. Volcanol. Geotherm. Res.* 195, 97-105.

Humphreys, M. C. S., Edmonds, M., Christopher, T. & Hards, V. (2010). Magma hybridisation and diffusive exchange recorded in heterogeneous glasses from Soufrière Hills Volcano, Montserrat. *Geophys. Res. Lett.* 37, L00E06. doi:10.1029/2009GL041926.

Humphreys, M., Christopher, T. & Hards, V. (2009). Microlite transfer by disaggregation of mafic inclusions following magma mixing at Soufrière Hills volcano, Montserrat. *Contrib. Mineral. Petrol.***157**, 609-624. Doi: 10.1007/s00410-008-0356-3.

Humphreys, M.C.S., Christopher, T., Hards, V., (2009). Microlite transfer by disaggregation of mafic inclusions following magma mixing at Soufrière Hills volcano, Montserrat. *Contrib. Mineral. Petrol*. 157, 609-624

Humphreys, M.C.S., Edmonds, M., Christopher, T., Hards, V., (2010). Magma hybridisation and diffusive exchange recorded in heterogeneous glasses from Soufrière Hills, Montserrat. *Geophys. Res. Lett.* 37, L00E06, doi:10.1029/2009GL041926

Humphreys, M.C.S., Edmonds, M., Plail, M., Barclay, J., Parkes, D., Christopher, T. (2012). A new method to quantify the real supply of mafic components to a hybrid andesite. *Contrib. Mineral. Petrol.* 165, 191-215

Jaupart, C., (1998). Gas loss from magmas through conduit walls during eruption. *Geol. Soc. Lon. Spec. Publ.* 145, 73-90

Jaupart, C., Allegre, C.J., (1991). Gas content, eruption rate and instabilities of eruption regime in silicic volcanoes. *Earth. Planet. Sci. Lett*. 102, 413-429

Jenner, F.E., O'Neill, H.C., Arculus, R.J., Mavrogenes, J.A., (2010). The magnetite crisis in the evolution of Arc-related magmas and the initial concentration of Au, Ag and Cu. *J. Petrol.* 51, 2445-2464

Johannes, W. Koepke, J., Behrens, H., (1993). Partial melting reactions of plagioclase and plagioclase-bearing assemblages. In: I. Parson (Ed.), Feldspars and their reactions. Klower, Dordrecht, 161-194

Kendrick, J.E., Lavallée, Y., Ferk, A., Perugini, D., Leonhardt, R., Dingwell, D.B., (2012). Extreme frictional processes in the volcanic conduit of Mount St. Helens (USA) during the 2004-2008 eruption. *J. Struct. Geol.* 38, 61-76

Keppler, H., Wyllie, P.J., (1991). Partitioning of Cu, Sn, Mo, W, and Th between melt and aqueous fluid in the systems haplogranite-H2O-HCl and haplogranite-H2O-HF. *Cont. Mineral. Petrol.* 109, 139-150

Komorowski, J.-C., Legendre, Y., Christopher, T., Bernstein, M., Stewart, R., Joseph, E., Fournier, N., Chardot, L., Finizola, A., Wadge, G., Syers, R., Williams, C., Bass, V., (2010). Insights into processes and deposits of hazardous vulcanian explosions at Soufrière Hills Volcano during 2008 and 2009 (Montserrat, West Indies). *Geophys. Res. Lett*. 37, L00E19 doi:10.1029/2010GL042558

LaTourrette, T., Hervig, R. L., & Holloway, J. R. (1995). Trace element partitioning between amphibole, phlogopite, and basanite melt. *Earth and Planetary Science Letters*, 135, 13-30.

Lacroix, A., (1949). La Montagne Pelee et ses eruptions. Paris: Masson et Cie. Sur les enclaves endopolygenes de Saint-Vincent. *Bull. Soc.fr. Mineral. Crislallogr*. 72, 571-90.

Langmuir, C. H., Vocke Jr, R. D., Hanson, G. N., & Hart, S. R. (1978). A general mixing equation with applications to Icelandic basalts. *Earth and Planetary Science Letters*, 37, 380-392.

Larocque, A.C.L., Stimac, J.A., Siebe, C., Greengrass, K., Chapman, R., Mejia, S.R., (2008). Deposition of a high-sulfidation Au assemblage from a magmatic volatile phase, Volcán Popocatépetl, Mexico. *J. Volcanol. Geotherm. Res.* 170, 51-60

Lavallée, Y., Mitchell, T.M., Heap, M.J., Vasseur, J., Hess, K.U., Hirose, T., Dingwell, D., (2012). Experimental generation of volcanic pseudotachylytes: Constraining rheology. *J. Struct. Geol*. 38, 222-233

Leake, B. A., Woolley, A. R., Arps, C. E. S., Birch, W. D., Gilbert, M. C., Grice, J. D., Hawthorne, F. C., Kato, A., Kisch, H. J., Krivovichev, V. G., Linthout, K., Laird, J., Mandarino, J. A., Maresch, W. V., Nickel, E. H., Rock, N. M. S., Schumacher, J. C., Smith, D. C., C.N, S. N., Ungaretti, L., Whittaker, E. J. W. & Youhzi, G. (1997). Nomenclature of Amphiboles: Report of the Subcommitte on Amphiboles of the International Mineralogical Association, commission on new minerals and mineral names. *The Canadian Mineralogist* 35, 219-246.

Lemarchand, F., Villemant, B., & Calas, G. (1987). Trace element distribution coefficients in alkaline series. *Geochimica et Cosmochimica Acta*, 51, 1071-1081.

Lensky, N.G., Sparks, R.S.J., Navon, O., Lyakhovsky, V. (2008). Cyclic activity at Soufrière Hills Volcano, Montserrat: degassing-induced pressurization and stick-slip extrusion. *Geol. Soc. Spec. Pub*. 307, 169-188

Liu, Y., Zhang, Y., Behrens, H., (2005). Solubility of H2O in rhyolitic melts at low pressures and a new empirical model for mixed H2O-CO2 solubility in rhyolitic melts. *J. Volcanol. Geotherm. Res*. 143, 219-235

Liu, Y., Samaha, N-T., Baker, D.R., (2007). Sulphur concentration at sulphide saturation (SCSS) in magmatic silicate melts. *Geochim. Cosmochim. Acta* 71, 1783-1799

Loughlin, S. C., Calder, E. S., Clarke, A., Cole, P. D., Luckett, R., Mangan, M. T., Pyle, D.M., Sparks, R.S.J., Voight, B.,Watts, R. B. (2002). Pyroclastic flows and surges generated by the 25 June 1997 dome collapse, Sonfière Hills Volcano, Montserrat. *Geolog. Soc. Lon., Memoirs*, 21(1), 191-209.

Lowensten, J.B., Mahood, G.A., Rivers, M.L. Sutton, S.R., (1991). Evidence for extreme partitioning of copper into a magmatic vapour phase. *Science* 252, 1405-1409

Luhr, J. F., & Carmichael, I. S. (1985). Jorullo Volcano, Michoacán, Mexico (1759–1774): the earliest stages of fractionation in calc-alkaline magmas. *Contributions to Mineralogy and Petrology*, 90, 142-161.

Mann, C.K. (2010). Magma chamber dynamics at Soufrière Hills Volcano, Montserrat. PhD thesis, McGill University

Martin, V. M., Holness, M. B. & Pyle, D. M. (2006a). Textural analysis of magmatic enclaves from the Kameni Islands, Santorini, Greece. *J. Volcanol. Geotherm. Res.* 154, 89-102.

Martin, V. M., Pyle, D. M. & Holness, M. B. (2006b). The role of crystal frameworks in the preservation of enclaves during magma mixing. *Earth Planet. Sci. Lett.* 248, 787-799.

Matsui , Y. (1977). Crystal structure control in trace element partitioning between crystal and magma. *Bull. Soc. Fr. Mineral. Cristallogr.* 100, 315-324.

Matthews, S. J., Gardeweg, M. C., & Sparks, R. S. J. (1997). The 1984 to 1996 cyclic activity of Lascar Volcano, northern Chile: cycles of dome growth, dome subsidence, degassing and explosive eruptions. *Bull.Volcanol*. 59, 72-82.

Mattioli, G. S. & Herd, R. (2003). Correlation of cyclic surface deformation recorded by GPS geodesy with surface magma flux at Soufrière Hills Volcano, Montserrat. *Seismol. Res. Lett* 74, 230.

McKenzie, D. A. N., & O'nions, R. K. (1991). Partial melt distributions from inversion of rare earth element concentrations. *Journal of Petrology*, 32, 1021-1091.

Melnik, O., & Sparks, R. S. J. (1999). Nonlinear dynamics of lava dome extrusion. *Nature* 402, 37-41.

Melnik, O., Sparks, R.S.J. (2002). Dynamics of magma ascent and lava extrusion at Soufriere Hills volcano, Montserrat. In: Druitt, T.H. Kokelaar, B.P., (Eds), The eruption of Soufriere Hills volcano, Montserrat from 1995 to 1999. *Geol. Soc. Lon. Memoirs.* 21, 153-171

Melnik, O., & Sparks, R. S. J. (2005). Controls on conduit magma flow dynamics during lava dome building eruptions. *J. Geophys. Res. Solid Earth (1978–2012)*, 110 (B2) 1-21.

Miller, C. F., Furbish, D. J., Walker, B. A., Claiborne, L. L., Koteas, G. C., Bleick, H. A., & Miller, J. S. (2011). Growth of plutons by incremental emplacement of sheets in crystal-rich host: Evidence from Miocene intrusions of the Colorado River region, Nevada, USA. *Tectonophysics*, *500*, 65-77.

Mirwald, P.W., (1982). A high pressure phase transition in cordierite. *American mineral.* 96, 277-283

Molina, I. Kumagai, H., Yepes, H., (2004). Resonances of a volcanic conduit triggered by repetitive injections of an ash-laden gas. *Geophys. Res. Lett.* 31, L03603

Murphy, M. D., Sparks, R. S. J., Barclay, J., Carroll, M. R. & Brewer, T. S. (2000). Remobilization of Andesite Magma by Intrusion of Mafic Magma at the Soufrière Hills Volcano, Montserrat, West Indies. *J. Petrol*.41, 21 - 42.

Murphy, M. D., Sparks, R. S. J., Barclay, J., Carroll, M. R., Lejeune, A. M., Brewer, T. S., Macdonald, R., Black, S. & Young, S. (1998). The Role of Magma Mixing in Triggering the Current Eruption at the Soufrière Hills Volcano, Montserrat, West Indies. *Geophys. Res. Lett.* 25, 3433-3436.

Murphy, M.D., Sparks, R.S.J., Barclay, J., Carroll, M.R., Brewer, T.S., (2000). Remobilization of andesite magma by intrusion of mafic magma at the Soufrière Hills Volcano, Montserrat, West Indies. *J.Petrol*. 41, 21-42

Nakagawa, M., Wada, K. & Wood, C. P. (2002). Mixed Magmas, Mush Chambers and Eruption Triggers: Evidence from Zoned Clinopyroxene Phenocrysts in Andesitic Scoria from the 1995 Eruptions of Ruapehu Volcano, New Zealand. *J. Petrol.* 43, 2279-2303.

Nakamura, M. (1995). Continuous mixing of crystal mush and replenished magma in the ongoing Unzen eruption. *Geology*, 23, 807-810.

Nelson, S. T. & Montana, A. (1992). Sieve-textured plagioclase in volcanic rocks produced by rapid decompression. *American Mineralogist* 77, 1242-1249.

Neuberg, J. (2000). Characteristics and causes of shallow seismicity in andesite volcanoes. *Philosophical Transactions of the Royal Society of London. Series A: Mathematical, Physical and Engineering Sciences*, 358(1770), 1533-1546.

Neuberg, J.W., Tuffen, H., Collier, L., Green, D., Powell, T., Dingwell, D., (2006). The trigger mechanism of low-frequency earthquakes on Montserrat. *J. Volcanol. Geotherm. Res.* 153, 37-50

Odbert, H.M., Stewart, R.C., Wadge, G., (2014). Cyclic phenomena at the Soufrière Hills Volcano, Montserrat. In Wadge, G., Robertson, R. and Voight, B. (eds). The eruption of Soufrière Hills Volcano, Montserrat from 2000 to 2010. *Geol. Soc. Lon. Memoir*

Okumura, S., Nakamura, M., Uesugi, K., Nakono, T., Fujioka, T., (2013). Coupled effect of magma degassing and rheology on silicic volcanism. *Earth Planet. Sci. Lett.* 362, 163-170

Oppenheimer, C., Edmonds, M., Francis, P., & Burton, M. (2002). Variation in HCl/SO2 gas ratios observed by Fourier transform spectroscopy at Soufrière Hills Volcano, Montserrat. *Geological Society, London, Memoirs*, 21, 621-639.

Pallister, J.S., Hoblitt, R.P., Reyes, A.G., (1991). A basalt trigger for the 1991 eruptions of Pinatubo volcano? *Nature* 356, 426-428

Pallister, J. S., Hoblitt, R. P. & Reyes, A. G. (1992). A basalt trigger for the 1991 eruptions of Pinatubo volcano? *Nature* 356, 426-428.

Pallister, J.S., Cashman, K., Hagstrum, J.T., Beeler, N.M., Moran, S.C., Denlinger, R.P. (2012). Faulting within the Mount St. Helens conduit and implications for volcanic earthquakes. *Geol. Soc. America. Bull*. doi: 10.1130/B30716.1

Paulatto, M., Annen, C., Henstock, T. J., Kiddle, E., Minshull, T. A., Sparks, R. S. J., & Voight, B. (2012). Magma chamber properties from integrated seismic tomography and thermal modeling at Montserrat. *Geochemistry, Geophysics, Geosystems*, 13 (1)

Philpotts, J. A., & Schnetzler, C. C. (1970). Phenocryst-matrix partition coefficients for K, Rb, Sr and Ba, with applications to anorthosite and basalt genesis. *Geochimica et Cosmochimica Acta*, 34, 307-322.

Plank, T., (2005). Constraints from Thorium/Lanthanum on sediment recycling at subduction zones and the evolution of continents. *J. Petrol.* 46, 921-944

Plechov, P.Y., Tsai, A.E., Shcherbakov, D., Dirksen, O.V. (2008). Opacitization conditions of hornblende in Bezymyannyi Volcano andesites (March 30 1956 eruption) *Petrology* 16, 19-35

Ridolfi, F. & Renzulli, A. (2011). Calcic amphiboles in calc-alkaline and alkaline magmas: thermobarometric and chemometric empirical equations valid up to 1,130 °C and 2.2 GPa. *Contrib. Mineral. Petrol.* 163, 877-895.

Rea, W. J. (1974). The volcanic geology and petrology of Montserrat, West Indies. *Journal of the Geological Society*, 130, 341-366.

Reagan, M. K., Gill, J. B., Malavassi, E., & Garcia, M. O. (1987). Changes in magma composition at Arenal volcano, Costa Rica, 1968–1985: Real-time monitoring of open-system differentiation. *Bulletin of Volcanology*, 49, 415-434.

Reubi, O., & Blundy, J. (2009). A dearth of intermediate melts at subduction zone volcanoes and the petrogenesis of arc andesites. *Nature*, *461*, 1269-1273.

Rollinson, H. R., & Data, U. G. (1993). Evaluation, Presentation, Interpretation.

Ronov, A. B., & Yaroshevsky, A. A. (1976). A new model for the chemical structure of the Earth's crust. *Geochem. Int*, *13*, 89-121.

Rose, W. I. (1973). Pattern and mechanism of volcanic activity at the Santiaguito volcanic dome, Guatemala. *Bulletin Volcanologique* 37, 73-94.

Rose, W. I. (1987). Volcanic activity at Santiaguito volcano, 1976–1984. *Geological Society of America Special Papers*, 212, 17-28.

Rowe, M. C., Thornber, C. R., & Kent, A. J. (2008). Identification and evolution of the juvenile component in 2004-2005 Mount St. Helens ash. *US Geological Survey professional paper*, (1750), 629-646.

Rudnick, R. L. (1995). Making continental crust. *Nature*, *378*, 571-577.

Ruprecht, P. & Wörner, G. (2007). Variable regimes in magma systems documented in plagioclase zoning patterns: El Misti stratovolcano and Andahua monogenetic cones. *J. Volcanol. Geotherm. Res.*165, 142-162.

Rust, A.C., Cashman, K., Wallace, P.J., (2004). Magma degassing buffered by vapour flow through brecciated conduit margins. *Geology* 32, 349-352

Rutherford, M. J. & Devine, J. D. 2003. Magmatic Conditions and Magma Ascent as Indicated by Hornblende Phase Equilibria and Reactions in the 1995-2002 Soufrière Hills Magma. *J. Petrol.* 44, 1433-1453.

Schaefer, B., Frischknecht, R., Gunther, D., Dingwell, D.B., (1999). Determination of trace-element partitioning between fluid and melt using LA-ICP-MS analysis of synthetic fluid inclusions in glass. *Eur. J. Mineral.* 11, 415-426

Schwartzkopf, L.M. Schmincke, H-U., Troll, V.R., (2002). Friction marks on blocks from pyroclastic flows at the Soufriere Hills volcano, Montserrat: Implications for flow mechanisms: Comment: COMMENT. *Geology.* 30, 190

Schock, H. H. (1979). Distribution of rare-earth and other trace elements in magnetites. *Chemical Geology*, 26, 119-133.

Shepherd, J. B., Tomblin, J. F., & Woo, D. A. (1971). Volcano-seismic crisis in Montserrat, West Indies, 1966–67. *Bulletin Volcanologique*, 35, 143-162.

Simkin, T., Fiske, R.S., (1983). Krakatau 1883 – a centennial retrospective on the eruption and its atmospheric effects. *Weatherwise* 36, 244-255

Simon, A.C., Candela, P.A., Piccoli, P.M., Mengason, M., Englander, L. (2008). The effect of crystal-melt partitioning on the budgets of Cu, Au and Ag. *American Mineralogist.* 93, 1437-1448

Simon, A.C., Pettke, T., Candela. P.A., Piccoli, P.M., Heinrich, C.A., (2006). Copper partitioning in a melt-vapour-brine-magnetite-pyrrhotite assemblage. *Geochim. Cosmochim. Acta* 70, 5583-5600

Singer, B. S., Dungan, M. A. & Layne, G. D. (1995). Textures and Sr, Ba, Mg, Fe, K and Ti compositional profiles in volcanic plagioclase clues to the dynamics of calc-alkaline magma chambers. *American Mineralogist* 80, 776-798.

Sisson, T. W. (1994). Hornblende-melt trace-element partitioning measured by ion microprobe. *Chemical Geology*, 117, 331-344.

Smith, J.V., Miyake, Y., Oikawa, T. (2001). Interpretation of porosity in dacite lava domes as brittle-ductile failure textures. *J. Volcanol. Gotherm. Res.* 112, 25-35

Snyder, D., & Tait, S. (1996). Magma mixing by convective entrainment. *Nature*, 379, 529-531.

Snyder, D., Crambes, C., Tait, S. & Wiebe, R. A. (1997). Magma Mingling in Dikes and Sills. *J. Geol.* 105, 75-86.

Sparks, S. R., & Sigurdsson, H. (1977). Magma mixing: a mechanism for triggering acid explosive eruptions. *Nature*, 267, 315-318.

Sparks, R. S. J. & Marshall, L. A. (1986). Thermal and mechanical constraints on mixing between mafic and silicic magmas. *J. Volcanol. Geotherm. Res.* 29, 99-124.

Sparks, R. S. J. (1997). Causes and consequences of pressurisation in lava dome eruptions. *Earth Planet. Sci. Lett.* 150, 177-189.

Sparks, R.S.J., Murphy, M.D., Lejeune, A.M., Watts, R.B., Barclay, J. & Young, S.R. (2000). Control on the emplacement of the andesite lava dome of the Soufrière Hills volcano, Montserrat by degassing-induced crystallization. *Terra Nova* 12, 14-20.

Sparks, R. S. J., Barclay, J., Calder, E. S., Herd, R. A., Komorowski, J. C., Luckett, R., Norton, G., Ritchie, L.J., Voight, B.,Woods, A. W. (2002). Generation of a debris avalanche and violent pyroclastic density current on 26 December (Boxing Day) 1997 at Soufriere Hills Volcano, Montserrat. *Geological Society, London, Memoirs*, 21(1), 409-434.

Sparks, R.S.J., (2003). Forecasting volcanic eruptions. *Earth Planet. Sci. Lett.* 210, 1-15

Spray, J.G. (1987). Artificial generation of pseudotachylyte using friction welding apparatus - simulation on a fault plane. *J. Struct. Geol.* 9 , 49-60

Stasiuk, M.V., Barclay, J., Carroll, M.R., Jaupart, C., Ratté, J.C., Sparks, R.S.J., Tait, S.R. (1996). Degassing during magma ascent in the Mule Creek vent (USA). *Bull. Volcanol.* 58, 117-130

Stinton, A.J., Cole, P.D., Odbert, H.M., Christopher, T., Avard, G., Bernstein, M. 2014. Dome growth and valley fill during Phase 5 (8 October 2009 – 11 February 2010) at the Soufrière Hills Volcano, Montserrat. In Wadge, G., Robertson, R. and Voight, B. (eds). The eruption of Soufrière Hills Volcano, Montserrat from 2000 to 2010. *Geol. Soc. Lon. Memoir*

Stinton, A.J., Cole, P.D., Odbert, H.M., (2014) Geomorphic changes at the Soufrière Hills Volcano, Montserrat, during a short intensive episode of dome growth: 4 October 2009 - 11 February 2010. In Wadge, G., Robertson, R. and Voight, B. (eds). The eruption of Soufrière Hills Volcano, Montserrat from 2000 to 2010. *Geol. Soc. Lon. Memoir*

Sun, S. S., & McDonough, W. (1989). Chemical and isotopic systematics of oceanic basalts: implications for mantle composition and processes. *Geological Society, London, Special Publications*, 42, 313-345.

Sun, W., Arculus, R.J., Kamenetsky, V.S., Binns, R.A., 2004. Release of gold-bearing fluids in convergent margin magmas prompted by magnetite crystallization. Nature 431, 975-978

Taylor, B. E., Eichelberger, J. C., & Westrich, H. R. (1983). Hydrogen isotopic evidence of rhyolitic magma degassing during shallow intrusion and eruption. *Nature*, 306, 541-545.

Tepley, F. J., Davidson, J. P. & Clynne, M. A. (1999). Magmatic Interactions as Recorded in Plagioclase Phenocrysts of Chaos Crags, Lassen Volcanic Center, California. *J. Petrol.* 40, 787-806.

Thomas, N. & Tait, S. R. (1997). The dimensions of magmatic inclusions as a constraint on the physical mechanism of mixing. *J. Volcanol. Geotherm. Res.* 75, 167-178.

Thompson, P., Harley, S.L., Carrington, P., (2002). Sodium and potassium in cordierite – a potential thermometer for melts*? Eur. J. Mineral.* 14, 459-469

Tsuchiyama, A. (1985). Dissolution kinetics of plagioclase in the melt of the system diopside-albite-anorthite, and origin of dusty plagioclase in andesites. *Contrib. Mineral. Petrol*. 89, 1-16

Tuffen H. and Dingwell, D.B. (2005). Fault textures in volcanic conduits: evidence for seismic trigger mechanisms during silicic eruptions. *Bull. Volcanol*. 67, 370-387

Tuffen, H., Dingwell, D. B., Pinkerton, H., (2003). Repeated fracture and healing of silicic magma generate flow banding and earthquakes? *Geology* 31, 1089-1092

Turnbull, R., Weaver, S., Tulloch, A., Cole, J., Handler, M. & Ireland, T. (2010). Field and Geochemical Constraints on Mafic–Felsic Interactions, and Processes in High-level Arc Magma Chambers: an Example from the Halfmoon Pluton, New Zealand. *J. Petrol.* 51, 1477-1505.

Villemant, B. (1988). Trace element evolution in the Phlegrean Fields (Central Italy): fractional crystallization and selective enrichment. *Contributions to Mineralogy and Petrology*, 98, 169-183.

Wadge, G., Voight, B., Sparks, R.S.J., Cole, P., Loughlin, S.C., (2014). An overview of the eruption of Soufrière Hills Volcano from 200-2010. In Wadge, G., Robertson, R. and Voight, B. (eds). The eruption of Soufrière Hills Volcano, Montserrat from 2000 to 2010. *Geol. Soc. Lon. Memoir*

Walker, G.P.L. (1969). The breaking of magma. *Geological Magazine*. 106, 166-173.

Wallace, P. J. (2001). Volcanic SO_2 emissions and the abundance and distribution of exsolved gas in magma bodies. *J. Volcanol. Geotherm. Res.* 108, 85-106.

Wallace, P. J., & Edmonds, M. (2011). The sulfur budget in magmas: evidence from melt inclusions, submarine glasses, and volcanic gas emissions. *Reviews in Mineralogy and Geochemistry*, 73, 215-246.

Watts, R.B., Herd, R.A., Sparks, R.S.J., Young, S.R. (2002). Growth patterns and emplacement of the andesitic lava dome at Soufrière Hills Volcano, Montserrat. In Druitt, T.H. & Kokelaar, B.P. (eds) The eruption of soufriere Hills Volcano, Montserrat, from 1995-1999. *Geol. Soc. Lon. Memoir*. 21, 115-152

Weatherley, D.K. and Henley, R.W. (2013). Flash vaporization during earthquakes evidenced by gold deposits. *Nat. Geosci*. 6, 294-298

Webster, J.D., (1997). Exsolution of magmatic volatile phases from Cl-enriched mineralizing granitic magmas and implications for ore metal transport. *Geochim. Cosmochim. Acta*. 61, 1017-1029

Werner, C. A., Doukas, M. P., & Kelly, P. J. (2011). Gas emissions from failed and actual eruptions from Cook Inlet Volcanoes, Alaska, 1989–2006. *Bull. Volcanol*. 73, 155-173.

Wiebe, R. A. (1993). The Pleasant Bay Layered Gabbro—Diorite, Coastal Maine: Ponding and Crystallization of Basaltic Injections into a Silicic Magma Chamber. *J. Petrol*. 34, 461-489.

Wiebe, R. A., Smith, D., Sturm, M., King, E. M. & Seckler, M. S. (1997). Enclaves in the Cadillac Mountain Granite (Coastal Maine): Samples of Hybrid Magma from the Base of the Chamber. *J. Petrol*. 38, 393-423.

Willam-Jones, A.E., Heinrich, C.A., (2005). Vapour transport of metals and the formation of magmatic-hydrothermal ore deposits. *Econ. Geol*. 100, 1287-1312

Williams, T.J., Candela, P.A., Piccoli, P.M., (1995). The partitioning of copper between silicate melts and two-phase aqueous fluids: An experimental investigation at 1 kbar, 800°C and 0.5 kbar, 850°C. *Contrib. Mineral. Petrol*. 121, 388-399

Wood, C.P., (1994). Mineralogy at the magma-hydrothermal system interface in andesite volcanoes, New Zealand. *Geology* 22, 75-78

Woods, A. W., & Koyaguchi, T. (1994). Transitions between explosive and effusive eruptions of silicic magmas. *Nature* 370, 641-644.

Zack, T., Foley, S. F., & Jenner, G. A. (1997). A consistent partition coefficient set for clinopyroxene, amphibole and garnet from laser ablation microprobe analysis of garnet pyroxenites from Kakanui, New Zealand. *Neues Jahrbuch Fur Mineralogie-Abhandlungen*, 172, 23-42.

Zajacz, Z., Candela, P.A., Piccoli, P.M., Wälle, M., Sanchez-Valle, C., (2012). Gold and copper in volatile saturated mafic to intermediate magmas: Solubilities, partitioning,

and implications for ore deposit formation. *Geochim. Cosmochim. Acta* 91, 140-159

Zajacz, Z., Halter, W.E., Pettke, T., Guillong, M., (2008). Determination of fluid/melt partition coefficients by LA-ICPMS analysis of co-existing fluid and silicate melt inclusions: Controls on element partitioning. *Geochim. Cosmochim. Acta.* 72, 2169-2197

Zajacz, Z., Seo, J.H., Candela, P.A., Piccoli, P.M., Heinrich, C.A., Guillong, M., (2010). Alkali metals control the release of gold from volatile-rich magmas. *Earth Planet. Sci. Lett.* 297, 50-56

Zellmer, G. F. Hawkesworth., C. J. Sparks, R. S. J. Thomas, L. E. Harford, C. L. Brewer, T. S. Loughlin, S. C. (2003a). Geochemical Evolution of the Soufrière Hills Volcano, Montserrat, Lesser Antilles Volcanic Arc. *J. Petrol.* 44, 1349 -1374.

Zellmer, G. F., Sparks, R. S. J., Hawkesworth, C. J., & Wiedenbeck, M. (2003b). Magma emplacement and remobilization timescales beneath Montserrat: insights from Sr and Ba zonation in plagioclase phenocrysts. *J. Petrol. 44*, 1413-1431.

APPENDIX

The following is contained in an electronic appendix at the back of the thesis:

- Sample information
- Mineral analyses
- Geochemical data